Faculdade de Engenharia da Universidade do Porto

Novel Methodologies to Study the Crosstalk Between Neurons and Bone Using Advanced Microfluidic Platforms Containing Microelectrodes

Kristine Heiney

Dissertação realizada no âmbito do
Mestrado em Engenharia Biomédica

Orientador: Paulo Aguiar
Co-orientador: Meriem Lamghari

27 Julho 2018

U.PORTO
FEUP FACULDADE DE ENGENHARIA
UNIVERSIDADE DO PORTO

SERVIÇOS ACADÉMICOS

Entrega de dissertação/tese

Identificação Pessoal

Nome Kristine Heiney

E-mail up201600443@fe.up.pt **Telefone** 915 425 271

Identificação da dissertação/ tese

☒ Dissertação de Mestrado

Título Novel Methodologies to Study the Crosstalk Between Neurons and Bone Using Advanced Microfluidic Platforms Containing Microelectrodes

Palavras-chave neuroscience, electrophysiology, microfluidic platforms, bone innervation

Orientador Dr. Paulo Aguiar **Ano** 2018

Entrega da tese/dissertação

Deposito na FEUP, com o conhecimento do meu orientador, o texto da minha dissertação/tese em formato electrónico e autorizo a mesma a arquivar com as restrições abaixo indicadas, bem como a convertê-lo para qualquer formato, mantendo eu os direitos de autor.

Porto, 10 de Julho de 2018

(Assinatura do autor)

(Assinatura do orientador)

Pedido de confidencialidade

☒ Solicita-se que a dissertação/tese não seja colocada em consulta pública em papel ou formato electrónico, por um período de __1 ano__ (máx. 3 anos).

☐ Solicita-se que a parte constituída pelos anexos da minha dissertação/tese não seja colocada em consulta pública em papel ou formato electrónico por um período de _____ (máx. 3 anos).

Motivo: A manuscript on the computational tool developed in this dissertation project is awaiting publication.

(Assinatura do autor)

Concordo com o pedido formulado referente à confidencialidade da dissertação/tese. Existe um Acordo de Confidencialidade, anexo ao Contrato para a realização de Dissertação/Tese Sim:____ Não: X

(Assinatura do orientador)

Resumo

Os recentes avanços nas tecnologias de microfluídicas e microeléctrodos levaram ao desenvolvimento de dispositivos que combinam essas duas tecnologias para o uso experimental em neurociências. Através do confinamento a um microcanal, estes dispositivos permitem a localização precisa de axónios sobre os elétrodos de registo e a medição dos sinais electrofisiológicos que se propagam ao longo destes axónios. Tais dispositivos podem ser usados para observar a dinâmica da rede de culturas de neurónios, ou a comunicação entre duas populações de células plaqueadas em compartimentos de cultura isolados fluidicamente. O uso de plataformas microfluídicas em combinação com arranjos de microeléctrodos fornece novas capacidades para experiências *in vitro* em neurociência, permitindo o controlo da fonte, polarização e alvo dos sinais que se propagam ao longo de axónios confinados a microcanais, bem como amplificando os sinais extracelulares registados dos axónios. O objetivo principal do presente trabalho foi o desenvolvimento de uma ferramenta computacional para permitir a identificação e caracterização de potenciais de ação que se propagam ao longo dos axónios confinados aos microcanais de dispositivos microfluídicos, que contêm os microeléctrodos. Espera-se que este software, denominado µSpikeHunter, melhore o potencial de investigação de plataformas microfluídicas contendo microeléctrodos, fornecendo aos investigadores uma plataforma acessível com métodos avançados de análise de dados electrofisiológicos. O software desenvolvido contém um algoritmo robusto para a deteção de propagação de sinais, dois métodos para estimar a velocidade de propagação de sinais detetados e uma ferramenta de separação de sinais fácil de usar. Os algoritmos de estimativa de deteção e de velocidade de propagação de sinais foram validados usando dados sintéticos e dados experimentais de registos de neurónios corticais, tendo demonstrado excelente desempenho. O objetivo secundário deste trabalho foi aplicar o µSpikeHunter à investigação preliminar da faceta electrofisiológica do *crosstalk* entre neurónios sensoriais e osso, no contexto de um projeto de investigação, em andamento, financiado para este tópico. Para este fim, experiências recorrendo a explantes dos gânglios da raiz dorsal foram realizadas, tendo-se feito registos destes explantes cultivados num compartimento de um dispositivo microfluídico, com meio de cultura condicionado por osteoclastos adicionado no outro compartimento. Os resultados indicam que a atividade neuronal foi estimulada imediatamente após a adição do meio condicionado pelos osteoclastos e que a velocidade de propagação aumentou nas 24 horas após a incubação. O papel da inervação óssea no processo de remodelação óssea e os mecanismos subjacentes à sensação de dor óssea tornaram-se recentemente importantes alvos de investigação, e ambos

permanecem pouco caracterizados. Em particular, a faceta elétrica do *crosstalk* entre neurónios e osso tem sido pouco estudada, em grande parte devido à falta de ferramentas e metodologias adequadas para monitorizar a comunicação electrofisiológica entre as duas populações de células. Os resultados do presente trabalho fornecem um primeiro passo para a melhoria da compreensão da resposta eletrofisiológica dos neurónios à atividade dos osteoclastos, e o µSpikeHunter provará ser uma ferramenta valiosa no avanço desta linha de investigação.

Abstract

Recent advancements in microfluidic and microelectrode technology have led to the development of devices combining these two technologies for use in neuroscience experiments. These devices enable the precise localization of axons above recording electrodes by confinement to a microchannel and the targeted recording of electrophysiological signals propagating along these confined axons. Such devices can be used to observe the network dynamics of cultured neurons or the communication between two populations of cells plated in fluidically isolated culture compartments. The use of microfluidic platforms in combination with microelectrode arrays provides novel *in vitro* capabilities in neuroscience experiments by enabling the control of the source, polarization, and target of signals propagating along axons confined to microchannels as well as amplifying the extracellular signals recorded from the axons. The primary aim of the present work was the development of a computational tool to enable the identification and characterization of action potentials propagating along axons confined to the microchannels of microfluidic devices containing microelectrodes. This software, called μSpikeHunter, is expected to enhance the research potential of microfluidic platforms containing microelectrodes by providing researchers with a user-friendly platform with advanced methods for electrophysiological data analysis. The developed software contains a robust algorithm for the detection of propagating signals, two methods of estimating the propagation velocity of detected signals, and an easy-to-use graphical spike sorting tool. The spike detection and propagation velocity estimation algorithms were validated using synthetic data and experimental data from cortical neuron recordings and were demonstrated to show excellent performance. The secondary aim of this work was to apply μSpikeHunter to the preliminary investigation of the electrophysiological facet of the crosstalk between sensory neurons and bone in the context of a larger ongoing funded research project on this topic. To this end, experiments were carried out by recording DRG explants cultured in one compartment of a microfluidic device with osteoclast-conditioned culture medium added to the other compartment. The results indicate that neuronal activity was stimulated immediately upon the addition of osteoclast-conditioned medium and that the propagation velocity increased within 24 h after incubation. The role of the innervation of bone in the bone remodeling process and the mechanisms underlying the sensation of bone pain have recently become important targets of interest in research studies, and both remain poorly characterized. In particular, the electrical facet of the crosstalk between neurons and bone has been little studied, largely because of the lack of adequate tools and methodologies to monitor the

electrophysiological communication between the two cell populations. The results of the present work provide a first step toward improving the present understanding of the electrophysiological response of neurons to osteoclast activity, and μSpikeHunter will prove to be a valuable tool in advancing this line of research.

Acknowledgements

First and foremost, I would like to thank my advisor, Dr. Paulo Aguiar[1], for his support. His guidance and insight were invaluable in the creation and refinement of the software developed in this project, and I am grateful for his ability to foster innovation and excitement not only in my work but in the work of the whole NCN group. I would also like to thank my co-advisor, Dr. Meriem Lamghari[2] for helping me gain some perspective on the innervation of bone. I am very grateful to Dr. Cátia Lopes[1] and Dr. Estrela Neto[2] for maintaining the cell cultures used in the experiments here and sharing their expertise in cell culture with me. I also appreciate the work José Mateus[1] did in obtaining electrophysiological recordings for this work. Finally, I would like to thank the rest of my colleagues in the NCN group[1] and everyone from the GCB laboratory[3] for providing such a wonderful work environment at i3S.

[1] NCN – Neuroengineering and Computational Neuroscience group, i3S – Instituto de Investigação e Inovação em Saúde

[2] NSC – Neuro-Skeletal Circuits group, i3S

[3] GCB – Glial Cell Biology group, i3S

Contents

List of figures

List of tables

Abbreviations and symbols

List of abbreviations

ACh	Acetylcholine
AP	Action potential
AR	Adrenergic receptor
CGRP	Calcitonin gene-related peptide
CNS	Central nervous system
CPV	Cluster propagation velocity
CRL	Calcitonin receptor-like receptor
CSV	Comma-separated value
DIV	Days *in vitro*
DRG	Dorsal root ganglion
DSP	Digital signal processor
EAP	Extracellular action potential
ECM	Extracellular matrix
EEG	Electroencephalography
GUI	Graphical user interface
GUIDE	GUI development environment
HDF5	Hierarchical data format
HH	Hodgkin–Huxley
ID	Identification number
LSA	Line source approximation
MAD	Median absolute deviation
MCS	Multichannel systems
MEA	Microelectrode array
NE	Norepinephrine
NGF	Nerve growth factor
NK_1	Neurokinin-1
NPY	Neuropeptide Y
OC	Osteoclast-conditioned
PDMS	Poly(dimethylsiloxane)
PNS	Peripheral nervous system
RAMP	Receptor activity-modifying protein
RC	Resistor–capacitor

ROI	Region of interest
SNR	Signal-to-noise ratio
SP	Substance P
SPV	Single-sequence propagation velocity
UV	Ultraviolet
VIP	Vasoactive intestinal peptide

List of symbols

C_e	Electrode capacitance
C_{hd}	Capacitance of the membrane–electrolyte interface
C_m	Membrane capacitance
CI	Confidence index
$D_{i,j}$	Inter-electrode distance between electrodes i and j
E_{ion}	Reversal potential for a specific ion
E_m	Membrane reversal potential
g_{ion}	Conductance of a specific ion channel
$\bar{g}_{\text{ion}}$	Maximum conductance of a specific ion channel
I_{inj}	Injected current
I_{ls}	Amplitude of current from a linear current source
I_m	Transmembrane current
I_{out}	Longitudinal current in the extracellular space
m, h, n	Gating variables for sodium and potassium
n_E	Number of electrodes
n_{ev}	Number of events
R_a	Longitudinal resistance of the axonal intracellular space
R_e	Electrode resistance
R_{gap}	Gap resistance
R_m	Membrane resistance
R_{out}	Resistance in the extracellular space
R_{seal}	Sealing resistance
R_{spread}	Spreading resistance
Δs	Length of a linear current source
t	Time
v	Propagation velocity
V	Voltage
V_D	Event detection threshold
V_{in}	Intracellular potential
V_m	Membrane potential
V_{out}	Extracellular potential
x	Longitudinal distance along an axon
$\mathbf{X}_{i,j}$	Cross-correlation of ith and jth voltage traces of a propagation sequence
$Z_e{}'$	Effective electrode impedance
Z_a	Electrode amplifier impedance
$Z_a{}'$	Effective electrode amplifier impedance

α	Forward rate coefficient for gating variable
β	Backward rate coefficient for gating variable
λ	Length constant
ρ	Resistivity of extracellular fluid
σ	Conductivity of extracellular fluid
τ	Lag in cross-correlation
τ_b	Kendall rank coefficient
τ_m	Membrane time constant

Subscripts

C	cluster-based value
i, j	electrode indices
n	noise
p, q	propagation sequence indices
peak	corresponding to the peak value of the cross-correlation
s	signal
S	single-sequence value

Chapter 1

Introduction

The nervous system is responsible for the control of many functions in the body, and the mechanisms governing this control are complex and multifaceted. The fundamental unit of the nervous system is the neuron, and the basis by which neurons encode information and communicate with each other and other organs in the body is the generation and propagation of electrical signals. These electrical signals can initiate a cascade of events in innervated tissue or provide information to the brain about perceived changes to the environment or the body itself. Neuronal electrophysiology is commonly studied by recording neuronal activity using electrodes, and recent advancements in microelectrode technologies have provided researchers with an increasingly detailed view into the behavior of neurons [1].

Neurons are characterized by elongated processes that extend from the cell body and can span distances orders of magnitude greater than the size of the cell body [2]. However, these processes are very small in diameter, and many studies involving the recording of neuronal signals have focused on the more easily accessible cell body [3]. Recent advancements in microfluidic technology have provided an unprecedented amount of control over the growth and targeted recording of neuronal processes. With the use of compartmentalized microfluidic platforms, neurons can be cultured so that their cell bodies remain in one compartment while their axons are able to extend through microchannels into other fluidically isolated compartments [4], [5]. Electrodes can also be positioned beneath these microchannels to allow the targeted recording of axonal signals [6]. This type of device has also proven useful in co-culture experiments, as different cell types can be maintained in tailored microenvironments [4].

The role of the nervous system in bone repair and the maintenance of bone homeostasis has recently become the subject of a number of studies. It is now known that the sensory and sympathetic nervous systems are involved in these processes; however, the precise mechanisms remain to be fully elucidated [7], [8]. Additionally, bone pain is a major issue in a number of diseases, including cancer and osteoarthritis, yet the causes of bone pain remain poorly described [9], [10]. Achieving a better understanding of the crosstalk between neurons and bone, particularly the electrophysiological component of this crosstalk, which has been largely neglected in previous studies, would give greater insight the role of bone innervation

in musculoskeletal disorders like osteoarthritis and provide a foundation for the development of treatments for bone pain.

1.1 Motivation

The *in vitro* study of neuron electrophysiology is complicated by a number of factors. First, neurons are difficult to culture because mature neurons do not undergo cell division [11]. Second, it is difficult to target individual cells for electrophysiological observation. Intracellular recording techniques can be used for this, but these techniques cannot be used to observe the same cell over long periods time because they disrupt the cell membrane [1]. Using nondestructive recording techniques involves plating the neurons on top of microelectrodes, and the positioning of the cells cannot be controlled with sufficient accuracy to ensure that cells are close enough to the electrodes to allow a signal to be recorded. Third, the propagation of signals along the neuronal membrane and their transmission from cell to cell are difficult to track because the change in the potential outside of the cell resulting from the electrical activity is very small and thus difficult to record [12].

Microfluidic technology has been adopted in neuronal cell culture in an effort to overcome these latter two problems. A compartmentalized microfluidic platform for use in neuroscience research was developed in 2003 [13], [14], and this device has opened the door to novel research possibilities. This device consists of two culture chambers connected by tunnels with cross-sectional dimensions on the order of micrometers. The size of the microtunnels means that somata can be excluded from entering, thus isolating the axons from the cell bodies. When combined with substrate-embedded microelectrodes, microfluidic devices enable the targeted recording of signals propagating along specific axons, and the small dimensions of the microchannels to which the axons are confined increase the resistance of the extracellular space, thereby amplifying the extracellular voltage signals [6], [12]. The compartmentalization of the microfluidic culture device enables the co-culture of neurons with other cell types while still allowing both types of cells to reside in environments tailored to their needs [4].

The use of microfluidic platforms containing microelectrodes for the co-culture of neurons and bone cells would provide new insights into the crosstalk between these two types of cells. Much of the existing literature on the communication between neurons and bone has focused on the molecular facet (see [8] and Sections 2.3.3—2.3.5 of the present paper). The use of microelectrode recordings from axons confined to microchannels in these combined microelectrode—microfluidic (μEF) devices would allow the researcher to observe the direction and velocity of signals propagating bidirectionally between the two culture chambers.

Furthermore, with the increased use of microfluidic platforms containing microelectrodes in neuronal cell culture experiments (e.g., [15]–[17]), there is a need for methods of analyzing the recordings obtained in such experiments. Although there have been advancements in commercially available devices for MEA recordings and microfluidic devices, there remains a gap in terms of user-friendly software allowing the analysis of the large amounts of data collected using such systems. This is an important gap to fill, as many researchers investigating the molecular facet of neuronal behavior and communication may not have the expertise necessary for electrophysiological data analysis and are thus likely to

neglect this fundamental and crucial aspect of neuronal behavior. An easy-to-use tool for the visualization and analysis of such recordings would prove useful not only in the abovementioned bone–neuron co-culture experiments but also other similar experiments in which the direction and velocity of propagating signals are of interest.

1.2 Objective

The aim of this dissertation project was twofold and involves a methodological component as the primary objective and answering a neurobiology research question as a secondary component. First, an advanced computational tool for the identification and characterization of propagating neuronal signals recording using a µEF device was developed in MATLAB (version 2016b, The MathWorks, Inc.). This tool, called µSpikeHunter, allows the user to visualize propagating signals obtained using electrodes recording from different points along the same axon and determine the direction and velocity of the propagation from the recordings.

µSpikeHunter contains a robust algorithm for the detection of propagating signals and two separate algorithms for the estimation of the propagation velocity. The software also includes an easy-to-use graphical spike sorting tool that allows the user to sort spikes into clusters considered to have arisen from different axons in the same microchannel based on the spike waveforms. Two interactive features, a kymograph and an audio playback function, are also included to allow the user to further qualitatively engage with the spike analysis process. µSpikeHunter was developed to be applicable to data recorded using a variety of experimental setups and devices: it is not only compatible with recordings obtained using a custom setup but also with recordings from a line of commonly used commercial devices for 60-, 120-, and 256-electrode MEAs (MEA2100, Multichannel Systems (MCS)). The performance and precision of µSpikeHunter were validated using synthetic data generated in MATLAB (MathWorks) and tested using actual data recorded from cortical neurons before applying the software to experimental data analysis. A paper on µSpikeHunter has been submitted for publication (Nature Methods, submission reference number: NMETH-A35206), and an open-source version of the code and a user manual (Appendix B) will be released along with the publication.

The second aim of this work was to gain a better understanding of the key aspects of the electrophysiological crosstalk between neurons and bone. To this end, simple experiments were designed to assess the impact of cell culture medium conditioned by osteoclasts on the spiking behavior of DRG neurons. The outcomes of these experiments are expected to provide crucial insights into phenomena underlying bone pain and the remodeling of bone. The analysis of the data collected in these experiments was only made possible by the availability of µSpikeHunter, and it is expected that this tool will continue to prove itself invaluable in ongoing research on this topic.

1.3 Document overview

This paper is organized as follows. Chapter 2 presents a review of the existing literature on the three main subjects with which this work is concerned: neuron electrophysiology,

microfluidic platforms in cell culture research, and the crosstalk between neurons and bone. Section 2.1 presents some basic models describing the mechanisms underlying the electrical behavior of neurons and discusses the use of microelectrodes to stimulate and record neuronal activity. Section 2.2 explains the advantages of using microfluidic platforms in cell culture research, specifically in the realm of neuroscience. A thorough review of past studies using microfluidic devices containing microelectrodes is given in this section to demonstrate the current state of this technology and provide some insight into the types of research questions being addressed using these devices. Section 2.3 provides some background on the biological topic this work will be addressing: the bidirectional communication between sensory neurons and bone cells. Chapter 3 presents the methods used in this work. Section 3.1 gives a detailed mathematical description of the algorithms used in μSpikeHunter and outlines the analysis capabilities of the software. The methods for the validation of the software and the experimental methods are described in Sections 4.1–5.1.3. Chapter 4 presents the results obtained in this work. Section 4.1 presents the results of the validation of the software conducted using synthetic electrophysiological data. Section 5.2 presents the experimental results obtained in this work, including an experimental demonstration of the software using cortical neurons and the preliminary investigation of the effect of the osteoclast secretome on the spiking behavior of sensory neurons. The implications of these results and expected future work using this computational tool are discussed in Chapter 6, and Chapter 7 concludes the paper.

Chapter 2

Literature review

This chapter will present a literature review of the three main topics underpinning this dissertation: the recording of neuronal signals, the use of microfluidic devices in cell culture, and the crosstalk between neuronal cells and bone cells. In the first section, the mechanisms behind the production of the electrical signals neurons use to communicate are presented, along with an overview of how microelectrodes are used to stimulate neuronal activity and record neuronal signals. In the second section, the use of microfluidics in cell culture, with a focus on neuronal culture, is described in comparison with other conventional techniques. The historical development of microfluidics is also discussed to provide context for this discussion. A detailed review of past studies using neurons cultured in microfluidic platforms containing microelectrodes is then presented, followed by a review of neuroscience studies using compartmentalized microfluidic devices for the co-culture of different types of cells with neurons. The third section outlines the current perspective on the communication between bone and neurons. Evidence for the role of different neurotransmitters in the remodeling of bone is presented, and potential mechanisms of bone pain are discussed. The final section provides an outlook on the present work on the basis of this review.

2.1 Neuron electrophysiology: Information processing and communication in the nervous system

The nervous system is a complex system of organs responsible for a wide range of functions in the human body, including the voluntary and involuntary control of other organ systems and the detection of and response to changes to the environment [18]. The nervous system is customarily divided into two parts: the central and peripheral nervous systems (CNS and PNS). The CNS comprises the brain and spinal cord, and the PNS consists of nerve cells whose processes extend to and innervate tissue outside of the CNS. The neuron is the fundamental cell providing the nervous system with its functional capabilities by forming vast communication networks within the body. Neurons encode information in electrical signals, conduct these signals along their extensive processes, and transmit them to other neurons or non-neuronal tissue [19]. Recording these signals as they are propagated and transmitted is a

fundamental task in understanding the function and connectivity of neurons comprising different networks in the body.

This section first provides an overview of how neurons generate and transmit waveforms called action potentials (APs), the primary unit of communication in neurons, by presenting some basic circuit models describing the electrophysiology of the neuron. Some important aspects of obtaining extracellular recordings and stimulating neuronal activity using microelectrodes are then discussed.

2.1.1 Circuit models of neuron electrophysiology

As stated above, the physiology of a neuron is fundamentally governed by the generation of electrical signals, the conduction of these signals along the axon, and their transmission to other cells. The basic anatomy of the neuron is shown in Figure 2.1.

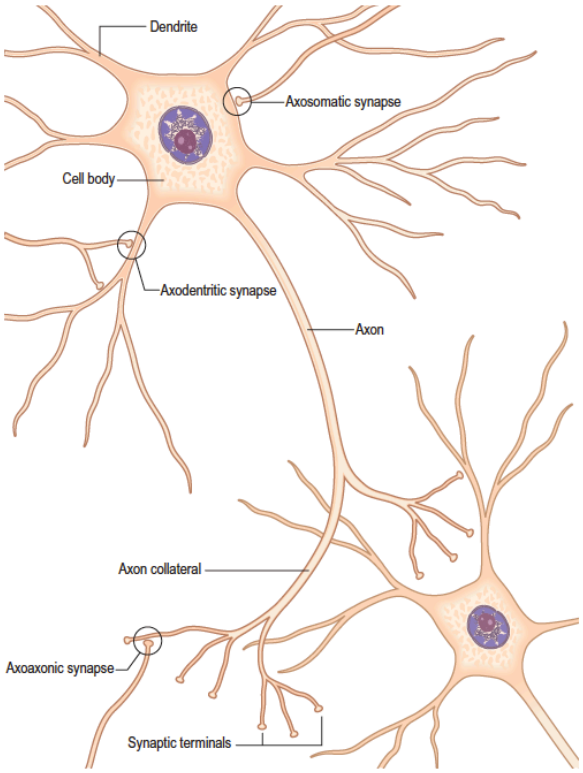

Figure 2.1 – Anatomy of the neuron. The neuron is composed of a cell body called the soma, relatively short processes called dendrites, and a long process called the axon. Electrical inputs are generally input to the dendrites and propagated along the axon to the axon terminal, where they are transmitted to the post-synaptic neuron electrically via a gap junction or chemically via the release of neurotransmitters. Reproduced from *Gray's Clinical Neuroanatomy* [20].

The neuron has three main components: the soma, dendrites, and axon. Electrical signals are typically generated by the excitation or inhibition of the dendrites, propagated along the axon, and transmitted to another neuron or other type of cell via a cell–cell junction called a synapse; however, excitation can arrive at the soma or axon as well. The structure of the neuronal membrane enables the propagation of a specific type of electrical signal, called an AP, without attenuation along the axon [19]. When the excitation is below a certain level, the electrical response from the membrane does not propagate and the membrane is said to be in the passive state; conversely, a section of membrane conducting an AP is said to be in

the active state. In the following, a circuit model for an infinitesimal patch of passive membrane is first presented, and the Hodgkin–Huxley (HH) model of the AP is then briefly discussed. Although this model was developed on the basis of recordings taken from the giant axon of a squid [21], the HH formalism is the foundation for many neuron models, and the model provides insight into the basic mechanisms governing AP generation and propagation [19]. The cable equation extending the point representations given by these models to an elongated cable-like structure similar to an idealized axon is then given [22]. This discussion provides a foundation for the discussion in the subsequent section on the use of microelectrodes in studying neuronal electrophysiology.

The neuronal membrane is composed of a lipid bilayer with ion channels embedded in it. Ion channels are transmembrane proteins that selectively allow the passage of ions between the intracellular and extracellular spaces [19]. The insulating lipid bilayer separating the two conductive fluid spaces acts as a capacitor, and the membrane capacitance is given by V_m. When the membrane is in the passive state, the ion channels offer an approximately constant resistance to ion flow, and because the ion channels are characterized by their selectivity for certain ion types, this resistance is different for each type of ion.

Ion flow through the membrane is governed by two phenomena: diffusion and electrical drift [19]. Diffusion is driven by the existence of a concentration gradient of a particle in solution, and particles tend to diffuse from areas of higher concentration to areas of lower concentration. Electrical drift is the movement of charged particles in an electric field, with positively charged particles tending to move toward areas of lower potential. In the case of the neuron, the concentration of potassium ions inside the cell is greater than that outside, and the opposite is true for sodium ions. Thus, sodium tends to diffuse into the cell, and potassium tends to diffuse out of the cell. However, the presence of other ions inside and outside of the cell that are selectively blocked by the ion channels generates a potential difference across the membrane that produces an electrical drift of the ions. It should be noted that there are other ions involved in the electrical activity of the neuron, but sodium and potassium ions are the main drivers of AP generation; thus, the present conversation focuses on these two ions.

Thus, there exists a potential at which the net flux of ions due to diffusion is balanced with that due to their electrical drift [19]. This potential is called the membrane reversal potential E_m. It should be noted here that the membrane potential V_m is conventionally defined as the intracellular potential V_{in} with the extracellular potential V_{out} as a reference; with this sign convention, the membrane reversal potential is approximately −70 mV. There also exists a reversal potential for each type of ion, which is defined based on the known equilibrium intracellular and extracellular concentrations of that ion. Thus, each type of ion channel in the passive membrane can be modeled as a constant resistance in series with a voltage source equal to the reversal potential of that ion, and ion channels are connected in parallel with each other and with the capacitor representing the lipid bilayer to represent an infinitesimal patch of passive membrane (Fig. 2.2(a)). To simplify this model, an equivalent circuit with only one resistor and one voltage source can be obtained using Thévenin's theorem; the resistance of this circuit is called the membrane resistance R_m, and the voltage is the membrane reversal potential E_m mentioned previously. This passive membrane model is shown as the first circuit model in Figure 2.2(a). As shown in this model, the circuit is a simple resistor–capacitor (RC) circuit. Thus, when the membrane is in the passive state, small

perturbations from the reversal potential—applied in the form of injected current or changes in potential—cause the membrane potential to slowly decay to the new potential induced by the excitation and then back to the reversal potential once the excitation is removed.

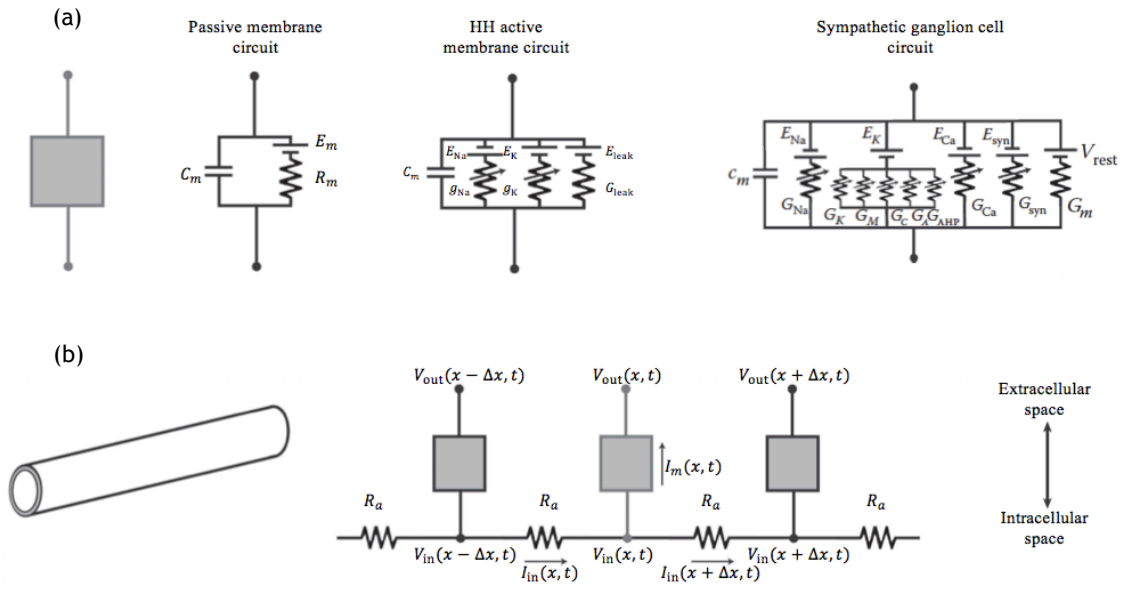

Figure 2.2 – Circuit models of (a) an infinitesimal patch of the neuronal membrane and (b) the axon. In the passive state, the neuronal membrane behaves as an RC circuit. In the active state, the electric activity of the neuronal membrane is fundamentally governed by the conductance of the ion channels, which are functions of the membrane potential. The axon can be modeled as a collection of point representations connected in series to form a two-dimensional cable-like structure. Modified from Anastassiou et al. [23].

To consider the spatial spread of an injected current or perturbation to the membrane voltage at a specific point x along the axon, this RC point representation must be extended. When considering an axon, this model can be extended to a one-dimensional model because of the large longitudinal extent of the axon relative to its diameter [23]. A representation of the cable circuit model is shown in Figure 2.2(b), where the grey boxes representing the cell membrane correspond to the passive circuit model in Figure 2.2(a) in the case of the cable model. In this representation of the model, it is assumed that the longitudinal conductance of the intracellular space is much greater than that of the extracellular space ($R_a \ll R_{\text{out}}$) and thus all of the longitudinal current flows through the axon ($I_{\text{out}} \approx 0$). This is generally true, as the extracellular fluid is present in fairly large quantities, giving it a high resistance, and it conducts electrical signals in a largely capacitive manner. In a later discussion in Section 2.2.3, this assumption is rejected when the axon is considered to be confined to a small volume of extracellular fluid.

The cable equation is derived here by solving the circuit shown in Figure 2.2(b) with the passive membrane model after Dayan and Abbott [22]. It should be noted prior to the derivation that the longitudinal and membrane resistances R_{in} and R_m and the membrane capacitance C_m are functions of the axonal dimensions and the infinitesimal longitudinal distance Δx as $R_a = \rho_{\text{axon}}\Delta x/(\pi a^2)$, $R_m = \rho_m/A$, and $C_m = c_m A$, where ρ_{axon} is the longitudinal resistivity inside the axon, ρ_m is the membrane resistivity, c_m is the specific membrane capacitance, a is the radius of the axon, and $A = 2\pi a\Delta x$ is the surface area of a

patch of membrane. In the following derivation, all of these parameters are all considered to be constant over time and space.

From Kirchoff's law, the currents in the cable circuit model, with the inclusion of an external inward-directed current I_{inj} injected at x, are related as

$$I_{\text{in}}(x+\Delta x,t) - I_{\text{in}}(x,t) + I_m(x,t) - I_{\text{inj}} = 0. \tag{1}$$

The membrane current $I_m(x,t)$ has a resistive component, which can be solved using Ohm's law, and a capacitive component, and is given as

$$I_m(x,t) = C_m \frac{\partial V_m(x,t)}{\partial t} + \frac{V_m(x,t) - E_m}{R_m} = 2\pi a \Delta x \left(c_m \frac{\partial V_m(x,t)}{\partial t} + \frac{V_m(x,t) - E_m}{\rho_m} \right), \tag{2}$$

where the membrane potential V_m $(= V_{\text{in}} - V_{\text{out}})$ is the potential across the membrane with V_{out} taken as a reference, as stated previously. In this alternate definition of V_m, V_{in} and V_{out} are defined with respect to a distant reference electrode in the extracellular fluid. The longitudinal current inside the axon at x and $x+\Delta x$ can be solved using Ohm's law considering the voltage drops across R_{in} as

$$\begin{aligned} I_{\text{in}}(x,t) &= -\frac{V_m(x,t) - V_m(x-\Delta x,t)}{R_a} = -\left(\frac{\pi a^2}{\rho_{\text{axon}}}\right)\left(\frac{V_m(x,t) - V_m(x-\Delta x,t)}{\Delta x}\right) \\ I_{\text{in}}(x+\Delta x,t) &= -\frac{V_m(x+\Delta x,t) - V_m(x,t)}{R_a} = -\left(\frac{\pi a^2}{\rho_{\text{axon}}}\right)\left(\frac{V_m(x+\Delta x,t) - V_m(x,t)}{\Delta x}\right), \end{aligned} \tag{3}$$

where positive current is considered to flow in the direction of increasing x. Substituting Eqs. (2) and (3) into Eq. (1) and dividing by $2\pi a \Delta x$ yields

$$c_m \frac{\partial V_m(x,t)}{\partial t} + \frac{V_m(x,t) - E_m}{\rho_m} = \left(\frac{a}{2\rho_{\text{axon}}}\right)\left(\frac{V_m(x+\Delta x,t) - 2V_m(x,t) + V_m(x-\Delta x,t)}{\Delta x^2}\right) + i_{\text{inj}}, \tag{4}$$

where $i_{\text{inj}} = I_{\text{inj}}/(2\pi a \Delta x)$ is the amount of injected current per unit area of membrane. Letting $\Delta x \to 0$ in Eq. (4) yields the cable equation:

$$c_m \frac{\partial V_m(x,t)}{\partial t} = \frac{a}{2\rho_{\text{axon}}} \frac{\partial^2 V_m(x,t)}{\partial x^2} - \frac{V_m(x,t) - E_m}{\rho_m} + i_{\text{inj}}. \tag{5}$$

This equation represents the temporal and spatial spread of injections of charge into the neuronal membrane. An alternate form can be obtained by multiplying Eq. (5) by ρ_m and considering two constants that describe the passive spread and decay of the current. The time constant $\tau_m = R_m C_m = \rho_m c_m$ represents the time scale over which the current decays, and the length constant or electrotonic length $\lambda = \sqrt{R_m/R_a} = \sqrt{a\rho_m/(2\rho_{\text{axon}})}$ represents the spatial spread of the current. With these two constants, the cable equation can be rewritten as

$$\tau_m \frac{\partial V_m(x,t)}{\partial t} = \lambda^2 \frac{\partial^2 V_m(x,t)}{\partial x^2} - (V_m(x,t) - E_m) + R_m I_{\text{inj}}. \tag{6}$$

The passive membrane model must be adjusted when considering an active membrane. The fundamental mechanism underlying the attenuationless propagation of APs along the neuronal membrane is the change in ion channel conductance (the inverse of resistance) in response to changes in the membrane potential. This means that when a portion of the

membrane depolarizes past a certain threshold above the reversal potential[1], nearby ion channels respond to the change, propagating this change in potential along the membrane.

In a series of five papers, Hodgkin and Huxley [21], [24]–[27] presented a mathematical model of the generation and propagation of the AP in a squid giant axon. They developed this model on the basis of electrophysiological measurements in which they isolated the behavior of the sodium and potassium ion channels in response to changes in membrane potential. Through their experiments, they showed that the conductances g_{K} and g_{Na} of the potassium and sodium channels are functions of the membrane potential V_m. They attributed this voltage dependence to 'gating particles', which bind to receptors in the ion channels and cause them to go from a closed state, in which they are less permeable to ions, to an open state, in which they are more permeable. This binding and thus the closing and opening of the individual channels is stochastic, and the behavior of an individual channel can be represented by the rate equation $\mathrm{C} \rightleftharpoons \mathrm{O}$, where C is the closed state, O is the open state, and the forward and backward rate coefficients α and β are functions of the membrane potential.

From the rate coefficients, continuous variables n_{ion} called gating variables, which represent the fraction of open channels, can be defined and used in quasi-Ohmic equations of the form $I_{\mathrm{ion}} = n_{\mathrm{ion}}\, \bar{g}_{\mathrm{ion}}(V_m - E_{\mathrm{ion}})$ to model the relationship between the current I_{ion} for a specific ion and the membrane potential V_m. In this quasi-Ohmic equation, there can be more than one gating variable to represent both the activation and inactivation of the ion channel, and the gating variables can be raised to different powers to best fit the measured quasi-Ohmic current–voltage ($I–V$) characteristic for that ion channel. Additionally, this representation includes the maximum conductance $\bar{g}_{\mathrm{ion}}$ of the ion channel as a parameter, putting all the voltage-dependence on the gating variable. It is now known that ion channels can be gated by a number of different mechanisms; some ion channels are ligand-gated, which means they open or close in response to a specific ligand binding to receptors in the ion channel, and some are voltage-gated, which means they change their configuration as a direct consequence of the changing membrane potential. The complete HH model also includes a 'leak' conductance—which is not voltage-dependent—and potential. These account for the movement of other less prevalent types of ions across the membrane. The complete HH circuit model is shown as the second circuit model in Figure 2.2(a). The final form of the HH model combines the capacitive component with the injected current and the currents through each type of channel, and it is given as

$$\begin{aligned} C_m \frac{\partial V_m}{\partial t} &= I_{\mathrm{inj}} - \bar{g}_L(V_m - E_L) - \bar{g}_{\mathrm{Na}} m^3 h (V_m - E_{\mathrm{Na}}) - \bar{g}_{\mathrm{K}} n^4 (V_m - E_{\mathrm{K}}) + \frac{a}{2R_{\mathrm{in}}} \frac{\partial^2 V_m}{\partial x^2} \\ \frac{\mathrm{d}X}{\mathrm{d}t} &= \alpha_X(1 - X) - \beta_X X, \qquad X = m, h, n, \end{aligned} \tag{7}$$

where m and h are the gating variables for sodium, n is that for potassium, and the subscript L represents the leak component. The behavior of the sodium channels is modeled using two

[1] Although the term 'threshold' is commonly used in the discussion of active versus passive neuronal membrane behavior, there is not a precise cutoff membrane potential above which APs are suddenly generated. Rather, neuronal responses lie on more of a continuum between passivity and activity, and the rate of change of the membrane potential is also important in evoking AP generation; however, the span of voltages between those at which the membrane definitively acts as either an RC circuit and those at which it definitively generates an AP is negligibly small for the purposes of the present discussion, and the neuron can thus be considered to demonstrate simple threshold-based behavior.

gating variables because the sodium channels show an inactivating type behavior, by which the channels are rapidly made impermeable to sodium, rather than simply moving between the closed and open states. As stated previously, the forward and backward rate components for each of these gating variables are dependent on the membrane potential; their specific forms are not provided here. Note also that Eq. (7) contains a term describing the spatial spread of the current in a manner similar to the cable equation (Eq. (5)).

The HH model has revealed the temporal progression of ion movement across an patch of membrane during an AP to be as follows [21]. When the membrane reaches a certain voltage, the sodium channels become activated, causing a sudden influx of sodium into the cell. This increases the membrane potential further, causing more sodium channels to open and producing a snowball effect responsible for the sharp increasing phase of the AP. When the membrane potential reaches its peak, the potassium channels begin to activate to repolarize the cell by producing an efflux of potassium. The response of the potassium channels to the voltage is slower, so the repolarization of the cell occurs more slowly than the initial depolarization. During repolarization, the sodium channels also inactivate, aiding in the repolarization. The activation of the potassium channels and inactivation of the sodium channels continues after the membrane has reached its reversal potential, causing it to dip below this value; this produces what is called the refractory period, during which it is more difficult for the membrane to produce a new AP. This mechanism ensures that the signal does not propagate backward. Finally, at the end of the refractory period, the membrane potential decays back to its reversal potential.

As stated previously, the HH formalism has been used to develop models of many different types of neurons with different levels of model complexity. The HH formalism essentially involves selecting the ion channels to be included in the model, obtaining their $I-V$ characteristic in isolation from other channels, and determining how to model the gating behavior of each channel in terms of what exponent to use and whether an inactivating gating variable should be included in addition to the activating variable [19]. An example of a more complex model built using this formalism is shown in the final circuit model of Figure 2.2(a). In addition to the potassium and sodium ion channels described above, this model also includes a calcium channel model and potassium channels with different gating mechanisms. To represent more complex morphologies, discrete segments of the membrane, called compartments, can each be individually modeled using the cable equation (Eq. (6)) or the HH equation (Eq. (7)) for and then connected with appropriate boundary conditions. It should be noted that although the axon has been conventionally considered to faithfully conduct signals from the soma to the axon terminal with no variation in the conduction velocity given the same inputs at the dendrites, recent studies have demonstrated that the axon also plays a role in information processing, as described in detail in Appendix A.

After the electrical signal has been conducted to the axon terminal, it must then be transmitted to other cells, which is done across a cell–cell junction called a synapse. Synapses enable communication through either electrical or chemical means. Gap junction channels are the main functional unit of electrical synapses. They are composed of a pair of hemichannels in the membranes of the pre- and postsynaptic neurons that bridge the gap between the two cells. Electrical synapses are used to transmit simple depolarizing signals from neuron to neuron, and transmission is instantaneous. In a chemical synapse, the axon terminal of the presynaptic neuron responds to the change in voltage caused by the arrival of

the signal by releasing a chemical messenger called a neurotransmitter. This neurotransmitter binds to the postsynaptic neuron and either inhibits or excites activity in that neuron. Neurotransmitters may also bind to other cell types and affect various changes in innervated tissue. Effects of specific neurotransmitters on bone cells will be discussed in Sections 2.3.3 and 2.3.4.

2.1.2 Recording and stimulating neuronal activity using microelectrodes

As stated at the start of this section, recording the electrical activity of neurons is fundamental in understanding how information is communicated among neuronal networks. Various methods of recording neuronal signals have been developed, ranging from patch-clamp methods at the scale of single ion channels to electroencephalography (EEG) at the macroscale. In the patch-clamp technique, an electrode inside a micropipette containing an electrolyte solution is brought into contact with the membrane of the cell to be recorded and suction is applied to create a high-resistance seal. The experimenter can then control the membrane potential V_m or the current I_m passing through the membrane and measure the response of the uncontrolled parameter [1]. Potentials are defined or measured with respect to a reference electrode placed in the bath containing the cell. This method enables measurements with high spatial resolution and low noise but is difficult to implement and causes damage to the cell membrane. In EEG, electrical activity in the brain is detected using electrodes placed on the scalp, and it can be used to observe responses to specific stimuli in the time domain or spectral characteristics of signals in the frequency domain. Microelectrode arrays (MEAs) enable the measurement of activity at the single-cell level, and network dynamics can be observed by recording across numerous electrodes integrated into the array [3]. MEAs also have the benefit of interfacing nondestructively with the cell, thus enabling *in vivo* stimulation and recordings as well as long-term recordings of the same culture. This section first presents models of the extracellular potential measured by MEAs during an AP and of the cell–electrode interface and then describes the general characteristics of MEA systems with particular focus on the commercial system to be used in the present work.

The flow of ions across the membrane of a neuron in a conducting medium induces the formation of electric fields within the medium, and when an AP occurs, the variations produced in the extracellular potential V_{out} are sufficiently large to be recorded using microelectrodes. Signals recorded extracellularly during an AP are hereafter referred to as spikes or extracellular action potentials (EAPs). Modeling a neuron as a point current source, Coulomb's law states that the extracellular potential is given by $V_{\mathrm{out}} = I_{ls}/4\pi\sigma r$, where I is the amplitude of the source current, σ is the conductivity of the medium, and r is the distance from the source to the measurement point. The extracellular potential arising from an elongated current source like the axon, as represented by the cable equation (Section 2.1.1), has been derived using the line source approximation (LSA) as [23], [28]

$$V_{\mathrm{out}}(r,h) = \frac{1}{4\pi\sigma}\int_{-\Delta s}^{0} \frac{I_{ls}}{\Delta s\sqrt{r^2+(h-s)^2}}\,\mathrm{d}s = \frac{I_{ls}}{4\pi\sigma\Delta s}\log\left(\frac{\sqrt{h^2+r^2}-h}{\sqrt{l^2+r^2}-l}\right), \tag{8}$$

where Δs is the length of the axon; r is the radial distance from the axon; and h and $l = h + \Delta s$ are the longitudinal distances from the end and origin of the axon, respectively.

Gold et al. [28] used the NEURON simulation environment [29] to model the time course of the extracellular potential during an AP by computing the transmembrane currents for a

given neuron assuming a constant zero extracellular potential. From these currents, they then calculated the time course of the extracellular potential at select positions outside of the neuron using the LSA under the assumption that changes in the extracellular potential are too small to affect the trasmembrane currents or the membrane potential. The membrane model they used included 12 different voltage-gated ion channels modeled using the HH formalism. Figure 2.3(a) shows examples of simulated EAPs at different positions outside of the cell [28]. As shown by the plots of the total transmembrane currents in the second column in Figure 2.3(d), the waveforms of the EAPs are proportional to these currents, in accordance with Eq. (8). Figure 2.3(b) shows an enlarged view of a spike simulated near the position of an actual recording electrode and the experimentally recorded spike, demonstrating the agreement between the waveforms of the two. The shape of the spike, which was recorded near the axon of the neuron, includes a brief positive peak, a sharp negative peak, and a longer positive phase that slowly decays back to rest.

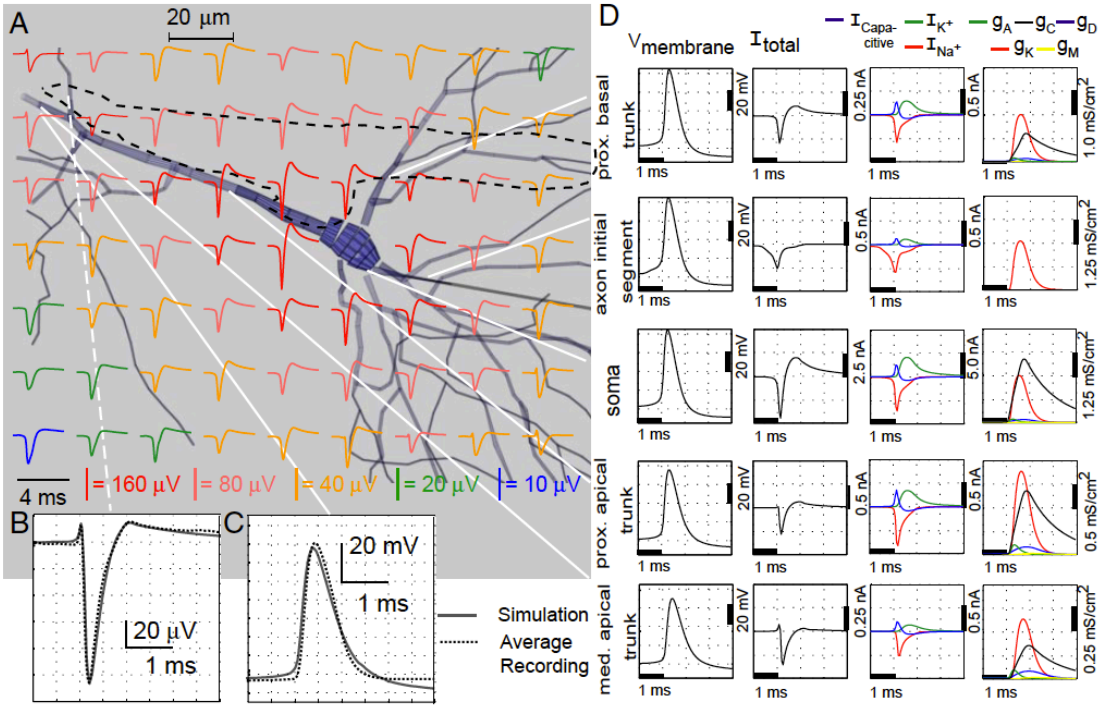

Figure 2.3 – Recording and simulation of EAPs. The neuron measured in experiments was simulated in the NEURON simulation environment. (a) Simulated EAPs in the region surrounding the soma, dendrites, and the recording electrode used in the experiment. (b) Simulated EAP at the estimated electrode position overlaying the actual average recorded EAP. (c) Simulated intracellular AP overlaying the actual average intracellular recording. (d) Various simulated parameters in specific compartments over the course of an AP. From left to right, the columns show the membrane potential, the total transmembrane current, each of the components of the transmembrane current, and the conductances of each of the considered ion channels. Reproduced from Gold et al. [28].

The reason for this triphasic shape can be qualitatively described by considering current sources and sinks in the extracellular fluid [30]. An extracellular source is defined as a cationic current from the intracellular to the extracellular space or an anionic current in the opposite direction, and a sink is defined as the converse. This means that, for example, Na^+ ions flowing into the cell produce an extracellular sink and K^+ ions flowing out of the cell produce an extracellular source. When the membrane is depolarized, the net flow of cations

is inward, and thus the extracellular space at the depolarized region acts as an extracellular sink. Thus, in regions of the membrane adjacent to the depolarized region, cationic currents flow outward to provide a source for the sink at the depolarized region. As the AP propagates along the axon, the extracellular sink propagates alongside it in the extracellular fluid. As depicted in Figure 2.4(a), the propagation of the sink (represented by minus signs) along the surface of the axon results in a stationary recording electrode first seeing an extracellular source, causing it to register a positive potential with respect to a distant reference electrode. The arrival of the sink beneath the electrode then produces a large negative peak in the recorded potential, followed by another positive peak as the AP propagates away from the electrode.

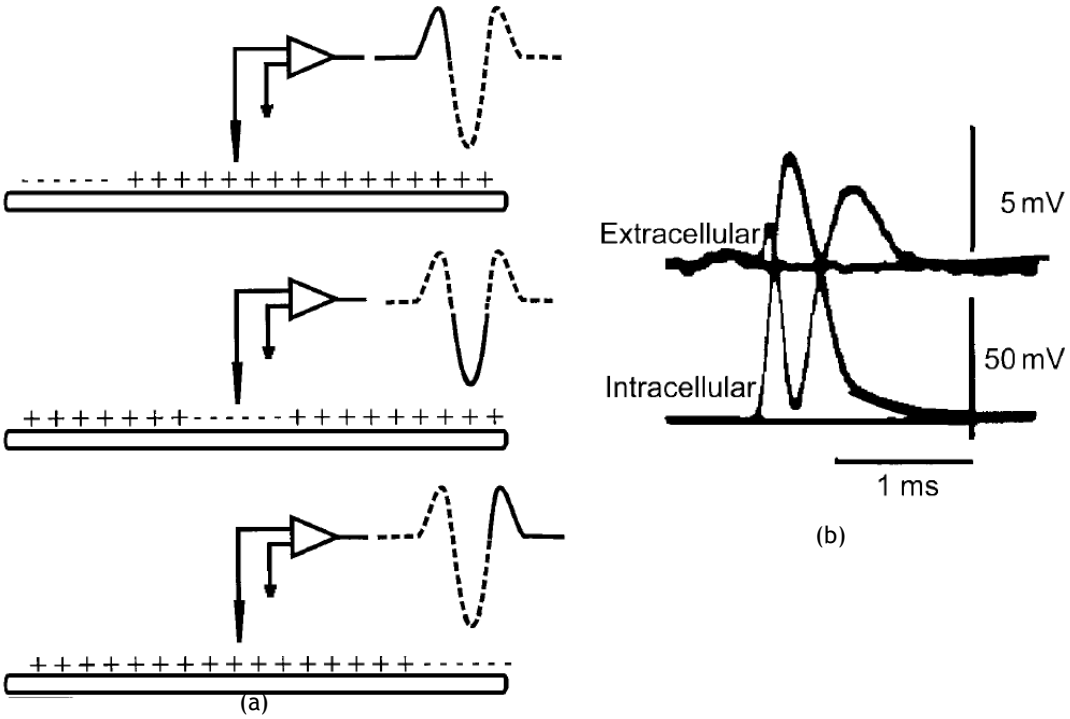

Figure 2.4 – Origins of the triphasic waveform of the EAP. (a) Schematic describing the propagation of sources and sinks during an action potential. As the AP travels along the axon, the recording electrode sees variations in the potential arising from the varying distribution of sources and sinks relative to the electrode. (b) Simultaneous intra- and extracellular recordings showing the temporal correlation between the intra- and extracellular potentials. Note the different scales of the two recordings. Modified from Heinricher [30].

The shape of the waveform shown in Figure 2.4(a) is purely illustrative; the spatial and temporal distributions of the magnitude of the ionic fluxes produce the more asymmetric shapes simulated by Gold et al. [28] (Figure 2.3). Figure 2.4(b) shows simultaneous intracellular and extracellular recordings of an AP taken from a motor neuron in the ventral horn of a cat [31]. As shown in this figure, the sharp negative phase of the EAP corresponds to the positive peak of the intracellularly recorded AP, and the slowly decaying positive phase corresponds to the repolarization of the axon. It should be noted that a similar phenomenon occurs with recordings taken at the soma, but because there is no period of ‘approach’ (as represented by the top schematic in Figure 2.4(a)), the recorded spike is biphasic rather than triphasic, with an initial negative peak followed by a positive peak.

Regardless of whether extracellular recordings are taken at the soma or along the axon, the signal amplitude is much weaker than that obtained for intracellular recordings, as demonstrated by the different scales in Figure 2.4(b). Furthermore, the strength of the EAP signal decays with increasing distance from the cell, as described by Eq. (8) and shown in Figure 2.3). Thus, it is important to ensure the recording electrode is in as close contact with the cell membrane as possible. The interface between a neuron and a substrate-integrated microelectrode has been conventionally described using the point-contact model, as shown in Figure 2.5(a), which is then generalized in Figure 2.5(b) to represent the case in which the electrode potential comprises contributions from multiple sources along the length of the neuron [1]. This generalization is based on the assumption that the impedance Z_a of the MEA amplifier is large compared with the impedance of the culture medium or tissue, meaning the electrode has a negligible effect on the extracellular potential. The membrane model in Figure 2.5(a) is the HH model described earlier, and the contact between the membrane and the electrode is represented by a collection of resistances and capacitances. The physical significance of each of the model components in the two models is described here. The sealing resistance R_{seal} in the point contact model describes how well the cell is attached to the electrode, and it is a function of the resistivity of the medium and the average distance between the neuron and the electrode. The gap resistance R_{gap} is the resistance in the fluid gap separating the membrane from the electrode; this resistance is often considered to be negligible [32]. Other versions of the point contact model also include a capacitance C_{hd} in series with R_{gap} to represent the capacitance of the interface between the membrane and the electrolyte [32], [33].

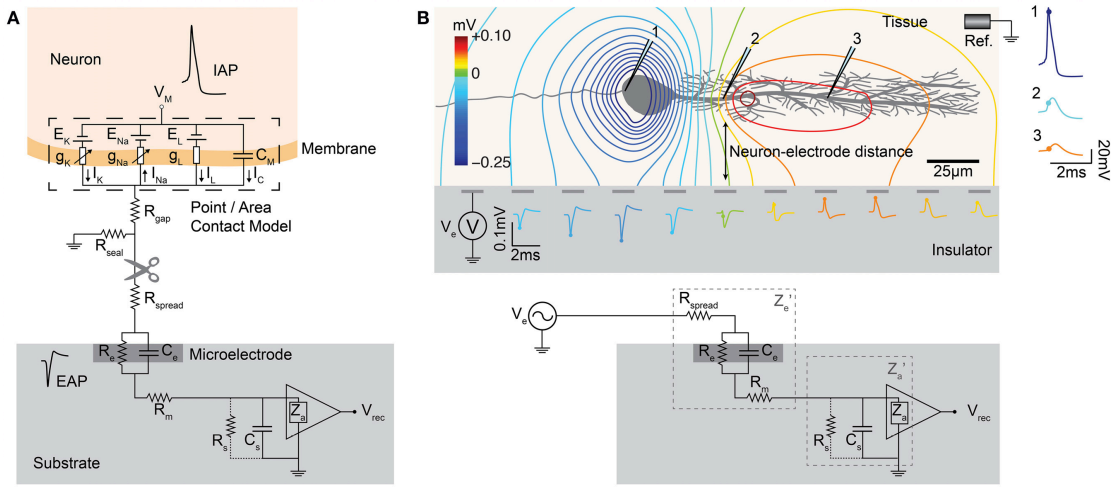

Figure 2.5 – Models of the neuron–electrode interface. (a) Classic point contact model describing the coupling between a patch of membrane and the recording electrode. (b) Generalized model describing the contributions from multiple sources along the neuron to the electrode potential. The parameters in these models are described in the text. Reproduced from Obien et al. [1].

In the generalized model shown in Figure 2.5(b), these components are eliminated, and the contributions to the electrode potential are modeled as a voltage source with its voltage calculated as the sum of all the contributions from the point sources along the neuron. This leaves the electrode side of the model, which is equivalent to that in the point source model. The effective electrode impedance $Z_e{}'$ consists of R_{spread}, R_m, R_e, and C_e. The spreading

resistance R_{spread} represents the resistance encountered by a current spreading from the recording electrode to the reference electrode placed in the bath. The resistance R_e and capacitance C_e of the electrode comprise a model of the layer of water molecules and ions in solution that forms when a conductor is placed in an electrolyte [33], and R_m represents the metallic part of the electrode [1]. It is important for the electrode to have a low impedance to yield a good signal-to-noise ratio (SNR), but it can be difficult to achieve low impedance when fabricating electrodes composed of conductors. One method of reducing the impedance has been to increase the surface area through surface modification techniques [1]. The effective amplifier input impedance $Z_a{}'$ is composed of the actual input impedance Z_a and the shunting path to ground composed of R_s and C_s.

MEAs are also well-suited to provide stimulation to neurons. In *in vivo* applications, stimulation is commonly used to transmit sensory information to the brain, such as in retinal and cochlear implants; to treat neurological disorders, such as Parkinson's or epilepsy; and to enable control, as in rehabilitation after an injury to the nervous system [1]. Biphasic pulses are typically used to balance the flow of charges and prevent damage to the tissue or the electrodes themselves. One interesting application of MEA stimulation is the use of it as a trigger in stimulus-triggered averaging [1]. In this technique, the response of the neuron to the same stimulus repeated in numerous trials can be averaged as a countermeasure against recording noise, yielding clear traces of recorded spikes. Bakkum et al. [3] used this method to track the propagation of APs along axons of individual neurons from recordings taken using a high-density MEA containing 11,011 microelectrodes. The high spatiotemporal resolution of recordings obtained using this high-density MEA and the ability to stimulate at precise locations without producing major artifacts in the recorded signal allowed them to follow the propagation of APs with many recording sites along a single axon. They showed substantial variations in the propagation velocity along a single axon, indicating the activation of local mechanisms such as those described in the previous section.

Although some researchers fabricate their own MEAs customized to suit their experimental needs, many use commercially available MEA systems. One popular choice of manufacturer is MCS, whose products include both *in vitro* and *in vivo* systems as well as an automated patch-clamp system. The most versatile line of their *in vitro* systems is the MEA2100-System [34] for MEAs with 32, 60, 120, or 256 electrodes [35]. This system comprises two components: a headstage and an interface board. The headstage of the system houses the MEA in a central chamber with contact pins aligned with the contact pads around the periphery of the MEA. Data acquisition is performed by the headstage, and the sampling rate and other parameters can be set using MCS software. Amplification is performed by a built-in amplifier in the headstage to ensure low noise levels, and the data are then sampled at the desired sampling rate. The headstage also contains a stimulus generator to enable the targeted stimulation of the culture. The interface board contains a digital signal processor (DSP). The inclusion of a DSP integrated into the hardware of the system enables the real-time filtering and analysis of acquired data. The standard MCS MEAs contain 60 electrodes of 10, 20, or 30 µm in diameter in an 8 × 8 grid with center-to-center interelectrode distances of 100, 200, or 300 µm. The standard MCS MEAs are composed of TiN electrodes with Ti or ITO tracks insulated by SiN. TiN is a stable material that gives the MEAs a long life and allows them to be reused. The impedance of a flat round TiN electrode with a diameter of 10 µm is approximately 400 kΩ. MEAs with 256 electrodes with similar dimensions and spacings are also available. In the present study, recordings will be taken with a 256-electrode MCS MEA.

As described in this section, the electrical signals generated by ion channels embedded in the neuronal membrane are the fundamental means by which information is conveyed in the nervous system. The membrane behavior during the generation of an AP is conventionally modeled using the HH framework [21], which describes the responses of the conductivity different types of channels to changes in the membrane potential. Because of the small size of axons and the small magnitude of the changes they induce in extracellular potential recordings during an AP, the measurement of the propagation velocity along the axon is quite difficult. However, Bakkum et al. [3] were able to track the propagation of APs over axons in a network of neurons cultured on a high-density MEA using stimulus-triggered averaging to reduce the effect of noise on the recorded signal. MEA technology provides the ability to measure the electrical behavior of neurons in culture over a long period without disrupting or damaging the cells. In the following section, the use of microfluidic chambers in neuronal cell culture will be presented, and it will be demonstrated that this technique is complementary to the use of MEA technology to measure AP propagation.

2.2 Microfluidics in cell culture

In this work, the bidirectional communication between bone cells and neurons was preliminarily investigated using a compartmentalized microfluidic platform containing microelectrodes. This section will discuss the use of microfluidic devices in neurobiological studies to provide some perspective on the scientific advancements that have been made through the use of microfluidic platforms and justify the use of a compartmentalized microfluidic platform in the present work. This section is organized as follows. First, an overview of the use of microfluidic devices in cell culture is presented. Their application in neuroscience research is then addressed, and the historical development of neuronal culture is provided to demonstrate the advantages of microfluidic devices over earlier culturing methods. A review of past neuroscience studies using microfluidic devices containing microelectrodes is then presented, followed by a brief review of studies using compartmentalized microfluidic devices for neuroscience research.

2.2.1 Microfluidic devices in cell culture

Tissue culture was first conceived as a method of studying the behavior of living animal cells at the start of the 1900s by Harrison [36], who employed the hanging drop method to observe the growth and development of frog nerve fibers; his employment of this technique led to the landmark finding that the nervous system is cellular rather than composed of acellular fibrils [2], [37], [38]. Since then, cell culture techniques have advanced to the more complex techniques used today, including the development of continuous cell lines in addition to primary cultures, the use of compartmentalized culture chambers, and the manipulation of isolated factors to determine their effect on the cultured cells.

One major advancement in cell culture is the use of microfluidic platforms to precisely define the cell microenvironment and control cell growth. Microfluidics involves the manipulation of volumes of fluids ranging from 10^{-9} to 10^{-18} L inside channels with dimensions on the order of tens of micrometers [5], [39]. Microfluidic platforms have opened the door to novel methods of biological analysis because they enable a high degree of environmental control and measurement sensitivity. Through the manipulation of the small amounts of

reagents and cells employed in microfluidic platforms, separations and detections can be rapidly conducted with high resolution and sensitivity [4], and cells can be analyzed and manipulated with a high degree of spatial and temporal resolution, with control extending even to the level of single cells [39], [40].

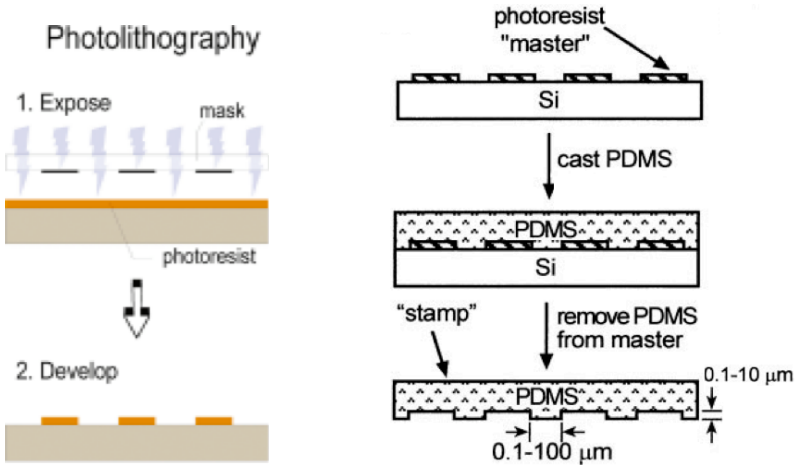

(a) (b)

Figure 2.6 – Schematic description of the process of soft lithography. (a) Fabrication of the master using photolithography. Reproduced from Folch and Toner [41]. (b) Casting of PDMS microfluidic device using master. Reproduced from Whitesides et al. [42].

One important feature of the use of microfluidic devices is that it enables the researcher to control the location of cells in culture. Confinement of cells to the desired location in the culture device with micrometer precision can be achieved by two methods: (1) the promotion of selective adhesion to the desired areas on the substrate by laying down a thin adhesive template composed of metal, polymers, or proteins to which the cell preferably adheres, and (2) the provision of a physical barrier that confines cells to within an enclosed space [41]. The foundational fabrication techniques for these two methods of micromanipulation are photolithography and soft lithography, a set of techniques based on photolithography for use elastomeric materials, which are characterized by their mechanical flexibility [42].

Photolithography involves spin-coating the substrate with a layer of photosensitive polymer, called the photoresist, in solution; covering the photoresist layer with an opaque mask containing the inverse of the desired pattern; and polymerizing the uncovered portions of the photoresist layer by exposure to ultraviolet (UV) light (Fig. 2.6(a)) [41]. This method is complex and requires clean room facilities for the spin-coating step to ensure even application of the photoresist. Soft lithography offers an inexpensive and simple alternative to photolithography. In soft lithography techniques, an elastomeric stamp or chamber is fabricated from a master support pattern made in advance using photolithography. The master is composed of a rigid polymer, and the elastomer is poured over this rigid support and cured. After curing, the flexible stamp or chamber can be peeled off of the master [41], [42]. Figure 2.6(b) shows the process of creating the elastomeric device from the master. This method limits the need for photolithography to the creation of the master, which can then be used to create numerous replicas of the elastomer device.

The customizability of these platforms means that they can be readily adapted not only to control the location of the cells in culture but also to realize highly controlled microenvironments with high reproducibility. Cells are sensitive to their microenvironment,

which is defined as the biochemical, mechanical, and physicochemical conditions in the immediate vicinity of a cell; examples of each of these types of conditions include the presence of nearby biomolecules, the mechanical properties and patterning of the substrate, and the pH and temperature of the environment, respectively [4], [43]. The microenvironment dictates the function, behavior, differentiation, proliferation, and survival of the cells. For an *in vitro* model to accurately reproduce the *in vivo* behavior of cells, the factors of the microenvironment must be tailored to mimic the *in vivo* conditions.

The biochemical and physical aspects of the microenvironment have been the primary focus of most research on the effects of the microenvironment conditions on the cell because the physicochemical properties (e.g., pH, temperature, osmality) are considered to be factors inherent to the *in vivo* environment and should thus necessarily be held constant to maintain cell survival [43]. Growth factors and hormones are among the relevant biomolecules present in the biochemical microenvironment, which are part of signaling pathways that play a large role in determining the fate of the cell. In cell culture, these biomolecules are provided by the culture medium, which includes basic compounds like salts and carbohydrates and is typically supplemented with serum to provide factors to promote growth and division. Because most cells are non-circulating, the physical microenvironment is largely dictated by the adhesion of the cell to the surrounding extracellular matrix (ECM) via integrins, specialized proteins responsible for both cell adhesion and the transduction of mechanical forces outside the cell to biochemical signals within the cell. Thus, most cells grow as adherent monolayers in culture and must attach to the substrate on which they are cultured before they can begin to proliferate [43], [44].

Conventional cell culture is performed on two-dimensional flat surfaces in plastic containers, such as polystyrene flasks and well plates, that have been plasma-treated and frequently coated with ECM proteins to facilitate cell adhesion. Many microfluidic platforms used for biological research are fabricated using soft lithography and are composed of poly(dimethylsiloxane) (PDMS), an optically transparent, flexible elastomer. This process is inexpensive and simple, and the small size of the platforms makes them readily portable. PDMS has a number of characteristics that make it well suited for use in cell culture and biological analysis, including its high gas permeability, optical transparency, biocompatibility, thermal stability, low cost, and ability to reversibly form a fluid-tight seal with dry substrates [2], [4], [5], [39], [43]. Its flexibility also allows the introduction of hydraulically controlled valves that can be used to manipulate the flow rate within the channels and chambers of devices could be controlled. Because the flow in microfluidic devices is laminar, chemical gradients can be precisely generated and regulated by merging, mixing, and splitting flow paths, which is useful in applications such as investigating dose response and chemotaxis [4], [39].

When performing *in vitro* experiments, the aim is to mimic the *in vivo* microenvironment with sufficient faithfulness without introducing so many complicating factors that the experiment cannot be replicated reasonably quickly and easily. Typically, the consideration of additional microenvironmental factors that influence cell behavior complicates the replication of the experiment; however, microfluidics is poised to offer high throughput without sacrificing the accuracy of the *in vitro* model [43]. Microfluidic platforms can be designed to carefully tailor the physical and biochemical aspects of the *in vitro*

microenvironment to mimic that *in vivo* and investigate the effect of variations to each environmental factor on cell behavior.

2.2.2 Microfluidic devices in neuroscience research

In cell culture, neurons pose a particular set of challenges. One major difficulty in culturing neuronal cells is that adult neurons do not undergo cell division [11]. This challenge can be addressed through the use of immortalized cell lines derived from neuronal tumors, such as the SH-SY5Y neuroblastoma-derived cell line. Immortalized cell lines have the advantages of unlimited proliferation, simpler culturing than primary neuronal cultures, and low variability among cultures. However, because they are derived from tumors, they show important physiological differences from neurons and often must be induced to show a neuronal phenotype through the addition of neuronal growth factors [11]. To accurately capture the *in vivo* behavior of neuronal cells, primary cultures are generally preferred over immortalized tumor-derived cell lines. With the use of primary cultures comes the difficulty of isolating the desired cell type from the extracted tissue, which will also contain astrocytes and oligodendrocytes. In this work, primary dorsal root ganglia (DRGs) from adult mice were used for the cell cultures.

For neuronal cultures to thrive, the substrate must be coated with proteins to mimic the ECM and allow the cells to adhere and form networks; typically, poly-D-lysine is used for this purpose in the culture of primary neurons [11], [44]. The composition of the culture medium is also very important in ensuring cell survival. Nerve growth factor (NGF) is often included in culture media, particularly when serum-free media are used.

Neurons are more sensitive than other cell types to characteristics of their microenvironment, such as temperature, pH, substrate roughness, calcium ion concentration, and the composition of the culture medium [5], and small changes to these factors can drastically alter their behavior. This sensitivity makes microfluidic neuronal culture very appealing because it provides the researcher with excellent control over the microenvironment and thus the behavior of the cultured neurons. Another unique feature of neurons is that they develop elongated and specialized processes that become highly branched over the course of their development [2]. As described in the previous section, these processes enable neurons to form complex networks and communicate amongst each other as well as with other cell types via chemical and electrical signals transmitted over large distances within the body. An important point regarding the formation of such networks in culture is that the terminal points of axons may reside far from the cell body of the corresponding neurons and thus may exist in a microenvironment that is markedly different from that of the soma, posing a particular challenge in recapitulating the *in vivo* condition *in vitro* [2].

Since the first neuronal culture experiments, culture methods have gone through a number of advancements. As stated previously, animal cell culture began in the early 1900s with the culture of frog nerve fibers by Harrison [36] using the hanging drop method. In this method, cells or tissue samples are placed on a coverslip and covered with a drop of serum, and the coverslip is inverted and sealed to a microscope slide with the drop hanging upside down. Harrison's work provided the first direct evidence that the nervous system is composed of discrete cells rather than a continuous network of fibers [2]. These initial successes also revealed the difficulty of achieving the necessary conditions for cell viability and longevity *in vitro* in terms of sterility and the provision of the nutrients needed for the cells to survive. In

the decades following, a great deal of research was dedicated to the development of protocols for defining the precise conditions required for culturing a wide range of animal tissues for a variety of purposes [2]. The development of the first culture flasks in 1923 was a big step in the improvement of culturing conditions, providing easy access to the cultured cells and enabling the exchange of media for longer-term culturing [2].

Although dissociated cell culture has been the more commonly used method in neuroscience research, brain tissue can also be maintained and studied in culture by removing the brain, slicing it thinly enough for oxygen to diffuse to the cells, and placing it in proper culturing conditions. Similarly, whole DRGs can also be maintained in culture. Such organotypic techniques have the advantage of largely preserving neuronal networks that had formed *in vivo*, thus maintaining tissue-level function; this makes them suitable for reverse engineering approaches [2], [45]. However, it is more difficult to observe individual neurons in this type of culture, and of course the neurons are not isolated from the other tissue components, including other cell types. Conventional dissociated cell culture in wells and Petri dishes is better suited for developmental studies, as cells tend to grow and develop a network guided by the same mechanisms as they are during development *in vivo* [45]. Microfluidic devices are typically used for dissociated neuronal culture; however, some experiments have been performed on organotypic cultures, including hippocampal slices [46] and DRGs [47], plated in compartments with their axons allowed to grow through microfluidic channels into separate compartments.

More recent advancements in the 1970s laid the groundwork for the type of microfluidic platform used in the present work. In 1976, Furshpan et al. [48] developed a novel co-culture method that enabled the spatial isolation of islands of cells to better characterize cell–cell interactions [2]. This approach, called micro-island culturing, involves the formation of small islands of substrates to which cells can adhere within a larger substrate that does not permit adhesion. By restricting cell contact between small numbers of sympathetic neurons and cardiac myocytes, Furshpan et al. [48] were able to control the location of formed neuromuscular connections, making them much easier to access and observe than in the random networks formed in conventional co-cultures. In 1977, Campenot [49] developed a three-chamber system comprising a Teflon divider attached on top of a glass substrate with parallel scratches to guide axonal growth from the central compartment containing the somata to the larger side compartments. This setup allowed the manipulation of the biochemical microenvironment and led to the discovery that NGF locally enhances neurite growth. The Campenot chamber was a direct precursor to the modern-day microfluidic device, and the basic concept behind it combined with technological advancements in microfabrication led to the production of more complex and controllable devices.

In 2003, Taylor et al. [13] developed the first multicompartment microfluidic device for use in neuroscience research. The general design of their device is now commonly used in neuroscience studies using microfluidic culture platforms. The fabrication process of the device is shown in Figure 2.7. The master for the device contains very small ridges polymerized from a thin layer of photoresist and larger regions formed from a subsequent thicker application of photoresist. These form the microgrooves and culture chambers in the final device, and open wells are punched into the PDMS at either end of the chambers to allow access for medium exchange once the device is sealed against the substrate. This device enables the separation of the somata from the axons via the physical partition

separating the two chambers in the PDMS device. This partition contains microgrooves that form microchannels when the PDMS is sealed to the substrate, and it was demonstrated that axons extend through these channels after 3–4 days *in vitro* (DIV). It was also demonstrated that the axonal and somal compartments can be maintained in fluidic isolation through hydrostatic pressure applied by adding a slightly higher volume to one chamber than the other, inducing a slow unidirectional laminar flow through the microchannels. The same lab later published a protocol for the fabrication of this type of device [14], and this protocol has been widely used in studies employing microfluidic neuronal culture. A number of variations have sprung rom this fundamental design depending on the aims of the study; these include punching a hole into one or both of the culture chambers to create an open compartment connected to the microchannels; varying the length, number, and arrangement of the microchannels; and including valves to enable flow control.

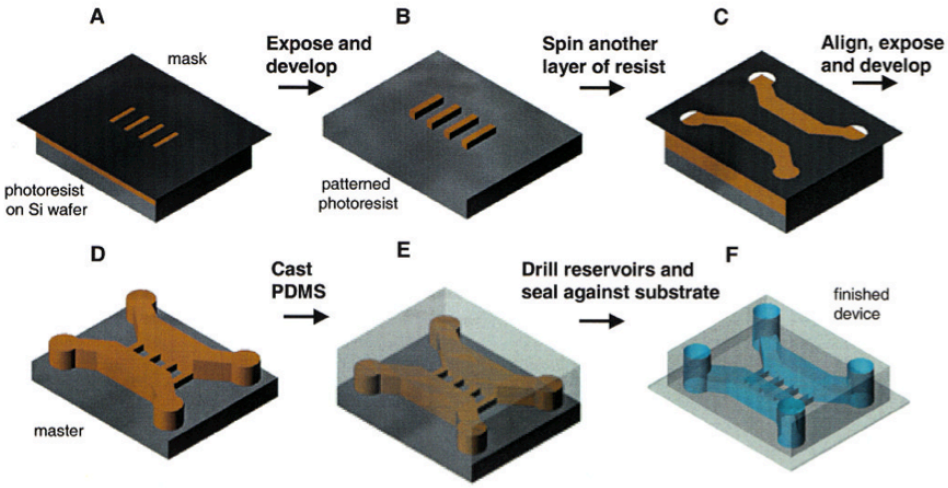

Figure 2.7 – Fabrication process of the multicompartment microfluidic device developed by Taylor et al. [13]. The device contains two culture chambers connected by microgrooves, and holes are punched into the device at both ends of the culture chambers. Once the device is sealed to a substrate, the culture chambers are enclosed and can be accessed by the open wells formed by the punched holes, and the microgrooves form closed microchannels connecting the two chambers. Reproduced from Taylor et al. [13].

As mentioned above, one important capability that microfluidic devices provides to neuronal cell culture experiments is the separation of somata from axons. The use of microfluidic devices enables the construction of physically confined channels that allow axonal passage but are too narrow for somata to traverse, thereby physically separating axons and cell bodies in two distinct regions. The cross-sectional dimensions of the microchannels in the conventional PDMS microfluidics device developed by Taylor et al. [13], [14] are 3 μm in height and 10 μm in width. Mammalian soma tend to be on the order of tens of micrometers in diameter, which is too large to pass through these channels, whereas axons are typically approximately 1 μm in diameter or smaller. Axonal guidance is known to be regulated *in vivo* by both long-range diffusive signals and short-range contact cues [2]. Regarding short-range contact, the substrate below microfluidic channels can be patterned by stamping or modified by the adhesion of compounds that are attractive or repulsive to growing axons. To mimic the long-range diffusive signals found *in vivo*, signaling molecules can be added to the compartment at the outlet of the microchannels. In this way, axon

growth through the microchannels can be manipulated and the effect of different conditions on their growth can be observed.

2.2.3 Microfluidic devices containing microelectrodes

This section presents an overview of previous studies involving the use of microelectrodes in combination with microfluidic devices. Hereafter, the term microfluidic–microelectrode (μEF) device is used to refer to a device consisting of a microfluidic platform mounted on a MEA such that the microchannels of the microfluidic platform align with the rows of microelectrodes. First, the advantages of using μEF devices to study the electrophysiology of neurons are presented, with particular focus on the mechanism of the amplification of extracellular signals by the confinement of axons within microchannels. A number of studies combining microfluidics with neuronal recordings are then discussed. The main focal points of these studies include propagation velocity along the axon [15]–[17], [50], pharmacological effects [15], [16], [51], [52], factors that affect the characteristics of the recorded signal [15], [53], [54], and controlled network formation among neuronal populations [17], [55]–[57] or organotypic cultures [46].

The use of μEF devices has greatly simplified the measurement of extracellular axonal potentials for two main reasons. First, the physical constraints imposed by the platform and any substrate patterning that is performed enable the isolation and targeting of individual axonal populations with low numbers of axons and ensures the axons are sufficiently close to the electrodes to record extracellular signals. Second, the small size of the microchannel causes the conductance inside the channel to be very low and thus amplifies the extracellular voltage signal received by the recording electrodes [12]. The amplification of the signal is crucial, as signals measured from axons using planar electrodes tend to be very low because of the low amount of axon–electrode contact [15]. As stated in Section 2.1.2, recording electrodes positioned outside of the cell record very low signals because the ionic currents passing through the membrane are small and the culture medium (or the extracellular fluid in the *in vivo* case) has a low resistivity and a high volume.

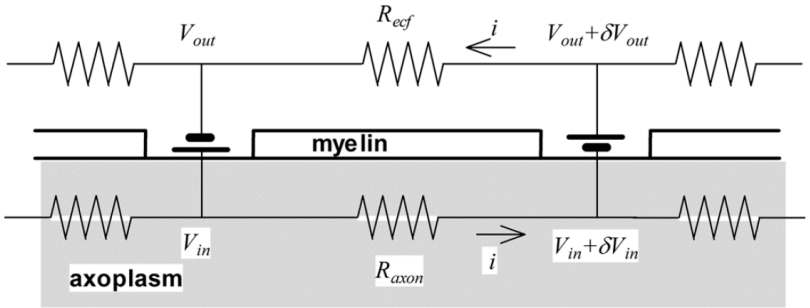

Figure 2.8 – Circuit model of an axon enclosed in a microchannel. This model is equivalent to the cable-like model presented previously (see Fig. 2.2(b)) but with the extracellular resistance considered to be nonnegligible in the case where the axon is enclosed in a small amount of fluid. Reproduced from FitzGerald et al. [12].

FitzGerald et al. [12] have presented the following explanation of the mechanism of this signal amplification. The membrane potential V_m has been previously defined in this manuscript as $V_m = V_{\text{in}} - V_{\text{out}}$. The propagation of an AP can be considered as the successive

depolarization of adjacent nodes in a mylenated axon, as illustrated in Figure 2.8; the circuit model given in this figure is essentially equivalent to the cable model discussed previously (see Fig. 2.2(b)) but with the inclusion of the extracellular resistance R_{out} and thus holds true for unmyelanted axons as well. In the propagation of an AP, the membrane potential differs along the axon as shown in the figure, meaning the potentials inside and outside of the cell also vary spatially. It can be considered that the change in the membrane potential is apportioned between the internal and external potentials as $\delta V_m = \delta V_{\mathrm{in}} - \delta V_{\mathrm{out}}$. In the loop between the depolarized and resting nodes (the left and right nodes in Figure 2.8, respectively), the currents through the extracellular (culture medium) and axonal resistances R_{out} and R_{in} are equal in magnitude, and thus the differences in the internal and external potentials at the two nodes the cell can be accounted for as drops across these resistances: $\delta V_{\mathrm{out}} = iR_{\mathrm{out}}$ and $\delta V_{\mathrm{in}} = iR_{\mathrm{in}}$. This yields the relationship between the changes in the internal and external potentials that occur during the propagation of an AP as [12]

$$\frac{\delta V_{\mathrm{out}}}{\delta V_{\mathrm{in}}} = -\frac{R_{\mathrm{out}}}{R_{\mathrm{in}}}. \tag{9}$$

Through their numerical simulations, FitzGerald et al. [12] demonstrated that, for unmyelinated axons, the extracellular potential during AP propagation is amplified roughly uniformly throughout the microchannel except near the entrances; that is, the amplitudes of the spikes recorded by electrodes within a microchannel would be uniform along the length of the microchannel except those positioned near the ends of the microchannel. Wang et al. [6] have described this phenomenon, which they call the phase-cancelling effect, in more detail. The phase-cancelling effect occurs as a result of spatial variations in the direction of the transmembrane current at different positions along the axon in different stages of the AP. This causes certain portions of the axon to produce extracellular currents in opposing directions along the microchannel, which combine destructively and prevent further increases in the spike amplitude. The impact of the phase-cancelling effect is dependent on the conduction velocity of the axon; for an axon with a greater conduction velocity, the length spanned by the initial positive phase of the AP is greater, and thus the AP is able to travel further along the microchannel before the negative phase begins to cancel out the positive phase [6].

From the equations described above, changes in the external potential seen by a recording electrode can be increased by increasing the extracellular resistance, which can be achieved in the *in vitro* case by either increasing the resistivity ρ of the culture medium or reducing the volume of the medium. The former option is possible by changing the composition of the medium, but this would also impact the culture conditions. Thus, the confinement of axons in microtunnels in a μEF device is a simple and effective method of increasing the recorded extracellular potential. It should be noted that in the case of microfluidics, the resistance seen by a recording electrode in a microchannel is the resistance along the path running from that electrode through the microchannel to the reference electrode in the nearest culture chamber [15]. The resistance of the culture medium scales with the length L, width W, and height H of the microtunnel as $R_{\mathrm{ext}} = \rho L/(WH)$. However, this representation of the resistance in a microchannel is not completely accurate, as the resistance of the confined axons is also included in the total resistance of a microchannel. Pan et al. [53] demonstrated that the impedance of the recording electrodes beneath the axons in the microchannels of their μEF device increased as the culture matured and more

axons grew through the tunnels up to 14 DIV; this increase in impedance was correlated with an increase in the amplitude of the recorded spike. They attributed this increase in impedance to not only the filling of the tunnel with axons but also the blocking of tunnel openings by somata and the adsorption of proteins to the electrode. Here, it should also be noted that the small dimensions of the microchannel cause the resistance to be the dominant component of the impedance in μEF devices; this is in contrast to conventional MEAs inside bulk media, where the capacitive behavior of the medium dominates the impedance [15].

A number of previous studies have experimentally demonstrated the substantial amplification of extracellular recorded spikes by their confinement to microchannels. For example, Pan et al. [53] measured spike amplitudes generally in the range of 1–3 mV, with spikes even exceeding 4 mV. In contrast, the spike amplitudes they recorded in culture chambers were generally less than 50 μV. The noise levels in the microchannels and chambers were 10 and 2.5 μV rms, corresponding to signal-to-noise ratios (SNRs) of approximately 450 and 80, respectively [53]. Dworak and Wheeler [15] measured spike amplitudes of approximately 200 μV; the lower signal level is attributable to the fact that the electrodes spanned all 11 microchannels in their device, thus showing 11 parallel paths to the reference electrodes in the culture chambers. Despite this, these signals are still larger than even typical somal recordings in culture wells, which range from 10 to 100 μV. Habibey et al. [16] recorded reservoir and microchannel signals with maximum amplitudes of 400 μV and 1 mV, respectively. These results demonstrate the level of amplification and improvement to the SNR that can be achieved by confining axons to microchannels.

μEF devices have been used to measure the propagation velocity of APs traveling along axons in culture. This is done by positioning multiple electrodes along the microchannels through which the axons grow and calculating the propagation velocity from the arrival times of spikes determined to be from the same AP recorded at each electrode and the distance between the electrodes. As an illustrative example, a schematic of the setup used by Habibey et al. [16] to measure the propagation velocity is shown in Figure 2.9(a), and a phase contrast microscopy image of the device with cultured cells is shown in Figure 2.9(b). It should be noted that the increase in the extracellular resistance described above is expected to produce a decrease in the conduction velocity because of the resulting decrease in the length constant (see Section 2.1.1 for an explanation of the length constant). FitzGerald et al. [12] have demonstrated through the numerical simulation of axons confined in cylindrical microchannels, with various combinations of axon diameter and channel area, that the conduction velocity is generally reduced by less than approximately 5% and 1% in the case of myelinated and unmyelinated axons, respectively. Although these changes are small, this point will be considered in the analysis of the results obtained in the present study.

Habibey et al. [16] used the 60-channel MCS MEA coupled with a microfluidic device to monitor axon morphology and electrophysiology in fetal rat cortical neurons over the course of 95 DIV. The results of their long-term study have provided new insights into the correlation among culture age, burst activity, and propagation velocity. In previous shorter-term experiments (a few DIV), higher activity levels were found to result in decreased AP propagation velocity; however, Habibey et al. [16] demonstrated that increasing culture age is correlated with increases in both activity level and propagation velocity. Their results suggest that conduction velocity increases with age and that burst activity is correlated with conduction velocity. They also found that the conduction velocity tends to be higher in

proximal sections of the axon than in distal sections. Hong et al. [50] have also investigated the variation in axonal propagation velocity over culture age using a μEF device. They used a custom 60-electrode MEA with two networks of hippocampal neurons cultured in the two compartments of the μEF device. Through measurements taken between 9 and 28 DIV, they also determined that the propagation velocity increases with culture age.

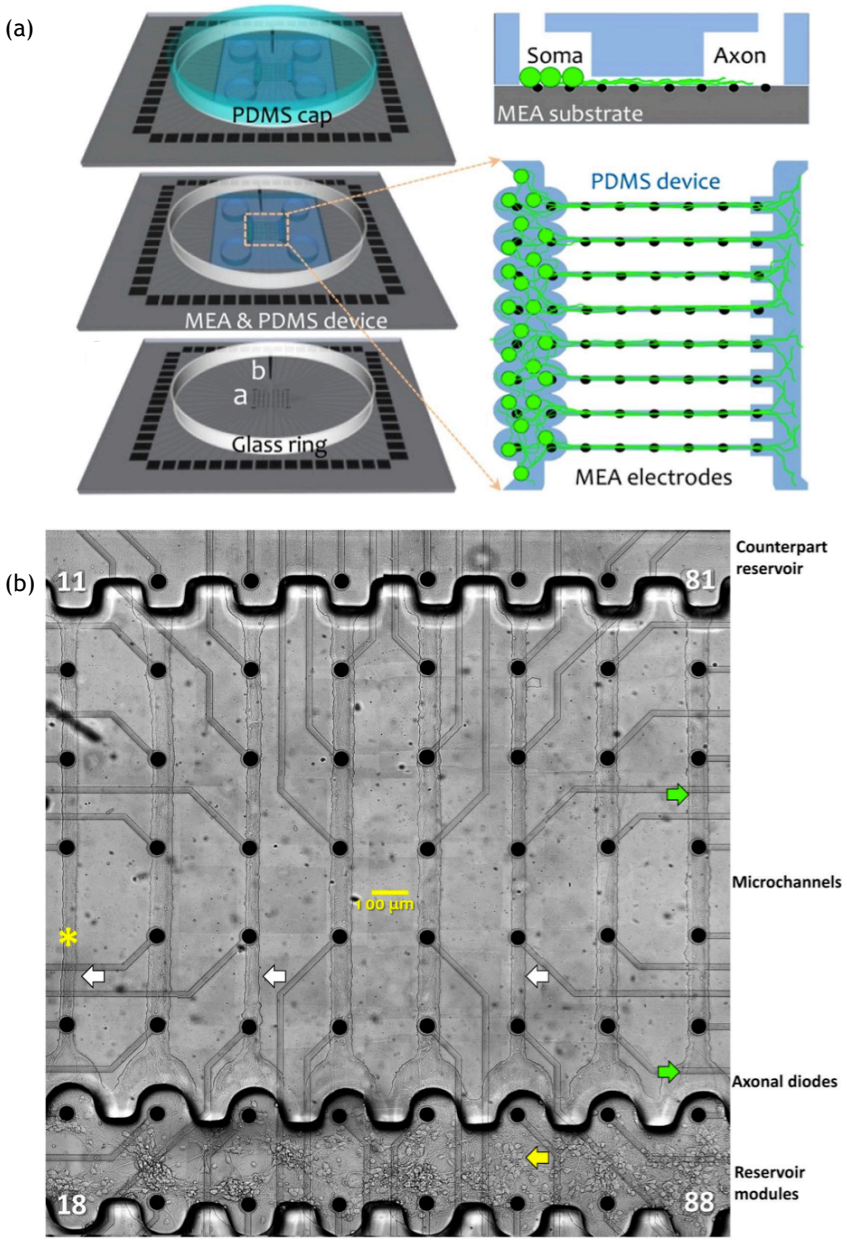

Figure 2.9 – Illustrative example of a μEF device. (a) Schematic of PDMS device mounted on a 60-electrode MEA chip. The somata are localized in the somal culture chamber, and the axons extend through the microchannels to the axonal compartment. MEA electrodes are regularly spaced beneath the microchannels. (b) Phase contrast microscopy image of the device. The white arrows indicate the three narrower microchannels (25 μm in width), and the remaining five are wider (40 μm in width). The yellow and green arrows indicate locations of somata and axonal projections in the device. Reproduced from Habibey et al. [16].

Lewandowska et al. [17] have measured APs traveling along axons confined to microchannels using a high-density MEA (11,011 platinum electrodes, 3161 electrodes/mm^2). Through recordings taken in the two culture chambers, which housed both somata and axonal

segments, they demonstrated that the two cultured groups of neurons were functionally connected, with bursts initiating in either chamber propagating through the axons in the microchannels and into the other chamber. Because of the high electrode density and the signal amplification achieved by the microtunnel confinement of the axons, they were also able to match activity from somata and their axons on the basis of the shape of the recorded signals and the delays between adjacent recorded spikes. Additionally, they monitored the evolution of spike shapes from the same axon over time using recordings from multiple electrodes along the channels with consistent spike shapes at a given time [17]. The results of their study have demonstrated the great potential for studies employing µEF devices in terms of the amplification of axonal signals to readily recordable levels that enable the clear visualization of AP shape, the high spatial resolution of spike recordings, and the possibility of conducting numerous simultaneous single-cell recordings.

The effect of drugs and chemical and electrical stimulation on propagation velocity and network activity has been investigated in a number of studies using µEF devices. A detailed discussion on the mechanisms underlying the axonal modulation of the propagation velocity can be found in Appendix A. Habibey et al. [16] were able to transiently increase the conduction velocity in individual neurons by stimulating them electrically with a low-frequency pulse, though this transient increase was not correlated with the overall network activity and did not affect the conduction behavior of post-synaptic neurons. This velocity increase, which was observed for spikes propagating 5–35 ms post-stimulus, was small (a factor of approximately 1.1) but significant ($p < 0.05$) [16]. Dworak and Wheeler [15] have shown that the propagation velocity can be changed and then reverted back to the original levels by the addition and subsequent washout of the drug mepivicaine, which blocks sodium channels. In one of the earliest applications of microfluidics in combination with MEAs, Claverol-Tinturé et al. [51] captured the spatial distribution of an action potential generated by pharmacological stimulation using an array of 18 electrodes spanning a single microchannel containing a single neuron extracted from a snail. Biffi et al. [52] investigated the electrical activity of twin neuronal networks under biochemical stimulation. They achieved the formation of two neuronal networks showing very similar electrophysiological activity after being cultured under highly similar conditions and were able to selectively stimulate each network with a test molecule. Their study highlights two important capabilities provided by µEF devices: greatly reduced culture-to-culture variability in comparison with conventional culture methods and targeted biochemical stimulation.

In addition to manipulating the propagation velocity, Dworak and Wheeler [15] have also investigated the effect of the size of recording electrodes and their distance from the nearest microchannel entrance on the characteristics of the recorded signal. In their microfluidic platform, electrodes of three different sizes were evenly spaced beneath microtunnels connecting four peripheral chambers to one central chamber. In their setup, the electrodes see two parallel paths running through the medium in the microchannels to the reference electrodes, which lie in the culture chambers, and the electrodes with the shorter paths to either of the two chambers (those on either end of the channels) showed lower impedances than the electrode with the longer paths (that in the center of the channels). Additionally, the smaller electrodes yielded smaller spike amplitudes than the larger electrodes.

Another major factor influencing the signal characteristics is the microtunnel width. In addition to their role in signal amplification, narrow microtunnels have been demonstrated to

improve the ability to distinguish APs arising from individual axons [54]. When a larger microtunnel is used, more axons are able to extend through the tunnel. Thus, a single electrode is more likely to record simultaneous APs arising from multiple axons in a single tunnel, and these overlapping spikes in the signal are very difficult to separate. In addition to increasing the signal amplitude, the use of a narrower microtunnel limits the number of axons present in the microtunnel, thereby reducing the likelihood of recording simultaneous spikes from different axons. In their study, Narula et al. [54] used *k*-means clustering to cluster individual action potential events in feature space and categorize them as being from the same axon. Each axon in their setup produced spikes of similar heights and widths that were distinct from spikes produced by other axons. Thus, if there are no overlapping spikes in a signal, the events would tightly cluster in feature space according to the axon from which they originated. It was demonstrated that narrower microtunnels produced tighter clusters than wider microtunnels because of the reduced likelihood of overlapping APs.

Network dynamics are also commonly investigated in microfluidics studies, as the microchannels provide the researcher with a high degree of control over the connectivity of isolated neuronal populations. Pan et al. [55] have developed a microfluidics model that enables the unidirectional propagation of single APs and bursting activity by the sequential plating of cortical neurons in two culture wells connected by microchannels. Cells were first plated in one well, and axons from that culture were allowed to grow through the microchannels for 10 days before cells were plated in the other well, such that there was little space for axons from the second culture to grow through the microchannels. The microfluidic device used by Pan et al. [55] was designed so that some microchannels could be aligned over neighboring pairs of electrodes from the center rows of the 60-channel MCS MEA. The inclusion of two electrodes in one channel enabled the determination of the propagation speed and direction. Using the same sequential plating configuration, Pan et al. [56] later investigated the influence of the number of tunnels in the μEF device on the network connectivity and burst propagation. In this later study, neurons were plated in the second well after the neurons in the first well had been in culture for seven days. They demonstrated that the inclusion of a greater number of microchannels resulted in a lower delay time between electrically stimulated bursting activity in the first well and subsequent bursting activity in the second well as well as a greater propagation likelihood. Selecting the number of channels to achieve a desired level of connectivity between cultured neuronal populations would enable the more accurate *in vitro* modeling of neurological diseases in which neuronal connectivity is affected [56].

Kanagasabapathi et al. [57] co-cultured dissociated cortical and thalamic cells in a dual-compartment device containing microelectrodes to provide further evidence of the recently hypothesized function of the thalamus as more than simply a relay station sending sensory signals from the periphery to the cortex. The reciprocal connectivity between the cortex and thalamus has attracted attention because of the role such network activity plays in pathological conditions such as Parkinson's, epilepsy, and schizophrenia. However, *in vivo* studies on this network does not provide sufficiently high spatial resolution, and the specific cortical–thalamic system cannot be isolated from other brain regions *in vivo*. The application of microfluidics to this topic enabled Kanagasabapathi et al. [57] to isolate the two cell populations while allowing them to form a network via axon growth through the microchannels. They first observed the distributions of the instantaneous firing rate of each cell type alone and plated together in a compartmentalized microfluidic device. As a result,

they found that the two cell populations formed reciprocal functional connections that may provide insight into the functional connections formed *in vivo*. Most bursts originated in the cortical chamber and propagated to the thalamic chamber, driving the bursting behavior of the entire network, but weak thalamo–cortical connections played a role in sustaining burst events.

Berdichevsky et al. [46] investigated the communication between the hippocampus and the cortex by co-culturing organotypic brain slices in two compartments connected by microchannels. Their setup enabled the highly controlled formation of an axonally linked circuit with two pharmacologically isolated chambers while maintaining the architecture and physiological activity of the studied brain regions. Pharmacological isolation was successfully achieved by placing more medium in the well with no drugs than in the well with the investigated drug to maintain a pressure gradient and counter diffusion of the drug through the microchannels. By conducting experiments with hippocampal–hippocampal and hippocampal–cortical organotypic slice co-cultures in their two-compartment device, Berdichevsky et al. [46] were able to demonstrate the formation of axonal connections between the two slices via the observation of burst synchronization. Furthermore, these observed bursts showed both positive and negative delays between the two compartments, indicating bidirectional burst initiation.

Many authors have used commercially available MCS MEA systems in their studies. In the software this system, spikes are detected as events where the signal exceeds five times the standard deviation of the background noise level estimated from periods of relative inactivity or a threshold defined manually by the user. However, some researchers have developed their own methods of spike detection as well as further methods of classifying spikes recorded on separate electrodes as being the same AP propagating along the same axon. In their study on the long-term behavior of fetal rat cortical neurons, Habibey et al. [16] analyzed recordings from microelectrodes positioned at 200 µm intervals along the axon microchannel. Although they used the 60-channel MCS MEA system for event detection, they had to perform further analysis to determine if the spikes identified in each recording had originated from the same source to calculate the conduction velocity. This was done with an in-house MATLAB script because existing spike sorting protocols were not robust enough against misattribution due to the close proximity of the axons in the microchannels. The criteria for a group of single-electrode spikes to be considered as a spike unit representing a propagating AP were that the AP must have traversed the entire microchannel and single-electrode spikes detected at neighboring electrodes must have been temporally separated by less than 2 ms (corresponding to a minimum propagation velocity of 0.1 m/s).

Lewandowska et al. [17] used three different methods to associate spikes recorded by different electrodes with a single AP traveling along the same axonal segment. In the first approach, they determined which electrodes were recording from spontaneously regularly spiking somata and used the somal spike as a trigger to find axonal spikes on electrodes in nearby channels. From this method, they found an average propagation velocity of 0.51 m/s ± 0.1 m/s. In the second approach, they used spike-triggered averaging, whereby the somal signals preceding recorded axonal spikes are averaged to determine which somal events consistently preceded axonal events. In the third approach, they applied a stimulus to axons within the MEA and determined which somata spiked. In all approaches, it was noted that the

general shape of axonal APs differ from that of somal APs. Of the three methods, spike-triggered averaging yielded the most robust results.

Dworak and Wheeler [15] clustered event waveforms considered to arise from distinct spike units using a valley-seeking algorithm, in which target elements are automatically clustered based on their proximity in feature space. This algorithm is fairly robust against noise because it considers different aspects of the AP waveform, such as the rising and falling slopes and the peak values, allowing an overall correspondence between the signals to be obtained rather than a close match with just one feature. To determine the propagation velocity, Dworak and Wheeler [15] identified highly correlated units among pairs of electrodes and discarded pairs with non-normal delay time distributions as identified by statistical analysis. The use of statistical analysis to discard pairs with unexpected delay times circumvents the need to impose a predefined range on the propagation velocity, as was done by Habibey et al. [16]; this increases the likelihood that only correct pairings are retained for the calculation of the propagation velocity. As one of their considerations was the effect of the addition of a drug on the propagation velocity, Dworak and Wheeler [15] identified neuronal units originating from the same axon under each of the considered conditions in the drug addition and washout tests as those signals that varied by less than 12 μV rms from each other on the basis of the assumption that the variation produced by the considered conditions is less than the variation among signals from different axons.

These studies demonstrate some of the benefits of using μEF devices in neuroscience research. The confinement of axons in microchannels not only allows compartmentalization, thereby enabling the control of the source, target, and polarization of the fibers [4], but also greatly amplifies the extracellular recordings of APs by increasing the extracellular resistance [12]. This allows APs to be more readily extracted from noisy recordings. The dimensions of the microchannels also play a role in enabling the isolation of individual axons such that the propagation of an AP along the length of the microchannel can be tracked without signal distortion due to overlapping APs detected at the same time on the same electrode [54]. A number of studies have demonstrated the utility of μEF devices in drug screening applications, as well as in the investigation of network dynamics.

2.2.4 Compartmentalized devices for neuron co-culture with other cells

This section discusses the advantages of using compartmentalized microfluidic devices to accurately recapitulate *in vivo* neurobiological systems and gives an overview of some past studies on the development and application of compartmentalized neuronal co-culture systems. Although the focus of the present study is the innervation of bone, this section presents a wide variety of neuronal co-cultures to provide a broad understanding of the advantages of co-culturing different types of cells in compartmentalized microfluidic devices and to demonstrate how microfluidic devices can be readily adapted to different applications. It should be noted here that all of the studies presented in this section involve microfluidic devices without microelectrodes and, to the best of the author's knowledge, no previous studies have been conducted using compartmentalized μEF devices to investigate the electrophysiological component of inter-system communication involving neurons.

As discussed previously, compartmentalized microfluidic devices are devices with multiple culture chambers connected by microchannels, and they enable the physical and fluidic separation of different types of cells. This separation is important in developing accurate *in vitro* models of various *in vivo* systems because different types of cells often

reside in different microenvironments while still maintaining functional connectivity. This is especially true of the nervous system, as neuronal cell bodies are often located very far from their corresponding axonal terminals. Conventional *in vitro* co-cultures involve plating multiple types of cells in one culture flask, meaning the cells are immersed in the same culture medium and are exposed to the same treated surface. In this conventional setup, the cells also take on a random distribution within the culture flask. In contrast, in a compartmentalized microfluidic device, the cells in the different compartments can be supplied with different culture media, and the small size of the channels connecting the two compartments means they remain fluidically isolated [58]. This fluidic isolation also enables the targeted delivery of drugs and other biomolecules to the somal or axonal compartment. In compartmentalized devices, different surface treatments can also be applied to mimic the physical aspects of the *in vivo* microenvironments of the different cells cultured in the device. Tailoring the microenvironments of the two compartments to the needs of the specific cells improves cell survival rate and enables longer-term studies than conventional co-culturing techniques.

Existing neurobiological studies employing compartmentalized microfluidic co-cultures can be classified into intra- and intersystem co-cultures, i.e., co-cultures involving only cells from the nervous system [59]–[62] and those involving cells from other systems as well [47], [63]–[67]. One major topic of study in work on the CNS is the process of myelination. Myelin is an insulating layer that envelops the axon and enhances signal transduction. It is produced by oligodendrocytes (OLs) in the CNS and Schwann cells in the PNS. In diseases involving the impairment of myelination, such as multiple sclerosis, signal conduction along nerves is impaired, and the affected axons eventually break down. However, the molecular basis of myelination remains poorly understood because of the limitations of conventional *in vitro* systems. Thus, many researchers are keen to develop systems that would allow them to gain a better understanding of the mechanisms of myelination. Park et al. [59] developed a circular two-compartment microfluidic device and verified that OLs aligned with axons in the axonal compartment in a manner similar to that seen *in vivo*. The circular design enhanced the ability of the user to isolate and target specific axons in the channels connecting the compartments, but the need to manually punch the hole for the central compartment was time consuming and introduced variations among devices. Thus, in a later study by the same group, they developed an improved neuron–glia co-culture device with a circular central somal compartment connected to six square peripheral glial compartments via approximately 30 radial channels for each compartment that could be fabricated using a hybrid microscale–macroscale approach [60], demonstrating the adaptability of microfluidic devices to the target purpose. With this device, they successfully observed the communication between axons and glia in the glial compartment, differentiated OL progenitor cells into OLs, and demonstrated the ability to carry out parallel pharmacological studies by targeting each of the six glial wells independently. They also demonstrated that mature OLs, as opposed to undifferentiated OL progenitor cells, are necessary to achieve myelination. However, they were unable to achieve a neuron–astrocyte co-culture using this device because the addition of astrocytes to the glial compartment after the neurons had extended their axons disrupted the established axonal layer, as they tended to adhere underneath the axons [60].

In another study using the standard two-compartment device with the neuronal compartment modified to be an open well to allow greater axon density, myelin formation in

the axonal compartment was quantified by applying a semi-automated algorithm to fluorescence images [61]. The compartmentalization of the neurons and OLs in the co-culture system ensured the OLs and axons in the axonal compartment were located close to one another, rather than randomly distributed as in a conventional co-culture system, and that there was no interaction between the distant somata and OLs. Using a different approach, Yang et al. [62] demonstrated the activity dependence of myelination by using a two-compartment device with stimulating electrodes extended into the two open culture wells containing OLs and DRG neurons. They showed that intermittent electrical stimulation (1 h/day) induced significant myelin formation, a result that may prove beneficial in the development of remyelination therapies for diseases like multiple sclerosis.

Intersystem co-cultures enable the recapitulation of PNS innervation of different types of tissue. It is known that innervation plays an important role in the formation and homeostasis of different tissues, such as bone and muscle, but the mechanisms inherent to their role remain largely unknown. Microfluidic devices provide the unique ability to maintain the viability of different types of cells requiring different media and substrate treatments for survival as well as the capability to readily and reproducibly isolate specific cell–cell interactions for observation or targeted therapy, making them well positioned for application in intersystem co-culture studies. Neto et al. [47] modified a conventional two-well co-culture platform to contain a localized open well for DRG explant culture to study the interaction between the DRG axons and osteoblastic cells cultured in the second compartment. They investigated the benefits of using different 2D and 3D substrates for the osteoblastic cell culture and quantified axonal outgrowth into the axonal compartment using a custom semi-automated algorithm. Through immunostaining and electron microscopy, they were able to establish the close interaction between the co-cultured cells and test for different neuronal markers. The modified microfluidic device developed in their study was used in the present experiments for DRG explant culture. In a related study involving the same lab and a collaborating lab, the innervation of dental tissue was investigated, again using explant cultures in the same type of microfluidic device [63]. Neurite growth was observed to be marked by the same attractive or repulsive effects as observed *in vivo* when cultured with postnatal or embryonic tooth germs, respectively; in the *in vivo* case, neurons surround but do not penetrate tooth germs during embryonic development and then begin to penetrate and fully innervate the developing tooth in the postnatal stage.

Co-cultures between neurons and myocytes have also been performed using microfluidic devices to observe the interaction between the nervous and muscular systems. Motor neurons are peripheral neurons whose cell bodies are housed in the spinal cord and whose axons extend to the periphery with their terminals in direct contact with muscle tissue. This contact constitutes the neuromuscular junction, an excitatory chemical synapse responsible for signal transmission from the neuron to the muscle. Neuromuscular signaling involves bidirectional communication between the neuron and myocyte: anterograde signaling to stimulate muscle contraction and retrograde signaling to maintain the health of the neuron [64]. Although the nature of this signaling is broadly understood, the specific mechanisms underlying the interaction have not yet been fully characterized, and this characterization would aid in understanding and treating motor neuron diseases. Compartmentalized co-cultures mimicking the *in vivo* separation of the soma from the neuromuscular junction have been achieved [64]–[66]. In one study, microelectrodes were used to stimulate the cultured neurons, and the response of the co-cultured myocytes was observed to be significantly

affected by variations in the neuronal stimulation frequency [65]. In another approach, it was demonstrated that proximal application of glial-derived neurotrophic factor has a different effect on motor neurons than distal application; axonal growth and branching were induced only by application to the axon, whereas survival pathways were triggered by application to both the soma and the axon, indicating unidirectional transport along the axon [66].

Microfluidic co-culture systems have proven to be extremely useful in unraveling the mechanisms of communication and interaction between neurons and other cell populations. These devices enable the physical separation of the two types of cells, the recapitulation of the microenvironments of each cell type, and the targeted stimulation of individual cell populations. The above discussion has demonstrated the technical advantages of microfluidic techniques in neuronal cell culture, and the following section will provide some background regarding the innervation of bone, which is the topic that will be addressed by the application of these techniques in this work.

2.3 Crosstalk between sensory neurons and bone

This section provides an overview of the current understanding of the communication between bone cells and the nerves that innervate the bone tissue. Bone was once considered to be a relatively static tissue, but it is now known that bone homeostasis is actively maintained through bone remodeling, which helps to maintain the strength of bone, replace old or damaged bone, and maintain mineral homeostasis. This section first gives an overview of the anatomy and physiology of bone and the sensory and sympathetic nervous systems. The process of bone remodeling is then introduced, and a review of the existing literature on the current understanding of the effects of different sensory and sympathetic neurotransmitters on the bone remodeling process is presented. Finally, this section closes with a brief discussion of retrograde signaling in sensory neurons innervating bone with a focus on the mechanisms of bone pain. Because the present study is concerned with the bidirectional communication between neurons and bone cells, the present discussion address both the effects of anterograde neuronal signaling on bone cells, namely in the bone remodeling process, as well as how bone may stimulate retrograde signals in sensory neurons, particularly with regard to bone pain.

2.3.1 Anatomy and physiology of bone and the sensory and sympathetic nervous systems

Bone anatomy

The main points of this overview of the anatomy of bone were largely adapted from recent reviews by Ralston [68] and Clarke [69]. Bone is a highly mineralized tissue that performs a variety of important functions. The skeletal system provides structural support to the body and protects internal organs, such as the heart and lungs, from external damage. It also provides a structure to which muscles can attach and gain leverage, thereby enabling locomotion. The marrow in the central cavity of some bones acts as a reservoir for growth factors and provides an environment for hematopoiesis (the production of blood cells and platelets). Bone also maintains the mineral homeostasis of the body. Different bones in the human skeletal system are typically classified into four categories based on shape: long bones

(e.g., the femur), short bones (e.g., the carpal and tarsal bones), flat bones (e.g., the skull), and irregular bones (e.g., the vertebrae). Bone contains an inorganic mineral phase, hydroxyapatite, as well as an organic phase consisting of type I collagen, noncollagenous proteins, proteoglycans, and other substances.

There are two macroscopic structural categories of bone: cortical bone and trabecular or cancellous bone. A schematic of the overall structure of a long bone showing the location of these two types of bone is presented in Figure 2.10. Cortical bone is highly mineralized, making it dense and compact, whereas trabecular bone is composed of a porous matrix of trabecular plates and rods. Cortical bone comprises approximately 80% of the skeleton is composed of cylindrical structures called Haversian systems, which consist of collagen fibrils arranged in concentric layers called lamellae surrounding a central lacuna called the Haversian canal containing the vessels that provide the blood supply of the bone. Haversian canals in neighboring Haversian systems are connected by canals called Volkmann's canals. There is a layer of cortical bone surrounding the medullary cavity in the diaphysis of long bones, and a thinner layer is present around the epiphysis and metaphysis (Fig. 2.10). The outer cortical surface of bone is surrounded by a sheath called the periosteum. The periosteum has two layers, a thin outer layer composed of fibrous connective tissue and an inner lining that houses osteoblast and osteoclast progenitor cells waiting to be recruited for bone remodeling.

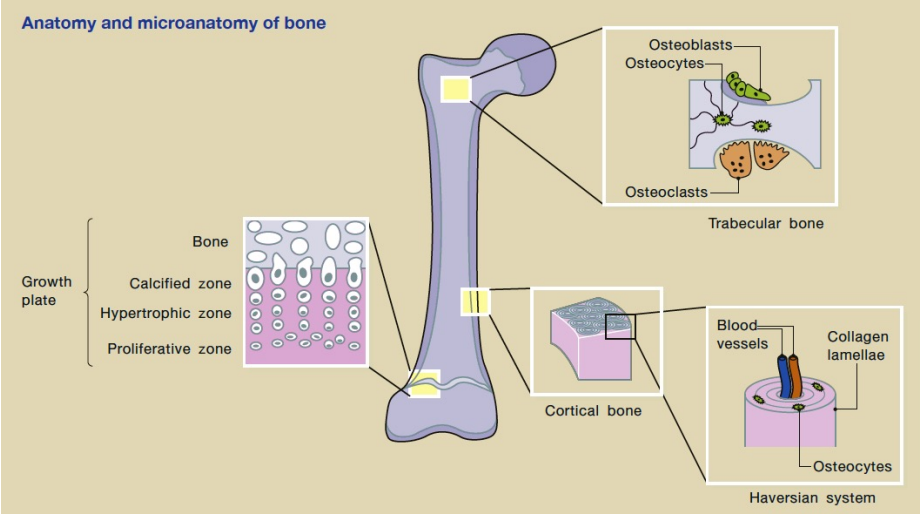

Figure 2.10 – Structure of a long bone. The outer layer is composed of cortical bone, and the central cavity is composed of trabecular bone. The three main types of bone cells are osteoblasts, osteoclasts, and osteocytes. The ends of the bone are referred to as the epiphyses, the straight long section is the diaphysis, and the narrow portion between the epiphysis and the diaphysis is the metaphysis. Reproduced from Clarke [69].

Trabecular bone is composed of plates and rods arranged in a matrix-like pattern with the spaces between filled with bone marrow. It fills the central cavity of long bones, flat bones, and vertebrae. Trabecular bone has a higher surface area than cortical bone and thus undergoes remodeling more rapidly. Cortical bone has an outer periosteal surface and an inner endosteal surface. The rate of bone formation on the periosteal surface outperforms the rate of bone resorption, and thus the overall diameter of bones tends to increase with age. In contrast, on the endosteal surface, the rate of bone resorption is greater than the rate of bone formation, meaning the diameter of the medullary cavity also increases with

age. Furthermore, the total rate of bone resorption on both surfaces exceeds that of bone formation, and thus the thickness of the cortical layer decreases with age. This is one cause of the reduced mechanical strength of bon that commonly occurs in the elderly.

Bone is also characterized by two microstructural categories: woven bone and lamellar bone. The organic phase of bone is dominated by type I collagen, which is a fibrillar protein and the most abundant type of collagen in the body. During bone formation or repair, individual collagen fibrils are typically laid down in an orderly fashion, with fibrils taking on a layered pattern. This pattern is a source of the strength of bone. However, when bone is formed rapidly, it is laid down in a disorganized, scattered pattern. Woven bone is weaker than lamellar bone and more susceptible to fracture. Woven bone is laid down rapidly and can be remodeled into lamellar bone, providing rapid response to mechanical changes or injury without long-term sacrifice of structural strength.

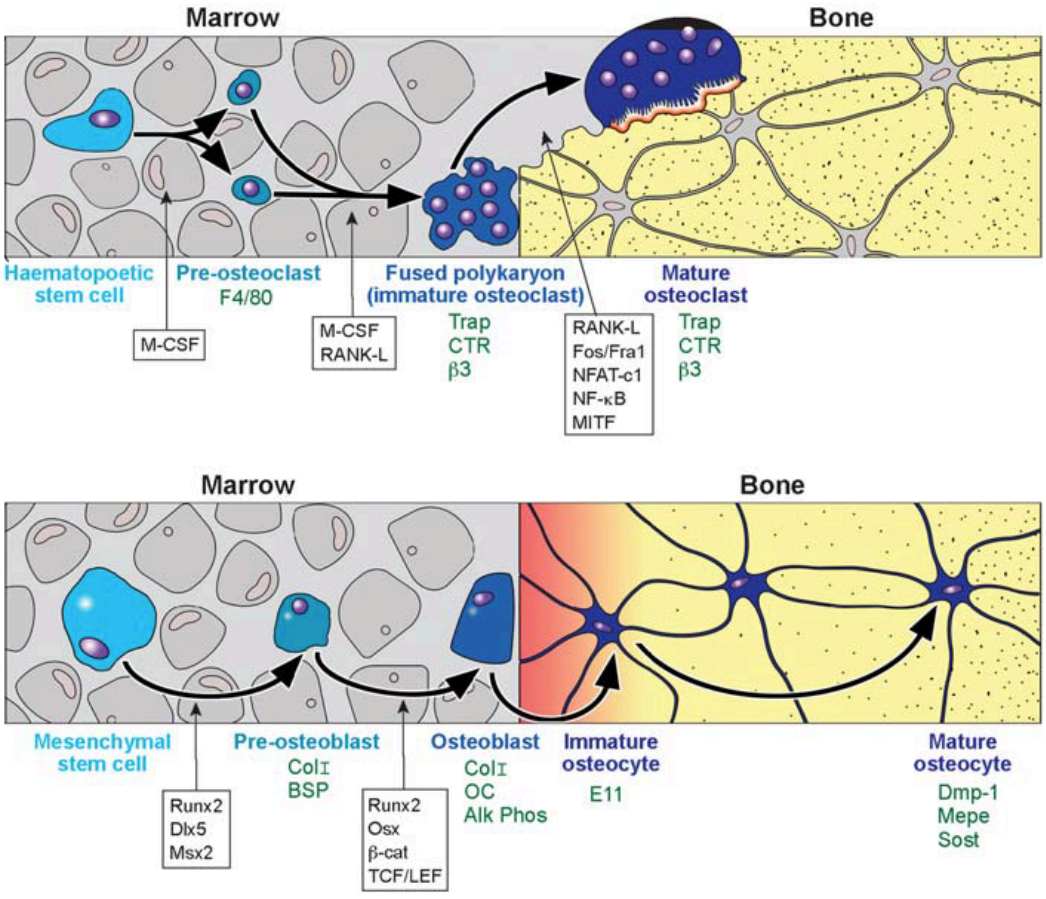

Figure 2.11 – Schematic of the differentiation of hematopoietic stem cells into mature osteoclasts and mesenchymal stem cells into osteoblasts and mature osteocytes. These stem cells are housed in the marrow, and the osteoclasts and osteoblasts act along the surface of the bone. Various pathways implicated in the different stages of differentiation are also listed in the figure. Reproduced from Robling et al. [70].

There are four main types of bone cells: osteoclasts, osteoblasts, osteocytes, and bone-lining cells. Osteoclasts are multinucleated cells responsible for the resorption of bone, and the are derived from a hematopoietic lineage. They bind to bone matrix via integrin receptors that link to bone matrix peptides and become polarized, which causes them to develop their characteristic ruffled border on the side nearest the bone to be resorbed.

Osteoblasts are derived from mesenchymal stem cells and are responsible for the formation of new bone via the synthesis of new bone matrix proteins on the bone surface. Osteoblasts that become surrounded by bone matrix become, which are mature bone cells osteocytes. Osteocytes comprise approximately 90% of the cells within the bone matrix. They are situated within lacunae in mineralized bone and form a network via filipodial extensions that enable them to transduce mechanical signals into biological activity. Osteoblasts may also remain on the surface and become quiescent, differentiating into bone-lining cells. These cells line the surface of bone when bone formation is not occurring. Figure 2.11 shows a schematic of the lineage of osteoclasts and osteoblasts and their roles in bone resorption and formation.

Sensory and sympathetic nervous system anatomy and physiology

This section briefly describes the anatomy and physiology of the PNS with a focus on the sensory nervous system. The information presented here is primarily derived from the well-known neuroscience textbooks by Kandel et al. [18] and Purves et al. [71].

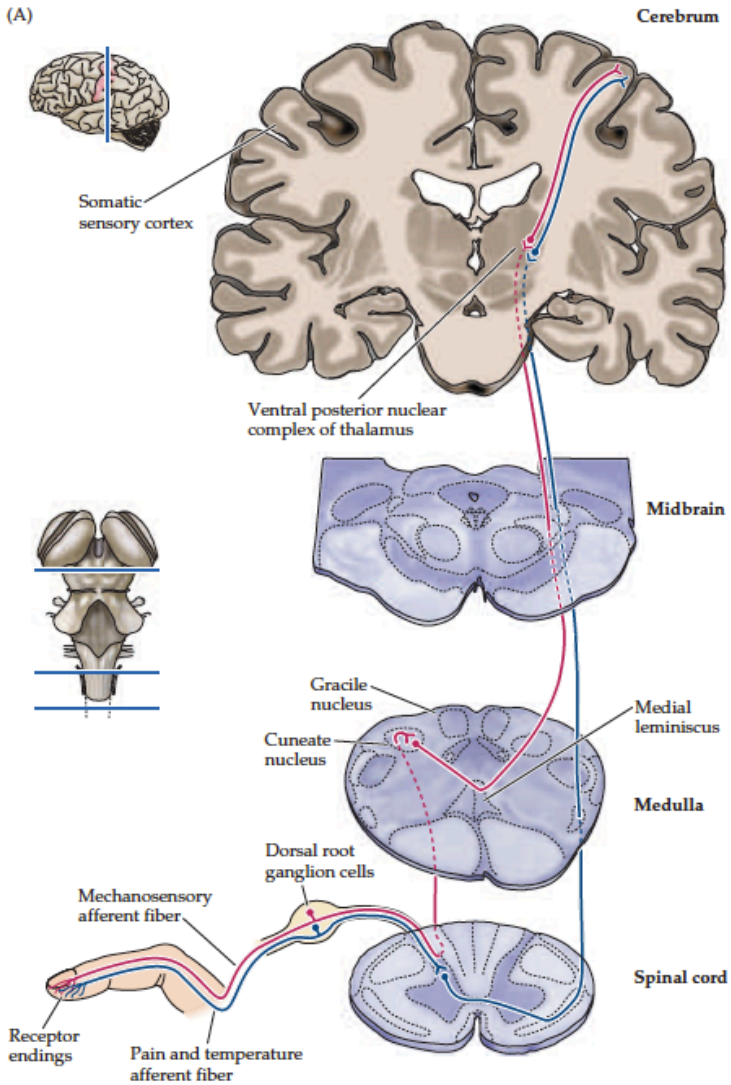

Figure 2.12 – General organization of the sensory nervous system. The cell bodies of the sensory neurons are housed in the DRGs. The axon has two branches extending peripherally to the innervated

tissue and centrally to the spinal cord. Different types of neurons are implicated in the sensation of mechanical stimuli and of pain and temperature. Reproduced from Purves et al. [71].

The somatic sensory system is the part of the sensory nervous system devoted to the conscious perception of stimuli experienced by the body, including touch, pressure, pain, and vibration. Neurons of the somatic sensory system have cell bodies that are housed in the dorsal root ganglia (DRGs) and an axon with two branches, one extending toward the periphery and terminating in the innervated tissue and one projecting to the central nervous system. The axon terminating in the innervated tissue is called the primary afferent fiber. Its terminal contains receptors that transduce the external sensory signal into an electrical signal, which is then transmitted along the fiber toward the centrally projecting fiber. This general organization of the sensory nervous system is depicted in Figure 2.12.

The somatic sensory system is divided into two subsystems, one for the detection of mechanical stimuli and one for the detection of pain and temperature. Different sensory neurons are categorized by the type of stimulus to which they respond as mechanoreceptors, which respond to mechanical stimuli; nociceptors, which respond to noxious or damaging stimuli and are responsible for the perception of pain; thermoceptors, which detect temperature; and proprioceptors, which provide information about where the different parts of the body are in space. Regardless of the stimulus to which a somatic sensory neuron responds, the manner in which they transduce sensory information into electrical activity is essentially the same: the applied stimulus produces a change in the receptor, which increases the permeability of the neuronal membrane to ions, thereby producing a membrane potential that may trigger an AP. In some cases, the receptors respond directly to the applied stimulus; in others, there is a chemical intermediate released by another tissue, and this chemical binds to the receptor. Some receptors, called phasic receptors, fire rapidly at the onset of stimulation and then cease firing when the stimulus is maintained, whereas others, called tonic receptors, continue to fire as long as a stimulus is present. The stimulus location and type can be determined from the properties of the receptor that fires, and the strength of the stimulus is encoded by the firing rate of the corresponding neuron.

Mechanosensors have myelinated axons, and thus mechanical signals are transmitted with a high conduction velocity; in contrast, nociceptive axons are mostly unmyelinated or at most lightly myelinated, and thus pain signals travel with a much slower conduction velocity. Most sensory innervation in bone consists of nociceptive fibers. There are generally considered to be two types of nociceptors: myelinated Aδ and unmyelinated C nociceptors, which have conduction velocities of approximately 20 and 2 m/s, respectively. The ‘first’ pain, the sharp and rapidly subsiding felt upon injury, is attributable to Aδ fibers, whereas the ‘second’ pain, the dull lingering pain felt following the injury, is attributable to C fibers. Nociceptors are also categorized by stimulus type into thermal, mechanical, and polymodal nociceptors, with thermal and mechanical nociceptors having Aδ axons and polymodal nociceptors having C axons. The centrally projecting fibers of nociceptive neurons form chemical synapses with spinal neurons and transmit signals via chemical neurotransmitters. The peripheral terminals of nociceptive neurons may also release these neurotransmitters in the innervated tissue, and the effect of these neurotransmitters on the target tissue is the focus of many studies on the effects of sensory innervation.

The sympathetic nervous system the subdivision of the autonomic nervous system that is involved in readying the body to respond to extreme circumstances by taking full advantage

of its resources. That is, when sympathetic neuronal activity levels are high, the body undergoes physiological changes such as dilation of the pupils to allow more light to hit the retina, increased heart activity to enhance blood supply to muscles and the brain, and contraction of the blood vessels in the gut and skin contract to redirect blood to the muscles, and the bronchi dilate to increase oxygenation. Peripheral sympathetic neurons are arranged with their axons terminating in the innervated tissue and their cell bodies housed in ganglia, most of which are in the sympathetic chains just ventral and lateral to the spinal cord. These postganglionic neurons receive signals from central sympathetic neurons, which extend from the spine and terminate in the sympathetic ganglia. The primary neurotransmitters associated with stimulating this activity are norepinephrine (NE) and acetylcholine (ACh). Most preganglionic neurons release ACh, which acts on cholinergic receptors in the postganglionic neuronal membrane, whereas postganglionic neurons release mostly NE, which acts on different adrenergic receptors in the innervated tissue. There are five types of adrenergic receptors classified into two categories, α and β adrenergic receptors (αARs and βARs). Neuropeptide y (NPY) is a common neurotransmitter that is present in up to 90% of cells and helps to enhance signal transmission from sympathetic neurons to the innervated tissue. It potentiates tissue response to both adrenergic and purinergic signals. Vasoactive intestinal peptide (VIP) is a neurotransmitter associated with cholinergic signals that acts as a vasodilator. The enhancement of blood flow by VIP may aid in signal transmission by ACh to the target tissue.

2.3.2 Bone remodeling

Although it has been demonstrated that bone is richly innervated by sensory and sympathetic nerves, the function of this innervation in various biological processes has not been definitively determined. This section first gives a brief overview of the anatomy of bone innervation and then describes the process of bone remodeling, which is now thought to be a target of control by neuronal signaling. Disruption in the body's ability to maintain skeletal homeostasis through bone remodeling has been observed in a number of pathologies, including stroke and spinal cord injuries [8]. The effects of sensory and sympathetic neurotransmitters on the bone remodeling process are then described in Sections 2.3.3 and 2.3.4, respectively.

Bone is innervated in accordance with Hilton's law, which states that the nerves supplying the muscles and skin overlying a given joint also supply that joint. Nerve fibers generally accompany the blood vessels that provide vascular support to bone, forming dense networks in close proximity to bone and bone marrow [7], [72]. The presence of nerve fibers has been demonstrated in the periosteum, bone marrow, and both trabecular and cortical bone, with the periosteum being the most densely innervated with sensory nerve fibers and the bone marrow containing the greatest number of fibers [9], [10]. In terms of sensory innervation, bone is largely innervated by nociceptive Aδ nerve fibers and shows little to no innervation by C fibers and non-nociceptive sensory fibers [10]. The absence of mechanoreceptors in bone is likely because, unlike skin, bone does not require touch feedback. The reason for the general lack of C fibers in bone is unknown, though it may be that there is less benefit to nociceptor redundancy in bone than in skin or muscle [10]. However, the periosteum is innervated with both Aδ and C fibers,

The periosteum is innervated with mostly sensory nerve fibers that are sensitive to both mechanical stimulation and pain [7]. The largest nerve enters the diaphysis and extends into

the medullary cavity, and most nerves innervating the bone marrow are considered to be sympathetic vasomotor [7], meaning they are responsible for controlling the level of constriction of blood vessels. Sensory nerve fibers run through the Haversian and Volkmann's canals in cortical bone and are abundant along epiphyseal and metaphyseal trabecules, though nerves are relatively sparse in the cortical bone and so most canals are not populated with nerve fibers [10]. Overall, the distribution of nerve fibers in bone indicates that few bone cells are in direct contact with axonal terminals, suggesting that communication between neurons and bone cells may be either nonsynaptic or involve communication through intercellular junctions [7].

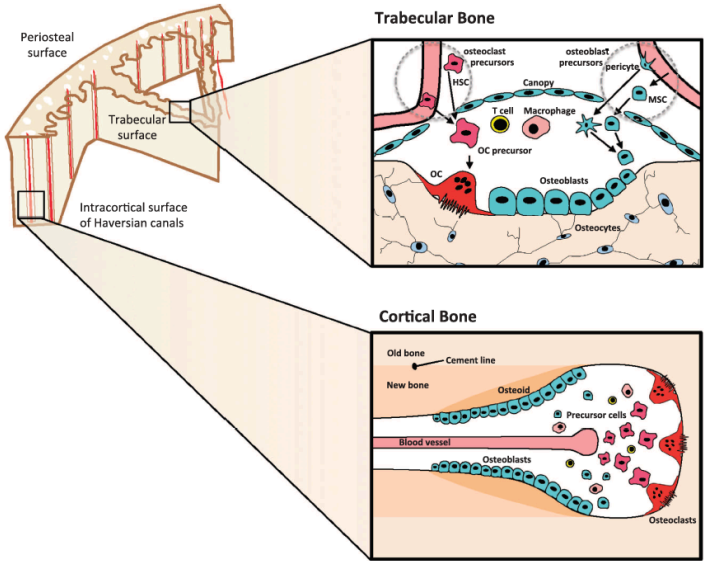

Figure 2.13 – Illustration of bone remodeling in trabecular and cortical bone. Bone remodeling takes place in isolated BMUs. In trabecular bone, BMUs are located on the surface of the bone and surrounded by a canopy of bone lining cells. In cortical bone, osteoclasts carve a path through the old bone, and osteoblasts and blood vessels follow, laying down new innervated, vascularized bone tissue. Reproduced from Sims and Martin [73].

The generation and maintenance of bone depends on both bone modeling and bone remodeling. Bone modeling is the process by which bone is formed at sites where it has not undergone prior resorption, altering the overall shape of bones in response to external stimuli, such as mechanical loading. This process causes bones to gradually adapt to accommodate the stresses applied to them. During this process, bone formation by osteoblasts and resorption by osteoclasts are not tightly coupled [69]. In contrast, bone remodeling is the process by which old bone is removed and replaced by new bone, and the resorption and formation processes are tightly coupled such that they occur sequentially on targeted discrete bone packets called basic multicellular units (BMUs) (Fig. 2.13) [69], [73]. The purposes of bone remodeling are to preserve the strength of the bone; provide a mechanism for adaptation to physical stress; replace damaged bone; and maintain mineral and ion homeostasis [69], [73], [74], though the demand for minerals may also be met simply by increasing osteoclast activity. The continual supply of newly formed bone, which has a lower mineral content than old bone, ensures that ions can be more readily exchanged with the extracellular environment [69]. A number of stimuli, including hormones, cytokines, and mechanical loading, are known to control bone remodeling by influencing the differentiation

of osteoclast- and osteoblast-lineage cells or by directly affecting bone formation and resorption. In particular, bone is known to undergo greater remodeling under mechanical loading, with bone formation focused in the areas that experience the highest stress [70]. Recently, interest has turned to how innervation is implicated in the remodeling process.

BMUs provide isolation so that bone remodeling at each BMU may happen independently and asynchronously with that at other BMUs. The bone remodeling process has four phases: activation of the bone surface to be remodeled, bone resorption by osteocytes, reversal from resorption to formation, and bone formation by osteoblasts [69]. The BMU structure and method of bone removal inside the BMU differ between trabecular and cortical bone, as shown in Figure 2.13 [73]. In trabecular bone, remodeling occurs on the surface, and the BMU is surrounded by a canopy. Recruited osteoclast precursor cells enter and differentiate beneath the canopy to resorb the target bone, and the space is refilled by osteoblasts. In cortical bone, osteoclasts cut a path through old bone and are followed by osteoblasts accompanied by blood vessels and nerves filling in the space.

2.3.3 Anterograde signaling: Sensory neurotransmitter effects on bone

This section will focus on evidence of the sensory innervation of bone and its observed effects on osteoblasts and osteoclasts. The cell bodies of sensory neurons are housed in the dorsal root ganglia (DRGs), and their axons extend to the periphery. Calcitonin gene-related peptide (CGRP) and substance P (SP) are two sensory neurotransmitters commonly associated with sensory nociceptive innervation, and their main respective receptors are the neurokinin-1 (NK_1) receptor and a complex consisting of the calcitonin receptor-like receptor (CRL) and receptor activity-modifying protein (RAMP) 1 [75]. SP and CGRP are synthesized in DRGs in response to stimulation of nociceptive nerve endings and are then transported to the axon terminals located in the innervated tissue, where they are released [76]. Because they are synthesized in response to pain, they have been shown to play a role in the body's inflammatory response.

CGRP is a 37-residue peptide with two isoforms, α-CGRP and β-CGRP, that differ by three residues. SP is an 11-residue peptide that has strong proinflammatory effects and is commonly expressed alongside CGRP in sensory nerves [75]. SP is released from nociceptive C fibers in response to tissue injury [18]. The patterns of sensory innervation in rat synovium, meniscus, and bone have been demonstrated through immunostaining for CGRP and SP (e.g., [77], [78]), and numerous studies have been conducted in an attempt to elucidate their influence on the cellular activity of osteoblasts and osteoclasts. The currently understood effects of both sensory and sympathetic neuropeptides on osteoblast and osteoclast differentiation and activity are summarized in Figure 2.14. It should be noted here that past studies have focused on the molecular mechanisms of bone–neuron crosstalk and the electrical component has been largely neglected.

Effects of CGRP on osteoblasts and osteoclasts

It has been demonstrated that cells in several osteoblastic cell lines as well as rat primary calvarial osteoblasts and human primary osteoblast cultures express CRLR and RAMP1 [8], indicting that osteoblastic function is regulated in some way by CGRP. A number of *in vitro* and animal model studies have experimentally demonstrated the anabolic effects of CGRP, with bone remodeling shifted in favor of bone formation when CGRP is present.

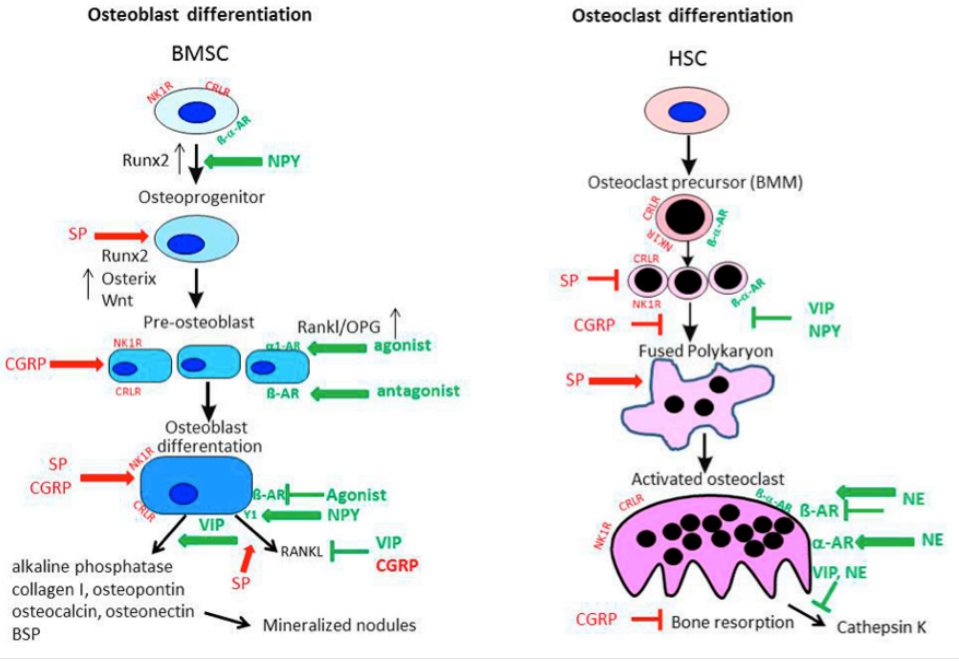

Figure 2.14 – Summary of effects of sensory (red) and sympathetic (green) neurotransmitters on osteoblast and osteoclast differentiation. Pointers ending in arrows indicate stimulation, and those ending in vertical lines indicate inhibition. Reproduced from Grässel and Muschter [8].

Schinke et al. [79] have demonstrated that mice that do not express α-CGRP display a reduced bone formation rate, indicating that α-CGRP is an activator of bone formation *in vivo*. CGRP has been observed *in vitro* to direct the differentiation of bone marrow stromal cells toward an osteoblastic lineage, as well as inhibit osteoclastogenesis [78]. Incubation of primary rabbit calvaria-derived osteoblasts with CGRP was shown to dose-dependently increase expression of differentiation markers of osteoblasts (namely activating transcription factor-4 and osteocalcin), suggesting CGRP plays a role in increasing osteoblast activity [80]. The effect of CGRP on regulating osteoclastogenesis was also observed in this study. The presence of CGRP had the effect of upregulating expression of osteoprotegerin (OPG) while downregulating receptor activator of nuclear factor κB ligand (RANKL); in combination, this regulation effect results in the inhibition of OPG/RANKL-regulated osteoclastogenesis, thereby reducing bone resorption [80]. CGRP has also been shown to dose-dependently inhibit the effect of interleukin-1β (IL-1β), a cytokine associated with the inflammatory response [81]. In the same study, IL-1β was shown to stimulate bone resorption in osteoclasts isolated from the long bones of newborn rats. This indicates that CGRP inhibits bone resorption either by acting directly on osteoclasts or by regulating the release of cytokines by osteoblasts [81].

The effect of CGRP on the OPG/RANKL pathway was also investigated by Yoo et al. [82]; however, in addition to CGRP, they also considered the effects of vasoactive intestinal peptide (VIP), a sympathetic neurotransmitter that will be discussed in more detail later, and compared the effects of the two neuropeptides with those of flow-induced stress. They found that mechanical loading and the application of either neuropeptide showed similar levels of OPG upregulation and RANKL downregulation relative to control levels and that combining mechanical stress with neuropeptides showed no enhancement to these regulatory effects. This is strong evidence of the important role these neurotransmitters play in bone remodeling, similar to that of mechanical loading [82]. Another study considering the relation

between mechanical loading and CGRP using α-CGRP and β-CGRP knockout mouse models was conducted by Sample et al. [83], who hypothesized that at least one of these isoforms is required in the transduction of mechanical loading into the biochemical signals required for bone formation. They found that load-induced activation of the periosteal mineralizing surface of the ulna did not occur in the α-CGRP knockout mouse, whereas no change was observed in the β-CGRP knockout mouse relative to the control. This indicates that the release of α-CGRP by sensory nerve fibers in bone plays an important role in bone formation in response to mechanical loading [83].

These studies provide strong evidence of the crucial role of CGRP in bone remodeling. Regarding its effects on osteoblasts, the elimination of α-CGRP *in vivo* has been shown to reduce bone mass [79] and suppress the load-induced activation of the periosteal surface [83], and *in vitro*, CGRP induces osteoblast differentiation and proliferation [78], [80]. These results indicate that CGRP stimulates bone formation, with the study considering mechanical loading revealing that CGRP is likely specifically involved in mechanical signal transduction. In terms of its effects on osteoclasts, CGRP has been found to inhibit osteoclastogenesis and osteoclast activity *in vitro* via regulation of both the OPG/RANKL pathway [78], [82] and IL-1β-mediated resorption [81]. Thus, in addition to stimulating bone formation, CGRP also inhibits bone resorption.

Effects of SP on osteoblasts and osteoclasts

The presence of SP and the NK_1 receptor have been detected in the bone tissue. Goto et al. [84] detected the expression of the NK_1 receptor in rat bone tissue through immunohistochemistry and found more receptors located in the cytoplasm and plasma membrane of osteoclasts than in osteoblasts or osteocytes. In a later study they conducted aiming to elucidate the effect of SP on bone formation by osteoblasts, they showed that rat calvarial osteoblastic cells expressed the NK_1 receptor after the cells were cultured for two weeks but not after only one week in culture [76]. As a result of this later-stage expression, the addition of SP stimulated bone formation only in the osteoblastic cells that had been cultured for enough time to express the NK_1 receptor, indicating that SP stimulates osteoblast activity only in later stages of bone formation.

Studies have also been conducted to determine the precise mechanisms and pathways by which SP induces osteoblast activity. Sun et al. [85] cultured osteoblasts with different combinations of SP and NK_1 receptor antagonists and demonstrated that SP binding to the NK_1 receptor stimulates the differentiation of mesenchymal stem cells into osteoblastic cells via gene expression regulation. Ma et al. [86] demonstrated that treatment with either SP or neuropeptide Y (NPY), a sympathetic neurotransmitter, stimulate osteoblast activity by enhancing gap junction intercellular communication, a method by which bone cells transmit signals mediating physiological functions such as differentiation, development, and remodeling. Mei et al. [87] have shown that SP enhances the differentiation of osteoblast-like cells of the MC3T3-E1 cell line extracted from mouse calvaria via the Wnt/β-catenin signaling pathway, which is known to play a role in bone maintenance.

In a recent study, Kodama et al. [88] investigated the bidirectional signaling between MC3T3-E1 cells and DRG neurons. In their *in vitro* model, efferent signaling from the neurons to the osteoblast-like cells was mediated by receptors for glutamate and SP, whereas afferent signaling was mediated by P2X receptors. P2X receptors are ligand-gated ion channels embedded in the neuronal membrane that are permeable to Na^+, K^+, and Ca^{2+} and

open in response to the binding of extracellular adenosine 5′-triphosphate (ATP). From this result, Kodama et al. [88] have theorized that osteoblasts and osteoclasts on the surface of bone act as sensors of mechanical and other stimuli and release ATP to transfer information to neurons via P2X receptors in the neuronal membrane.

The effects of SP signaling on osteoclast activity have also been investigated. It has been shown that SP upregulates osteoclastogenesis both directly and indirectly. In multiple studies, primary cultures of bone marrow macrophages, which are osteoclast precursors, have been shown to express NK_1 receptors, and incubation with SP has been shown to stimulate the differentiation of these cells into osteoclasts via the activation of nuclear factor κB, a key event in osteoclastogenesis [89], [90]. It has also been shown that synovial fibroblastic cells extracted from the rat knee joint express the NK_1 receptor and that these cells can be implicated in osteoclastogenesis induced by SP [91]. The synovium is a specialized connective tissue present around certain joints that releases a fluid to reduce friction and allow smooth joint movement. The addition of SP to cultures of synovial fibroblastic cells resulted in their proliferation, and when these cells were co-cultured with rat peripheral blood monocytes, the addition of SP resulted in increased osteoclastogenesis via regulation of the OPG/RANKL pathway [91].

From the above discussion, SP stimulates osteoblast differentiation and activity through a number of different mechanisms, but this stimulatory effect is considered to only occur in later stages of bone formation [76]. Additionally, afferent transduction of signals from osteoblasts is mediated by the release of ATP [88]. Regarding bone resorption, osteoclastogenesis is stimulated by SP by both direct [89], [90] and indirect [91] means. The fact that SP enhances both bone formation and bone resorption indicates that it is associated with overall higher bone turnover, though it remains to be seen how SP affects bone remodeling *in vivo*.

2.3.4 Anterograde signaling: sympathetic neurotransmitter effects on bone

As the focus of this study is sensory innervation, the role of the sympathetic innervation of bone will be discussed only briefly. The discussion in this section on the effects of sympathetic neurotransmitters was derived from reviews by Grässel and Muschter [8], Elefteriou et al. [7], Franquinho et al. [74], and Lerner and Persson [75]. This overview is provided to give a sense of the extensive mechanisms by which sympathetic innervation affects bone metabolism. As noted by Grässel and Muschter [8], the effects of sympathetic innervation on bone remain controversially discussed because sympathetic stimulation and inhibition have been shown to both produce opposing effects in terms of bone mass phenotype and bone cell proliferation and activity with the results entirely depending on the context of the experiment.

NE is a major actor in the role of sympathetic signaling in bone remodeling. As stated previously, there are two categories of NE receptors: βARs and αARs. Expression of adrenergic receptor β2AR has been detected in osteoblasts and osteoclasts, and detection of the other two βARs (β1AR and β3AR) has been reported to a lesser degree [7]. Use of a βAR-blocker has been found to induce proliferation in human osteoblasts, whereas application of a β2AR agonist inhibits osteoblast formation [8]. In line with this, osteoblast-specific inactivation of β2AR in mice has been found to result in high bone mass [7]. Most studies have shown that β2AR stimulation induces an osteoclastogenic response [7]; however, the results

of one study have shown β2AR stimulation to decrease osteoclastogenesis [8]. Overall, these results indicate that β2AR plays a role in reducing bone formation and enhancing bone resorption. The effects of αAR signaling have been studied less. However, studies indicate that αAR agonism induce osteoblast proliferation and osteoclast differentiation [8]; thus, αAR likely plays a role in stimulating both bone formation and bone resorption.

Functional VIP receptors have been detected in both osteoblasts and osteoclasts. The first observed effect of VIP on bone was a stimulatory effect on bone resorption in an *in vitro* study on calvarial bones. The results of later studies indicate that VIP has an initial inhibitory effect on osteoclasts, followed by delayed stimulation of osteoclast activity [75]. Despite this stimulatory effect, VIP has also been observed to inhibit osteoclastogenesis via a number of different pathways [75], including by regulating the expression of osteoclastogenic factors in osteoblasts [8]. Studies suggest that the greatest impact of VIP on bone remodeling is its stimulation of IL-6 production and its combined effect of inhibiting the upregulation of RANKL and counteracting decreases in OPG formation [75]; these effects both contribute to the reduction of osteoclastogenesis.

NPY has been implicated in the bone remodeling process via both central and peripheral pathways. The first evidence of the role the nervous system plays in bone remodeling was the observation that leptin-deficient mice showed a high bone mass phenotype, a result that was ultimately traced to control in the hypothalamus via the inhibition of NPY production [74]. It has since been demonstrated that local production of NPY in bone is also involved in the maintenance of bone homeostasis, though whether the effect is stimulatory or inhibitory remains controversial and the precise mechanisms remain poorly understood [74].

2.3.5 Effect of bone on sensory neurons: Axonal outgrowth and retrograde signaling

The above discussion focused on the effects of neurotransmitters on the bone remodeling process, representing the neuron-to-bone side of the communication between the two systems. This section focuses on the bone-to-neuron side of this communication by presenting the current understanding of the effects of molecular signaling in bone on neurite growth and the mechanisms underlying retrograde signals in sensory neurons innervating bone.

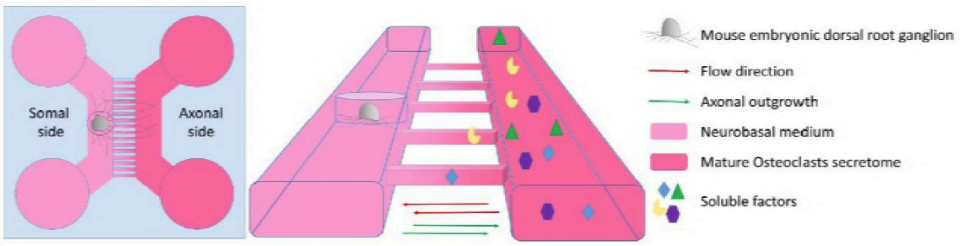

Figure 2.15 – Schematic of a DRG explant cultured in a microfluidic device with osteoclast-conditioned medium added to the axonal compartment. This setup was also used in the present work. Reproduced from Neto et al. [92].

A recent study on the effects of osteoclast-conditioned culture medium on the outgrowth of DRG axons was conducted by collaborators in the current project [92]. In this study, Neto et al. [92] measured the axonal outgrowth of DRGs cultured in a microfluidic device with mature osteoclast secretome added to the axonal compartment. A schematic of the experimental setup is shown in Figure 2.15. It was found that the administration of osteoclast

secretome induced increased neuronal outgrowth. Further investigation of the mechanisms behind this growth implicated the epidermal growth factor receptor in the process. Similar techniques used in this previous study, including the setup showing in Figure 2.15, were applied in the present study in a preliminary investigation on the effect of osteoclast-conditioned medium on the electrophysiological behavior of neurons (Section 5.2.4).

Most studies considering retrograde signaling in the context of bone innervation have focused on bone pain. As briefly discussed in Section 2.3.1, pain sensation begins in the periphery when specialized receptors at the terminals of nociceptive axons are activated. The signal then travels along the peripheral afferent branch of the axon to the cell body in the DRG and along the centrally projecting branch to the dorsal horn of the spinal cord, where the peripheral neurons synapse with nerves from the central nervous system, ultimately leading to the brain [18]. Apart from this type of nociceptive pain, which arises as a result of trauma experienced by the innervated tissue, there is also neuropathic pain, which is caused by direct damage to the sensory nerves. In bone pain, pain pathways may be activated by abnormal resorption or degradation of the bone or surrounding tissue, high levels of mechanical stress, or damage to the nerve fibers themselves [9]. Bone pain has both nociceptive and neuropathic components, and the mechanisms causing it have been difficult to study, making it difficult to study and treat [9].

Bone pain occurs in a number of pathologies, such as bone fracture, cancer, and osteoarthritis. Bone fracture provides a simple example of how the nervous system responds to noxious mechanical stimuli. In bone fracture, the mechanosensitive nociceptors in the Aδ fibers innervating the periosteum are thought to respond to the mechanical stress produced by the initial fracture. Subsequently, the second pain persists as a result of C fibers in both the periosteum and the bone marrow responding to factors released by the body as part of the inflammatory response [10].

Chronic pain associated with cancer has become a major problem as the progression of cancer treatments progressively improves survival time in cancer patients. Metastasis in bone is the most common cause of cancer-associated pain, and bone pain is experienced by 75% of patients with advanced cancer [9]. Cancer-induced bone pain can involve both nociceptive pain arising from inflammation at the site of tissue damaged by tumor growth and neuropathic pain resulting from nerve damage due to tumor growth. The presence of cancer cells also favors bone resorption, which has been reported to have a dual effect on pain perception [9]. First, increased resorption reduces the mechanical strength of bone, resulting in the application of abnormal mechanical stress on both bone cells, which produces a nociceptive response if the stress exceeds the pain threshold. Second, increased osteoclast activity reduces the pH of the local environment, which may sensitize the afferent fibers innervating the affected area [93]. This acidification of the local environment has also been shown to be a factor in bone pain induced by multiple myeloma [94].

The increased expression of certain ion channels has also been implicated as a possible additional mechanisms of cancer-related bone pain. In particular, the expression of the sodium channel SCN7A/Nax, which has been implicated in controlling the sodium intake of peripheral neurons by sensing the level of sodium in the body fluid, in DRG neurons has been shown to increase in response to sarcoma implantation in rats [95]. This increased expression was also linked to increased excitability in these neurons, pointing to a likely cause of bone pain. The upregulation of another sodium channel, Nav1.8, which is considered to contribute

the majority of the sodium current at AP initiation, has also been demonstrated in rats with cancer-induced bone pain, and this pain was alleviated by selectively blocking these channels [96]. These studies indicate the role of cancer in inducing changes to the electrophysiological behavior of peripheral axons, resulting in increased retrograde AP propagation and thus an increase in the perception of pain. However, it should be noted that although these studies implicate ion channel behavior in the sensation of bone pain, the electrical behavior of the neurons was not directly observed.

Osteoarthritis is a degenerative disorder of the synovial joints that results in cumulative damage to articular cartilage. Osteoarthritis is extremely common among the elderly and is accompanied by joint stiffness and pain. Despite osteoarthritis being the most common musculoskeletal condition worldwide, the mechanisms that lead to it remain largely unknown, though it is known that factors such as age-related wear, metabolic problems, and limb misalignment play a role in the progression of the disease; the role of the innervation of bone and cartilage in osteoarthritic bone and joint pain has recently become a subject of interest [8]. One cause of joint pain in osteoarthritis is the sprouting of nerves in articular cartilage accompanying increased levels of angiogenesis; cartilage is not normally innervated, and thus the presence of nerves in this tissue would cause them to be exposed to atypical chemical and mechanical stimulation [8]. The vascularization and accompanying innervation of joint cartilage may be caused by vascular channels containing both blood vessels and nerves breaking through subchondral bone and into the neighboring cartilage [97]. Neuropathic pain has also been implicated in osteoarthritis-associated pain [10].

It has been shown that bone pain in both osteoarthritis and cancer is associated with the pathological association between the sprouting and reorganization of sensory and sympathetic nerve fibers [9], [10]. This intermingling can lead to sympathetic signals, such as the release of noradrenaline [10], triggering the nociceptive excitation of nearby sensory nerve fibers, whereas such signals would not have a similar effect in healthy tissue. However, in the case of cancer, this nerve sprouting can result in extremely high-density innervation with nerve fibers expressing a unique morphology. In this case, pain is not only induced by errant signaling from sympathetic fibers but also has neuropathic origins as the sprouting neurons take on a neuroma-like structure [10]. Furthermore, as discussed previously it has been shown that osteoclasts and osteoblasts express molecules implicated in axonal guidance [92], [98], indicating the possible role of osteoclastic and osteoblastic activity in increased nerve sprouting.

2.4 Perspective on the present work

This literature review provided some background on the three main subjects combined in the present work: the use of MEAs in stimulating and recording neuronal activity, the application of microfluidic devices in neuronal cell culture experiments, and the crosstalk between bone and the sensory nerve fibers that innervate it. This section provides some perspective on how MEA and microfluidic methodologies are well-suited to providing greater understanding the crosstalk between neurons and bone cells and discusses how the program developed in this study will serve to advance work in this area.

As stated in Section 1.2, the software developed in the present work, µSpikeHunter, was developed for electrophysiological data analysis in the context of the ongoing work on the communication between neurons and bone, and some such data analysis was preliminarily

conducted in the present work. Additionally, μSpikeHunter will be made available as an open-source AP propagation analysis tool that can be applied in a variety of experimental setups with different commercial and custom electrode layouts, as described in detail in Section 3.1.1 and the user manual in Appendix B. Thus, this work involved both a methodological aspect and a biological research aspect, with the methodological component as the primary aim of the work.

MEA technology enables the nondestructive long-term monitoring of the same population of neurons with a high spatial resolution. Unlike intracellular methods, like patch-clamp recording, MEA stimulation and recording is achieved with the electrode positioned outside of the cell, avoiding the disruption of the membrane and allowing the formation of the neuronal network to be observed over time. Furthermore, the small size of MEA electrodes, which generally have diameters of 10–50 μm, means that individual cells can be targeted, and high-resolution maps of AP propagation across populations can be obtained, as achieved by Bakkum et al. [3] in their study on the tracking of APs using a high-density MEA (see Section 2.1.2). Microfluidic technology provides control of the spatial localization of neurons. Axons growing from neurons cultured in a compartment near microchannels extend through these microchannels, whereas the somata are too large to enter the microchannels. When these two technologies are combined in μEF devices, axons can be targeted for recordings, and if multiple electrodes are present along a single channel, the direction and velocity of a propagating signal can be extracted. In this context, μSpikeHunter enables the analysis of the propagation of signals along specific axons isolated in a μEF culture on both the single- and multi-spike levels, providing the user with powerful computational tools to characterize the communication among different populations of cells in compartmentalized μEF devices.

In terms of the biological component of this work, the innervation of bone has been implicated in the process of bone remodeling as well as the sensation of bone pain, as discussed in Section 2.3. The molecular mechanisms behind the crosstalk between bone and sensory neurons have been fairly well studied (see Sections 2.3.3 and 2.3.4); however, the electrical component of this communication has not been well characterized. Data from preliminary electrophysiological experiments expanding on the work conducted by Neto et al. [92] were analyzed using μSpikeHunter, and the results indicate that the osteoclast secretome may have the effect of increasing the anterograde activity of sensory neurons as well as the propagation velocity of individual spikes. It is expected that μSpikeHunter will act as a foundational tool in unraveling the complex mechanisms by which bone and sensory neurons communicate as work on this subject is advanced.

Chapter 3

μSpikeHunter: A computational tool for the characterization of propagating neuronal signals

3.1 Development of computational tool

The main goal of this project was to develop a user-friendly program for the identification and characterization of APs propagating along axons confined to the microchannels of a μEF device. With this program, propagating signals can be readily identified in μEF culture recordings, and the direction of travel, SNR, propagation velocity, and inter-spike intervals of the detected spikes can be easily determined using the software outputs. Furthermore, the inclusion of an easy-to-use graphical spike sorting tool allows the user to determine if there are multiple sources of activity in a single microchannel and obtain averages for clusters of spikes sorted according to their source. Additionally, μSpikeHunter contains two interactive elements, a kymograph and an audio playback function, that further engage the user with the spike characterization process. Together with the detailed quantitative methods, these two functions allow the users to qualitatively detect traveling waves in two different modalities: visual and auditory.

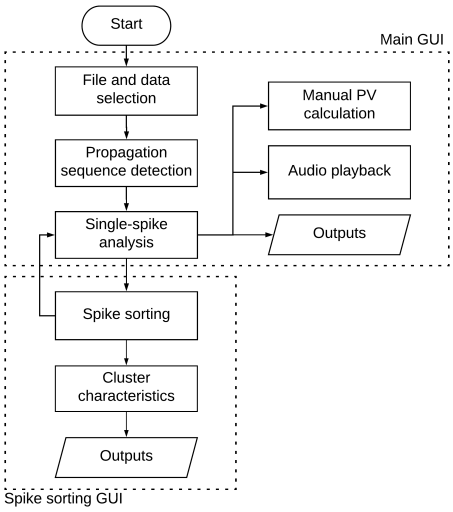

Figure 3.1 – Overall program workflow of μSpikeHunter. The main and spike sorting GUIs are presented in Section 3.1.2. The algorithms developed for propagation sequence detection, propagation velocity calculation, and spike sorting are described in Sections 3.2.1–3.2.4, and the kymograph (manual PV calculation) and audio playback function are presented in Sections 3.2.5 and 3.2.6.

A diagram of the overall workflow of µSpikeHunter is shown in Figure 3.1. This section first describes the overall development of the software and the graphical user interfaces (GUIs) it comprises. The main algorithms included in µSpikeHunter are then presented. These algorithms are an algorithm for the robust detection of spikes, two methods of computing the propagation velocity, and a spike sorting algorithm. Additionally, the kymograph and audio playback function are described in detail here, and the program outputs that can be saved for analysis outside of µSpikeHunter are briefly presented. Detailed instructions for using µSpikeHunter may be found in the user manual in Appendix B.

3.1.1 Software development and compatibility

µSpikeHunter was developed using the GUI development environment (GUIDE) in MATLAB R2016b (The MathWorks, Inc.). This program is an advanced computational tool consisting of two GUIs called the main GUI and the spike sorting GUI. Special care was taken to allow µSpikeHunter to be compatible with both Microsoft Windows and Macintosh environments. The layout of the objects in the two GUIs were adjusted in the GUIDE Layout Editor as needed to allow the program to be run in both Microsoft Windows and Macintosh operating systems. This involved the manual graphical resizing and relocation of all objects in the program as well as writing code for the programmatic adjustment to the sizes and locations of certain interactive objects.

µSpikeHunter was also developed to be compatible with electrophysiological recordings obtained using both custom laboratory setups and a commonly used line of commercial MEAs in conjunction with their corresponding *in vitro* recording systems (MEA2100, Multichannel Systems). Recordings obtained with a custom setup may be imported as comma-separated value (CSV), data, or text files (extensions .csv, .dat, and .txt) that have been formatted as instructed in the user manual in Appendix B. In brief, the first column of such files should contain the time stamps for the data in units of milliseconds, and each subsequent column should contain the recorded voltage data in units of microvolts progressing along the analyzed microchannel of the µEF device from the electrode closest to the somal compartment to that closest to the axonal compartment. In terms of the commercial systems, µSpikeHunter is compatible with recordings obtained from *in vitro* recording systems for 60-, 120-, and 256-electrode MEAs (MEA2100, Multichannel Systems) and converted to a hierarchical data format (HDF5) file using the MCS data conversion software (Multichannel Data Analyzer, Multichannel Systems). Recordings from a series of up to 16 electrodes in a single microchannel of a µEF device can be analyzed with µSpikeHunter. No filters are included in µSpikeHunter, so any filtering should be performed prior to data importation.

3.1.2 Layout of graphical user interfaces

A screen capture of the main GUI is shown in Figure 3.2. This GUI allows the user to select a file for analysis (Fig. 3.2(a)); additionally, if a commercial MCS recording system was used for data collection, the time range (Fig. 3.2(b)) and electrodes (Fig. 3.2(c)) can also be selected for analysis. Once the desired file and data have been selected and the event detection parameters (Fig. 3.2(d)) set, the main GUI presents the user with a list of detected propagation sequences (Fig. 3.2(e)). In this thesis, the term “propagation sequence” (or “sequence”) is used to indicate a series of events detected on all of the electrodes selected for analysis that can be considered to represent an AP traveling along an axon within the microchannel containing the electrodes. This GUI allows the user to analyze the spiking

behavior at the single-spike level and includes an algorithm for the estimation of the propagation velocity called the single-sequence propagation velocity (SPV) estimate.

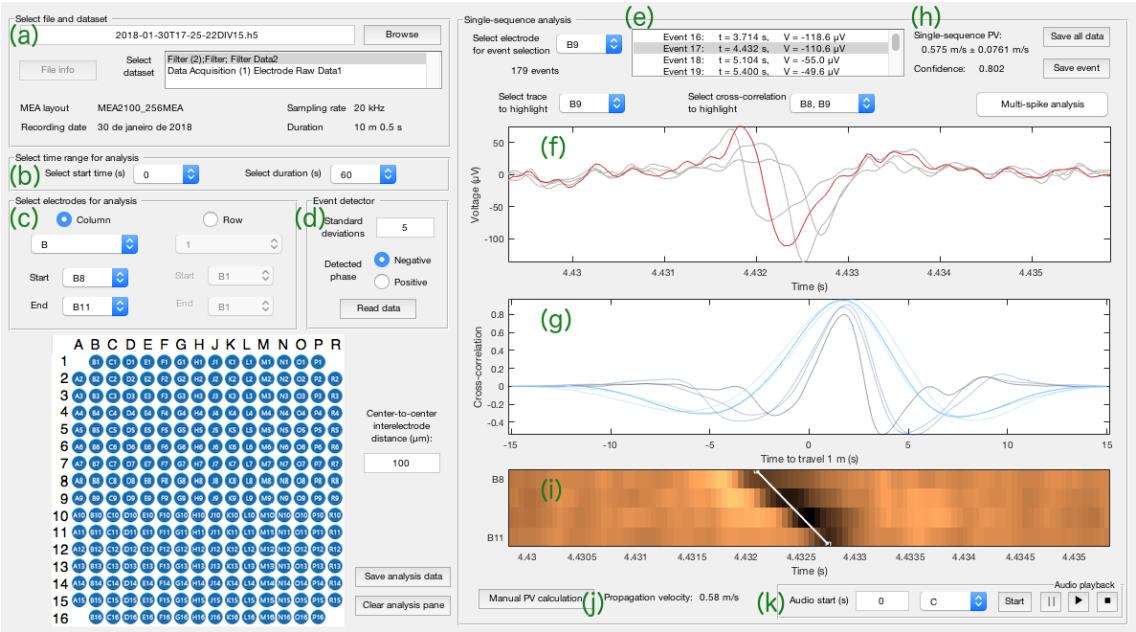

Figure 3.2 – Screen capture of the main GUI of µSpikeHunter. Different parts of the GUI are labeled for reference in the main text. (a) File selection. (b) Analysis time selection. (c) Analysis electrodes selection. (d) Event detection parameters. (e) List of detected propagation sequences. (f) Plot of voltage traces. (g) Plot of inter-electrode cross-correlations. (h) SPV estimate of the propagation velocity. (i) Kymograph. (j) Manual propagation velocity estimate. (k) Audio playback.

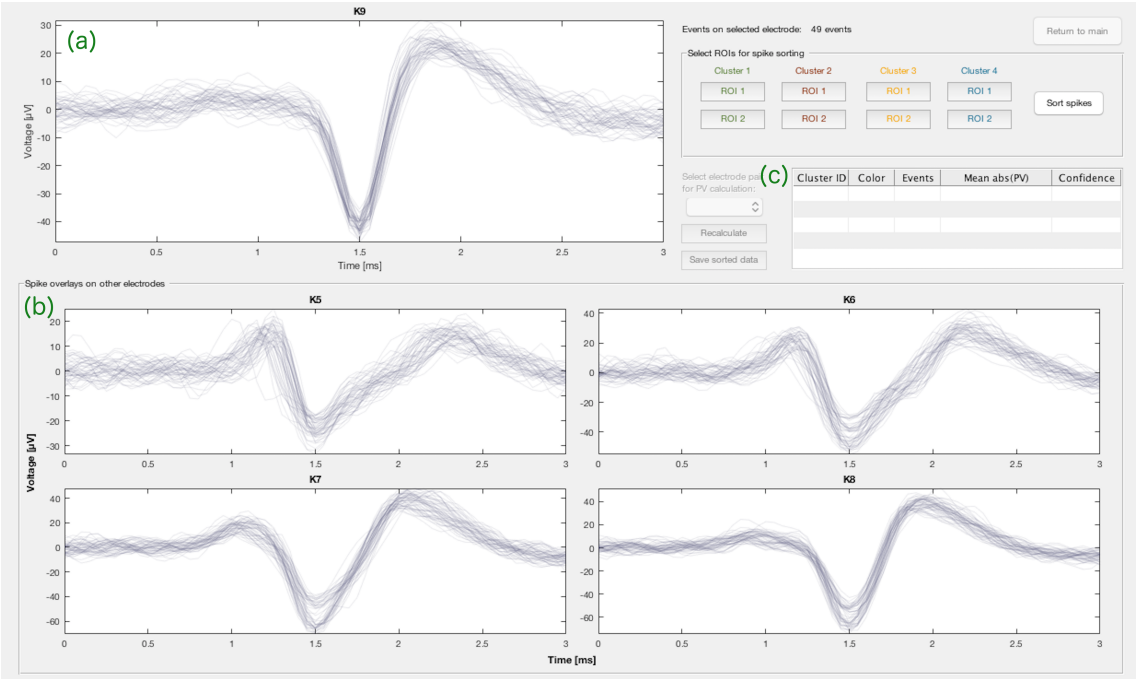

Figure 3.3 – Screen capture of the spike sorting GUI. Different parts of the GUI are labeled for reference in the main text. (a) Spike overlay for the event electrode. (b) Spike overlay for all other plots. (c) Spike sorting results table.

A screen capture of the spike sorting GUI is shown in Figure 3.3. The spike sorting GUI presents the user with a spike overlay for each of the electrodes showing all the events on that electrode detected as part of propagation sequences. In this GUI, the user can sort the spikes into source clusters, which are collections of propagation sequences that are presumed to have arisen from different axons in the analyzed microchannel. The spike overlay plots presented to the user are aligned about the peak voltage values for each detected event. The spike sorting GUI also computes the cluster propagation velocity (CPV), which is another estimate of the propagation velocity based on the characteristics of the sorted clusters.

3.2 Algorithms and interactive features

3.2.1 Propagation sequence detection algorithm

Propagation sequences are detected by first applying a threshold-based event detector to the ith electrode closest to the center of the microchannel and using three criteria to determine whether each detected event is part of a propagation sequence. Before instructing the program to read the data from the selected file, the user must first define the event detection parameters. The threshold for event detection is set as a user-input number of standard deviations of the noise from the median of the noise, and the user may select positive or negative phase detection. The event detector uses a two-step process to determine the threshold for detection. First, outliers are eliminated by excluding any data points that are more than three scaled median absolute deviations (MADs) from the median of the signal. The scaled MAD is calculated as

$$MAD_{sc} = C \operatorname{median}\left[S - \operatorname{median}\left(S\right)\right], \tag{10}$$

where S is the discrete recorded signal, $C = -1/\left[\sqrt{2}\,\mathrm{erfc}^{-1}(3/2)\right]$ is a scaling constant, and $\mathrm{erfc}^{-1}(\cdot)$ is the inverse error function. With the outliers excluded, the median M_n and standard deviation σ_n of the remaining data are obtained; these are considered to be the median and standard deviation of the noise. The detection threshold V_D is then calculated as the user-defined number n_σ of standard deviations above or below the median, as

$$V_D = M_n \pm n_\sigma \sigma_n. \tag{11}$$

The detection threshold is presented to the user in the main GUI beside the list of detected events. This threshold gives an indication of the noise amplitude.

This two-step process is used instead of simply calculating the mean and standard deviation of the original signal to ensure the detection threshold is actually based on the signal noise and is not inappropriately inflated by the occurrence of numerous large spikes. That is, the recorded voltage data, including the spikes, have a roughly Gaussian distribution with a large central peak at 0 μV accompanied by two smaller peaks at the positive and negative voltages corresponding to the amplitudes of the positive and negative phases of the spike waveforms. If the signal amplitudes are small and the spikes are infrequent, the standard deviation of the signal is approximately equal to the standard deviation of the noise. However, if there are many spikes with a very high SNR, the standard deviation of the signal may no longer be a good estimate of the standard deviation of the noise. Thus, the removal of outliers prior to the calculation of the standard deviation yields a threshold more closely approximating the characteristics of the noise.

This step is important in this particular application of propagation sequence detection for two reasons. First, it is common to record spikes with high SNRs in μEF devices because of the amplifying effect of the microchannels (see Section 2.2.3), making it more likely that the standard deviation of the signal will be a poor estimate of that of the noise. Second, because the number of standard deviations used to define the threshold is the same for each electrode, if outliers are not excluded, the user cannot simply scale the value of n_σ to compensate for the overestimation of the standard deviation of the noise (i.e., for the threshold being set too high) as they could if only one electrode were being used.

Once the threshold has been defined, events are obtained on the ith electrode as regions of the signal that exceed the detection threshold. The amplitude of the detected event is then defined as the peak voltage reached when the switching variable was in the on state. The time of the pth event on the ith electrode is denoted $t_{p,i}$ and is defined as the time at which this peak voltage occurs.

For an event detected on the central ith electrode to be considered part of a propagation sequence, all of the following three conditions must be met.

(1) Temporally linked events are detected on all other electrodes.
(2) The times of the linked events on the first and last electrodes correspond to a propagation velocity of less than 100 m/s.
(3) The absolute value of the Kendall rank coefficient τ_b between the electrode indices and the times of the linked events on the electrodes is greater than 0.8.

For condition (1), a search window $[T_{s,\min}, T_{s,\max}]$ is defined for each electrode based on the distance to the first electrode as

$$T_{s,\min} = t_{p,1} - C_s D_{1,i}, \qquad T_{s,\max} = t_{p,1} + C_s D_{1,i}, \tag{12}$$

where $D_{1,i}$ is the distance from the ith electrode to the first electrode and C_s is a search window coefficient defined to correspond to a minimum propagation velocity of 0.1 m/s. The event detection thresholds are also obtained for all of the electrodes using the two-step procedure described above. A set of temporally linked events is considered to exist only if an event is detected on every electrode within the corresponding search window. The times of the pth propagation sequence are given by the vector $\mathbf{t}_p = [t_{p,1}\ t_{p,2}\ \ldots\ t_{p,n_E}]$, where n_E is the number of electrodes.

For condition (2), as stated previously, the times of the events are defined as the times at which the peak voltages are recorded. From this definition, a sequence is rejected if the following condition is not met:

$$\frac{D_{1,n_E}}{\left|t_{p,n_E} - t_{p,1}\right|} < 100 \text{ m/s}. \tag{13}$$

In condition (3), the Kendall rank coefficient τ_b is an index describing the ordinal association between two sets of numbers. For this condition, τ_b is obtained for the correlation between a vector of the electrode indices, given by $\mathbf{E} = [1\ 2\ \ldots\ n_E]$, and the pth propagation sequence time vector $\mathbf{t}_p = [t_{p,1}\ t_{p,2}\ \ldots\ t_{p,n_E}]$, as

$$\tau_b = \frac{2K}{n_E(n_E - 1)}, \tag{14}$$

where

$$K = \sum_{i=1}^{n_E-1} \sum_{j=i+1}^{n_E} \xi^*\left(E_i, E_j, t_{p,i}, t_{p,j}\right),$$

$$\xi^*\left(E_i, E_j, t_{p,i}, t_{p,j}\right) = \begin{cases} 1, & (E_i - E_j)(t_{p,i} - t_{p,j}) > 0 \\ 0, & (E_i - E_j)(t_{p,i} - t_{p,j}) = 0 \\ -1, & (E_i - E_j)(t_{p,i} - t_{p,j}) < 0. \end{cases}$$

A sequence is rejected if the following condition is not met:

$$|\tau_b| > 0.8. \tag{15}$$

All as-detected propagation sequences are presented to the user in a list (Fig. 3.2(e)), and the user may view the voltage traces for each propagation sequence in a plot in the main GUI (Fig. 3.2(f)). Individual voltage traces may be highlighted by selecting the desired trace from a drop-down box. The number of events and the detection threshold are also shown. The following sections present the analysis that can be performed at the single-sequence level in the main GUI.

3.2.2 Single-sequence propagation velocity

The cross-correlations of the voltage traces for each possible pair of electrodes are calculated and plotted in the main GUI (Fig. 3.2(g)). These cross-correlations give a visual indication of the propagation velocity and if it is consistent across all electrodes. The plotted cross-correlations $\mathbf{X}_{i,j}$ between electrodes i and j are normalized such that all autocorrelations take a unit value at zero lag, as

$$\mathbf{X}_{i,j}(\tau) = \frac{\mathbf{V}_{p,j} \otimes \mathbf{V}_{p,i}(\tau)}{\mathbf{V}_{p,i} \otimes \mathbf{V}_{p,i}(\tau)}, \qquad \text{where } j > i. \tag{16}$$

Here, $\mathbf{V}_{p,i}$ and $\mathbf{V}_{p,j}$ are the voltage traces of the pth propagation sequence on the ith and jth electrodes, respectively; τ is the lag time between the voltage traces; and $\otimes$ represents the cross-correlation, which is calculated as a function of the lag τ. Additionally, the condition $j > i$ is defined so that the propagation velocity estimate described below yields positive and negative velocities for propagation from the somal to axonal and axonal to somal compartments, respectively. The time window for this cross-correlation is defined as a function of the distance between the electrodes as $t_{p,i} \pm WD_{i,j}$, where the time window constant W is 7.5 s/m.

A change of variable is also performed for the lag timescale of each cross-correlation so that the cross-correlations are given as functions of the inverse of the velocity, as

$$v_\tau^{-1} = \frac{\tau}{D_{i,j}}, \tag{17}$$

where v_τ is the velocity a wave would have to travel to have a lag time of τ between the ith and jth electrodes separated by a distance of $D_{i,j}$. On the basis of this change of variable, the cross-correlation time window corresponds to a minimum speed of 0.067 m/s. This change of variable also means that the peaks of the cross-correlations should align if the spike waveforms recorded on different electrodes are similar and the propagation velocity is

consistent across all electrodes, thus enabling the user to readily visually confirm the propagation velocity from this plot.

The time between spikes being recorded on two different electrodes can be obtained as the lag τ_{peak} at which the cross-correlation of their voltage traces is maximized, as

$$\tau_{\mathrm{peak}} = \arg\max_{\tau}\left(\mathbf{X}_{i,j}(\tau)\right). \tag{18}$$

From this lag time and the distance between the two electrodes, the single-sequence propagation velocity (SPV) is calculated as

$$v_{\mathrm{S}} = \frac{D_{i,j}}{\tau_{\mathrm{peak}}} = v_{\tau,\mathrm{peak}}. \tag{19}$$

The SPV for the selected propagation sequence is displayed beside the list of propagation sequences in the main GUI (Fig. 3.2(h)). The SPV can be obtained for any pair of electrodes or as the average of the SPV estimates for all pairs by selecting the desired pair from the corresponding drop-down box in the main GUI. However, it should be noted that the time resolution affects the accuracy of the SPV estimates in a nonlinear way and this is not taken into consideration when the average is computed. That is, when the lag is smaller, as for more proximal electrodes, small errors in the lag produce larger errors in the SPV. Thus, the SPV is less prone to error arising from the spatiotemporal resolution when a more distant pair of electrodes are selected. Additionally, regardless of the inter-electrode distance, an underestimation of the absolute value of the lag produces a larger error than an overestimation of the same magnitude, though the difference between the errors is larger for closer electrodes as a result of the τ^{-1} dependence. Because of this, the SPV tends to overestimate the propagation velocity when a closer electrode pair or the average of all pairs is selected for the estimation. The effects of the inter-electrode distance on the SPV will be demonstrated by the validation results in Section 4.2.3 and discussed further in the context of these results in Section 6.1.

The SPV is also paired with a confidence index, which indicates the similarity of the spike shapes recorded on the two electrodes. When a single electrode pair is selected for SPV calculation, the confidence index CI_{S} is the peak value of the normalized cross-correlation:

$$CI_{\mathrm{S}} = \max_{\tau}\left(\mathbf{X}_{i,j}(\tau)\right). \tag{20}$$

When the average of all pairs is selected, the confidence index is the peak value that is lowest among the electrode pairs.

3.2.3 Spike sorting algorithm

Spike sorting is performed based on regions of interest (ROIs) drawn by the user for up to four source clusters (clusters 1–4) with a fifth cluster (cluster 0) comprising any spikes not sorted into clusters 1–4. ROIs are drawn on the plot for the electrode selected in the main GUI prior to the spike sorting process (Fig. 3.3(a)); this electrode is referred to as the "event electrode." Up to two ROIs can be drawn for each cluster. Spikes are sorted sequentially from cluster 1 to 4 and are removed from the sorting pool once they have been assigned to a cluster. This means that ROIs drawn for clusters with higher cluster identification numbers (IDs) may be drawn less selectively than for clusters with lower cluster IDs. Examples of experimental spike sorting results will be presented in Section 5.2.1 (see Fig. 5.2).

Because the plotted events for each electrode are all part of propagation sequences, as described in Section 3.2.1, each event on the event electrode is tied to corresponding events on all other electrodes. Thus, once the spikes are sorted on the event electrode, the spikes are also sorted on all other electrodes in accordance with the propagation sequence to which they belong. The user may then visually confirm that the intra-cluster spike shapes are consistent not only on the event electrode but also on all other electrodes from the sorting results shown in the plots for the other electrodes (Fig. 3.3(b)).

Once the spikes have been sorted, various features of the sorted clusters are displayed in a table in the spike sorting GUI (Fig. 3.3(c)). This table includes the number of spikes in each cluster, the average propagation speed for the spikes in the cluster based on the CPV estimate of the propagation velocity, and the average confidence index for the CPV. The spike sorting results can then also be returned to the main GUI to allow the user to re-assess single propagation sequences in combination with the clustering results. Returning the results to the main GUI updates the list of propagation sequences (Fig. 3.2(e)) with the cluster ID and the CPV estimate for each sequence.

3.2.4 Cluster propagation velocity

The CPV estimate is based on the timing of the cluster voltage peaks and is calculated as follows. First, for each cluster, the events on each electrode are realigned based on the cross-correlation with every other event on the same electrode and in the same cluster. The time window of this cross-correlation is from 1.0 ms before to 1.0 ms after the time at which the peak voltage value is reached in each event. This realignment is then tied to a meaningful cluster-based feature by determining the time at which the mean of all the spikes in the cluster reaches a peak value, and the realignment times $t^*_{p,i}$ of each of the spikes are defined to correspond to this peak time.

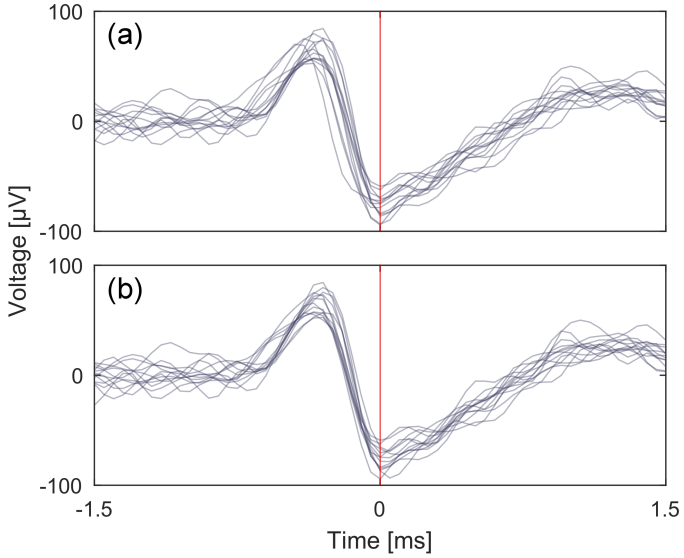

Figure 3.4 – Example of the spike realignment process for determining the CPV. (a) Spikes aligned about their minima. (b) Spikes aligned about their realignment times.

An example of this is shown in Figure 3.4. Figure 3.4(a) shows a plot of 13 events in the same cluster aligned about their minima, and Figure 3.4(b) shows the events realigned about their realignment times $t^*_{p,i}$. As shown in this figure, the spike waveforms within the cluster

match better when they are aligned about their realignment times than when they are aligned about their peak voltages, demonstrating that these times more accurately represent a consistent physiologically meaningful time point during the spikes.

From these realignment times, the CPV of the pth event is calculated as

$$v_{\mathrm{C}\,p} = \frac{t^*_{p,j} - t^*_{p,i}}{D_{i,j}}, \qquad \text{where } j > i. \tag{21}$$

Here, the condition $j > i$ is defined such that propagation from the somal to axonal compartment and from the axonal to the somal compartment yield positive and negative CPVs, respectively. The user may select any pair of electrodes to calculate the CPV; however, errors in the CPV due to the time resolution tend to be larger and more nonlinear for closer electrodes, as stated in the explanation of the SPV algorithm in Section 3.2.2. Again, this will be explored in more detail in the validation results in Section 4.2.3.

As with the SPV, the CPV is also accompanied by a confidence index, which indicates the similarity of the spike shapes recorded on the two selected electrodes i and j with all other spikes on the same electrode in the same cluster. This is represented by

$$\begin{gathered} CI_{\mathrm{C}\,p} = \min\left(CI_{\mathrm{C}\,p,i}, CI_{\mathrm{C}\,p,j}\right), \\ CI_{\mathrm{C}\,p,i} = \frac{1}{n_{ev}-1}\sum_{q=1}^{n_{ev}} \max_{\tau}\left[\frac{\mathbf{V}_{p,i} \otimes \mathbf{V}_{q,i}(\tau)}{\mathbf{V}_{p,i} \otimes \mathbf{V}_{p,i}(\tau)}\right], \qquad \text{for } q \neq p, \end{gathered} \tag{22}$$

where the cross-correlation is performed over the same time window as stated previously (from 1.0 ms before to 1.0 ms after the peak voltage in each event).

It should be noted that the SPV and CPV estimates of the propagation velocity are fundamentally different in their approaches. Whereas the SPV estimates the lag for a single propagation sequence by matching the spike waveforms detected on two electrodes, the CPV essentially estimates the delay between the peak voltages on two electrodes based on the timing of the peak voltage of a "master spike" representing the cluster. Therefore, when the waveforms are not consistent across all electrodes, the SPV and CPV can yield very different results, as the lag that yields the highest cross-correlation for the SPV may not correspond with the lag between the peak voltages on the two considered electrodes. This difference will be revisited in the experimental results (Section 5.2.3).

3.2.5 Kymograph

The main GUI µSpikeHunter also contains an interactive kymograph (Fig. 3.2(i)) to provide intuitive feedback to the user about the signal. A kymograph is an image representation of a dynamic process with one axis representing a spatial dimension and the other axis representing time; in the kymograph in µSpikeHunter, the voltage traces recorded on each electrode are shown over time, and the dynamic process is the propagation of the recorded AP. The kymograph in µSpikeHunter allows the user to readily visually assess the following features of detected events: (i) the existence of a traveling AP, (ii) the direction and speed of propagation of the AP, (iii) the duration of the waveforms recorded on each of the electrodes, and (iv) the relative magnitudes of the peak voltages on each electrode. The user may also obtain a manual estimate of the propagation velocity (Fig. 3.2(j)) using the

kymograph. An example of the kymograph along with the corresponding voltage traces is shown in Figure 3.5.

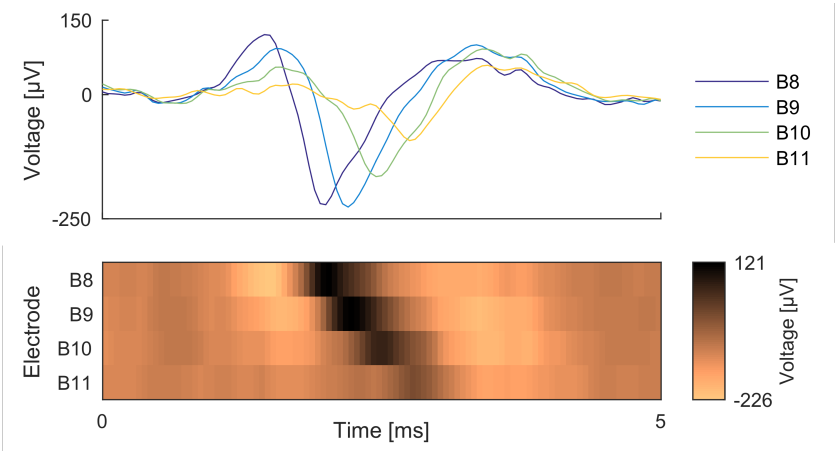

Figure 3.5 – Example of a kymograph of a detected propagation sequence along with the corresponding voltage traces. This example was obtained from a cortical culture at DIV 15.

The kymograph is generated as follows. The discrete voltage signals recorded by the electrodes during the event are normalized to the range of [0, 1] with respect to the maximum and minimum recorded voltages in the event time range. These normalized voltages are then converted to color map intensities and plotted in an image in time–electrode space. That is, the horizontal axis represents the time, and the vertical axis represents space, with each pixel width corresponding to an electrode.

Thus, when an AP propagates along an axon near a given electrode, the kymograph typically shows the characteristic triphasic extracellular spike waveform as a sequence of pixels that are first bright, then dark, then bright again in the row of pixels corresponding to that electrode. In some cases, not all phases are sufficiently large to provide an observable intensity change. For example, many spikes observed in the present study were recognizable only from their negative phase, and thus only a low-intensity region was observable for some electrodes; this is the case for electrode B11 in Figure 3.5.

With all selected electrodes plotted, the progression of this triphasic intensity is readily observable from top to bottom, providing an easily interpretable indication of the features listed previously. In the example shown in Figure 3.5, propagation from the somal to the axonal compartment (i.e., from B8 to B11) can be seen as the dark pixels on each electrode traveling from top to bottom as time progresses.

The user can also interact with the kymograph to obtain a manual estimate of the propagation velocity. A line can be drawn on the kymograph and adjusted as desired. Once the line is in the desired position, double clicking it finalizes the calculation, and the resulting manual estimate is output below the kymograph (Fig. 3.2(j)).

3.2.6 Audio playback

The user may also interact with the recorded signals via an audio playback function in the main GUI (Fig. 3.2(k)). This feature takes advantage of the ability of the human auditory system to recognize sound patterns and was inspired by the fact that many electrophysiologists use the audio outputs of amplifiers to detect spikes. The voltage data $\mathbf{V}_i$ on each electrode are first resampled to provide a degree of time dilation. The resulting data

are then converted to a normalized sound amplitude array $\widetilde{\mathbf{A}}_i$ for each electrode, and the amplitudes are used to generate a tone with time-varying sound intensity. A different audio frequency f_i is assigned to each electrode i. Mathematically, this process is described by

$$\begin{aligned} A_{k,i} &= \left|V_{k,i}\right|^{2.4} \\ \widetilde{\mathbf{A}}_i &= \frac{\mathbf{A}_i - \min\left(\mathbf{A}_k\right)}{\max(\mathbf{A}_k) - \min\left(\mathbf{A}_k\right)} \\ \mathbf{S}_{\text{audio}} &= \sum_{i=1}^{n_E} \widetilde{\mathbf{A}}_i \sin\left(2\pi f_i\, \mathbf{t}\right), \end{aligned} \tag{23}$$

where $A_{k,i}$ is the kth element of the audio amplitude array $\mathbf{A}_i$ for the ith electrode prior to normalization, and $\mathbf{S}_{\text{audio}}$ is the complete audio signal obtained by summing the tonal signals for each of the electrodes. An exponent of 2.4 was selected for the conversion of the voltage to the audio amplitude to provide greater amplification to the signal than the noise while allowing the noise to be audible to provide feedback to the user that the audio is still playing when no spikes are present.

Based on this conversion, when the magnitude of the deviation of the voltage signal from the mean increases on a given electrode, the tone assigned to that electrode becomes louder. In this way, as an AP propagates from one electrode to the next, the recorded spikes can be heard as a progression in tones over time with the tone frequency sequentially increasing for propagation from the somal to axonal compartment and decreasing for propagation in the reverse direction.

A timer is provided to display the time in the recording corresponding to the audio playback time. To slow down the playback to a speed at which the spike durations and inter-electrode delays are readily detectable by the human ear, the playback is executed at an audio sampling rate of 2 kHz, and the data are resampled at a rate of 500 times the ratio of the audio sampling rate to the recording sampling rate. This results in an approximately 500-fold time dilation; that is, a time period of 1 ms in the recording corresponds to approximately 0.5 s of audio playback time. Left uninterrupted, the audio playback plays 1 s of the recorded data, corresponding to 500 s of playback time. However, the user may pause, resume, and stop the playback as desired and can select the playback start time. The user may also choose from a list of different chord options to play different sequences of notes.

3.2.7 Program output files

µSpikeHunter also provides the user the option to save program outputs to CSV files for further analysis outside of the program. The outputs are briefly described here to provide context for the data analysis presented in the experimental validation results (Section 5.2). Detailed explanations of the output files are provided in the user manual in Appendix B.

In the main GUI, the times and peak voltages of all of the detected propagation sequences can be saved in a CSV file. These times are the times at which the peak voltages occur on each of the electrodes selected for analysis. In combination with the detection threshold, which is based on the standard deviation of the noise, this output file can be used to assess the SNR of the spikes. In the spike sorting GUI, CSV files for each cluster can be saved with the realignment times of each propagation sequence, along with the CPV and SPV

estimates for each sequence and the corresponding confidence indices. These two output files were used to obtain the results presented in the following sections.

Two other output files can also be saved from the main GUI: a file with all time and voltage data for the selected analysis period and electrodes and a file with the voltage traces on the selected electrodes for a single propagation sequence. The former file allows for the easy extraction of the voltage data from the HDF5 files output by the MCS software, and the latter allows the user to make their own plots of the propagation sequences outside of μSpikeHunter.

Chapter 4

Validation of algorithms

4.1 Generation of synthetic data

The performance of the software under different levels of noise was validated using synthetic data generated in MATLAB. The synthetic data represent traveling spikes recorded on four electrodes with an inter-electrode spacing of $D = 100$ µm and a sampling rate of $f = 20$ kHz, which correspond to the recording parameters used in the recording experiments in this project. The synthetic spike waveforms in each of the four voltage traces V_i $(i = 1,2,3,4)$ correspond to one phase of a sinusoidal wave with an amplitude of $V_{\text{peak}} = 60$ µV and a duration of $t_s = 1.5$ ms, and the delays between the spikes in each voltage trace were defined to correspond to a propagation velocity of 0.5 m/s. These spike parameters correspond to typical values obtained for actual cortical neuron recordings used to experimentally validate the system (see Section 5.2.1). The inter-spike interval was set to 25 ms. The synthetic dataset parameters for SNR validation are listed in Table 4.1.

Table 4.1 — Synthetic spike generation parameters for SNR validation.

Parameter	Value
Inter-electrode distance	100 µm
Number of electrodes	4
Sampling rate	20 kHz
Spike amplitude	60 µV
Spike duration	1.5 ms
Propagation velocity	0.5 m/s
Inter-spike interval	25 ms

The voltage traces were generated with different levels of added noise to observe the effect of the noise on the performance of the software. The noise added to the signals was defined to have a “memory” equal to the duration of the spikes ($t_s = 1.5$ ms). That is, rather than simply generating random numbers to add to the voltage traces, the noise value to be

added to the traces was generated as the normalized sum of s consecutive values in a vector R of randomly generated numbers. This was performed separately for each voltage trace, as

$$V_{\mathrm{noise},i} = \frac{V_{\mathrm{peak}}}{SNR}\, R \otimes k, \tag{24}$$

where $V_{\mathrm{noise},i}$ is the noise signal added to the ith voltage trace V_i, SNR is the SNR and is defined as the ratio of the spike amplitude V_{peak} to the maximum possible value of $V_{\mathrm{noise},i}$, R is a vector of random values drawn from a normal distribution (mean $\mu = 0$, variance $\sigma^2 = 1$), k is a one-dimensional convolution kernel of length s with every element equal to $1/s$, and $s\ (= ft_s)$ is the number of samples spanning a spike.

The considered SNRs ranged from 0.2 to 0.7 in intervals of 0.1, and three datasets were generated for each SNR. The durations of these synthetic recording datasets were defined based on the SNR to yield approximately 40–70 detectable spikes in each dataset to ensure sufficient statistics for analysis. The dataset durations and the number of spikes in each dataset for each of the considered SNRs are given in Table 4.2. At each SNR, the spike detection performance and the accuracy of different propagation velocity estimates were evaluated.

An event detection threshold of 2.2 standard deviations of the noise (see Section 3.2.1) was selected for analysis. This threshold was chosen to yield sufficiently few detected events when a dataset containing only noise on each of the electrodes was analyzed by μSpikeHunter. Three noise datasets of 100 s in duration were analyzed; each yielded fewer than five detected events at this threshold with an average of 1.3 events per dataset. The parameters for the noise datasets are also included in Table 4.2.

Table 4.2 — Validation dataset generation parameters for SNR validation.

SNR	Duration [s]	Number of spikes
0.7	2	78
0.6	3	118
0.5	5	198
0.4	15	598
0.3	100	3,998
0.2	600	23,998
0	100	0 (noise only)

To examine the effect of the spatiotemporal resolution of the recording on the different estimates of the propagation velocity, datasets were generated with two additional sets of recording parameters. These parameters are based on those for the dataset in Table 4.2 with an SNR of 0.7. In the first of these additional sets of parameters, the inter-electrode distance was set to 200 μm, and in the second, the sampling rate was set to 50 kHz. In both cases, all other parameters were the same as in Table 4.1. As with the SNR validation cases, three datasets were generated for each of these sets of parameters, and the mean and standard deviation of the propagation velocity estimates for each of these datasets were then averaged over the three datasets to obtain the final results.

4.2 Synthetic data validation results

As described in Section 4.1, μSpikeHunter was validated using datasets containing synthetic spikes generated as one period of a sinusoidal signal with different levels of added noise. SNRs ranging from 0.2 to 0.7 were considered, and three datasets were analyzed for each SNR. Examples of synthetic propagation sequences with no added noise and SNRs of 0.7 and 0.3 are shown in Figure 4.1. All of these example propagation sequences were successfully detected by μSpikeHunter, and their propagation velocities were accurately determined by the CPV estimate.

This section presents the performance of μSpikeHunter at different SNR levels in terms of the propagation sequence detection and the propagation velocity estimation for these synthetic validation datasets. The effect of the spatiotemporal resolution of the recorded data on different propagation velocity estimates was also investigated using additional datasets with different recording parameters.

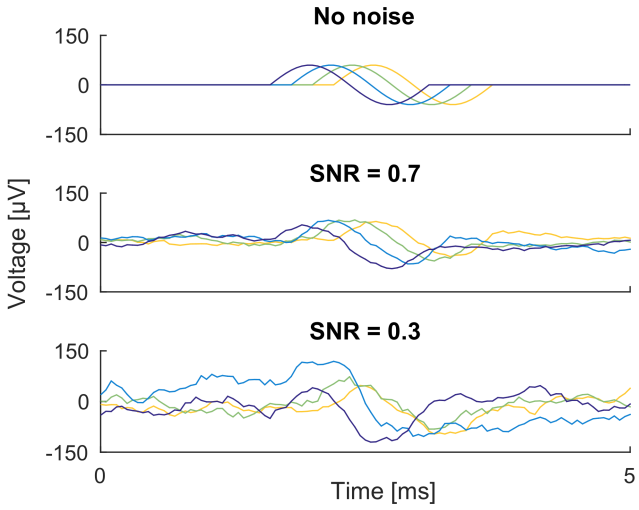

Figure 4.1 – Examples of synthetic propagation sequences detected by the propagation sequence detector in the case of no noise and SNRs of 0.7 and 0.3. In all cases, the propagation velocity was correctly estimated (error of 0%) by the CPV.

4.2.1 Propagation sequence detection performance

The performance of the propagation sequence detector in μSpikeHunter under different noise levels was evaluated based on two performance indices: the precision and the detection rate. The precision is defined as

$$PR = \frac{TP}{TP + FP}, \tag{25}$$

where TP is the number of true positives, i.e., the number of detected sequences that correspond to actual traveling waves, and FP is the number of false positives, i.e., the number of detected sequences that do not correspond to actual traveling waves. The detection rate is defined as

$$DR = \frac{TP}{NS}, \tag{26}$$

where NS is the total number of actual sequences in the recording dataset. Both of these performance indices range from 0 to 1.

A high precision indicates that the propagation sequence detector rarely yields temporally linked events that do not correspond to actual traveling waves. A high detection rate indicates that the propagation sequence detector is able to recognize a high percentage of the actual traveling waves in the data. It should be noted that in spike detection, a high precision is more important than a high detection rate; that is, it is more desirable to be certain that the analyzed detected events are actually spikes than to detect the majority of spikes in a recording.

The precision and detection rate results are shown in Figure 4.2 for the six considered SNRs. The plotted values are the averages of the values obtained for each of the three datasets with the same SNR. These results demonstrate that the propagation sequence detector shows very high precision up to an SNR of 0.4, with the precision approximately equal to 1 for SNR = 0.4 to 0.7. The precision decreased to 0.96 at $SNR = 0.3$, which is still quite high. However, at $SNR = 0.2$, the precision dropped to 0.80, demonstrating the poor performance of the propagation sequence detector at this noise level.

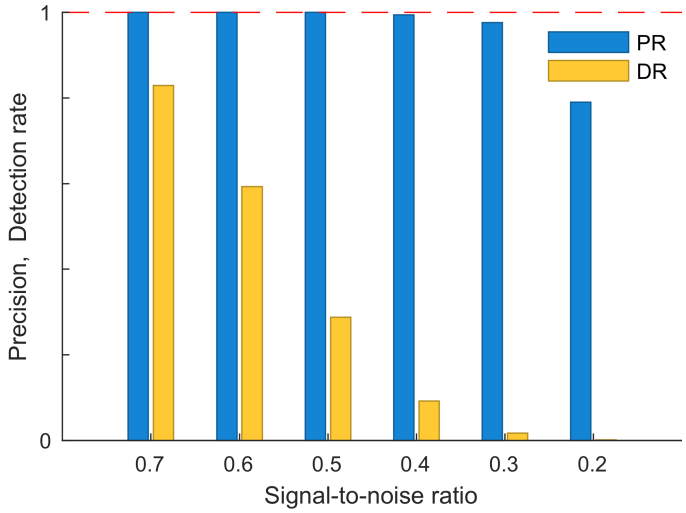

Figure 4.2 – Precision and detection rate of the propagation sequence detector obtained for the validation datasets at different SNRs. The dashed line indicates the target value of 1.0.

The detection rate dropped steadily as the noise was increased from $SNR = 0.7$ to 0.2. Whereas the propagation sequence detector was able to detect 82.9% of all actual propagation sequences at $SNR = 0.7$, at $SNR = 0.2$, only 0.1% of all propagation sequences were detected.

4.2.2 Propagation velocity estimation performance

The performance of the propagation velocity estimation methods of μSpikeHunter under different noise levels was assessed using three propagation velocity measures: the CPV calculated based on the arrival times on the most distant pair of electrodes, the SPV calculated based on the cross-correlation between the most distant pair of electrodes (SPV-far), and the SPV calculated using the average SPV for all electrode pairs (SPV-all).

For each of these three propagation velocity estimation methods, the average and standard deviation of the propagation velocities calculated for each propagation sequence

were obtained for each validation dataset, and these averages and standard deviations were then averaged over the three datasets for each SNR. Average confidence indices were also obtained in this manner for each SNR. Any estimates of infinite propagation velocities (zero time differences) were excluded from the results. In the case of the SPV-all estimates, this happened fairly often, whereas the CPV and SPV-far estimates only yielded infinite velocities at SNRs of 0.2 and 0.3. The results are shown in Figure 4.3, with the error bars representing the standard deviation and the number beside each estimate representing the confidence index.

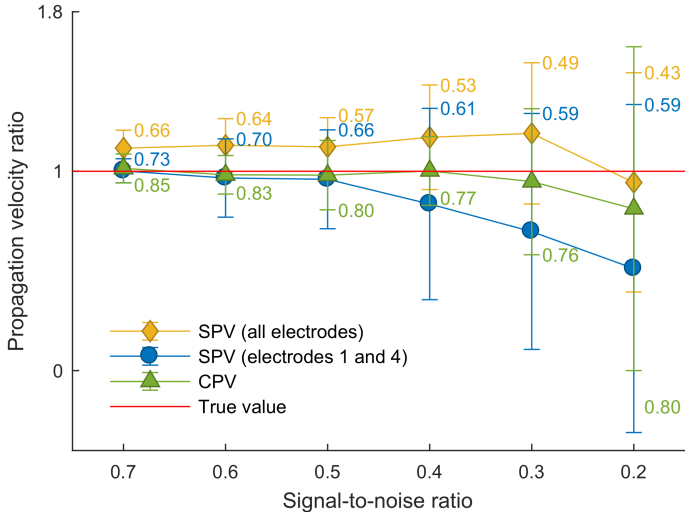

Figure 4.3 – Ratios of different propagation velocity estimates to the true propagation velocity at different SNRs. Estimates were obtained for three recording datasets with approximately 40–70 sequences each at each SNR and averaged over the three datasets. Error bars represent the standard deviations averaged over the three datasets.

These results indicate the average propagation velocity estimates over all detected propagation sequences. As shown in this figure, the CPV and SPV-far estimates showed good performance at low noise levels. Overall, the CPV showed good performance up to an SNR of 0.4, with the mean showing +2.2% error and the error at one standard deviation from the mean equaling +21%/−16%. The average CPV continued to show good performance at 0.3 with an error of −3.8%; however, the spread of the individual CPVs around the mean was much broader at 0.3 than at 0.4. This wider spread is attributable in part to the fact that approximately 4.4% of the detected propagation units did not correspond to actual traveling waves (see Fig. 4.2). Beyond 0.3, the performance of the CPV deteriorated. The SPV-far estimates showed good performance up to 0.5, with the mean having an error of −4.4% and the error at one standard deviation from the mean equaling approximately +30%/−21%. At SNRs beyond 0.5, the SPV-far performance deteriorated.

In contrast, the SPV-all estimate consistently overestimated the true propagation velocity. This overestimation is the result of the close proximity of the neighboring pairs of electrodes. In this simulation, the inter-electrode distance was set to 100 µm, the sampling rate was 20 kHz, and the propagation velocity was 0.5 m/s. For neighboring electrodes, this means that the difference in the spike arrival times is 0.2 ms. If the time difference estimate has an error of ±1 sample (±0.05 ms), this yields an error in the propagation velocity of +33%/−20%; thus, small errors in the lag computations over many propagation sequences

contribute disproportionately to overestimating the propagation velocity. Although this bias toward overestimation also occurs at larger distances, the magnitude of the bias is much smaller. This indicates that propagation velocity estimates should be used with the most distant possible electrodes to mitigate the effect of this bias.

The propagation velocity estimation results here demonstrate that for this set of recording parameters (Table 4.1), using the most distant electrodes to estimate the propagation velocity yields more reliable results than considering all electrodes. Furthermore, the CPV estimate was found to be more robust against noise than the SPV estimate and should be used when the SNR is low.

4.2.3 Effect of spatiotemporal resolution on propagation velocity estimates

To further elucidate the performance of the different propagation velocity estimates and the factors producing these performance results, two additional validation parameter sets were investigated. As mentioned in Section 4.1, these sets of parameters were defined by independently varying the parameters affecting the spatiotemporal resolution of the recorded data, namely the sampling rate f and the inter-electrode distance D. In the first set of recording parameters, the inter-electrode distance was changed from 100 to 200 µm, and in the second, the sampling rate was changed from 20 to 50 kHz. These cases are hereafter referred to as the spatial and temporal resolution cases, respectively. All other parameters were the same as in the SNR validation datasets with an SNR of 0.7 (see Tables 4.1 and 4.2), hereafter referred to as the baseline case.

Four different propagation velocity estimates were obtained from these three datasets, and their performance under the different recording parameters was assessed. The results are shown in Figure 4.4. The four propagation velocity estimates are as follows. CPV-far and SPV-far are the CPV and SPV estimates obtained using the most distant pair of electrodes, i.e., electrodes 1 and 4. CPV-close and SPV-close were obtained by averaging the CPV and SPV estimates obtained for all of the neighboring electrode pairs, i.e., averaging the estimates obtained for electrodes 1 and 2, electrodes 2 and 3, and electrodes 3 and 4.

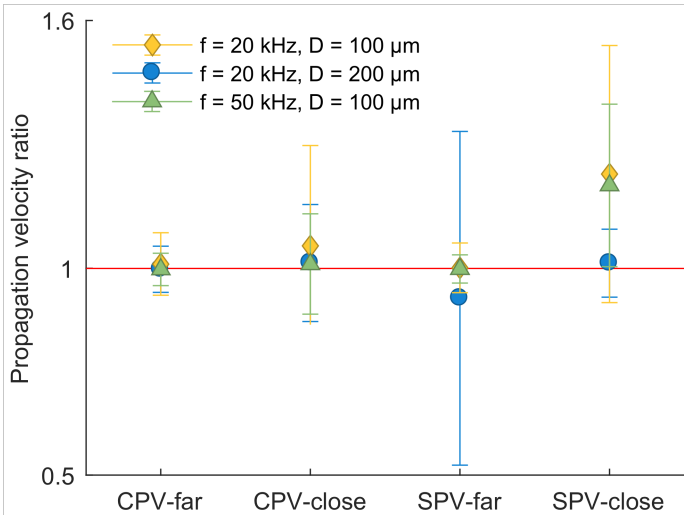

Figure 4.4 – Ratios of different propagation velocity estimates to the true propagation velocity obtained for datasets with different recording parameters and an SNR of 0.7. Estimates were obtained for three datasets for each set of recording parameters and averaged over the three datasets. Error bars represent the standard deviations averaged over the three datasets.

As shown in Figure 4.4, the CPV-far estimate showed consistently good performance regardless of the inter-electrode distance or sampling rate. This reaffirms the excellent performance of the CPV estimate when the most distant electrodes are used. The CPV-close estimate also showed good performance but had a wider margin of error under all sets of recording parameters. Additionally, as expected from the reasoning presented in the previous section, the mean of the CPV-close estimate in the baseline case overestimated the propagation velocity with an error of +5.4%. The reason the other two cases did not show this overestimation is because increasing the inter-electrode distance or the sampling rate increases the spatiotemporal resolution and thus reduces the difference between the magnitudes of the over- and underestimation of the propagation velocity resulting from a positive and negative time differences of the same magnitude.

The SPV estimates showed overall worse performance, as obtained in the previous results. However, the performance varied quite drastically depending on the spatiotemporal resolution of the datasets. In the baseline and temporal resolution cases, the SPV-far estimate showed very good performance, with results similar to the CPV-far estimates. In stark contrast, the SPV-far estimate in the spatial resolution case showed much poorer performance. The standard deviation of the SPV-far estimate in this case was very large; this large standard deviation is the result of the presence of a number of outliers in each of the datasets. These outliers are likely the result of the doubling of the cross-correlation window to account for the doubling of the inter-electrode distance (see Section 3.2.2), which can cause misleading peaks when the noise portions of the signals on the two electrodes align well. This is particularly important to note when actual experimental data is being analyzed, as large and/or consistent environmental noise recorded on all electrodes may cause an erroneous peak in the cross-correlation at a zero lag.

As in the validation with different levels of noise, the SPV-close estimate in the baseline case greatly overestimated the propagation velocity. Interestingly, the higher sampling rate in the temporal resolution case did little to improve the mean SPV-close estimate and only served to reduce the standard deviation. However, the SPV-close estimate in the spatial resolution case showed very good performance. These results indicate that the inter-electrode distance greatly impacts the reliability of the SPV estimates, and the electrode pair or pairs used for the SPV estimate should thus be selected carefully according to the inter-electrode distance.

Chapter 5

Analysis of *in vitro* neuronal recordings

5.1 Experimental methods

5.1.1 Preparation of microelectrode—microfluidic devices

The μEF devices were prepared by Dr. Cátia Lopes and José Mateus (NCN – Neuroengineering and Computational Neuroscience group, i3S – Instituto de Investigação e Inovação em Saúde) with assistance from the author.

The microfluidic devices were fabricated at INESC using the soft lithography method described by Taylor et al. [13] (see Fig. 2.7). Briefly, a master mold was fabricated using two photoresist layers of different thicknesses for the culture chambers and the microgrooves. PDMS was then cast on top of the master mold. Once the PDMS was removed from the master, four holes were punched to provide access to the culture chambers; in the case of the devices intended for use with DRG explants, a fifth hole was also punched in the somal chamber to allow the seeding of the DRG [47].

The μEF devices were prepared by placing the microfluidic devices against a pre-coated MEA (Multichannel Systems) with 120 or 256 electrodes of 30 μm in diameter with a center-to-center inter-electrode spacing of 100 μm. The MEAs were coated with 0.01 mg/ml of poly(D-lysine) (PDL, Corning), left overnight at 37 °C, washed with sterile water, and completely air-dried under sterile conditions. The microfluidic devices were sterilized with 70% ethanol and were gently attached to the PDL-coated MEAs, creating a μEF chamber composed of two separate compartments connected by microchannels with dimensions of 450 μm length × 9.6 μm height × 14 μm width. The medium reservoirs were loaded with 150 μl of 5 μg/ml laminin isolated from mouse Engelbreth-Holm-Swarm sarcoma (Sigma-Aldrich Co.) and incubated overnight at 37 °C. The unbound laminin-1 was removed, and the chambers were refilled with Neurobasal medium and left to equilibrate for at least 2 h at 37 °C prior to cell seeding.

The recording channels for the 120- and 256-electrode systems have been given alphanumeric labels by Multichannel Systems indicating the column and row with a letter and a number, respectively, with the location A1 corresponding to the upper left-hand corner of the MEA. For each μEF device used in the present experiments, the microchannels were

oriented vertically with respect to this MEA configuration, and the somal compartment was at the top, as schematically shown in Figure 5.1.

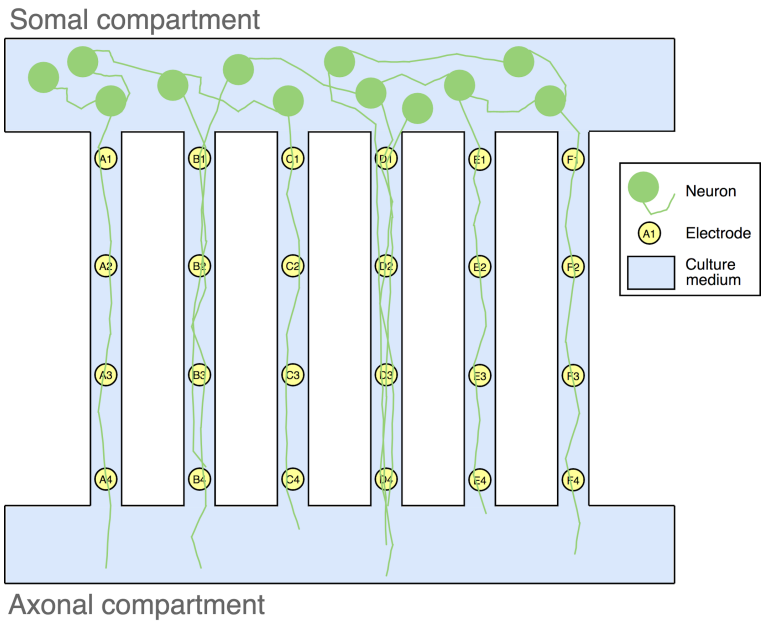

Figure 5.1 – Schematic of a μEF device. The electrodes are assigned alphanumeric labels as shown here.

5.1.2 Cell culture preparation

The cortical neuron and DRG explant cultures were prepared by Dr. Cátia Lopes (NCN, i3S) and Dr. Estrela Neto (NSC – Neuro-Skeletal Circuits group, i3S), respectively, with assistance from the author. Osteoclast cultures for conditioned medium collection were prepared by Dr. Estrela Neto (NSC, i3S) following the procedure reported in her previous work [92].

Experimental procedures involving animals were carried out in accordance with current Portuguese laws on Animal Care (DL 113/2013) and with the European Union Directive (2010/63/EU) on the protection of animals used for experimental and other scientific purposes. The experimental protocol (reference 0421/000/000/2017) was approved by the ethics committee of the Portuguese official authority on animal welfare and experimentation (Direção-Geral de Alimentação e Veterinária). All possible efforts were made to minimize the number of animals and their suffering. Unless otherwise stated, all reagents listed below are from Gibco, ThermoFisher Scientific.

Primary embryonic rat cortical neurons were isolated from prefrontal cortices of Wistar rat embryos (E18). The embryo cortices were dissected in Hank's Balanced Salt Solution (HBSS) and enzymatically digested in 0.6% trypsin (1:250) in HBSS for 15 min at 37 °C. Subsequently, tissue fragments were washed once with 10% (v/v) heat-inactivated fetal bovine serum (hiFBS, Biowest) in HBSS to inactivate trypsin and twice with HBSS to remove FBS from the solution. Tissue fragments were then mechanically dissociated with a 5 ml plastic pipette and subsequently with 1 ml pipette tips. Viable cells were counted using the trypan blue (0.4% (w/v), Sigma-Aldrich Co.) exclusion assay, and the cell density was adjusted to 2×10^7 viable cells/ml. Thereafter, 5 μl of the cell suspension was seeded in the cell body compartment of a μEF device, previously treated with 0.01 mg/ml PDL as described in Section 5.1. Cells were cultured in Neurobasal medium supplemented with 0.5 mM

glutamine, 2% B27, and 1% penicillin/streptomycin (P/S, 10,000 units/ml penicillin and 10,000 µg/ml streptomycin) and kept in a humidified incubator at 37 °C supplied with 5% CO_2.

Primary embryonic mouse DRG explants were isolated from wild-type C57BL/6 mice embryos (E16.5). Lumbar DRG explants were removed and placed in HBSS until use. Upon use, one DRG explant was seeded in the cell body compartment of a µEF device, previously treated with 0.01 mg/ml PDL plus laminin as described in Section 5.1. Cells were cultured in Neurobasal medium supplemented with 0.5 mM glutamine, 2% B27, 50 ng/ml of NGF 7S (Calbiochem®, Millipore), and 1% P/S, and kept in a humidified incubator at 37 °C supplied with 5% CO_2.

Bone marrow cells were isolated from the tibia and femur of adult C57BL/6 male mice by flushing the bone barrow with α-MEM containing 10% (v/v) FBS and 1% (v/v) P/S. Osteoclast precursors were produced by treating the bone marrow cell suspension with red blood cell lysis buffer (ACK Lysing Buffer) for 1 min at room temperature. After centrifugation, cells were plated in Petri dishes with 10 ng/ml macrophage colony-stimulating factor (M-CSF, PeproTech) for 24 h, after which the M-CSF concentration was increased to 30 ng/ml for an additional three days. Adherent cells were detached and re-seeded at a density of 5×10^4 cells/cm^2 in the presence of 30 ng/ml M-CSF and 100 ng/ml RANKL (PeproTech). Cells were kept in a humidified incubator at 37 °C supplied with 5% CO_2 for 3–4 days, after which the osteoclast-conditioned medium was collected and stored at −80 °C.

5.1.3 Electrophysiology experiments

The electrophysiological recordings used in this project were taken by José Mateus (NCN, i3S) with the assistance of the author. Electrophysiological recordings were obtained with 120- and 256-electrode MEAs and recording systems (MEA-2100, Multichannel Systems) using recording software (Multichannel Experimenter, Multichannel Systems) to control the system. The µEF devices prepared with these MEAs respectively had 16 and 12 microchannels with microelectrodes positioned beneath them, and four or five microelectrodes were positioned beneath each microchannel. All recordings analyzed in this work were taken with a sampling rate of 20 kHz and filtered using the recording software to eliminate frequencies outside of the known frequency band for electrophysiological activity; for this purpose, second-order Butterworth low- and high-pass filters with cutoff frequencies of 4 kHz and 300 Hz, respectively, were applied for filtering prior to analysis. All recorded activity was spontaneous activity.

The electrophysiological recordings described here were analyzed using µSpikeHunter to validate the experimental applicability of the software to various types of analysis and experimental conditions and preliminarily investigate the electrophysiological facet of the communication between bone and the sensory nervous system. Three sets of recorded data were used for this purpose. The first is a single recording obtained from a dissociated cortical neuron culture at DIV 15. This culture was used to test the computational and spike sorting capabilities of µSpikeHunter.

The second is a series of recordings obtained from a DRG explant culture on DIVs 4, 6, and 8. This culture was used to obtain a baseline understanding of the electrophysiological behavior and maturation of DRGs cultured in µEF devices, and this baseline information was used to set the recording time points in the third dataset.

The third dataset is a set of recordings obtained to preliminarily investigate the effect of culture medium conditioned by osteoclasts on DRG behavior. Recordings were obtained from two µEF devices, a device with osteoclast-conditioned (OC) medium added to the axonal compartment and a control device with Neurobasal (NB) medium added instead of OC medium. For both devices, baseline recordings were obtained at DIVs 4 and 6. After the baseline recording on DIV 6, culture medium was added, and additional recordings were taken immediately after the addition of medium and 24 h later (DIV 7). The two DIV 6 recordings before and after the addition of medium are hereafter referred to as DIV 6-pre and -post, respectively.

In the first two datasets, cells were seeded only in the somal compartment, and the axonal compartment was supplied with only Neurobasal medium. However, in both cultures, spikes were observe to propagate from the axonal to the somal compartment despite the axonal compartment containing no cells or conditioned media. The possible origins of these reverse propagating signals in these cultures was thus also assessed using these two datasets.

5.2 Experimental results

As described in Section 5.1.3, three sets of electrophysiological recordings were used to demonstrate the capabilities of µSpikeHunter in actual experimental data analysis. These recordings were obtained from cortical neurons at DIV 15; a DRG explant at DIVs 4, 6, and 8; and DRG explants with OC and NB culture media added to the axonal compartment. These recordings were each analyzed using the program outputs of µSpikeHunter. This section demonstrates the applicability of µSpikeHunter to experimental data analysis in terms of spike sorting, monitoring changes to a culture as it ages, and the assessment of the effects of molecules released by osteoclasts on the electrophysiological behavior of sensory neurons.

5.2.1 Cortical neurons: Spike sorting

The spike sorting performance of µSpikeHunter was experimentally tested using recordings obtained from cortical neurons at DIV 15 for an analysis duration of 100 s. Propagation sequences were detected with a threshold of 5 standard deviations of the noise and negative phase detection. From the spike waveforms observed in the spike sorting GUI, it was determined that multiple sources of activity were present in a number of microchannels. The spike sorting GUI was used to sort the waveforms into clusters, and the sorting results for two microchannels (B and M) are shown in Figure 5.2(a1) and (b1), along with the ROIs used to obtain these results (event electrodes: B9 and M11; see Section 3.2.3).

The characteristics of the sorted clusters are summarized in Figure 5.2(a2) and (b2). Using µSpikeHunter, the number of spikes in each cluster and the CPV and SPV estimates of their propagation velocities were obtained; both propagation velocity estimates were calculated using the first and last electrodes in the sequence (B8 and B11 or M8 and M11), and the means and standard deviations were calculated from the absolute values of the estimated velocities. The CPV estimate was selected for analysis in this case because the SPVs were found to have large standard deviations at low SNRs, as demonstrated in the validation results (Section 4.2.2), and the SNRs were low in cluster 0 in both channels.

In addition to the distinct waveforms, the propagation velocities of the sorted clusters provide further evidence of the spikes arising from different sources. For example, clusters 1 and 2 in channel B show significantly different CPVs with low standard deviations,

corresponding to errors of approximately 5% with respect to the means, and high confidence indices owing to the highly consistent waveforms in each cluster. The low standard deviations and high confidence indices indicate the high reliability of these estimates for the clusters 1 and 2 in channel B. Similar high reliability can also be observed in the CPV estimate for cluster 1 in channel M, which has an error of approximately 8% at one standard deviation.

However, the standard deviations of the CPV estimates were higher for cluster 0 in both channels B and M; in these cases, the error with respect to the mean exceeded 20%. This is likely because the SNRs of the spikes in these clusters were lower and the propagation velocity estimates were therefore more affected by noise. Alternatively, it may also be the case that these clusters actually represent more than one source but the waveforms are indistinguishable, again because of the SNR.

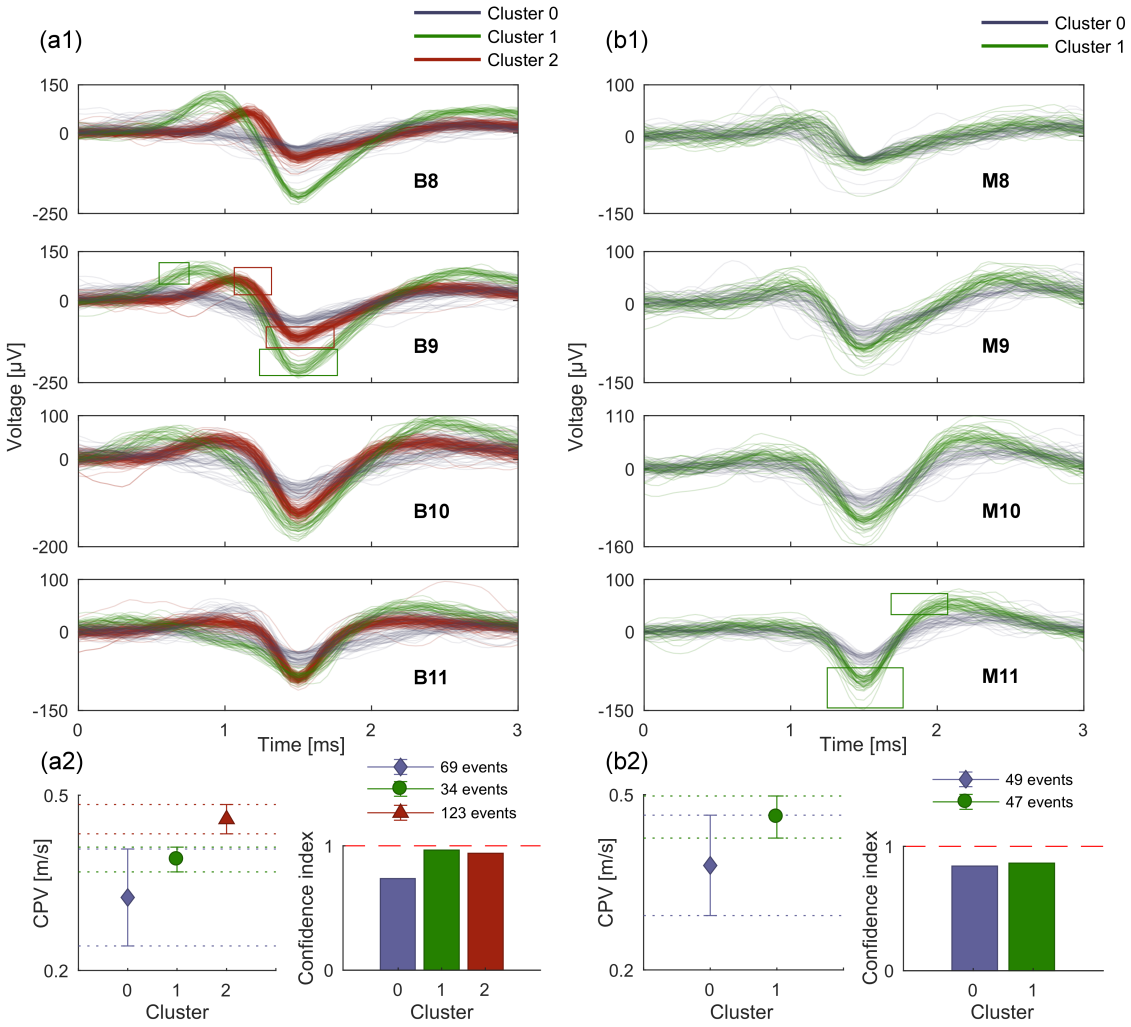

Figure 5.2 – Examples of µSpikeHunter spike sorting results for spikes recorded from cortical neurons at DIV 15 with a sampling rate of 20 kHz and an analysis period of 100 s. (a1) Microchannel B with three source clusters. The boxes on the B9 plot are the ROIs used for sorting. (a2) Intra-cluster averages of the CPV and confidence index for channel B events and the numbers of events in each cluster. (b1) Microchannel M with two source clusters. The boxes on the M11 plot are the ROIs used for sorting. (b2) Intra-cluster averages of the CPV and confidence index for channel M events and the numbers of events in each cluster.

Although the SPV did not yield reliable estimates of the propagation velocities for cluster 0 in both channels, likely because of the low SNRs, the SPV estimates using the first and last electrodes were computed for the other three clusters presented here and compared with the corresponding CPV estimates. In all cases, the CPVs yielded higher confidence indices and smaller standard deviations than the SPVs. The SPVs yielded fairly consistent results for clusters 1 and 2 in channel B and cluster 1 in channel M, with errors of approximately 10% to 15% at one standard deviation from the mean for each cluster.

However, even in cases where the SPV standard deviation was relatively low, the SPVs were much higher than the CPVs. For example, for cluster 1 in channel B, the mean CPV was 0.390 m/s (± 0.021 m/s), and the mean SPV was 0.480 m/s (± 0.046 m/s). This is because the waveforms recorded on different electrodes generally had very different shapes (see Section 3.2.4). This is particularly apparent for cluster 2 in channel B; the spike waveforms in this cluster on B8 and B9 have fairly large initial positive phases followed by smaller negative phases, whereas those on B10 and B11 are primarily composed of a large negative phase (Fig. 5.2(a1)). The difference between the waveforms on B8 and B11 resulted in the cross-correlation being maximized at a lag that is less than the delay between the minima recorded on the two electrodes.

5.2.2 Propagation of signals from axonal to somal compartment

Because the neurons in the experiments described in Sections 5.2.1 and 5.2.3 were cultured in the somal compartment (see Fig. 5.1(a)) with only Neurobasal medium present in the axonal compartment, it was expected that all of the observed propagation sequences would travel from the somal to the axonal compartment (forward propagation). However, a number of events were observed to travel from the axonal to the somal compartment (reverse propagation). Examples of propagation sequences showing reverse propagation observed in both the cortical and DRG experiments are shown in Figure 5.3. These examples also demonstrate the ease with which users may identify reverse propagation by observing the kymograph (cf. Fig. 3.5).

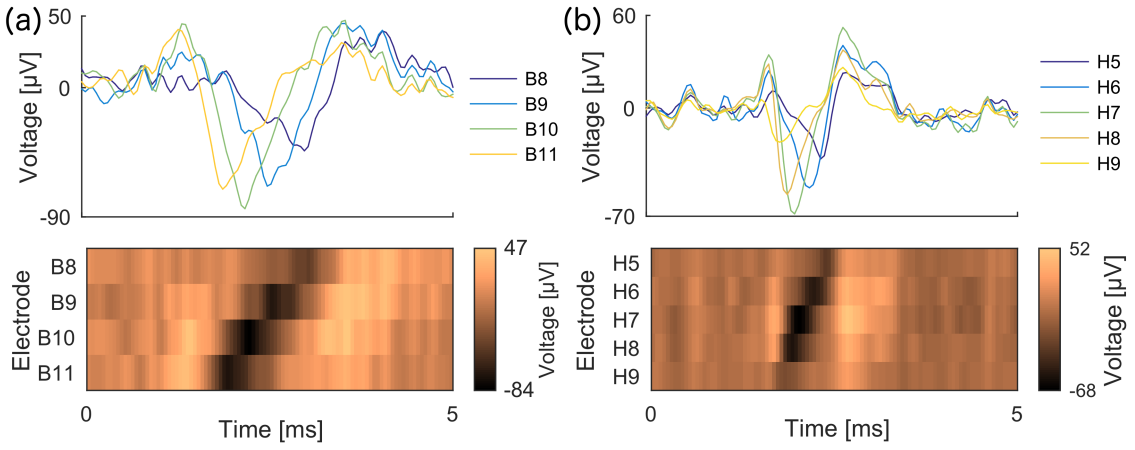

Figure 5.3 – Examples of voltage traces and kymographs from reverse propagating spikes detected from (a) cortical and (b) DRG culture recordings. Compare with the forward propagating example shown in Fig. 3.5.

To elucidate possible causes of the observed reverse propagation in the cortical culture, two sources of activity in two different microchannels (H and B) in the cortical neuron culture

that showed a high amount of reverse propagation activity at DIV 15 were investigated. Using μSpikeHunter, propagation sequences were detected in all 16 microchannels over an analysis duration of 100 s and sorted into source clusters as needed. Propagation sequences were detected with a threshold of 5 standard deviations of the noise and negative phase detection. The times and propagation velocities were then obtained for all propagation sequences in each source cluster, and the signs of the propagation velocities were assessed to identify if the sources showed reverse propagation. Channel H showed the largest number of reverse propagating spikes, with 63 of a total of 69 spikes showing reverse propagation. Only one source cluster was observed in channel H. As stated in Section 5.2.1, channel B contained three distinct clusters, and 33 of the 69 spikes in cluster 0 showed reverse propagation. A plot of all detected events from this recording is shown in Figure 5.4(a), and a larger view of only the events occurring between 52 and 56 s is shown in Figure 5.4(b). Events plotted as points and crosses represent forward and reverse propagating events.

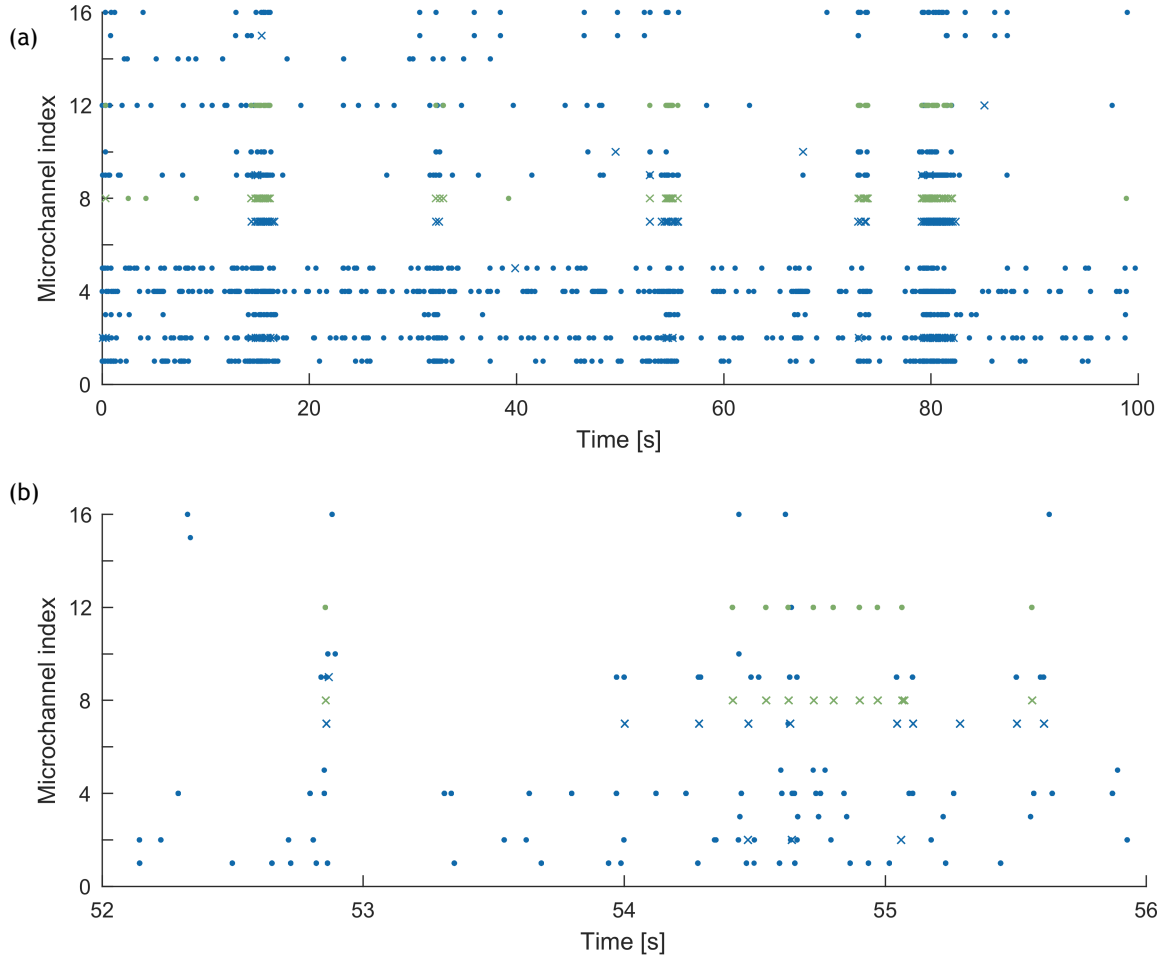

Figure 5.4 – Scatter plots showing the time of each detected event in the cortical culture recording at DIV 15 (a) over the entire 100 s and (b) during a period of high activity from 52 to 56 s. Points and crosses represent forward and reverse propagating events, respectively. The events from channel H and cluster 1 in channel M (microchannel indices of 8 and 12, respectively) are plotted in green.

The times at which the spikes arrived on the most distal electrodes (with respect to the somal compartment) for every source cluster in the 16 analyzed microchannels were then compared with those from the two abovementioned clusters in channels H and B to determine if any correlation existed. Correlation may indicate that either an axon from

another microchannel grew back through channel H or B or formed an excitatory axo-axonal synapse with the source in channel B or H, as schematically shown in the first two pairs of microchannels in Figure 5.5. A lack of such temporal correspondence may indicate that the spikes were spontaneously generated at the axonal terminal, as schematically shown by the rightmost microchannel in Figure 5.5.

A spike in channel H or B was considered to be potentially causally related to a spike from another microchannel if the time at which the spike arrived on the most distal electrode in channel H or B was within a predefined time window after the time at which the corresponding spike arrived on the most distal electrode in the other microchannel. The time window was defined to correspond to the mean velocity for the two considered sources (i.e., the source in channel B or H and the source in the other microchannel) and the distance between the ends of the two microchannels with an extra added distance of 500 µm to allow for the possibility of the axons growing into the axonal compartment before forming a synapse or growing back through channel H or B. That is, potential causal correspondence was considered if the following condition was met:

$$0 < t_{m,q} - t_{l,p} \leq \frac{D_{l,m} + 500\ \mu\text{m}}{(v_l + v_m)/2}, \tag{1}$$

where $t_{m,q}$ and $t_{l,p}$ are the times at which the qth and pth spikes in clusters m and l arrive on the most distal electrodes, respectively; $D_{l,m}$ is the distance between the two microchannels containing clusters l and m; and v_m and v_l are the average propagation velocities (CPV-far estimates) for clusters l and m.

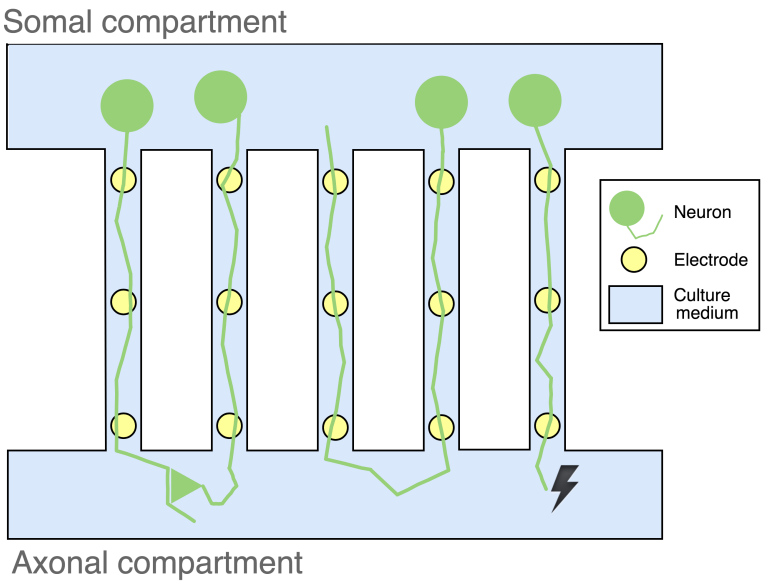

Figure 5.5 – Schematic of possible causes of reverse propagation. Left two channels: signal transmission via an excitatory axo-axonal synapse. Middle two channels: an axon growing back through a microchannel to the somal compartment. Rightmost channel: spontaneous signal generation from the axon terminal.

For channel H, 50 of the 63 reverse propagating events were found to have occurred after spikes in other channels within the defined time window, with 46 of these events found to temporally correspond to events from cluster 1 in channel M (see Section 5.2.1). This corresponds to 73% of all detected reverse propagating events from the source in channel H

and 98% of all detected events from cluster 1 in channel M. This high degree of temporal correlation is demonstrated in Figure 5.4, where the events from channel H and cluster 1 in channel M are plotted in red. Additionally, the average delay between the spike arrival times on electrodes M11 and H11 was 1.84 ms ± 0.07 ms; the distribution of the delays is shown in Figure 5.6, and it can be seen that this distribution is very narrow and well defined. These results indicate that either an axon grew through channel M and then backward toward the somal compartment through channel H or that two axons that grew through the two channels and formed an excitatory axo-axonal synapse. Moreover, this result further supports the sorting results presented in Section 5.2.1, particularly as there were no spikes from cluster 0 in channel M that were temporally linked to spikes in channel H.

For channel B, only 9 of the 33 reverse propagating spikes (27%) were found to have occurred after spikes in other channels within the defined time window, and these temporal links were scattered across six different sources in the other microchannels. This indicates that it is very unlikely that the reverse propagation was related to any of the sources in the 16 microchannels with microelectrodes beneath them; however, the µEF device used in this study has 20 microchannels, and so it is possible that an axon from one of the four silent microchannels may have been the source of the reverse propagation observed here.

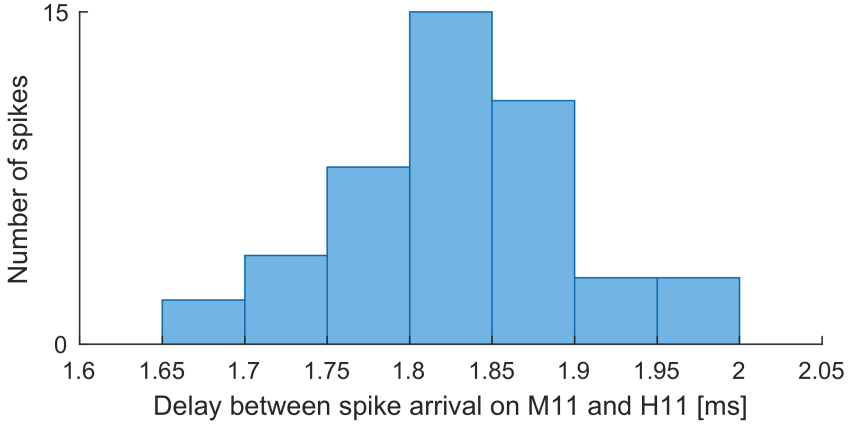

Figure 5.6 – Distribution of the delays ($t_{m,q} - t_{l,p}$) between the spike arrival times of temporally correlated events on electrodes M11 and H11.

The DRG culture showed reverse propagation without the same regularity as the cortical culture. Few reverse propagating events were observed, and they were often isolated events in different microchannels on different DIVs; for example, the reverse propagating event shown in Figure 5.3(b) was the only such event observed in that microchannel in a 10 min recording with a total of 84 detected events, and no potential causal spikes were observed in the other channels. In combination with the age of the culture, this indicates that these events likely represent the antidromic propagation of afferent signals produced in response to environmental factors rather than signals stimulated by another neuron in the same culture or that the spike arose spontaneously at the axon terminal (rightmost microchannel in Figure 5.5). This type of spontaneous antidromic signaling has been discussed as a potential cause of neuropathic pain, and the observation such signaling using µSpikeHunter for data analysis in the context of the highly controlled environment offered by µEF devices would be valuable in investigations on neuropathic pain.

5.2.3 Dorsal root ganglion: Monitoring a culture over multiple days *in vitro*

A DRG explant culture was also monitored as it aged *in vitro* to understand the baseline evolution of the spiking behavior of the DRG in this setup before conducting further experiments on the communication between sensory neurons and bone. Photographs of the DRG culture are shown in Figure 5.7. The photograph in Figure 5.7(a) shows the DRG explant in the somal compartment, and the image in Figure 5.7(b) shows the microchannels of the μEF device with axons growing through.

Recordings of 10 min in duration were obtained at DIVs 4, 6, and 8, and two microchannels (K and H, shown in the inset in Figure 5.7(b)) that each showed high levels of activity from a single source were selected for analysis. Propagation sequences were detected using a threshold of 3.5 standard deviations of the noise with negative phase detection. The activity was monitored by calculating the following parameters at each DIV: the number of spikes in each 10 min recording, the CPV estimate, and the SNR on each electrode. In the DIV 4 recording, an instance of equipment noise at approximately 7 s was detected as an event in all microchannels; this event was manually removed prior to analysis.

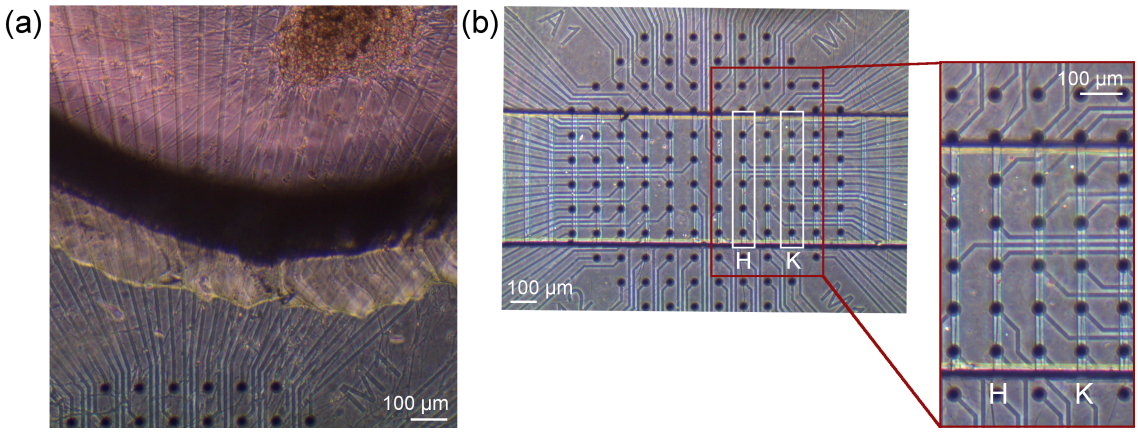

Figure 5.7 – Microscope images of the DRG explant culture in a μEF device. (a) The DRG explant in the somal compartment is visible at the top of the image. (b) Alignment of the microchannels over the microelectrodes. The inset shows a magnified view of the analyzed channels.

The results of this experiment are shown in Figure 5.8. Figure 5.8(a) shows the propagation velocity and number of events at the three measurement points for the two considered activity sources in channels K and H. As shown in this figure, from DIV 4 to DIV 8, the number of events in channel K increased steadily from 236 to 358 spikes. In contrast, the number of events in channel H initially increased from 84 to 120 spikes between DIVs 4 and 6 and then decreased to 8 spikes on DIV 8. Furthermore, in channel K, the propagation velocity was observed to increase from 0.57 to 0.77 m/s between DIVs 4 and 6 and then remain constant between DIVs 6 and 8, whereas in channel H, the propagation velocity initially remained constant at approximately 0.65 m/s and then decreased to 0.46 m/s at DIV 8.

Figure 5.8(b) shows the SNRs on each of the electrodes in channels K and H at the three measurement points. As shown in this figure, the SNR was highest on DIV 6 across all electrodes in both channels K and H. However, in channel K, the SNR was lowest on DIV 4, whereas in channel H, it was lowest on DIV 8. The SNR results also demonstrate that a higher

SNR is achieved recordings obtained from electrodes closer to the center of the microchannels, as has been described previously (Section 2.2.3) [12].

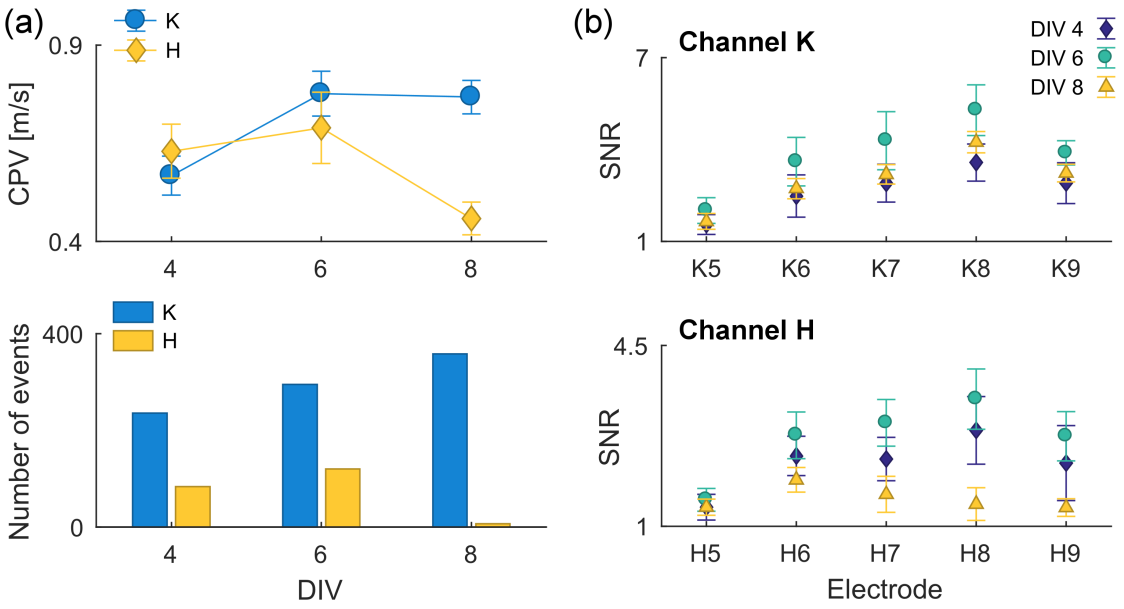

Figure 5.8 – Results of monitoring DRG culture activity over DIVs 4, 6, and 8. Results were obtained in channels K and H with a sampling rate of 20 kHz and a recording duration of 10 min. (a) Propagation velocity and number of spikes. (b) SNR for each electrode in the two microchannels.

These results give an indication of how the activity of a DRG culture changes as the culture matures under the baseline cell culture conditions. The results provided here indicate that the propagation velocity may increase with age in the early stages of the culture but that this increase ceases around DIV 6. It also appears that the overall activity level and signal amplitude for the culture peaks at DIV 6, though the activity level may continue to increase for some microchannels. These results served to help determine the recording time points and the time point for the addition of culture media in the experiment presented in Section 5.2.4.

5.2.4 Inter-system communication: Dorsal root ganglion and osteoclast-conditioned culture medium

The effect of the addition of OC medium (see Fig. 2.15) on the spiking behavior of DRG neurons was investigated to provide some insight into the mechanisms by which the molecules released by osteoclasts may induce changes in sensory nerve electrophysiology. It should be noted that the results presented here are preliminary and are included in this report to demonstrate the great research potential of μSpikeHunter in future and ongoing experiments on the possible mechanisms at work in the communication between bone and the sensory nervous system. Thus, further evidence would be required to ensure the robustness of the results and verify the hypotheses proposed herein.

Recordings were obtained at DIVs 4, 6-pre, 6-post, and 7 (see Section 5.1.3) with recording durations of 10, 5, 15, and 5 min, respectively. Propagation sequences were detected using a threshold of 3.5 standard deviations of the noise with negative phase detection. Instances of detected noise were removed manually prior to analysis. Propagating

spikes in the OC and NB (control) cultures were observed on five and four electrodes per channel in the two respective devices. In the NB culture, activity was observed at all four time points; however, no activity was observed in any of the microchannels of the OC device in the two baseline recordings (DIVs 4 and 6-pre). Thus, in the results presented here, the results obtained at DIV 4 for the NB culture are not considered, though it may be noted that they were similar to the DIV 6-pre recordings for the same culture. The results were analyzed for three channels showing moderate to high amounts of activity in each device: channels C, D, and H in the NB device and channels E, F, and G in the OC device.

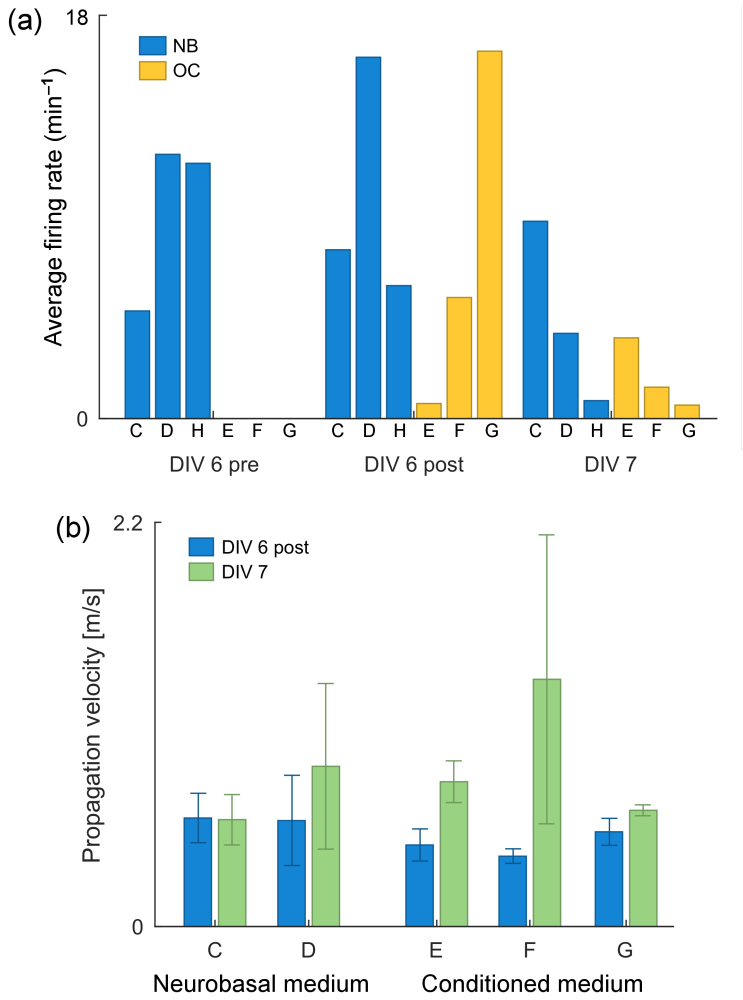

Figure 5.9 – Effects of the addition of culture medium on the electrophysiological behavior of a DRG explant culture. (a) Average firing rate based on the number of events detected in recordings obtained at three time points before and after the addition of two types of culture medium. (b) Mean propagation speeds (CPV-far estimate) of all spikes recorded from two channels of the NB device and three channels of the OC device at two time points. Error bars represent the standard deviation.

The effects of the addition of OC medium were investigated by considering three features of the recorded spikes: the average firing rate, the percentage of reverse propagating spikes, and the propagation velocity (CPV-far estimate). The results for the average firing rate and the propagation velocity at the three considered time points are shown in Figure 5.9(a) and (b), respectively. The average firing rates shown in Figure 5.9(a) were obtained by simply dividing the total number of detected spikes by the recording duration. In the case of the OC culture, after the addition of the culture medium, the number of spikes went from 0 for

every channel to a total of 10, 81, and 246 spikes in channels E, F, and G, respectively, during the 15-min recording (average firing rates of 0.7, 5.4, and 16.4 min^{-1}, respectively). This indicates that the addition of OC medium may have stimulated activity in the culture. In the NB culture, the numbers of events did not consistently increase or decrease across the considered channels.

The number of reverse propagating spikes was also investigated. Interestingly, only one reverse propagating spike was observed in the OC recordings; this spike was in channel G in the DIV 6-post recording and thus represented only 0.4% of all detected spikes in that recording. In contrast, the addition of NB medium was accompanied by an increase in the number of reverse propagating spikes in all three considered channels. In channels C, D, and H, there were 58, 15, and 14 reverse propagating spikes, corresponding to approximately 51%, 6%, and 15% of all spikes in those channels. In the DIV 6-pre and DIV 7 recordings, the numbers of spikes in these channels represented at most 5% of the total numbers of spikes.

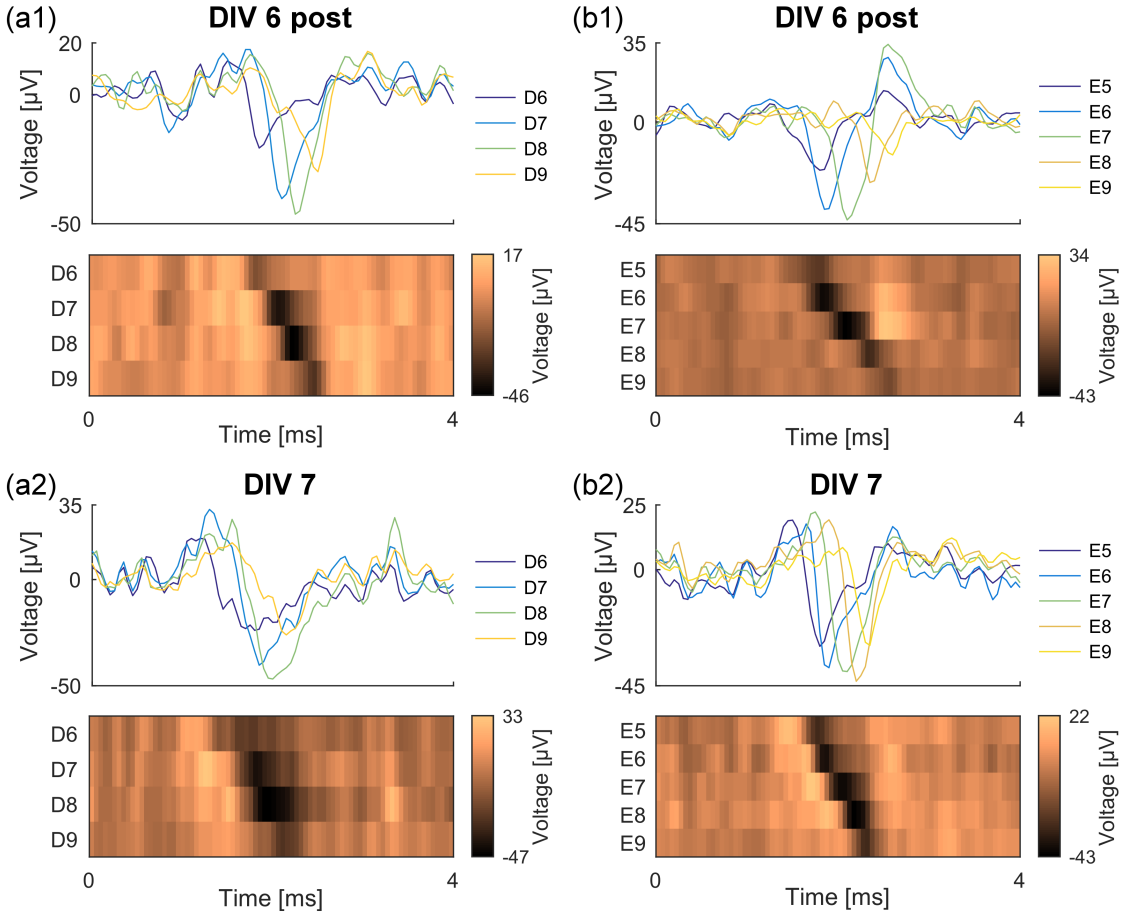

Figure 5.10 – Representative examples of voltage traces and kymographs of detected spikes in the (a) NB and (b) OC cultures. The examples were selected to have propagation velocities close to the mean for the corresponding datasets. (a1) Channel D, DIV 6-post, CPV = 0.6 m/s. (a2) Channel D, DIV 7, CPV = 0.86 m/s. (b1) Channel E, DIV 6-post, CPV = 0.5 m/s. (b2) Channel E, DIV 7, CPV = 0.73.

The most significant change to the OC culture that was not observed in the NB culture was an increase in the propagation velocity of the spikes. The propagation velocity results are shown in Figure 5.9(b). Because no spikes were observed in the DIV 6-pre recording for the OC culture, only the DIV 6-post and DIV 7 results are presented here; however, it should be

noted that the propagation velocity results for the NB culture at DIV 6-pre were very similar to those at DIV 6-post. In this figure, the results for channel H are excluded because the SNR of the four recorded spikes on DIV 7 was very low, causing the propagation velocity estimates to be highly unreliable. The propagation velocity was computed using the CPV estimate based on the most distant electrode pair (CPV-far; see Sections 3.2.4 and 4.2.3). For each considered channel, the mean and standard deviation across the spikes at the two considered time points are plotted in Figure 5.9(b). As shown in Figure 5.9(b), the propagation velocity remained roughly constant in both channels in the NB culture, whereas it increased significantly in all three channels in the OC culture.

Because there were not always a high number of spikes in the recordings and the spread of computed propagation velocities was sometimes quite large (specifically for channels D and F in the DIV 7 recording), the spikes were also observed in µSpikeHunter on a single-sequence basis to visually confirm this apparent increase in propagation velocity. As shown in Section 3.1.2, the main GUI of µSpikeHunter contains plots of the voltage traces and a kymograph for each propagation sequence, both of which provide an indication of the direction and speed of propagation. It was found that the spikes detected in the DIV 7 recording for the OC culture consistently showed noticeably higher propagation velocities than those in the DIV 6-post recording; this same increase was not observed for the NB culture.

Representative examples of traces and kymographs of detected spikes from channel D in the NB culture and channel E in the OC culture at both time points are shown in Figure 5.10(a) and (b), respectively. With a focus on the kymographs, it can be readily observed that the propagation velocity is approximately the same for the spikes in channel D from the two recordings (Fig. 5.10(a1) and (a2)), whereas the spike in channel E from the DIV 6-post recording (Fig. 5.10(b1)) showed a lower propagation velocity than that from the DIV 7 recording (Fig. 5.10(b2)). The example for channel D on DIV 7 (Fig. 5.10(a2)) also demonstrates that the CPV estimate (0.86 m/s) was not reliable in this case. This demonstrates the ease with which µSpikeHunter can be used to not only statistically evaluate the electrophysiological behavior of a culture but also qualitatively assess individual spikes to ensure the statistics are sufficiently representative of the actual spike features.

Chapter 6

Discussion

6.1 Validation with synthetic data

The validation of μSpikeHunter with synthetic datasets demonstrated the high level of performance of the software. In terms of the precision and detection rate, the propagation sequence detector yielded good results. The precision was very high for noise levels up to an SNR of 0.3, whereas the detection rate showed slowly deteriorating performance with increasing noise level. However, as stated previously, a high precision is more important than a high detection rate in electrophysiological experiments because it is important to ensure the events being analyzed correspond to actual spikes. One great benefit of using μEF devices in this context is that they allow an added level of robustness to spike detection algorithms. In μSpikeHunter, events are only considered as a part of propagation sequences if there are temporally linked events on each of the other electrodes and these events show ordinal association with the order of the electrodes (see Section 3.2.1). This also allows the detection threshold to be lower than typically used in electrophysiological experiments without any loss of precision.

The validation results also demonstrated the performance of the different propagation velocity estimation algorithms and indicated the considerations that should be made when selecting the most appropriate estimate for a given experimental setup. The recommended estimates for different sets of conditions based on the overall performance results are summarized in Table 6.1. In all cases, the CPV-far estimate yielded the best results.

Table 6.1 — Summary of the performance of the different propagation velocity estimates under different recording conditions in the case of four recording electrodes.

SNR	Inter-electrode distance	CPV-far	CPV-close	SPV-far	SPV-close
$0.2 < SNR < 0.5$	–	○	○	×	×
$SNR \geq 0.5$	$D = 100\ \mu m$	○	○	○	×
$SNR \geq 0.5$	$D = 200\ \mu m$	○	○	×	○

Notes:
○ Good performance
× Poor performance

In the case of high noise ($0.2 < SNR < 0.5$), the SPV yielded poor estimates regardless of which pair of electrodes was selected. In this case, the CPV estimate should be used; additionally, the CPV calculated suing more distant electrodes is somewhat more accurate than that using closer electrodes in all cases (Fig. 4.4).

In the case of low noise ($SNR \geq 0.5$), the CPV estimates continued to yield good results regardless of which electrode pair was selected. However, the SPV estimate performance was found to depend on the inter-electrode distance. When the inter-electrode distance is low, more distant electrode pairs should be selected, and when the inter-electrode distance is high, neighboring or nearby electrode pairs should be selected. On the basis of the results obtained using four electrodes with inter-electrode distances of 100 and 200 μm, the SPV estimate yields good results when the distance between the selected pair of electrodes is in the range of approximately 200–400 μm. At a distance of 100 μm (SPV-close in the case of $D = 100$ μm), the SPV performance was reduced by consistent overestimation, and at a distance of 600 μm (SPV-far in the case of $D = 200$ μm), the SPV performance was reduced by the presence of outliers.

The poor SPV-close estimate performance at the smaller inter-electrode distance is attributable to the bias towards overestimation due to the τ^{-1} dependence of the SPV estimate, as described earlier. At small inter-electrode distances, the SPV-close estimate is always biased toward overestimation; thus, the mean overestimates the true value, whereas the standard deviation is fairly low.

In contrast, the poor SPV-far estimate performance at the larger inter-electrode distance occurred because the cross-correlation window is scaled with the inter-electrode distance. In this larger window, the noise portion of the signals on the two electrodes may match well at an arbitrary time lag and the waveforms of the signals may be sufficiently distorted that this noise alignment lag can produce a higher peak in the cross-correlation than the spike alignment lag. At large inter-electrode distances, the SPV-far estimate is not biased toward over- or underestimation, and only a few outliers are present in the data; thus, the mean is close to the true value, whereas the standard deviation is quite high.

One important point to consider when selecting the propagation velocity estimate for analysis is the fact that the CPV and SPV are fundamentally different in terms of the times they use to calculate the propagation velocity, as mentioned in Section 3.2.4. In the case of the CPV, a “master spike” is obtained through the intra-cluster realignment and averaging of the spikes, and the delay between the spike arrival times on the two electrodes is based on the times of the peaks of the “master spikes.” In contrast, the SPV is calculated from the lag that yields the peak cross-correlation for the waveforms on the two electrodes in a single propagation sequence. Thus, essentially, the CPV measures the progression of the peak voltage from electrode to electrode, whereas the SPV measures the progression of the entire waveform. This means that when the SNR is high and either the CPV or the SPV may be selected for analysis, the user must determine which of these two quantities they wish to consider as the propagation velocity.

6.2 Experimental results

The experimental results obtained in this study demonstrated the great utility of μSpikeHunter in the analysis of recordings obtained from neuronal cultures in μEF devices. Additionally, the results obtained from the experiments using DRG cultures represent an early

step in understanding the electrophysiological facet of the flow of information between sensory neurons and bone, not only in terms of showing the applicability of µSpikeHunter to this line of research but also giving a possible direction for future investigation.

The overall performance of µSpikeHunter was first experimentally validated using a recording obtained from a dissociated cortical culture at DIV 15. The results obtained from this culture demonstrated the effectiveness and ease of use of the spike sorting tool and the high performance of the CPV estimation algorithm in an experimental context. Furthermore, reverse propagation was shown to be readily identifiable both inside the GUI by observing the kymograph and by using the program outputs to determine the sign of the propagation velocity. In the cortical culture, frequent reverse propagating signals observed in one of the microchannels were shown to have a definitive causal link to forward propagating signals from a source in another microchannel using the spike time outputs of µSpikeHunter. This result highlights the applicability of µSpikeHunter to the investigation of network dynamics. Importantly, in the context of the larger project on the study of the communication between sensory neurons and bone, this result also shows that, if all microchannels in the µEF device contain microelectrodes, it can easily be confirmed whether reverse propagating signals are in fact attributable to the stimulation of the axon terminals by the conditions in the axonal compartment or if they are in fact produced in response to excitatory stimulation by another neuron in the culture.

The results from the DRG cultures presented in this report represent a first step in assessing the electrophysiological facet of the effect of osteoclasts on sensory neurons. The results obtained using µSpikeHunter indicate that the osteoclast secretome may cause an increase in the number and/or amplitude of anterograde signals produced by sensory neurons upon first exposure as well as an increase in the propagation velocity of these signals after some incubation time. However, as stated previously, these results are preliminary, and more µEF cultures would need to be analyzed to confirm that the occurrence of the observed changes is consistent from trial to trial.

In the OC culture, the number of detected spikes prior to OC medium addition was zero in all channels; however, forward propagating signals were observed immediately after the addition of medium. The fact that no spikes were observed in the DIV 6-pre recording may have been because there was no activity or because the amplitude of the signals was below the detection limit. Thus, the addition of the OC medium appears to have either induced activity or increased the SNR of the spikes. It is interesting to note that almost no reverse propagating signals were recorded after the addition of OC medium, indicating that the OC medium may not have any notable effects on inducing afferent signaling in the DRG neurons. However, activity was not recorded in every microchannel where axons were observed to be present, and there may have been retrograde activity that fell below the detection threshold.

The propagation velocity results obtained from the OC culture provide compelling evidence that the osteoclast secretome in fact induces an increase in the propagation velocity. Such an increase was observed over three microchannels both in the statistical evaluation of all CPV estimates of the spikes and in the qualitative evaluation of the spike voltage traces and kymographs on the single-spike level. Possible causes of this increase in propagation velocity include the simple maturation of the culture with no influence by the OC medium, the OC medium inducing an increase in the diameter of the axon, and the

increased expression of sodium channels in the axonal membrane in response to the OC medium.

In terms of the maturation of the culture, it was seen in the results obtained from the DRG monitoring experiment (Section 5.2.3) that the propagation velocity tends to increase from DIV 4 to DIV 6 and then remain stable or decrease. This is supported by the results obtained from the control NB culture, which saw consistent CPV results from DIV 6 to DIV 7. This suggests that the increase observed between DIV 6-post and DIV 7 in the OC culture was the result of the addition of the conditioned medium.

The increase in diameter of the axons may be one cause of the observed propagation velocity increase. This is a good possibility, as axonal outgrowth has been observed under the culture conditions considered in this work, as reported in by Neto et al. [92] (see Section 2.3.5), and this outgrowth may be accompanied by an increase in girth. The propagation velocity is proportional to the square root of the diameter of the axon; thus, to achieve an increase to the propagation velocity in line with those observed in channels E and G in the OC culture (0.44 to 0.79 m/s and 0.51 to 0.63 m/s, respectively; Fig. 5.9(b)), the diameters of the axons would have to be increased by factors of 2.9 and 1.5, respectively. A nearly threefold increase in diameter seems unlikely; however, it is possible that the CPV estimates were affected by the change in the spike waveforms observed between DIV 6 and DIV 7 (Fig. 5.10(b1) and (b2)) and thus indicate a greater change than actually occurred. This would have to be taken into account when evaluating results obtained over many trials. Additionally, it may also be the case that an increase in diameter was only one mechanism of the propagation velocity increase.

It may also be the case that the OC medium induces an increased expression of certain sodium channels in the axon. This type of upregulated expression has been observed in studies on cancer-induced bone pain [95], [96] (see Section 2.3.5). Furthermore, the inactivation of sodium channels has been linked to a decrease in spike amplitude and a reduction in AP propagation velocity, indicating that the converse would occur were the expression of sodium channels to be increased [99] (see Appendix A). Thus, it is possible that this may have also been a factor in the increased propagation velocity observed in the OC culture.

6.3 Expected applications and future work

A paper on µSpikeHunter has been submitted to Nature Methods for publication (submission reference number: NMETH-A35206). It is expected that this software will prove useful not only in the ongoing work on the communication between bone and sensory neurons but also in other studies utilizing µEF devices for the study of neuron electrophysiology.

In relation to the present work, which was conducted in the context of a larger funded research project on the crosstalk between sensory neurons and bone, µSpikeHunter will continue to be used in the further analysis of electrophysiological signals recorded from µEF cultures of DRGs with added OC medium, as well as in recordings obtained from DRGs in co-culture with osteoblasts and osteoclasts. These experiments will give an indication of the mechanisms underlying bone pain and enhanced neurite outgrowth in the presence of osteoclasts as well as the effect of sensory innervation on bone remodeling. Additionally, because of the versatility and expected upcoming publication of µSpikeHunter, this tool may also be employed in other projects by our research team or other researchers in the

assessment of the crosstalk between neurons and other cells, such as myocytes or glial cells, as well as the investigation of network dynamics using the types of controlled feed-forward cultured neuronal network methods described previously [56] (see Section 2.2.3).

In combination with the commercial MCS 2100 recording systems and MEAs, µSpikeHunter greatly simplifies the process of obtaining and analyzing large amounts of electrophysiological data recorded from neurons *in vitro*. This is highly valuable, as many researchers studying the molecular aspect of neuronal communication do not have the expertise necessary for electrophysiological data acquisition and analysis. Thus, µSpikeHunter is expected to be a valuable tool that will open doors to new paths of investigation.

Chapter 7

Conclusion

In this work, a program called µSpikeHunter was developed for the analysis of electrophysiological signals recorded from neurons cultured in µEF devices. This software is expected to expand the research potential of such devices by providing new easy-to-use data analysis possibilities. This user-friendly tool aims to simplify the process of analyzing recordings obtained in this context and expand the possibility of readily coupling electrophysiological experimentation with other facets of neurobiological study.

µSpikeHunter contains a robust algorithm for the detection of propagating signals recorded using a µEF device, two different methods of estimating the propagation velocity that can be applied using any pair of recording electrodes, and a graphical spike sorting tool that allows the user to sort spikes into source clusters based on their waveforms. The propagation sequence detection method showed very high precision in the validation of the program using synthetic data, with high performance up to an SNR of 0.3. The CPV estimate, which is based on the intra-cluster alignment of the spike waveforms, also showed high accuracy and reliability up to an SNR of 0.4, with the accuracy remaining fairly high at an SNR of 0.3 despite some loss in reliability. The SPV estimate showed good performance up to an SNR of 0.5. It was also demonstrated that the spatiotemporal resolution of the data (i.e., the sampling rate and the inter-electrode distance) needs to be taken into account when considering which electrodes to use for the SPV estimate. Most critically, the electrode pair selected for this estimate should be separated by a distance of approximately 200—500 µm. µSpikeHunter also showed good performance in the analysis of a recording obtained from a cortical culture in terms of spike sorting, propagation velocity estimation, and the investigation of the cause of reverse propagating signals observed in the culture.

µSpikeHunter was then applied to the analysis of results obtained in a preliminary experiment on how the osteoclast secretome affects the spiking behavior of sensory neurons. A DRG explant culture was monitored to observe the evolution of the electrophysiological behavior with culture age. It was found that the propagation velocity increases with culture age in the early stages and levels off by around DIV 6. A further experiment was conducted in which OC medium was added to the axonal compartment at DIV 6 and recordings obtained before and after the addition of the medium were compared. The results indicate that the addition of OC medium may have excited activity as well as increased the propagation velocity after 24 h incubation. Although these results are preliminary and more trials are

required to confirm the repeatability of this experiment, they not only provide guidance for future experiments in this ongoing project but also demonstrate the great utility of µSpikeHunter in this type of analysis.

References

[1] M. E. J. Obien, K. Deligkaris, T. Bullmann, and D. J. Bakkum, “Revealing neuronal function through microelectrode array recordings,” *Front. Neurosci.*, vol. 8, pp. 1–30, 2015.

[2] L. J. Millet and M. U. Gillette, “Over a century of neuron culture: From the hanging drop to microfluidic devices,” *Yale J. Biol. Med.*, vol. 85, pp. 501–521, 2012.

[3] D. J. Bakkum *et al.*, “Tracking axonal action potential propagation on a high-density microelectrode array across hundreds of sites,” *Nat. Commun.*, vol. 4, 2013.

[4] E. Neto *et al.*, “Compartmentalized Microfluidic Platforms: The Unrivaled Breakthrough of In Vitro Tools for Neurobiological Research,” *J. Neurosci.*, vol. 36, no. 46, pp. 11573–11584, 2016.

[5] J. Wang *et al.*, “Microfluidics: A new cosset for neurobiology,” *Lab Chip*, vol. 9, no. 5, pp. 644–652, 2009.

[6] L. Wang, M. Riss, J. O. Buitrago, and E. Claverol-Tinturé, “Biophysics of microchannel-enabled neuron-electrode interfaces,” *J. Neural Eng.*, vol. 9, no. 2, 2012.

[7] F. Elefteriou, P. Campbell, and Y. Ma, “Control of Bone Remodeling by the Peripheral Sympathetic Nervous System,” *Calcif. Tissue Int.*, vol. 94, no. 1, pp. 140–151, 2014.

[8] S. Grässel and D. Muschter, “Peripheral nerve fibers and their neurotransmitters in osteoarthritis pathology,” *Int. J. Mol. Sci.*, vol. 18, no. 5, 2017.

[9] S. Falk and A. H. Dickenson, “Pain and nociception: Mechanisms of cancer-induced bone pain,” *J. Clin. Oncol.*, vol. 32, no. 16, pp. 1647–1654, 2014.

[10] P. W. Mantyh, “The neurobiology of skeletal pain,” *Eur. J. Neurosci.*, vol. 39, no. 3, pp. 508–519, Feb. 2014.

[11] J. Gordon, S. Amini, and M. K. White, *Neuronal Cell Culture*, vol. 1078. Totowa, NJ: Humana Press, 2013.

[12] J. J. FitzGerald, S. P. Lacour, S. B. McMahon, and J. W. Fawcett, “Microchannels as axonal amplifiers,” *IEEE Trans. Biomed. Eng.*, vol. 55, no. 3, pp. 1136–1146, 2008.

[13] A. M. Taylor, S. W. Rhee, C. H. Tu, D. H. Cribbs, C. W. Cotman, and N. L. Jeon, “Microfluidic Multicompartment Device for Neuroscience Research,” *Langmuir*, vol. 19, no. 5, pp. 1551–1556, Mar. 2003.

[14] J. W. Park, B. Vahidi, A. M. Taylor, S. W. Rhee, and N. L. Jeon, “Microfluidic culture platform for neuroscience research,” *Nat. Protoc.*, vol. 1, no. 4, pp. 2128–2136, 2006.

[15] B. J. Dworak and B. C. Wheeler, “Novel MEA platform with PDMS microtunnels enables the detection of action potential propagation from isolated axons in culture,” *Lab Chip*, vol. 9, no. 3, pp. 404–410, 2009.

[16] R. Habibey, S. Latifi, H. Mousavi, M. Pesce, E. Arab-Tehrany, and A. Blau, “A multielectrode array microchannel platform reveals both transient and slow changes in axonal conduction velocity,” *Sci. Rep.*, vol. 7, no. 1, pp. 1–14, 2017.

[17] M. K. Lewandowska, D. J. Bakkum, S. B. Rompani, and A. Hierlemann, “Recording large extracellular spikes in microchannels along many axonal sites from individual neurons,” *PLoS One*, vol. 10, no. 3, pp. 1–24, 2015.

[18] E. R. Kandel, J. H. Schwartz, and T. M. Jessell, *Principles Of Neural Science*, 4th ed. McGraw-Hill Medical Publishing Division, 2000.

[19] D. Sterratt, B. Graham, A. Gilllies, and D. Willshaw, *Principles of Computational Modelling in Neuroscience*. 2012.
[20] E. L. Mancall and D. G. Brock, Eds., “Gray’s Clinical Neuroanatomy: The Anatomic Basis for Clinical Neuroscience,” Philadelphia, PA: Elsevier, 2011.
[21] A. L. Hodgkin and A. F. Huxley, “A quantitative description of membrane current and its application to conduction and excitation in nerve.,” *J. Physiol.*, vol. 117, no. 4, pp. 500–544, Aug. 1952.
[22] P. Dayan and L. F. Abbott, *Theoretical Neuroscience: Computational and Mathematical Modeling of Neural Systems*, 6th ed. Massachusetts Institute of Technology Press, 2005.
[23] C. Anastassiou, G. Buzsáki, and C. Koch, “Biophysics of Extracellular Spikes,” in *Principles of Neural Coding*, CRC Press, 2013, pp. 15–36.
[24] A. L. Hodgkin, A. F. Huxley, and B. Katz, “Measurement of current-voltage relations in the membrane of the giant axon of Loligo,” *J. Physiol.*, vol. 116, no. 4, pp. 424–448, 1952.
[25] A. L. Hodgkin and A. F. Huxley, “Currents carried by sodium and potassium ions through the membrane of the giant axon of Loligo,” *J. Physiol.*, vol. 116, no. 4, pp. 449–472, Apr. 1952.
[26] A. L. Hodgkin and A. F. Huxley, “The components of membrane conductance in the giant axon of Loligo,” *J. Physiol.*, vol. 116, no. 4, pp. 473–496, Apr. 1952.
[27] A. L. Hodgkin and A. F. Huxley, “The dual effect of membrane potential on sodium conductance in the giant axon of Loligo,” *J. Physiol.*, vol. 116, no. 4, pp. 497–506, Apr. 1952.
[28] C. Gold, D. A. Henze, C. Koch, and G. Buzsáki, “On the Origin of the Extracellular Action Potential Waveform: A Modeling Study,” *J. Neurophysiol.*, vol. 95, no. 5, pp. 3113–3128, May 2006.
[29] M. L. Hines and N. T. Carnevale, “The NEURON simulation environment,” *Neural Comput.*, vol. 9, no. 6, pp. 1179–209, Aug. 1997.
[30] M. M. Heinricher, “Principles of Extracellular Single-Unit Recording,” in *Microelectrode Recording in Movement Disorder Surgery*, Z. Israel and K. Burchiel, Eds. Thieme, 2004, pp. 8–13.
[31] C. A. Terzuolo and T. Araki, “An analysis of intra- versus extracellular potential changes associated with activity of single spinal motoneurons,” *Ann. N. Y. Acad. Sci.*, vol. 94, no. 2, pp. 547–558, Dec. 2006.
[32] N. Joye, A. Schmid, and Y. Leblebici, “Electrical modeling of the cell-electrode interface for recording neural activity from high-density microelectrode arrays,” *Neurocomputing*, vol. 73, no. 1–3, pp. 250–259, 2009.
[33] P. Massobrio, G. Massobrio, and S. Martinoia, “Interfacing cultured neurons to microtransducers arrays: A review of the neuro-electronic junction models,” *Front. Neurosci.*, vol. 10, no. JUN, pp. 1–13, 2016.
[34] MultiChannel Systems, *MEA2100-System: User manual*. 2017.
[35] MultiChannel Systems, *Microelectrode array (MEA): User manual*. 2017.
[36] R. G. Harrison, “Observations of the living developing nerve fiber,” *Anat. Rec.*, vol. 1, no. 5, pp. 116–128, Jun. 1907.
[37] R. G. Harrison, “The outgrowth of the nerve fiber as a mode of protoplasmic movement,” *J. Exp. Zool.*, vol. 9, no. 4, pp. 787–846, Dec. 1910.
[38] I. Meyvantsson and D. J. Beebe, “Cell Culture Models in Microfluidic Systems,” *Annu. Rev. Anal. Chem.*, vol. 1, no. 1, pp. 423–449, 2008.
[39] G. M. Whitesides, “The origins and the future of microfluidics,” *Nature*, vol. 442, pp. 368–373, 2006.
[40] B. Xiong, K. Ren, Y. Shu, Y. Chen, B. Shen, and H. Wu, “Recent developments in microfluidics for cell studies,” *Adv. Mater.*, vol. 26, no. 31, pp. 5525–5532, 2014.
[41] A. Folch and M. Toner, “Microengineering of Cellular Interactions,” *Annu. Rev. Biomed. Eng.*, vol. 2, no. 1, pp. 227–256, Aug. 2000.
[42] G. M. Whitesides, E. Ostuni, S. Takayama, X. Jiang, and D. E. Ingber, “Soft Lithography in Biology and Biochemistry,” *Annu. Rev. Biomed. Eng.*, vol. 3, no. 1, pp. 335–373, Aug. 2001.

[43] E. W. K. Young and D. J. Beebe, “Fundamentals of microfluidic cell culture in controlled microenvironments,” *Chem. Soc. Rev.*, vol. 39, no. 3, p. 1036, 2010.
[44] I. R. Freshney, *Culture of Animal Cells: A Manual of Basic Technique*, 5th ed. Hoboken, New Jersey: John Wiley & Sons, 2005.
[45] F. Morin *et al.*, “Constraining the connectivity of neuronal networks cultured on microelectrode arrays with microfluidic techniques: A step towards neuron-based functional chips,” *Biosens. Bioelectron.*, vol. 21, no. 7, pp. 1093–1100, 2006.
[46] Y. Berdichevsky, K. J. Staley, and M. L. Yarmush, “Building and manipulating neural pathways with microfluidics,” *Lab Chip*, vol. 10, no. 8, pp. 999–1004, 2010.
[47] E. Neto *et al.*, “Sensory neurons and osteoblasts: close partners in a microfluidic platform,” *Integr. Biol.*, vol. 6, no. 6, pp. 586–595, 2014.
[48] E. J. Furshpan, P. R. MacLeish, P. H. O’Lague, and D. D. Potter, “Chemical transmission between rat sympathetic neurons and cardiac myocytes developing in microcultures: evidence for cholinergic, adrenergic, and dual-function neurons.,” *Proc. Natl. Acad. Sci. U. S. A.*, vol. 73, no. 11, pp. 4225–9, Nov. 1976.
[49] R. B. Campenot, “Local control of neurite development by nerve growth factor,” *Proc. Natl. Acad. Sci. U. S. A.*, vol. 74, no. 10, pp. 4516–9, 1977.
[50] N. Hong, S. Joo, and Y. Nam, “Characterization of axonal spikes in cultured neuronal networks using microelectrode arrays and microchannel devices,” *IEEE Trans. Biomed. Eng.*, vol. 64, no. 2, pp. 492–498, 2017.
[51] E. Claverol-Tinturé, J. Cabestany, and X. Rosell, “Multisite recording of extracellular potentials produced by microchannel-confined neurons in-vitro,” *IEEE Trans. Biomed. Eng.*, vol. 54, no. 2, pp. 331–335, 2007.
[52] E. Biffi *et al.*, “A microfluidic platform for controlled biochemical stimulation of twin neuronal networks,” *Biomicrofluidics*, vol. 6, no. 2, pp. 1–10, 2012.
[53] L. Pan, S. Alagapan, E. Franca, T. DeMarse, G. J. Brewer, and B. C. Wheeler, “Large Extracellular Spikes Recordable From Axons in Microtunnels,” *IEEE Trans. Neural Syst. Rehabil. Eng.*, vol. 22, no. 3, pp. 453–459, May 2014.
[54] U. Narula, A. Ruiz, M. McQuaide, T. B. DeMarse, B. C. Wheeler, and G. J. Brewer, “Narrow microtunnel technology for the isolation and precise identification of axonal communication among distinct hippocampal subregion networks,” *PLoS One*, vol. 12, no. 5, pp. 1–15, 2017.
[55] L. Pan, S. Alagapan, E. Franca, G. J. Brewer, and B. C. Wheeler, “Propagation of action potential activity in a predefined microtunnel neural network,” *J. Neural Eng.*, vol. 8, no. 4, p. 046031, Aug. 2011.
[56] L. Pan *et al.*, “An in vitro method to manipulate the direction and functional strength between neural populations,” *Front. Neural Circuits*, vol. 9, no. July, pp. 1–14, 2015.
[57] T. T. Kanagasabapathi *et al.*, “Functional connectivity and dynamics of cortical-thalamic networks co-cultured in a dual compartment device,” *J. Neural Eng.*, vol. 9, no. 3, 2012.
[58] C. a Brunello *et al.*, “Microtechnologies to fuel neurobiological research with nanometer precision.,” *J. Nanobiotechnology*, vol. 11, p. 11, 2013.
[59] J. Park, H. Koito, J. Li, and A. Han, “Microfluidic compartmentalized co-culture platform for CNS axon myelination research,” *Biomed. Microdevices*, vol. 11, no. 6, pp. 1145–1153, Dec. 2009.
[60] J. Park, H. Koito, J. Li, and A. Han, “Multi-compartment neuron–glia co-culture platform for localized CNS axon–glia interaction study,” *Lab Chip*, vol. 12, no. 18, p. 3296, Mar. 2012.
[61] B. E. Kerman *et al.*, “In vitro myelin formation using embryonic stem cells,” *Development*, vol. 142, no. 12, pp. 2213–2225, 2015.
[62] I. H. Yang *et al.*, “Axon myelination and electrical stimulation in a microfluidic, compartmentalized cell culture platform,” *NeuroMolecular Med.*, vol. 14, no. 2, pp. 112–118, 2012.
[63] P. Pagella, E. Neto, L. Jiménez-Rojo, M. Lamghari, and T. A. Mitsiadis, “Microfluidics co-culture systems for studying tooth innervation,” *Front. Physiol.*, vol. 5 AUG, no. August, pp. 1–8, 2014.
[64] K. A. Southam, A. E. King, C. A. Blizzard, G. H. McCormack, and T. C. Dickson, “Microfluidic primary culture model of the lower motor neuron-neuromuscular

junction circuit," *J. Neurosci. Methods*, vol. 218, no. 2, pp. 164–169, 2013.
[65] A. Takeuchi *et al.*, "Device for co-culture of sympathetic neurons and cardiomyocytes using microfabrication," *Lab Chip*, vol. 11, no. 13, p. 2268, 2011.
[66] E. E. Zahavi, A. Ionescu, S. Gluska, T. Gradus, K. Ben-Yaakov, and E. Perlson, "A compartmentalized microfluidic neuromuscular co-culture system reveals spatial aspects of GDNF functions," *J. Cell Sci.*, vol. 128, no. 6, pp. 1241–1252, 2015.
[67] G. Adriani, D. Ma, A. Pavesi, R. D. Kamm, and E. L. K. Goh, "A 3D neurovascular microfluidic model consisting of neurons, astrocytes and cerebral endothelial cells as a blood–brain barrier," *Lab Chip*, vol. 17, no. 3, pp. 448–459, 2017.
[68] S. H. Ralston, "Bone structure and metabolism," *Medicine (Baltimore).*, vol. 45, no. 9, pp. 560–564, 2017.
[69] B. Clarke, "Normal bone anatomy and physiology," *Clin. J. Am. Soc. Nephrol.*, vol. 3 Suppl 3, pp. 131–139, 2008.
[70] A. G. Robling, A. B. Castillo, and C. H. Turner, "Biomechanical and Molecular Regulation of Bone Remodeling," *Annu. Rev. Biomed. Eng.*, vol. 8, no. 1, pp. 455–498, 2006.
[71] D. Purves *et al.*, Eds., *Neuroscience*, 3rd ed. Sunderland, MA: Sinaur Associates, Inc., 2004.
[72] C. Chenu, "Role of innervation in the control of bone remodeling," *J. Musculoskelet. Neuronal Interact.*, vol. 4, no. 2, pp. 132–134, 2004.
[73] N. A. Sims and T. J. Martin, "Coupling the activities of bone formation and resorption: a multitude of signals within the basic multicellular unit," *Bonekey Rep.*, vol. 3, no. September 2013, pp. 1–10, 2014.
[74] F. Franquinho, M. A. Liz, A. F. Nunes, E. Neto, M. Lamghari, and M. M. Sousa, "Neuropeptide y and osteoblast differentiation - The balance between the neuro-osteogenic network and local control," *FEBS J.*, vol. 277, no. 18, pp. 3664–3674, 2010.
[75] U. H. Lerner and E. Persson, "Osteotropic effects by the neuropeptides calcitonin gene-related peptide, substance P and vasoactive intestinal peptide," *J. Musculoskelet. Neuronal Interact.*, vol. 8, no. 2, pp. 154–165, 2008.
[76] T. Goto, K. Nakao, K. K. Gunjigake, M. A. Kido, S. Kobayashi, and T. Tanaka, "Substance P stimulates late-stage rat osteoblastic bone formation through neurokinin-1 receptors," *Neuropeptides*, vol. 41, no. 1, pp. 25–31, 2007.
[77] M. Hukkanen, Y. T. Konttinen, R. G. Rees, S. Santavirta, G. Terenghi, and J. M. Polak, "Distribution of nerve endings and sensory neuropeptides in rat synovium, meniscus and bone.," *Int. J. Tissue React.*, vol. 14, no. 1, pp. 1–10, 1992.
[78] L. Wang *et al.*, "Calcitonin-gene-related peptide stimulates stromal cell osteogenic differentiation and inhibits RANKL induced NF-κB activation, osteoclastogenesis and bone resorption," *Bone*, vol. 46, no. 5, pp. 1369–1379, 2010.
[79] T. Schinke *et al.*, "Decreased bone formation and osteopenia in mice lacking α-calcitonin gene-related peptide," *J. Bone Miner. Res.*, vol. 19, no. 12, pp. 2049–2056, 2004.
[80] H. He *et al.*, "CGRP may regulate bone metabolism through stimulating osteoblast differentiation and inhibiting osteoclast formation," *Mol. Med. Rep.*, vol. 13, no. 5, pp. 3977–3984, 2016.
[81] K. Lian, J. Du, Z. Rao, and H. Luo, "The experimental study on the effect calcitonin gene-related peptide on bone resorption mediated by interleukin-1.," *J. Tongji Med. Univ.*, vol. 21, no. 4, pp. 304–7, 2001.
[82] Y. M. Yoo, J. H. Kwag, K. H. Kim, and C. H. Kim, "Effects of neuropeptides and mechanical loading on bone cell resorption in vitro," *Int. J. Mol. Sci.*, vol. 15, no. 4, pp. 5874–5883, 2014.
[83] S. J. Sample *et al.*, "Role of calcitonin gene-related peptide in functional adaptation of the skeleton," *PLoS One*, vol. 9, no. 12, pp. 1–18, 2014.
[84] T. Goto, T. Yamaza, M. A. Kido, and T. Tanaka, "Light- and electron-microscopic study of the distribution of axons containing substance P and the localization of neurokinin-1 receptor in bone," *Cell Tissue Res.*, vol. 293, no. 1, pp. 87–93, 1998.
[85] H. B. Sun, J. C. Chen, Q. Liu, M. F. Guo, and H. P. Zhang, "Substance P stimulates differentiation of mice osteoblast through up-regulating Osterix expression," *Chin J*

Traumatol, vol. 13, no. 1, pp. 46–50, 2010.
[86] W. H. Ma, Y. J. Liu, W. Wang, and Y. Z. Zhang, “Neuropeptide Y, substance P, and human bone morphogenetic protein 2 stimulate human osteoblast osteogenic activity by enhancing gap junction intercellular communication,” *Brazilian J. Med. Biol. Res.*, vol. 48, no. 4, pp. 299–307, 2015.
[87] G. Mei *et al.*, “Substance P activates the wnt signal transduction pathway and enhances the differentiation of mouse preosteoblastic MC3T3-E1 cells,” *Int. J. Mol. Sci.*, vol. 15, no. 4, pp. 6224–6240, 2014.
[88] D. Kodama, T. Hirai, H. Kondo, K. Hamamura, and A. Togari, “Bidirectional communication between sensory neurons and osteoblasts in an in vitro coculture system,” *FEBS Lett.*, vol. 591, no. 3, pp. 527–539, Feb. 2017.
[89] S. J. Sohn, “Substance P upregulates osteoclastogenesis by activating nuclear factor kappa B in osteoclast precursors,” *Acta Otolaryngol.*, vol. 125, no. 2, pp. 130–133, 2005.
[90] L. Wang *et al.*, “Substance P stimulates bone marrow stromal cell osteogenic activity, osteoclast differentiation, and resorption activity in vitro,” *Bone*, vol. 45, no. 2, pp. 309–320, 2009.
[91] T. Matayoshi, T. Goto, E. Fukuhara, H. Takano, S. Kobayashi, and T. Takahashi, “Neuropeptide substance P stimulates the formation of osteoclasts via synovial fibroblastic cells,” *Biochem. Biophys. Res. Commun.*, vol. 327, no. 3, pp. 756–764, 2005.
[92] E. Neto *et al.*, “Osteoclasts control sensory neurons axonal growth through epidermal growth factor receptor signaling,” *bioRxiv*, 2018.
[93] T. Yoneda, M. Hiasa, Y. Nagata, T. Okui, and F. A. White, “Acidic microenvironment and bone pain in cancer-colonized bone,” *Bonekey Rep.*, vol. 4, no. March, pp. 1–9, 2015.
[94] M. Hiasa *et al.*, “Bone Pain Induced by Multiple Myeloma Is Reduced by Targeting V-ATPase and ASIC3,” *Cancer Res.*, vol. 77, no. 6, pp. 1283–1295, Mar. 2017.
[95] C. B. Ke, W. S. He, C. J. Li, D. Shi, F. Gao, and Y. K. Tian, “Enhanced SCN7A/Nax expression contributes to bone cancer pain by increasing excitability of neurons in dorsal root ganglion,” *Neuroscience*, vol. 227, pp. 80–89, 2012.
[96] X. D. Liu, J. J. Yang, D. Fang, J. Cai, Y. Wan, and G. G. Xing, “Functional upregulation of Nav1.8 sodium channels on the membrane of dorsal root ganglia neurons contributes to the development of cancer-induced bone pain,” *PLoS One*, vol. 9, no. 12, pp. 1–17, 2014.
[97] A. Eitner, G. O. Hofmann, and H.-G. Schaible, “Mechanisms of Osteoarthritic Pain. Studies in Humans and Experimental Models,” *Front. Mol. Neurosci.*, vol. 10, no. November, pp. 1–22, 2017.
[98] A. Togari, M. Mogi, M. Arai, S. Yamamoto, and Y. Koshihara, “Expression of mRNA for axon guidance molecules, such as semaphorin-III, netrins and neurotrophins, in human osteoblasts and osteoclasts,” vol. 878, pp. 204–209, 2000.
[99] K. Moradmand and M. D. Goldfinger, “Computation of long-distance propagation of impulses elicited by Poisson-process stimulation,” *J. Neurophysiol.*, vol. 74, no. 6, pp. 2415–2426, Dec. 1995.
[100] T. Sasaki, “The axon as a unique computational unit in neurons,” *Neurosci. Res.*, vol. 75, no. 2, pp. 83–88, 2013.
[101] D. Bucher and J. M. Goaillard, “Beyond faithful conduction: Short-term dynamics, neuromodulation, and long-term regulation of spike propagation in the axon,” *Prog. Neurobiol.*, vol. 94, no. 4, pp. 307–346, 2011.
[102] D. Debanne, “Information processing in the axon,” *Nat. Rev. Neurosci.*, vol. 5, no. 4, pp. 304–316, 2004.
[103] C. E. Carr and M. Konishi, “Axonal delay lines for time measurement in the owl’s brainstem,” *Proc. Natl. Acad. Sci.*, vol. 85, no. 21, pp. 8311–8315, 1988.
[104] C. E. Carr and M. Konishi, “A circuit for detection of interaural time differences in the brain stem of the barn owl,” *J. Neurosci.*, vol. 10, no. 10, pp. 3227–46, 1990.
[105] D. Debanne, E. Campanac, A. Bialowas, E. Carlier, and G. Alcaraz, “Axon Physiology,” *Physiol. Rev.*, vol. 91, no. 2, pp. 555–602, Apr. 2011.
[106] J. R. P. Geiger and P. Jonas, “Dynamic Control of Presynaptic Ca2+ Inflow by Fast-

Inactivating K+ Channels in Hippocampal Mossy Fiber Boutons," *Neuron*, vol. 28, no. 3, pp. 927–939, 2000.
[107] T. H. Bullock, "Facilitation of conduction rate in nerve fibers," *J. Physiol.*, vol. 114, no. 1–2, pp. 89–97, Jun. 1951.
[108] T. Sasaki, N. Matsuki, and Y. Ikegaya, "Action-Potential Modulation During Axonal Conduction," *Science (80-.).*, vol. 331, no. 6017, pp. 599–601, 2011.
[109] D. Debanne, N. C. Guérineau, B. H. Gähwiler, and S. M. Thompson, "Action-potential propagation gated by an axonal IA-like K+ conductance in hippocampus," *Nature*, vol. 389, no. 6648, pp. 286–289, Sep. 1997.
[110] H. Higashimori, T. P. Whetzel, T. Mahmood, and R. C. Carlsen, "Peripheral axon caliber and conduction velocity are decreased after burn injury in mice," *Muscle and Nerve*, vol. 31, no. 5, pp. 610–620, 2005.
[111] J. G. Thalhammer, S. A. Raymond, F. A. Popitz-bergez, and G. R. Strichartz, "Modality-Dependent Modulation of Conduction by Impulse Activity in Functionally Characterized Single Cutaneous Afferents in the Rat," *Somatosens. Mot. Res.*, vol. 11, no. 3, pp. 243–257, Jan. 1994.
[112] O. Obreja *et al.*, "Patterns of activity-dependent conduction velocity changes differentiate classes of unmyelinated mechano-insensitive afferents including cold nociceptors, in pig and in human," *Pain*, vol. 148, no. 1, pp. 59–69, Jan. 2010.
[113] J. Tigerholm *et al.*, "Modeling activity-dependent changes of axonal spike conduction in primary afferent C-nociceptors," *J. Neurophysiol.*, vol. 111, no. 9, pp. 1721–1735, 2014.

Appendix A

Axonal regulation of action potential waveform and propagation

The involvement of the axon in the modulation of the AP waveform and propagation velocity has recently become a subject of interest. The computational tool developed in this study would be applicable in the investigation of the mechanisms underlying the processing of information in the axon; thus, this subject is addressed here as a point of consideration.

The general flow of information in a neuron can be considered to have four phases: the integration of synaptic inputs at the dendrites, the generation and subsequent propagation of an AP, and the transmission of the signal at the axon terminal [100]. The conventional view of axons is that once an AP has been generated in the initial segment, it is faithfully conducted along the axon and transmitted to the postsynaptic neuron without distortion to the waveform or variation in the propagation velocity from AP to AP. Because of this all-or-nothing view of the axonal trunk as a simple conducting cable and the greater difficulty of recording signals from the axon than from the soma, signal propagation in the axon has long been neglected in neuroscience studies. However, recent experiments have demonstrated that the waveforms and propagation velocities of APs can be modified by changes to ion channel activation in the axonal membrane. The great number of different ion channels in the axonal membrane and the diversity among the time and voltage dependence of their ion conductance behavior has been shown to produce activity-dependent variation in the AP shape and membrane reversal potential, affecting the conduction fidelity and the release of neurotransmitters at the axon terminal [100]–[102]. However, the interplay among the conductances of different ion channels producing changes in excitability, AP waveform, and conduction velocity is very complex.

The transmission of APs along the axon introduce a delay in signal transmission that can be important in encoding the transmitted information. In a famous example, Carr and Konishi [103], [104] demonstrated that differences in the delay of axonal conduction of auditory signals from each ear in the auditory system of the barn owl are important in the sensitive determination of the location of the sound source. In this case, the differences in the conduction delays are due to differences in axonal length, but such variations in delay can also be introduced by other axonal structures, including branch points, varicosities, and

variations in diameter [102]. Although the overall structure of axons remains stable over time, it has been shown that axon morphology is actually quite dynamic, with variations in axonal branching and the number and size of axonal boutons varying in the range of a few tens of micrometers [105]. Such variation demonstrates the existence of a morphological mechanism for activity-dependent variation in AP conduction along the axon.

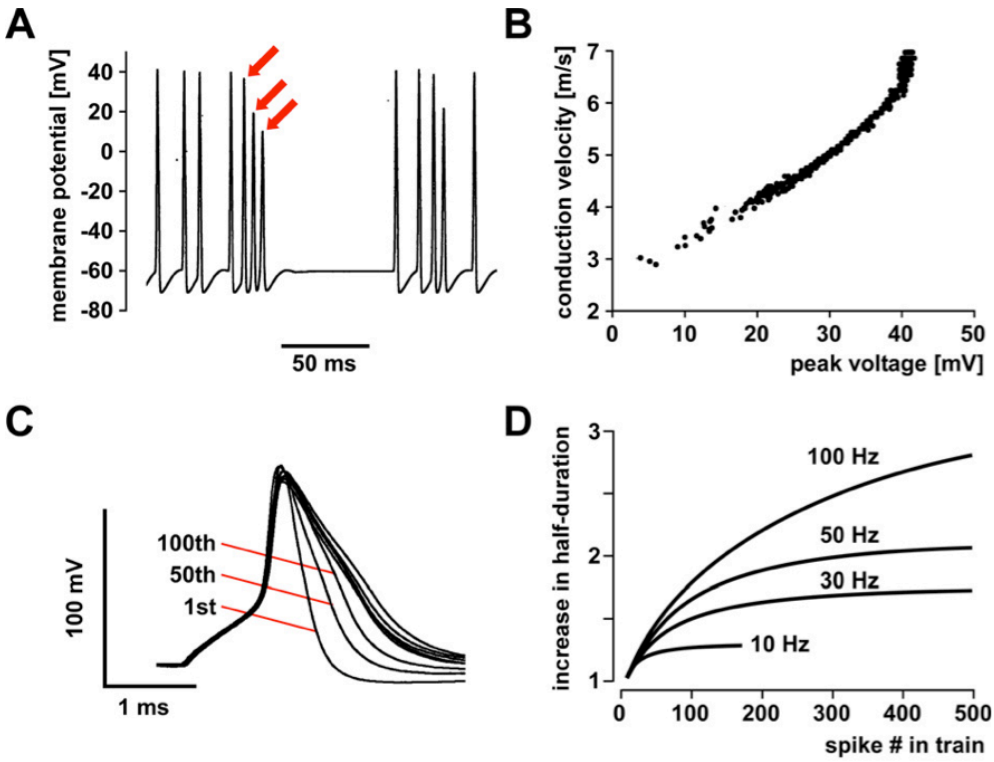

Figure A.1 – Effects of the inactivation of sodium and potassium channels on the AP shape and propagation velocity. (a) Inactivation of sodium channels in a HH-type model has been shown to result in the reduction of the AP amplitude at small interspike intervals [99]. (b) This amplitude reduction has been shown to correspond to decreases in the conduction velocity [99]. (c) In hippocampal mossy fibers, it has been shown that potassium channel inactivation leads to the activity-dependent broadening of the AP waveform [106]. (d) The extent of this broadening depends on the stimulation frequency [106]. Reproduced from Bucher and Goaillard [101].

The shape of the AP waveform is an important factor underlying the propagation velocity of APs, and the two main drivers shaping the AP waveform are the sodium and potassium channels. The rapid activation of sodium channels produces the initial steep upward slope, and the delayed activation and deactivation of potassium channels and the inactivation of the sodium channels together produce the refractory period. The responses of the conduction velocity and the AP waveform to repeated stimulation is useful in demonstrating some of the ionic mechanisms underlying axonal modulation of signal conduction. In one of the first demonstrations of activity-dependent variation in AP conduction velocity, Bullock [107] measured the changes in the conduction velocity and axonal excitability of earthworm and frog axons in response to repeated stimuli. He stimulated the neurons with a conditioning pulse followed by a test pulse after different intervals and compared the results to those obtained for a lone pulse. His results demonstrated that the conduction velocity and excitability were reduced when the two pulses were applied within a few milliseconds of each other but that at longer intervals on the order of tens of milliseconds, the conduction

velocity and excitability were increased. Later studies have aided in unraveling the mechanisms behind these changes.

Sodium inactivation plays a role in determining the AP amplitude during repetitive firing, which has an effect on the propagation of the AP along the axon [101], [102]. Using the HH model, Moradmand and Goldfinger [99] demonstrated that the sodium channel inactivation that occurs during the refractory period causes the AP amplitude to decrease when the interval between APs is small and that this reduction in amplitude is correlated with a decrease in the conduction velocity (Fig. A.1(a) and (b)). This is attributable to two mechanisms regarding the inactivated sodium channels [101]. First, if fewer sodium channels can be activated, a higher voltage is needed to achieve the influx of sodium needed to initiate an AP. Second, the reduced AP amplitude reduces the distance over which neighboring areas of membrane can be depolarized.

In contrast, the inactivation of certain types of potassium channels induced by repeated high-frequency stimulation has been shown to cause the AP waveform to broaden in hippocampal mossy fiber boutons (Fig. A.1(c) and (d)) [106]. This in turn results in more calcium ions entering the axon terminal, which produces a greater excitatory response in the postsynaptic CA3 pyramidal cell. A similar effect has been produced by the local application of glutamate to the axonal shaft [108], demonstrating that waveform modulation and the resulting boost in signal transmission can be induced by chemical means as well as electrical activity. Furthermore, the activation of the same type of potassium conductance in the hippocampus by applying a brief hyperpolarization before the application of the stimulus has been shown to cause AP propagation to fail [109]. The above results indicate that as a general rule, the sodium current drives AP generation and propagation and the potassium conductance opposes AP propagation and signal transmission.

Although most reviews on the axonal modulation of signal conduction and transmission have focused on CNS neurons [100]–[102], [105], studies have also been conducted on PNS neurons. For example, in an early experimental study on the axonal modulation of the propagation velocity, Higashimori et al. [110] used a mouse model to investigate the effect of burn injuries on the magnitude and conduction velocity of peripheral motor and sensory neurons. Following the burn injury, the conduction velocities in both motor and sensory axons were found to deteriorate, with motor neurons experiencing a greater effect. This conduction velocity reduction was not accompanied by any alterations in axon myelination or axon degeneration, and thus it was theorized that these effects may have been the result of shifts in electrolyte concentrations as part of the activation of inflammatory pathways. In nociceptors, which are specialized sensory neurons responsible for the sensation of pain, the pronounced activity-dependent slowing of the conduction velocity and an increased rate of conduction failure have been demonstrated by comparing the change in the conduction velocity of nociceptors and non-nociceptive fibers in response to repeated stimulation [111], and the degree of activity-dependent slowing among different types of nociceptors has been investigated [112]. Tigerholm et al. [113] have developed a model that accurately reproduces the activity-dependent slowing of the axonal propagation velocity in an effort to investigated some of the hypothesized mechanisms producing this change. Their model indicates that increasing intracellular sodium concentration is the parameter that has the greatest effect on the propagation velocity. It is considered that the function of activity-dependent slowing in

nociceptors is to limit the hyperexcitability of nociceptors, thereby reducing the chronic sensation of pain [113].

The modulation of AP propagation behavior in the axon equips both CNS and PNS neurons with the capability to modulate the flow of information in a more complex way than previously considered. The mechanisms underlying this modulation involve activity-dependent changes in the axonal morphology and the ion conductances of the membrane, and such changes can be induced by electrical or chemical stimulation. In particular, inactivation of sodium channels reduces the AP amplitude and propagation velocity [99], whereas inactivation of potassium channels broadens the AP waveform and boosts signal transmission to the postsynaptic neuron [106]. In the sensory nervous system, the activity-dependent slowing of the AP propagation velocity specifically in nociceptors has been identified [111], [112] and is considered to be linked to functionally mitigating the chronic perception of pain [113].

Appendix B

User Manual: µSpikeHunter

A manuscript on µSpikeHunter has been submitted for publication (submission reference number: NMETH-A35206). The user manual for µSpikeHunter that will be included with the publication is provided in this appendix. This user manual includes an overview of how to use the program and detailed descriptions of each of the functions presented so that they can be understood by users without a computational or programming background. It is expected that this software will expand the possibilities of neuroscience studies involving microfluidic devices by simplifying the process of incorporating electrophysiological experimentation in such studies.

µSpikeHunter: User Manual

Software for the identification and characterization of signal propagation along neuronal processes in cultures with a controlled microtopology

Kristine Heiney, Paulo de Castro Aguiar

Neuroengineering and Computational Neuroscience (NCN) Group,
i3S – Instituto de Investigação e Inovação em Saúde

Porto, Portugal

June 2018

1 Introduction

Electrophysiology constitutes an important facet of neuronal communication, and recordings of neuronal electrophysiological behavior provide great insight into the manner in which they encode and transmit information. Recently, microelectrode–microfluidic (μEF) devices [1] have seen increased use in electrophysiological experiments on neurons. Such devices are composed of a microfluidic device mounted on a microelectrode array (MEA) with the microchannels of the microfluidic device aligned with the rows of microelectrodes in the MEA, as shown in Fig. 1.1. This type of device allows for the targeted observation of action potentials (APs) traveling along axons confined to the microchannels, which are too small for somata to enter. In past studies, μEF devices have been used to characterize network dynamics [2]–[4] and observe changes to the propagation velocity [5]–[7], and compartmentalized microfluidic devices without recording electrodes have also been used to observe communication between cells from different organ systems (reviewed in [8]).

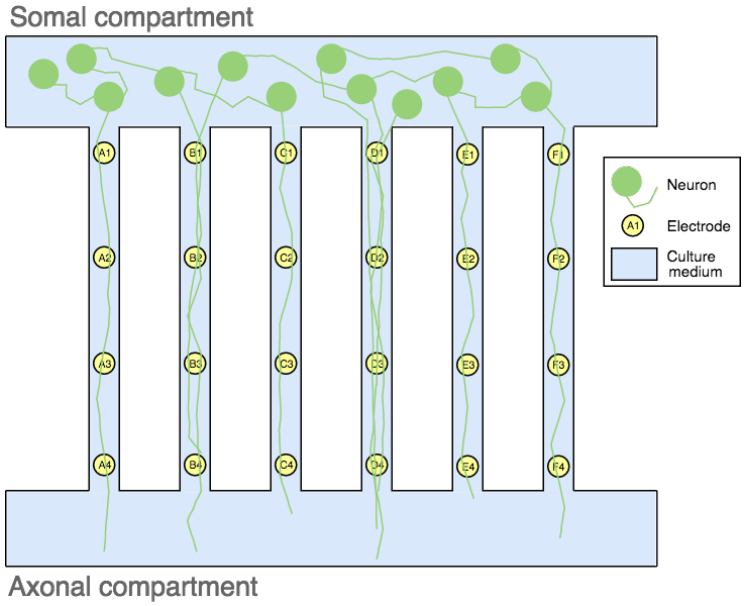

Fig. 1.1. Schematic of a μEF device with cultured neurons. The dimensions of the microchannels are such that somata are excluded but axons may grow through. The electrodes are positioned at regular intervals below the microchannels to record signals propagating along the axons confined to the microchannels.

The experimental tools necessary to obtain electrophysiological recordings using μEF devices are readily available. To complement these experimental tools, a user-friendly data analysis program called μSpikeHunter was developed for the identification and characterization of APs traveling along axons cultured in μEF devices. μSpikeHunter allows the user to readily confirm the presence of traveling waves in recorded data, determine their direction of travel, estimate their propagation velocity, and sort them into clusters based on their source.

This manual is organized as follows. A quick start guide to μSpikeHunter is first presented in Section 2, and Section 3 outlines the compatibility of μSpikeHunter with different data files. Sections 4 and 5 give a detailed explanation of how to use μSpikeHunter and describe the algorithms used in the program, and Section 6 explains how to save files with different outputs.

2 Quick start guide to µSpikeHunter

This section presents a brief explanation of how to use µSpikeHunter by guiding the user through the analysis of an example file provided in conjunction with this manual. µSpikeHunter consists of two graphical user interfaces (GUIs): the Main GUI and the Spike Sorting GUI. Diagrams of the Main and Spike Sorting GUIs are presented here, and step-by-step instructions on how to use each GUI are also provided. The remainder of the user manual will refer back to the labels and names of the objects given in the diagrams.

The example file was recorded from cortical neurons at DIV 15. The sampling rate of the recording is 50 kHz, and the duration is 1 min. Screen captures of different steps of the analysis process are shown for this example file after the step-by-step guide for each GUI.

2.1 Main GUI

2.1.1 List of objects in Main GUI

This section presents a labeled diagram of the Main GUI with brief descriptions of each labeled object in the diagram. The objects in the data selection panel are labeled in red and numbered D1–D12, and those in the analysis panel are labeled in green and numbered A1–A10. Additionally, the file saving objects are labeled in purple and numbered F1–F3.

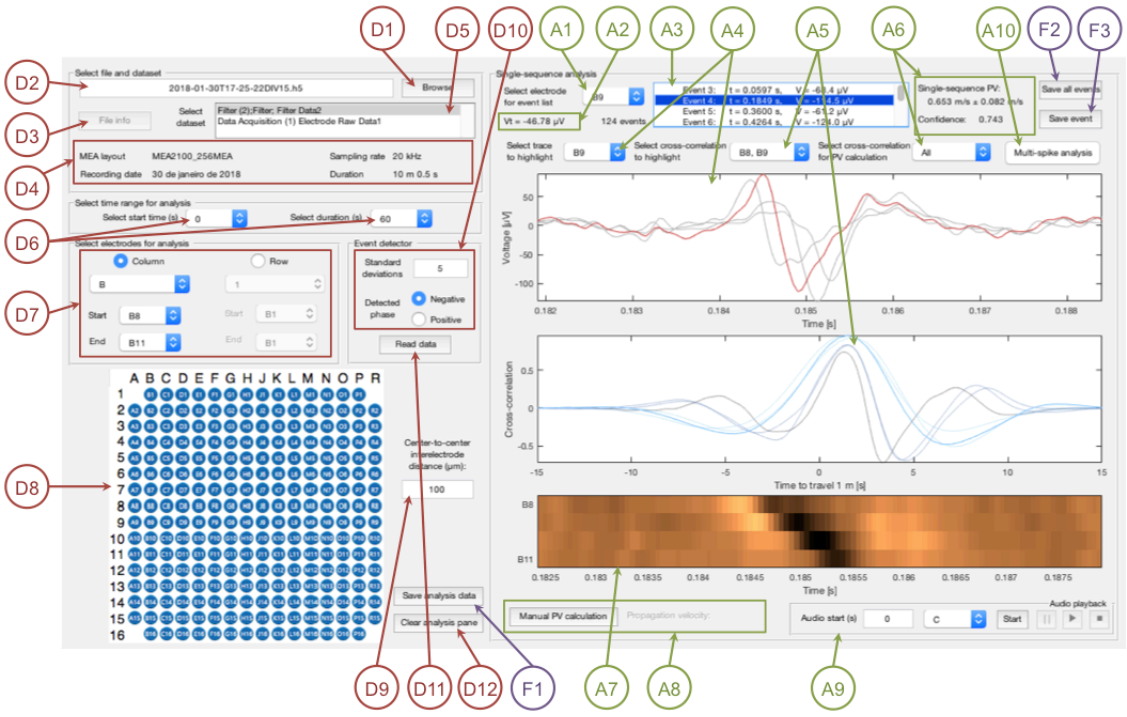

File and data selection panel

(D1) **Browse Button**: Click to select recording file (.h5, .csv, .dat, .txt)

(D2) **Filename Textbox**: Displays name of selected file

(D3) **File Information Button**: Click to display information about the file

For custom files: Displays file information in (D4)

For MCS files: Displays file information in (D4), lists recorded datasets in (D5), updates data selection lists in (D6) and (D7), and displays the electrode layout (60-, 120-, or 256-electrode layout) in (D9)

(D4) **File Information Text**: Displays MEA layout, sampling rate, and duration, along with the recording date if the file is an MCS file

(D5) **Dataset List** (MCS files only): Lists recorded datasets included in the HDF5 file

(D6) **Analysis Start Time and Duration Menus** (MCS files only): Select desired time range for analysis

(D7) **Electrode Selection Menus** (MCS files only): Select electrodes in a single row or column of the MEA for analysis

(D8) **MEA Layout Image**: Displays the MEA layout for MCS files or a MEA photograph for custom files

(D9) **Inter-Electrode Spacing Textbox**: Input the center-to-center inter-electrode distance in micrometers (default value of 100 or automatically determined for certain MCS files)

(D10) **Event Detector Parameters**: Input the number of standard deviations of the signal noise to be used as the event detector threshold and select positive or negative phase for detection

(D11) **Read Button**: Click to read the data, apply event detection, and populate the analysis pane with the results

(D12) **Clear Button**: Click to clear the analysis panel

Analysis panel

(A1) **Event Electrode Menu**: Select the electrode used to populate the Event List (A3)

(A2) **Threshold Text**: Displays the threshold used for event detection on the selected event electrode

(A3) **Event List**: Lists the events on the event electrode for each detected propagation sequence; select an event from this list for single-sequence analysis

(A4) **Voltage Trace Plot and Highlight Menu**: Plots the voltage data for all electrodes around the event selected in the event list; the electrode selected in the highlight menu is plotted in red with all other electrodes plotted in gray

(A5) **Cross-Correlation Plot and Highlight Menu**: Plots cross-correlations between all pairs of electrodes with the plots colored according to the distance between the electrode pair; the electrode pair selected in the highlight menu is plotted with full opacity with all others plotted with 35% opacity

(A6) **Single-Sequence Propagation Velocity Text and Menu**: Displays the SPV along with the confidence index for the selected event based on the electrode pair(s) selected in the drop-down menu

(A7) **Kymograph**: Displays a kymograph for the selected event

(A8) **Kymograph Propagation Velocity Tools**: Allows the user to manually estimate the propagation velocity based on a line drawn on the kymograph

(A9) **Audio Playback**: Allows the user to play an audio representation of the recorded data with 500× time dilation

(A10) **Multi-Spike Analysis Button**: Opens the Spike Sorting GUI

Saving files

(F1) **Save Analysis Data Button**: Saves all analyzed voltage and time data to a CSV file

(F2) **Save All Events Button**: Saves the times and amplitudes of the spikes on each of the electrodes for all detected propagation sequences to a CSV file

(F3) **Save Event Button**: Saves voltage and time data corresponding to the voltage trace plot in (A4) to a CSV file

2.1.2 Main GUI: Step-by-step guide

***File and data selection panel:** Custom setup files*

1. Click the Browse Button (D1) and select a data file for analysis.
2. Click the File Information Button (D3).
3. Define the inter-electrode distance in the Inter-Electrode Spacing Textbox (D9).
4. Define the number of standard deviations for the detection threshold and positive or negative phase detection in the Event Detector Parameters (D10).
5. Click the Read Button (D11).

***File and data selection panel:** MCS files*

1. Click the Browse Button (D1) and select a data file for analysis.
2. Click the File Information Button (D3).
3. Select the data stream for analysis in the Dataset List (D5).
4. Select the time range for analysis in the Analysis Start Time and Duration Menus (D6).
5. Select the desired electrode range in the Electrode Selection Menus (D7).
6. Define the inter-electrode distance in the Inter-Electrode Spacing Textbox (D9).
7. Define the number of standard deviations for the detection threshold and positive or negative phase detection in the Event Detector Parameters (D10).
8. Click the Read Button (D11).

Analysis panel

General analysis

1. Select the event electrode from the Event Electrode Menu (A1).
2. Select the event for analysis from the Event List (A3).
3. Select the voltage trace and/or cross-correlation plot to highlight from the Voltage Trace Highlight Menu (A4) and the Cross-Correlation Highlight Menu (A5).

Manual propagation velocity estimation

1. Click the “Manual PV calculation” button in the Kymograph Propagation Velocity Tools (A8).
2. Draw a line as instructed in Section 4.3.4 and adjust the ends as needed.
3. Once the line is finalized, double click to see the manual propagation velocity estimate.

Audio playback

1. Define the desired start time in the textbox in the Audio Playback (A9).
2. Select the desired chord from the drop-down menu.
3. Click the “Start” button.
4. The playback may be paused, resumed, and stopped by clicking the corresponding buttons in the Audio Playback (A9).

Open Spike Sorting GUI

1. Click the Multi-Spike Analysis Button (A10).
2. See Section 2.2.2 for a step-by-step guide on how to use the Spike Sorting GUI.

Save files

1. Click the Save All Events Button (F2) to save a CSV file with all the voltage data for each of the selected electrodes along with the corresponding time stamps.
2. Click the Save Event Button (F3) to save a CSV file with the voltage data for the event currently selected in the Event List (A3) along with the corresponding time stamps.

File and data selection panel: MCS files

Opening screen

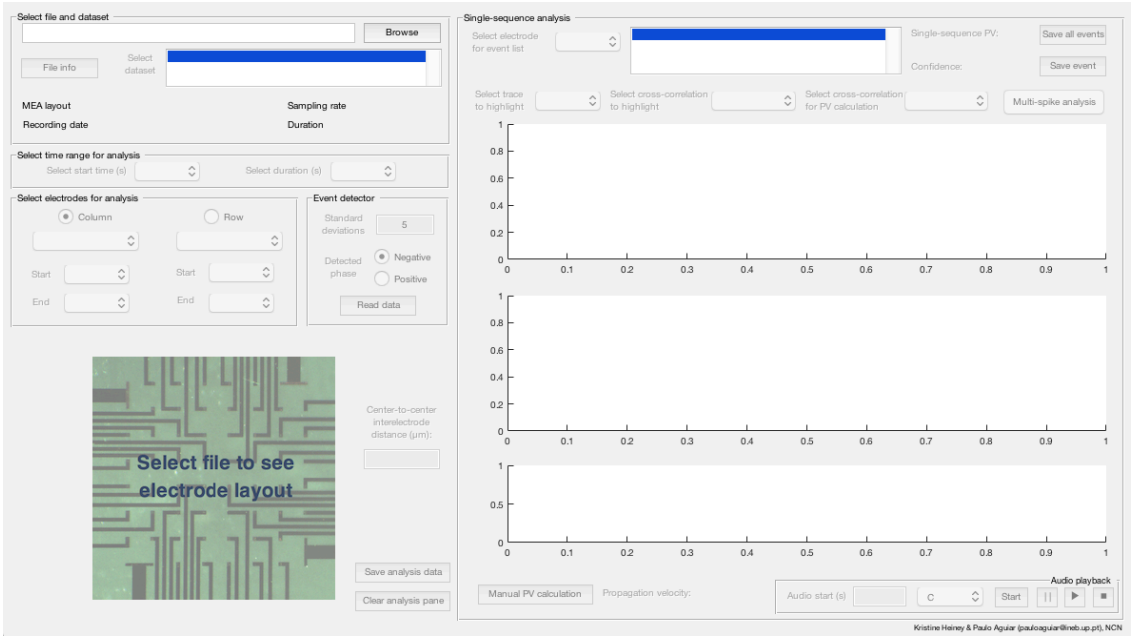

Select the example file for analysis

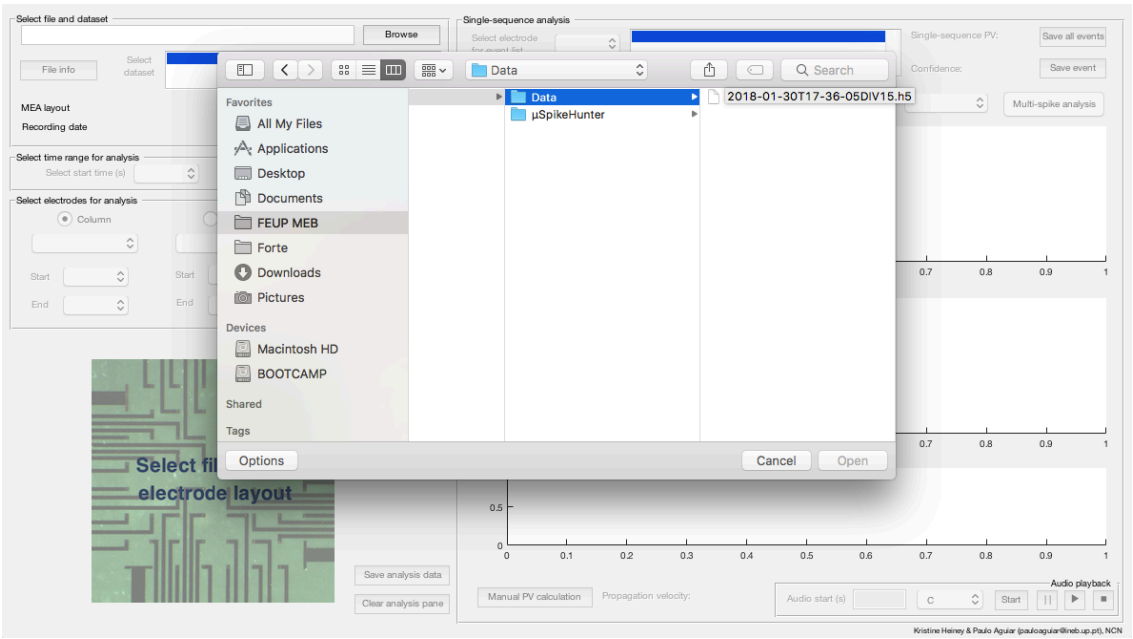

Click the File Information Button (D3)

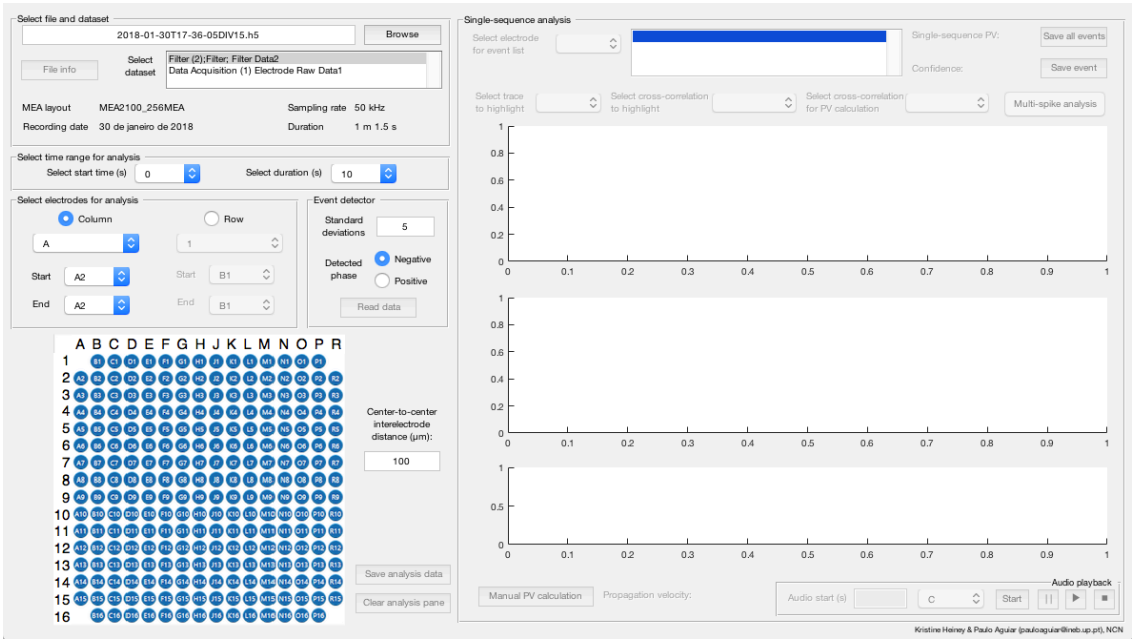

Select the data parameters as shown below

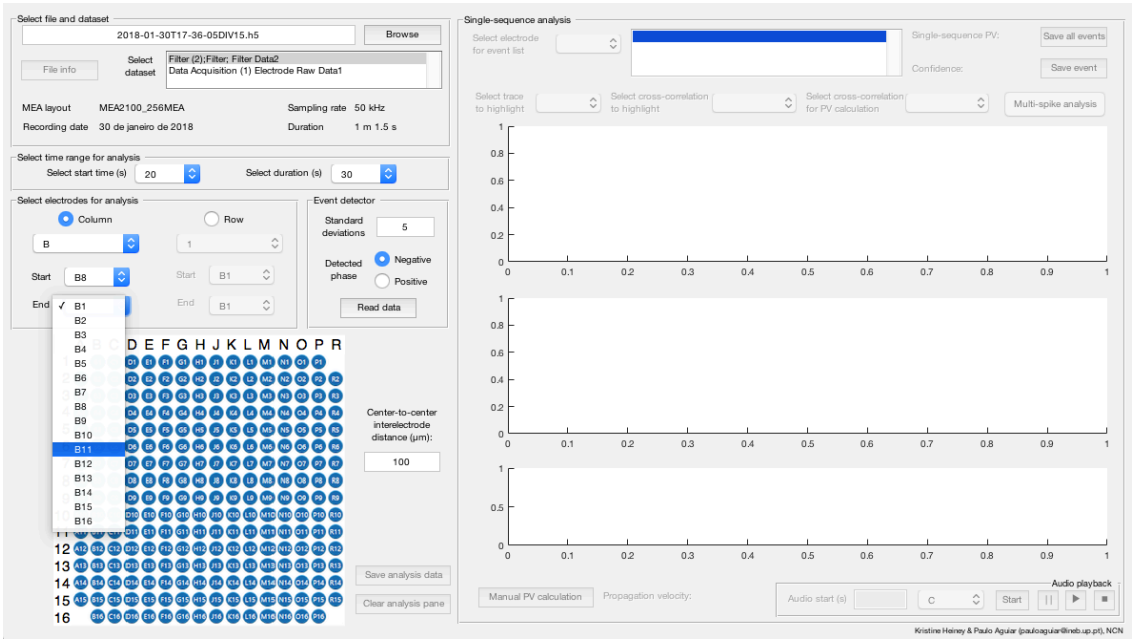

Click the Read Button (D11)

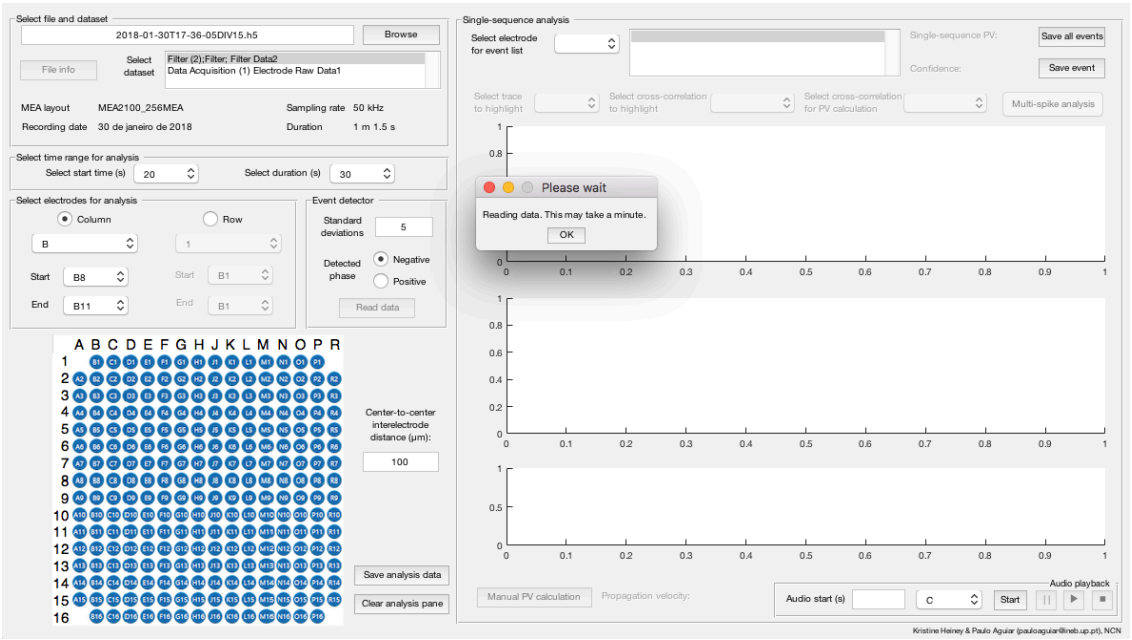

Analysis panel

General analysis

The plots and SPV estimates can be viewed for any event selected from the Event List (A3)

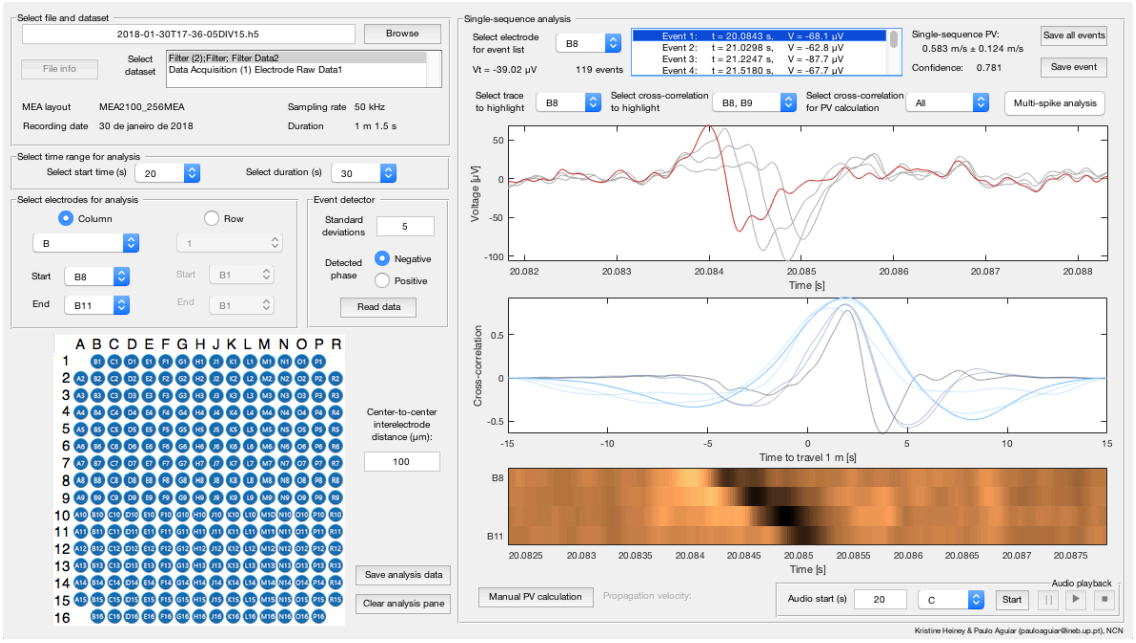

Manual propagation velocity estimation

The line for the manual propagation velocity estimate should be drawn as shown below

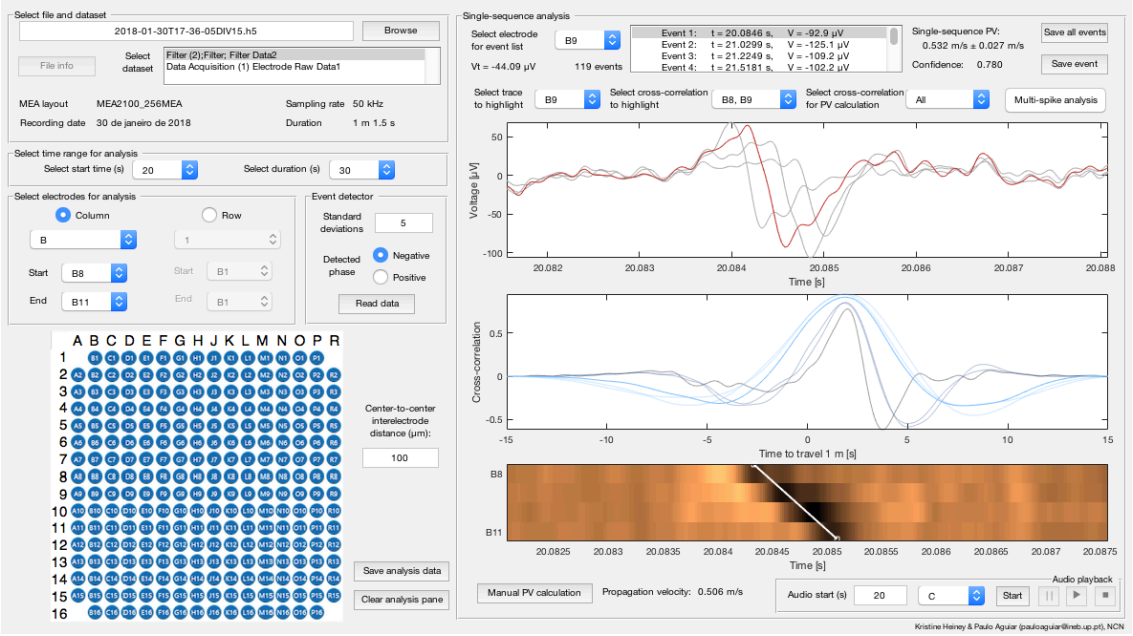

Audio playback

Set the start time and select the desired chord in the Audio Playback (A9)

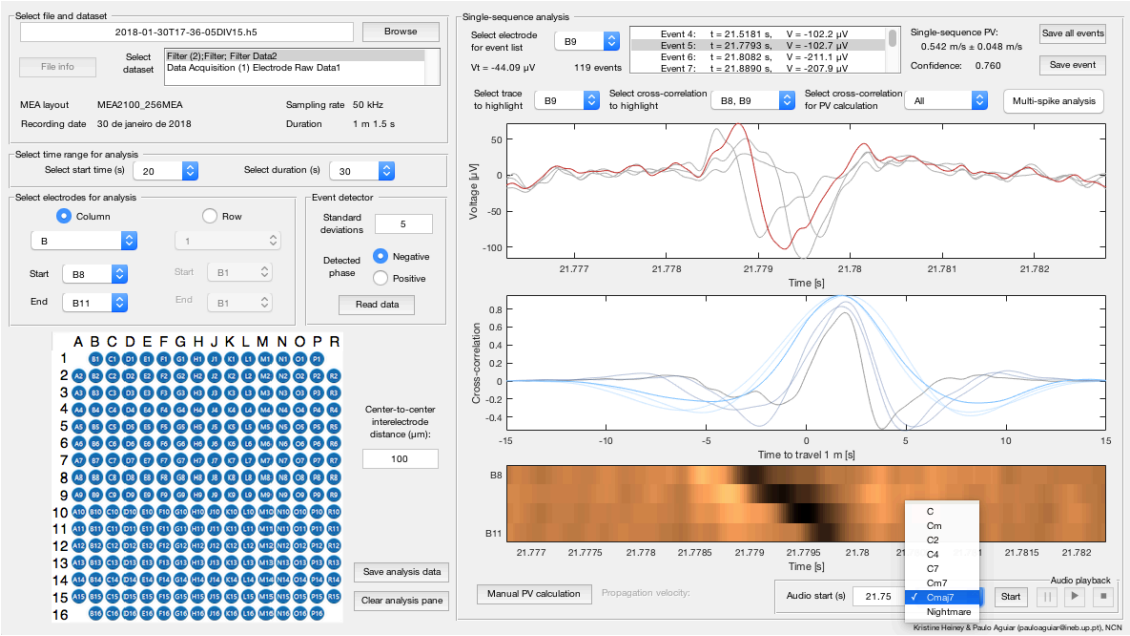

Click the “Start” button to start the audio playback and pause, resume, and stop the playback as desired

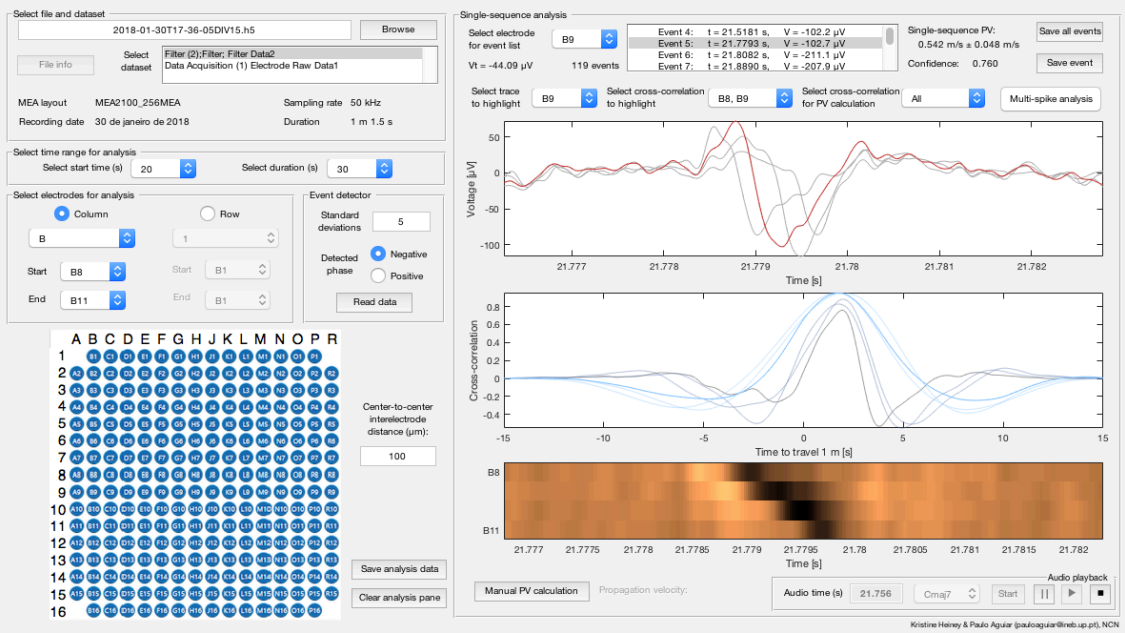

2.2 Spike Sorting GUI

2.2.1 List of objects in Spike Sorting GUI

This section presents a labeled diagram of the Spike Sorting GUI with brief descriptions of each labeled object. The objects in the Spike Sorting are labeled in orange and numbered S1–S7, and the file saving object is labeled in purple and numbered F4.

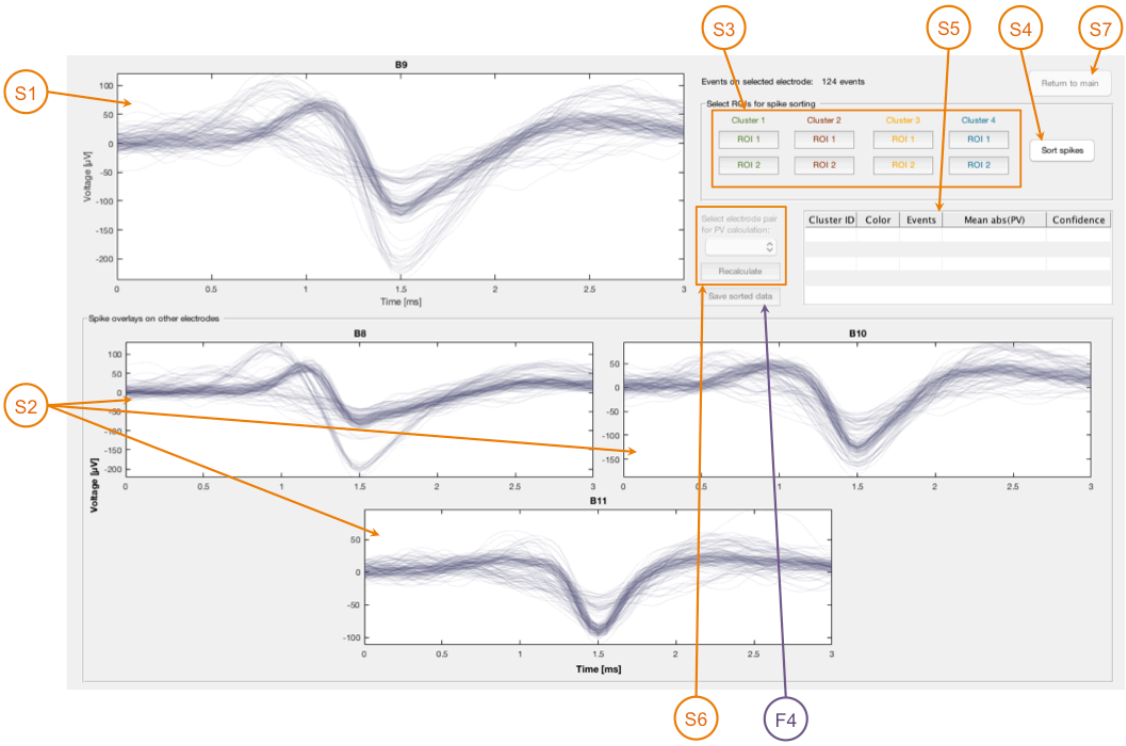

Spike Sorting GUI

(S1) **Event Electrode Spike Overlay Plot**: Shows a plot of all the events on the event electrode detected as part of propagation sequences aligned based on their minima

(S2) **Other Electrode Spike Overlay Plots**: Show plots of events corresponding to the events detected on the event electrode on each of the other electrodes

(S3) **ROI Definition Tools**: Allow the user to draw one or two ROIs for up to four clusters to sort the plotted events

(S4) **Sort Spikes Button**: Sorts the events into source clusters based on the defined ROIs and outputs the results into the Sorting Results Table

(S5) **Sorting Results Table**: Displays the results of the spike sorting, including the cluster ID, plotting color, number of events, and mean propagation speed for each cluster

(S6) **Cluster Propagation Velocity Electrode Selection**: Allows the user to select the electrode pair for calculating the CPV

(S7) **Return to Main GUI Button**: Sends cluster IDs and CPV estimates back to the Event List (A3) in the Main GUI

Saving files

(F4) **Save Sorted Data Button**: Saves a CSV file per source cluster with the spike times on each electrode, the CPV, the SPV, and the CPV and SPV confidence indices

2.2.2 Spike Sorting GUI: Step-by-step guide

Define ROIs

1. Click on any of the ROI buttons in the ROI Definition Tools (S3).
2. Draw a rectangular ROI by clicking and dragging on the Event Electrode Spike Overlay Plot (S1).
3. Adjust the bounds of the ROI by clicking and dragging on any of the edges or corners of the ROI.
4. Repeat for as many clusters as desired with up to two ROIs defining the conditions for each of the clusters. The ROIs can be defined in any order and for any number of clusters.
5. To delete an ROI, right click on the ROI and select “Delete” from the menu.
6. If an ROI has already been drawn and the corresponding button for that ROI is clicked again, the ROI is deleted and a new version of it can be drawn.

Sort spikes and display results

1. Click the Sort Spikes Button (S4).
2. To use electrodes other than the most distant pair for CPV calculation, select the desired electrode pair from the Cluster Propagation Velocity Electrode Selection (S6) and click the “Recalculate” button.

Return spike sorting results to Main GUI

1. Click the Return to Main GUI Button (S7).
2. View the sorting and CPV estimation results in the Event List (A3) in the Main GUI.

Save sorting results

1. Click the Save Sorted Data Button (F4) to save a CSV file for each source cluster with information about each propagation sequence in that cluster: the spike times on each electrode, the CPV estimate for the sequence, the SPV estimate for the sequence, and the confidence indices for the two propagation velocity estimates.

Spike Sorting GUI

In the example presented below, B9 was selected as the event electrode in the Event Electrode Selection Menu (A1) in the Main GUI. Open the Spike Sorting GUI from the Main GUI by clicking the Multi-Spike Analysis Button (A10).

Define ROIs

Draw ROIs on the Event Electrode Spike Overlay Plot (S1) as shown below using the ROI Definition Tools (S3)

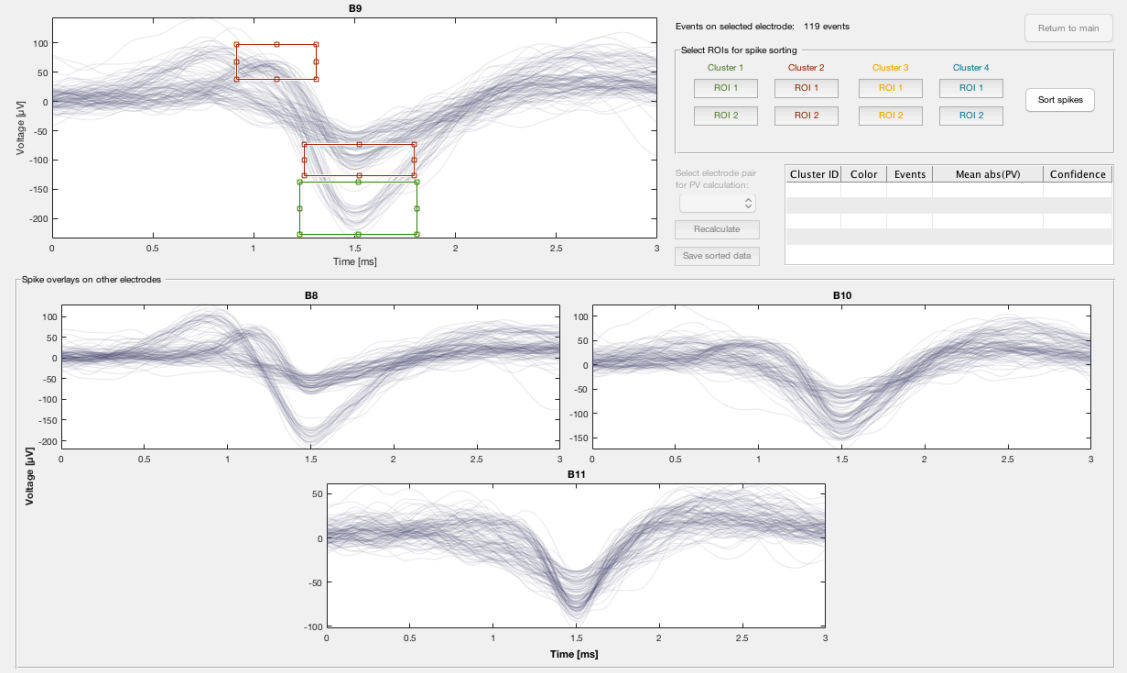

Sort spikes and display results

Click the Sort Spikes Button (S4)

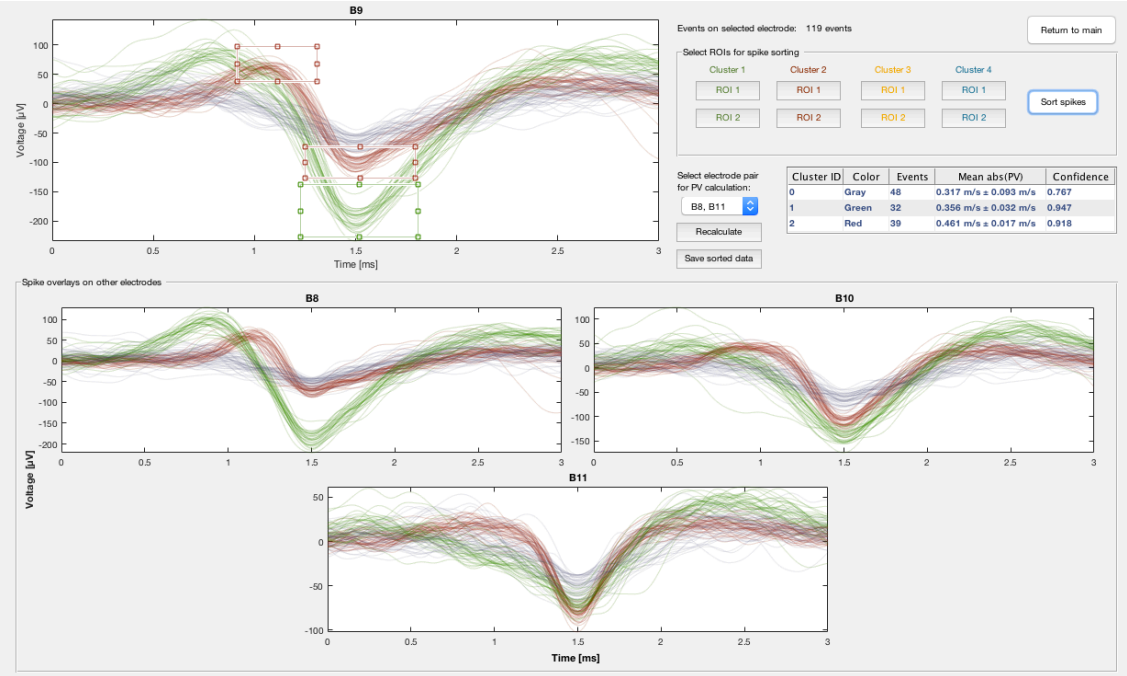

Return spike sorting results to Main GUI

Click the Return to Main GUI Button (S7) to see the Event List (A3) updated with the cluster ID and CPV estimate for each spike

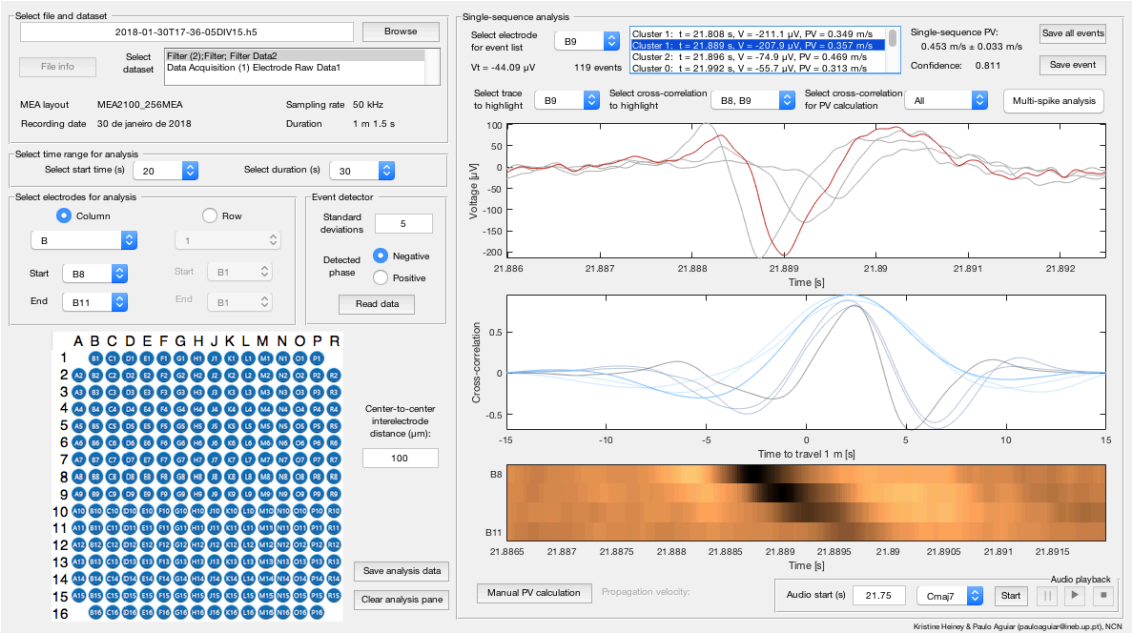

3 Data compatibility

µSpikeHunter is compatible with recordings obtained using both custom µEF setups and the commercial MCS MEA2100 systems (Multi Channel Systems GmbH, Reutlingen, Germany). This section provides guidance on how to format custom files to be read by µSpikeHunter and which MCS recording systems can be used in conjunction with µSpikeHunter.

It should be noted that µSpikeHunter does not contain any data filtering tools. Thus, it is recommended that the user filter the data prior to importing it for analysis in µSpikeHunter. The example data shown in this manual have been filtered with a low-pass Butterworth filter with a cutoff frequency of 4 kHz followed by a high-pass Butterworth filter with a cutoff frequency of 300 Hz. Filtering was performed using the MCS recording software Multi Channel Experimenter. Additionally, it is recommended that a sampling frequency of at least 10 kHz be used when taking recordings.

3.1 Custom setup recording files

The user may load data in CSV format from recordings obtained using a custom recording setup. This data should be formatted in columns with the first column corresponding to the time in milliseconds and all subsequent columns corresponding to the recorded voltages in microvolts for each electrode to be analyzed, progressing from one electrode to the next inside a single microchannel of the µEF device. An example of the organization that should be used is shown in Fig. 3.1. This example shows 1 ms of recorded data on four electrodes. µSpikeHunter can handle data from up to 16 electrodes with a uniform inter-electrode spacing.

	Time (ms)	A1 (µV)	A2 (µV)	A3 (µV)	A4 (µV)
	1	2	3	4	5
1	0	4.7700	4.3200	5.6800	8.6400
2	0.0500	14.7700	16.2500	19.8900	27.7300
3	0.1000	18.0700	26.0200	30.2300	36.9300
4	0.1500	11.7000	27.3900	27.9500	31.2500
5	0.2000	5.6800	23.0700	16.9300	23.1800
6	0.2500	6.0200	14.6600	7.3900	17.6100
7	0.3000	9.0900	5.9100	5	14.2000
8	0.3500	10.4500	3.8600	5.4500	12.2700
9	0.4000	10.4500	6.4800	3.3000	10.5700
10	0.4500	10.8000	6.3600	0.2300	8.4100
11	0.5000	10.5700	4.6600	2.0500	5.1100
12	0.5500	7.5000	6.1400	7.6100	1.1400
13	0.6000	2.3900	10.2300	9.5500	-1.3600
14	0.6500	-0.4500	12.6100	6.7000	-2.3900
15	0.7000	-0.6800	10.4500	4.0900	-5.9100
16	0.7500	-2.5000	7.1600	2.5000	-12.5000
17	0.8000	-3.9800	4.7700	0.6800	-17.5000
18	0.8500	-3.7500	-0.4500	-1.3600	-15.9100
19	0.9000	-2.7300	-7.9500	-2.9500	-9.6600
20	0.9500	-4.3200	-10.4500	-3.6400	-4.5500
21	1	-10.2300	-6.5900	-5.1100	-3.4100

Fig. 3.1. Data recorded on four electrodes formatted for analysis in µSpikeHunter. The time values are given in milliseconds, and the voltages are given in microvolts. The columns are labeled to correspond to the electrodes in one of the microchannels in the example µEF configuration shown in Fig. 1.1.

It is suggested that the second column correspond to the electrode at the most proximal end of the microchannel and the final column to that at the most distal end; this will yield results in the GUI with forward propagation corresponding to propagation from the soma to the axon terminal. If the example data in Fig. 3.1 correspond to the third microchannel from the left in the example setup shown in Fig. 1.1, this would mean that columns 2–5 in the CSV file represent data from electrodes C1–C4, respectively.

3.2 Multi Channel Systems recording files

µSpikeHunter is compatible with HDF5 files generated from MCS recordings obtained using the MCS MEA2100-60-System, MEA2100-120-System, and MEA2100-256-System, which can be used in conjunction with 60-, 120-, and 256-electrode MEAs produced by MCS. Once recordings have been obtained using the MCS recording software Multi Channel Experimenter, they can be converted to HDF5 files using the MCS data handling software Multi Channel DataManager. Users are directed to the MCS documentation on the corresponding equipment and software for instructions on data recording and conversion.

4 Main GUI

This section presents the capabilities of the Main GUI of µSpikeHunter. This GUI allows the user to select the data for analysis and analyze the data at the single-propagation-sequence level. The Main GUI consists of two panels: the file and data selection panel and the analysis panel. The functionality of each item in the two panels, except for the buttons to save files, is described in this section.

4.1 List of objects in Main GUI

This section shows again the labeled diagram of the Main GUI with brief descriptions of each labeled object in the diagram. The objects in the data selection panel are labeled in red and numbered D1–D12, and those in the analysis panel are labeled in green and numbered A1–A10. Additionally, the file saving objects are labeled in purple and numbered F1–F3.

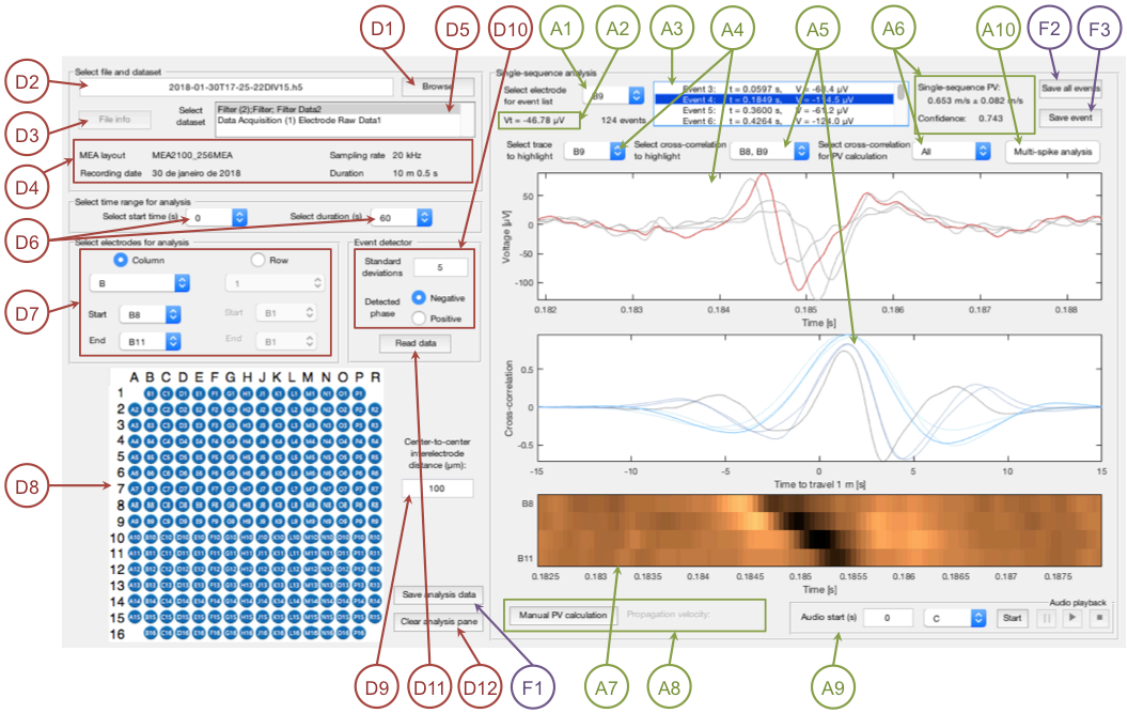

File and data selection panel

(D1) **Browse Button**: Click to select recording file (.h5, .csv, .dat, .txt)

(D2) **Filename Textbox**: Displays name of selected file

(D3) **File Information Button**: Click to display information about the file

For custom files: Displays file information in (D4)

For MCS files: Displays file information in (D4), lists recorded datasets in (D5), updates data selection lists in (D6) and (D7), and displays the electrode layout (60-, 120-, or 256-electrode layout) in (D9)

(D4) **File Information Text**: Displays MEA layout, sampling rate, and duration, along with the recording date if the file is an MCS file

(D5) **Dataset List** (MCS files only): Lists recorded datasets included in the HDF5 file

(D6) **Analysis Start Time and Duration Menus** (MCS files only): Select desired time range for analysis

(D7) **Electrode Selection Menus** (MCS files only): Select electrodes in a single row or column of the MEA for analysis

(D8) **MEA Layout Image**: Displays the MEA layout for MCS files or a MEA photograph for custom files

(D9) **Inter-Electrode Spacing Textbox**: Input the center-to-center inter-electrode distance in micrometers (default value of 100 or automatically determined for certain MCS files)

(D10) **Event Detector Parameters**: Input the number of standard deviations of the signal noise to be used as the event detector threshold and select positive or negative phase for detection

(D11) **Read Button**: Click to read the data, apply event detection, and populate the analysis pane with the results

(D12) **Clear Button**: Click to clear the analysis panel

Analysis panel

(A1) **Event Electrode Menu**: Select the electrode used to populate the Event List (A3)

(A2) **Threshold Text**: Displays the threshold used for event detection on the selected event electrode

(A3) **Event List**: Lists the events on the event electrode for each detected propagation sequence; select an event from this list for single-sequence analysis

(A4) **Voltage Trace Plot and Highlight Menu**: Plots the voltage data for all electrodes around the event selected in the event list; the electrode selected in the highlight menu is plotted in red with all other electrodes plotted in gray

(A5) **Cross-Correlation Plot and Highlight Menu**: Plots cross-correlations between all pairs of electrodes with the plots colored according to the distance between the electrode pair; the electrode pair selected in the highlight menu is plotted with full opacity with all others plotted with 35% opacity

(A6) **Single-Sequence Propagation Velocity Text and Menu**: Displays the SPV along with the confidence index for the selected event based on the electrode pair(s) selected in the drop-down menu

(A7) **Kymograph**: Displays a kymograph for the selected event

(A8) **Kymograph Propagation Velocity Tools**: Allows the user to manually estimate the propagation velocity based on a line drawn on the kymograph

(A9) **Audio Playback**: Allows the user to play an audio representation of the recorded data with 500× time dilation

(A10) **Multi-Spike Analysis Button**: Opens the Spike Sorting GUI

Saving files

(F1) **Save Analysis Data Button**: Saves all analyzed voltage and time data to a CSV file

(F2) **Save All Events Button**: Saves the times and amplitudes of the spikes on each of the electrodes for all detected propagation sequences to a CSV file

(F3) **Save Event Button**: Saves voltage and time data corresponding to the voltage trace plot in (A4) to a CSV file

4.2 File and data selection panel

The file and data selection panel allows the user to select the file containing the recording data; set the event detection parameters; define the inter-electrode distance; and, in the case of MCS files, select the desired electrodes and timespan for analysis. Once all these parameters have been set, the user may then send the data to the analysis pane. This section describes this procedure for both custom setup recording files and MCS recording files.

***Note**: Changing any parameters in the data selection panel will automatically clear the analysis panel.*

4.2.1 Data selection

This section describes the process of selecting the data to be analyzed in the case where custom and MCS setups are used for recording.

4.2.1.1 Selection of custom setup recording files

If a custom recording setup is used, the user may import a CSV file containing the data for up to 16 electrodes contained within a single microchannel of the µEF device. µSpikeHunter supports files with file extensions of .csv, .dat, and .txt. The data should be formatted as described in Section 3.1. As stated in Section 3, µSpikeHunter does not contain any filtering tools, and imported data should thus be filtered prior to analysis in this program.

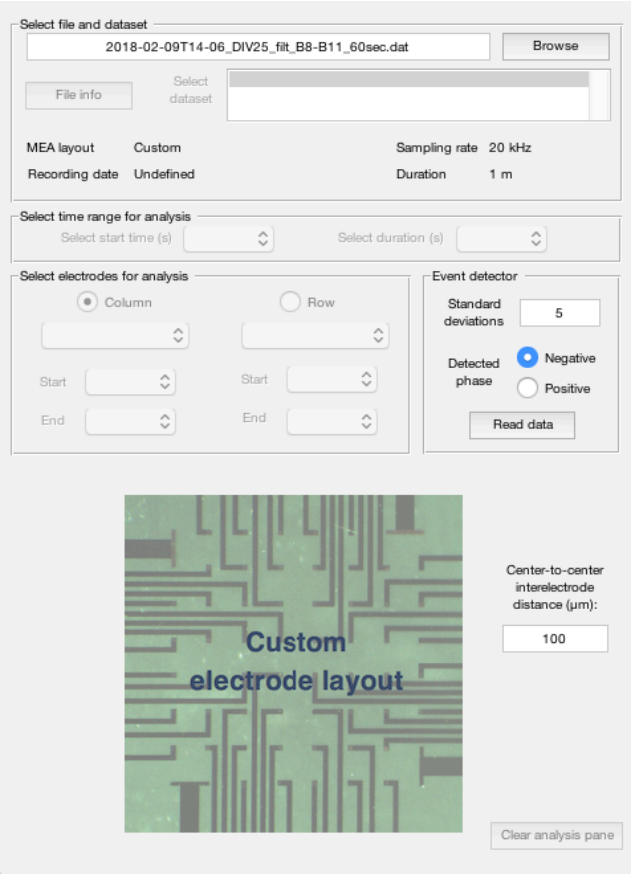

Fig. 4.1. Appearance of the file and data selection panel when a custom setup recording file is selected for analysis.

The desired file can be selected by clicking the Browse Button (D1) and navigating to the file in the file selection window. Once the data file has been selected, the filename will appear in the Filename Textbox (D2). Clicking the File Info Button (D3) will then list the sampling rate and the recording duration for the data contained in the file in the File Information Text (D4).

Before analysis, the user must input the inter-electrode distance into the Inter-Electrode Spacing Textbox (D9). Figure 4.1 shows an example of the appearance of the file and data selection panel when a custom setup recording file has been selected for analysis.

4.2.1.2 Selection of Multi Channel Systems recording files

µSpikeHunter is compatible with data files recorded using Multi Channel Experimenter in conjunction with MCS MEA2100-Systems with 60-, 120-, or 256-electrode MEAs and converted to HDF5 files using Multi Channel DataManager, as described in Section 3.2. Users are directed to the MCS documentation on the corresponding equipment and software for instructions on data recording and conversion. As stated in Section 3, µSpikeHunter does not contain any filtering tools, and imported data should thus be filtered prior to analysis in this program. Multi Channel Experimenter and Multi Channel Analyzer both provide the ability to filter raw data recorded using the MCS MEA2100-Systems.

Once the recording file has been selected, clicking the File Info Button (D3) will then list the sampling rate and the recording duration for the data contained in the file as well as the MEA system used for the recording and the recording date in the File Information Text (D4). A list of data streams (e.g., raw data, filtered data) is also provided in the Dataset List (D5). It is recommended that the user select the filtered data stream for analysis.

4.2.1.3 Selection of Multi Channel Systems data for analysis

Clicking the File Info Button (D3) also populates the data selection menus, which enable a limited set of recorded data to be selected for analysis. Data recorded using MEAs with a large number of electrodes can be cumbersome to handle, and this selection capability allows the user to control the amount of data for analysis to prevent overly long computation times. The start time and duration and duration of the data for analysis can be defined in the Analysis Start Time and Duration Menus (D6). The start times can be selected in increments of 10 s, and the analysis duration may range from 10 s to 10 min.

Beneath the Analysis Start Time and Duration Menus (D6), the user may select the range of electrodes for analysis in the Electrode Selection Menus (D7). The electrode layout for the selected file is shown in the MEA Layout Image (D8) to provide the user with visual feedback regarding the electrode positioning. The inter-electrode spacing in micrometers must then be provided in the Inter-Electrode Spacing Textbox (D9). The default value for the inter-electrode spacing is 100 µm. For some MCS recordings, this

value is able to be automatically detected; however, the user should always check to ensure this value is correct.

Because μSpikeHunter is intended for use with μEF devices or other similar recording setups with structured topologies, the electrodes to be selected for analysis in the Electrode Selection Menus (D7) must be within a single row or column of electrodes in the MEA. These selected electrodes should correspond to the electrodes positioned beneath a single microchannel of the μEF device.

In the example shown in Fig. 1.1, the user would select the “Column” radio button and could then select any of the column names for analysis; for example, column A could be selected to analyze the electrodes in the leftmost microchannel. It is suggested that the start electrode be at the most entrance of the microchannel most proximal to the somal compartment and the end electrode the most distal. In this case, A1 would then be the start electrode and A4 the end electrode. This selection choice yields results in the GUI with forward propagation corresponding to propagation from the soma to the axon terminal.

4.2.2 Event detection and sending data to the analysis panel

Before sending the data to the analysis panel, the Event Detector Parameters (D11) must be set. The number of standard deviations used to define the detection threshold is input into the textbox, and the detected phase is set using the radio buttons.

The event detector uses a two-step process to determine the threshold for event detection. First, outliers are eliminated by excluding any data points that are more than three scaled median absolute deviations from the median of the recorded signal. The remaining data points in the selected time range (Analysis Start Time and Duration Menus (D6)) are considered to represent the signal noise. With the outliers excluded, the median and standard deviation of the signal are then obtained. The detection threshold is defined as the given number of standard deviations above or below the median for this second calculation. During analysis, the detection threshold for the event electrode can be found in the Detection Threshold Text (A2).

Clicking the Read Button (D11) applies the event detector to one of the electrodes selected for analysis in the Electrode Selection Menus (D7) and obtains the times for each of the events on that electrode. The detection thresholds are also calculated for each of the other electrodes. A detected event is considered to be part of a propagation sequence if three criteria are met, as described below.

First, event detection is applied to the other electrodes, but only within a specific temporal search window. The search window on each electrode is defined for each of the detected events based on the distance to the electrode on which event detection is applied. This search window is defined to correspond to an AP traveling at a minimum propagation velocity of ±0.1 m/s. For example, for three electrodes with an inter-electrode distance of 100 μm, the maximum time delay between spikes recorded on

the first and second or second and third electrodes would be 1 ms, and that between spikes on the first and third electrodes would be 2 ms. The first criterion is met for a given event if there are events on every other electrode within the as-defined search window.

Second, to deal with cases in which instrument noise produces simultaneous or near-simultaneous peaks on all electrodes, the times of the events on the most distant electrodes in the range of electrodes selected for analysis are compared. The second criterion is met when the lag between these two event times corresponds to a propagation velocity that is below 100 m/s.

Third, to ensure the propagation direction is consistent throughout the propagation sequence, the Kendall rank coefficient of the electrode number and the spike arrival time on each electrode is obtained. The third criterion is met when the Kendall coefficient is at least 0.8.

Once all of the propagation sequences have been obtained, the results are sent to the data analysis panel for visualization and analysis. The analysis panel can be cleared by clicking the Clear Button (D12).

4.3 Analysis panel

The analysis panel of the Main GUI allows the user to select an event from the list of detected events on the selected event electrode and view and interact with a number of analysis tools for the propagation sequence corresponding to that event, including voltage traces, inter-electrode cross-correlations, a kymograph, and an audio playback tool. This section describes the information presented in each of the analysis objects in the analysis panel and how to use each object. This section refers back to the labels given in the diagram on page 12, and a separate image of the analysis panel is shown in Fig. 4.2 to show a detailed view of this panel.

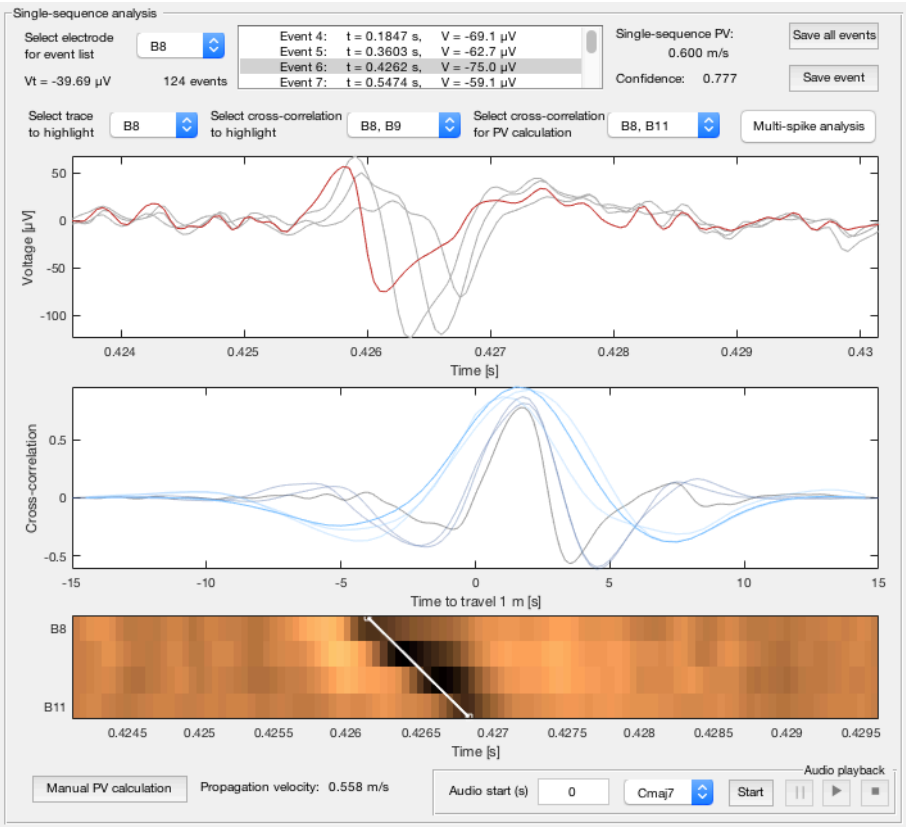

Fig. 4.2. Analysis panel of Main GUI. See the diagram on page 12 for names and labels of analysis objects.

This analysis panel allows data analysis on the single-sequence level. To perform multi-sequence analysis, the user may click the Multi-Spike Analysis Button (A10), which opens the Spike Sorting GUI in a separate window. For a description of the capabilities of the Spike Sorting GUI and instructions on how to use it, see Section 5.

4.3.1 Event list

The Event List (A3) lists all events on the event electrode that are part of detected propagation sequences. The event electrode can be set by selecting the desired electrode from the Event Electrode Menu (A1). The detection threshold for the event electrode is displayed in the Threshold Text (A2), and the total number of propagation sequences is also listed below the Event Electrode Menu (A1). Each event in the Event List (A3) gives the event number, the time at which the peak voltage occurs, and the peak voltage value. Selecting an event from this list allows the user to perform

single-sequence analysis on the propagation sequence corresponding to the selected event.

4.3.2 Voltage traces

The Voltage Trace Plot (A4) shows a plot of the voltage traces on all electrodes within a time window defined based on the time of the selected event in the Event List (A3). All plots are shown in gray except for the trace selected in the Voltage Trace Highlight Menu (A4), which is highlighted in red. From this plot, the user is often able to visually determine whether the propagation sequence shows anterograde or retrograde propagation.

4.3.3 Cross-correlation plots and single-sequence propagation velocity

The Cross-Correlation Plot (A5) shows plots of inter-electrode cross-correlations for all possible electrode pairs for the selected electrodes. The plots are colored according to the distance between the electrode pair, with the lightest color corresponding to the closest pairs (neighboring electrodes) and the darkest to the most distant pair (the start and end electrodes defined in the Electrode Selection Menus (D7)). The electrode pair selected in the Cross-Correlation Highlight Menu (A5) is plotted with full opacity, and all other cross-correlations are plotted with 35% opacity.

The cross-correlation values are normalized so that all autocorrelations take a unit value at zero lag. The lag timescale of the cross-correlation is also normalized with respect to the distance between the electrodes for which the cross-correlation is being performed; the normalized lags thus correspond to the time in seconds it would take an event to travel 1 m. This means that the horizontal axis of the cross-correlation is equivalent to the inverse of the propagation velocity of a spike for each plotted time lag; thus, under the assumption that the propagation velocity is constant across all electrodes, the peaks of all cross-correlations should be aligned.

The single-sequence propagation velocity (SPV) is displayed in the Single-sequence Propagation Velocity Text (A6) along with the confidence index for the estimate. By default, the SPV is calculated as the average propagation velocity obtained for each electrode pair, which is calculated by determining the time at which each cross-correlation achieves a maximum value and calculating the speed from this time and the distance between the two electrodes. The SPV is presented along with the standard deviation of the velocities obtained with the different electrode pairs. The confidence index is the peak value of the autocorrelation-normalized cross-correlation with the lowest peak among all of the electrode pairs. In the case of the propagation sequence shown in Fig. 4.2, this value is the peak value of the black curve, which is the cross-correlation between the two most distant electrodes (B8 and B11). However, when one of the cross-correlations takes a peak at time zero, this causes the average over all the electrode pairs to be indeterminate. Therefore, the user can select the desired electrode pair from the Single-sequence Propagation Velocity Menu (A6).

The user should consider the following two factors when selecting which SPV estimate to use. First, the propagation velocities calculated for each electrode pair have different resolutions because of the different distances between electrode pairs, and this is not taken into consideration when the average SPV estimate is used. That is, the estimate for each pair is simply averaged without any weighting based on the error due to discretization. Second, the confidence index presented for each estimate is an indication only of the cross-correlation, i.e., the degree of similarity between the signals detected on the two selected electrodes. This means that the confidence index does not in any way represent the error due to discretization.

4.3.4 Kymograph

A kymograph is a single-image representation of a dynamic process. The Kymograph (A7) in the Main GUI shows the voltage signals for the selected electrodes, with the horizontal axis of the kymograph in this GUI representing the recording time and each row of pixels representing a single electrode. The top row represents the start (most proximal) electrode in in the Electrode Selection Menus (D7), and the bottom row represents the end (most distal) electrode.

The intensity of each pixel corresponds to the value of the voltage signal at each sampling point. The recorded voltages on all of the electrodes shown in the plotting window are rescaled so that all values lie in the range of [0, 1], and these values are translated into pixel intensities in the color map. Thus, when an AP propagates along an axon near a given electrode, the kymograph typically shows the characteristic triphasic extracellular spike as a sequence of pixels that are first bright, then dark, then bright again. In some cases, not all phases are sufficiently large to provide an observable intensity change; for example, a number of spikes in the example data shown in this manual were recognizable only from their negative phase, and thus only a low-intensity region was observable for some electrodes, as with electrode B11 (bottom row of pixels) in Fig. 4.2.

With all selected electrodes plotted, the progression of this triphasic intensity is readily observable from top to bottom, providing an easily interpretable indication of the following features: (i) the existence of a traveling AP, (ii) the direction and speed of propagation of the AP, (iii) the duration of the spike waveforms recorded on each of the electrodes, and (iv) the relative magnitudes of the peak voltages on each electrode. In the example shown in Fig. 4.2, anterograde propagation can be seen as the dark pixels on each electrode traveling from top to bottom (i.e., from B8 to B11) as time progresses.

The user can interact with the Kymograph (A7) to obtain a manual estimate of the propagation velocity. Clicking the “Manual PV calculation” button in the Kymograph Propagation Velocity Tools (A8) allows the user to draw a line on the kymograph. The end points of the line can be adjusted once it has been drawn by clicking and dragging. As shown in the example in Fig. 4.2, the end points of the line should align with the uppermost end of the pixel in the upper electrode selected for manual calculation to

the lowermost end of the pixel in the lower electrode. This ensures that the calculated distance between the two points on the kymograph corresponds to the actual spacing between the electrodes. Once the line is in the desired position, double clicking it finalizes the calculation, and the resulting manual estimate is output in the text in the Kymograph Propagation Velocity Tools (A8).

4.3.5 Audio playback

The user may also interact with the recorded signals via an Audio Playback (A9) function. This feature takes advantage of the ability of the human auditory system to recognize sound patterns and is related to the fact that many electrophysiologists rely on the audio outputs of amplifiers to detect spikes. The voltage data are normalized and converted to sound intensities, and each electrode is assigned a tone (single audio frequency). Based on this conversion, when the magnitude of the deviation of the voltage signal from the mean increases on a given electrode, the tone assigned to that electrode becomes louder. In this way, as an AP propagates from one electrode to the next, the recorded spikes can be heard as a progression in tones over time with the tone frequency sequentially increasing for anterograde propagation and decreasing for retrograde propagation.

A timer is provided to show the user the time in the recording corresponding to the audio playback time. To slow down the playback to a speed at which the spike durations and inter-electrode delays are readily detectable by the human ear, the playback is executed at an audio sampling rate of 2 kHz, and the data are resampled at a rate of 500 times the ratio of the audio sampling rate to the recording sampling rate. This results in an approximately 500-fold time dilation; that is, a time period of 1 ms in the recording corresponds to approximately 0.5 s in the audio playback. Left uninterrupted, the audio playback plays 1 s of the recorded data, corresponding to 500 s of playback time. The user may also choose from a list of different chord options to play different sequences of notes.

The start time for the audio playback can be selected by typing the desired time into the Audio Playback textbox (A9). Clicking the “Start” button begins the audio playback and the timer. The audio playback can also be paused, resumed, and stopped by clicking the corresponding buttons in the Audio Playback (A9) section.

5 Spike Sorting GUI

The Spike Sorting GUI of µSpikeHunter can be opened by clicking the Multi-Spike Analysis Button (A10) in the Main GUI. This opens a new window with plots of spike overlays for each electrode and a collection of tools for spike sorting and source cluster analysis. A source cluster is a collection of sorted propagation sequences considered to arise from the same neurite. This section gives an overview of the objects in the Spike Sorting GUI and describes the spike sorting process and results.

***Note**: The Spike Sorting GUI is tied to the Main GUI. Closing the Main GUI while the Spike Sorting GUI is open will also close the Spike Sorting GUI.*

5.1 List of objects in Spike Sorting GUI

This section shows again the labeled diagram of the Spike Sorting GUI with brief descriptions of each labeled object in the diagram. The objects in the Spike Sorting are labeled in orange and numbered S1–S7, and the file saving object is labeled in purple and numbered F4.

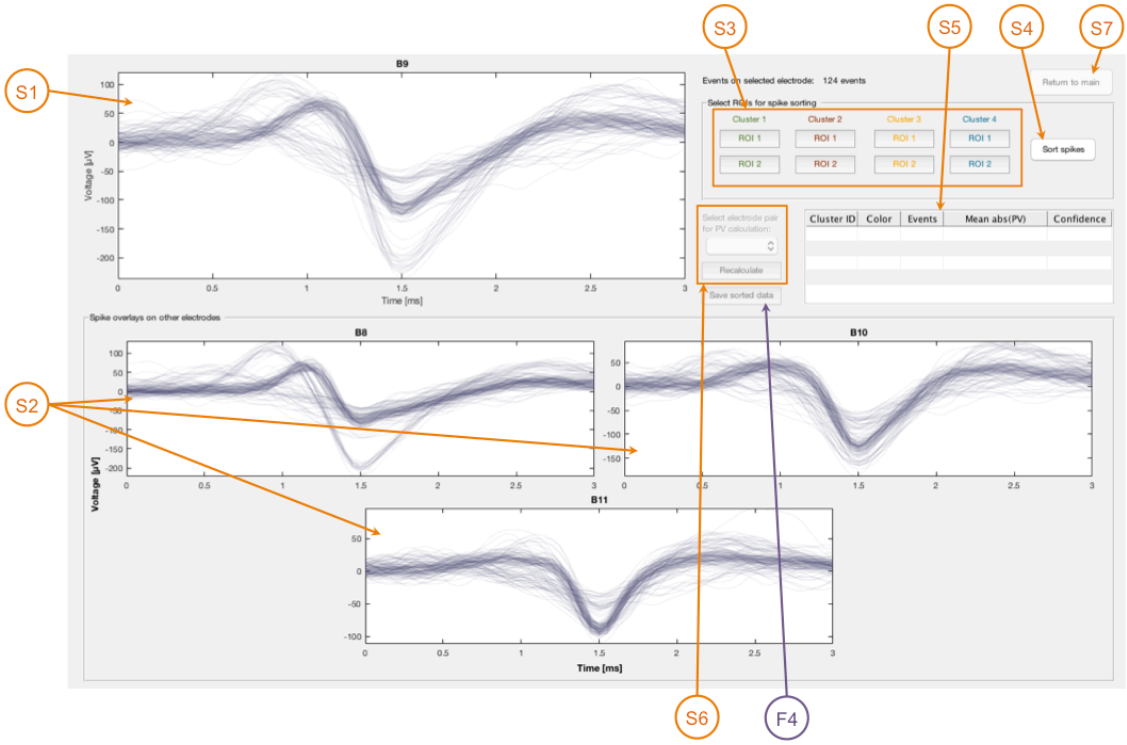

Spike Sorting GUI

(S1) **Event Electrode Spike Overlay Plot**: Shows a plot of all the events on the event electrode detected as part of propagation sequences aligned based on their minima

(S2) **Other Electrode Spike Overlay Plots**: Show plots of events corresponding to the events detected on the event electrode on each of the other electrodes

(S3) **ROI Definition Tools**: Allow the user to draw one or two ROIs for up to four clusters to sort the plotted events

(S4) **Sort Spikes Button**: Sorts the events into source clusters based on the defined ROIs and outputs the results into the Sorting Results Table

(S5) **Sorting Results Table**: Displays the results of the spike sorting, including the cluster ID, plotting color, number of events, and mean propagation speed for each cluster

(S6) **Cluster Propagation Velocity Electrode Selection**: Allows the user to select the electrode pair for calculating the CPV

(S7) **Return to Main GUI Button**: Sends cluster IDs and CPV estimates back to the Event List (A3) in the Main GUI

Saving files

(F4) **Save Sorted Data Button**: Saves a CSV file for each source cluster with the spike times on each electrode, the CPV, the SPV, and the CPV and SPV confidence indices for each propagation sequence in that cluster

5.2 Spike overlays and ROI definition

When it opens, the Spike Sorting GUI shows plots of all of the events detected on the event electrode in the Event Electrode Spike Overlay Plot (S1) and corresponding events on all other electrodes in the Other Electrode Spike Overlay Plots (S2). The number of detected propagation sequences is given beside the Event Electrode Spike Overlay Plot (S1). The events for each electrode are aligned about their peak voltage values (maxima for positive phase detection and minima for negative phase detection).

The user may draw one or two regions of interest (ROIs) on the Event Electrode Spike Overlay Plot (A1) for up to four source clusters for the spike sorting process. An ROI is drawn by clicking one of the ROI buttons for one of the clusters in the ROI Definition Tools (R3). Any combination of ROIs can be drawn in any order; that is, ROI 2 can be drawn for a cluster without first drawing ROI 1, and ROIs for each cluster can be drawn without first defining ROIs for clusters with lower cluster IDs.

Once an ROI has been drawn, the locations of its edges can be adjusted by clicking and dragging. ROIs may also be deleted by right clicking and selecting “Delete” from the menu that appears. If the button for an ROI that has already been drawn is clicked, that ROI is deleted and the user may redraw it.

Spikes are assigned to source clusters sequentially from Cluster 1 (green) to Cluster 4 (blue) and taken out of the sorting pool once they have been assigned a cluster. This means that ROIs should be drawn more selectively for clusters with lower cluster IDs and ROIs for clusters with higher cluster IDs may be drawn to encompass spikes from clusters with lower cluster IDs. An example of this is described in more detail in the next section.

Note: *When drawing an ROI in a region where the signals are rapidly changing (i.e., have a steep positive or negative slope), the user should bear in mind that µSpikeHunter is dealing with discrete data and ensure the height of the ROI is sufficiently large to capture at least one data point for each spike. See Fig. 5.1 on the next page for an example.*

In regions where the voltage is rapidly changing, the recorded voltage at one sampling point is much higher or lower than that at the subsequent sampling point. This means that if the height of the ROI is smaller than the magnitude of this change, one data point may be above the ROI and the next may be below it; thus, even though the plotted trace appears to pass through the ROI, the event would not be assigned to the cluster for that ROI; this is the case for the results in Fig. 5.1(a). Although drawing an ROI with a greater height fixes this problem (Fig. 5.1(b)), the problem is best avoided by drawing ROIs in regions of low change (i.e., near the peaks of the spikes), as in Fig. 5.1(c).

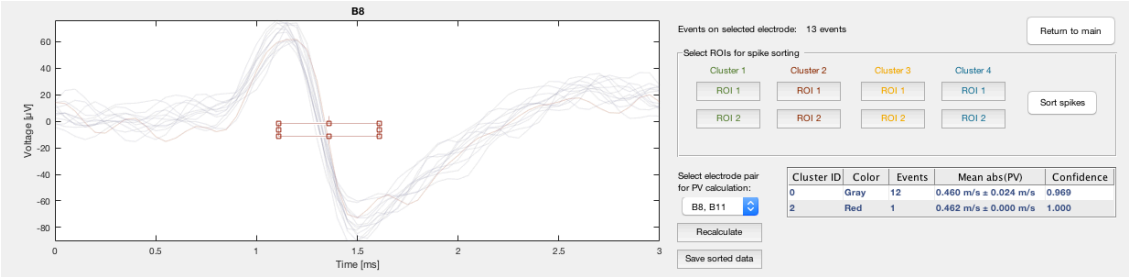

(a) Sorting results for ROI with small height in high-gradient region

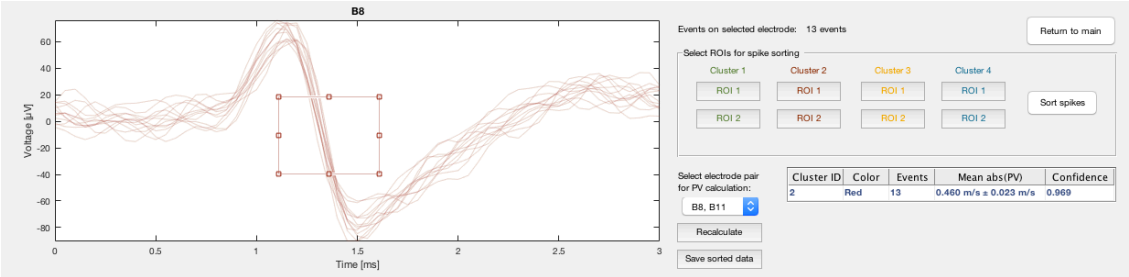

(b) Sorting results for ROI with large height in high-gradient region

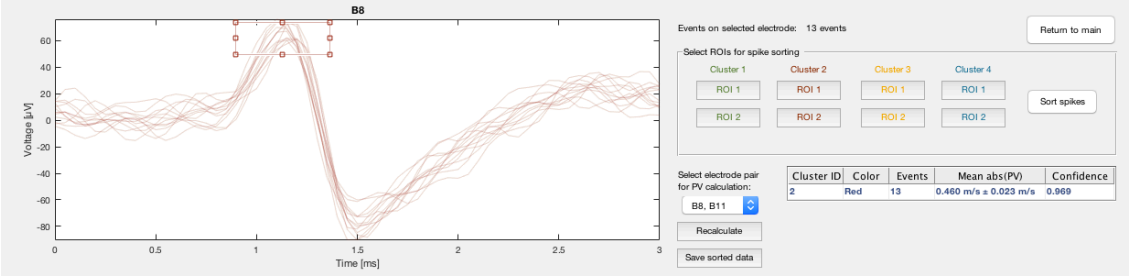

(c) Sorting results for ROI in low-gradient region (recommended)

Fig. 5.1. *Examples of spike sorting results on the event electrode for (a) an ROI with a small height in a region of rapidly changing voltage, (b) an ROI with a large height in a region of rapidly changing voltage, and (b) an ROI drawn near a voltage peak (recommended).*

5.3 Spike sorting process and results

Clicking the Sort Spikes Button (S4) sorts the spikes into source clusters based on the ROIs drawn on the Event Electrode Spike Overlay Plot (S1) and outputs the results into the Sorting Results Table (S5). An example of the spike sorting result is shown in Fig. 5.2.

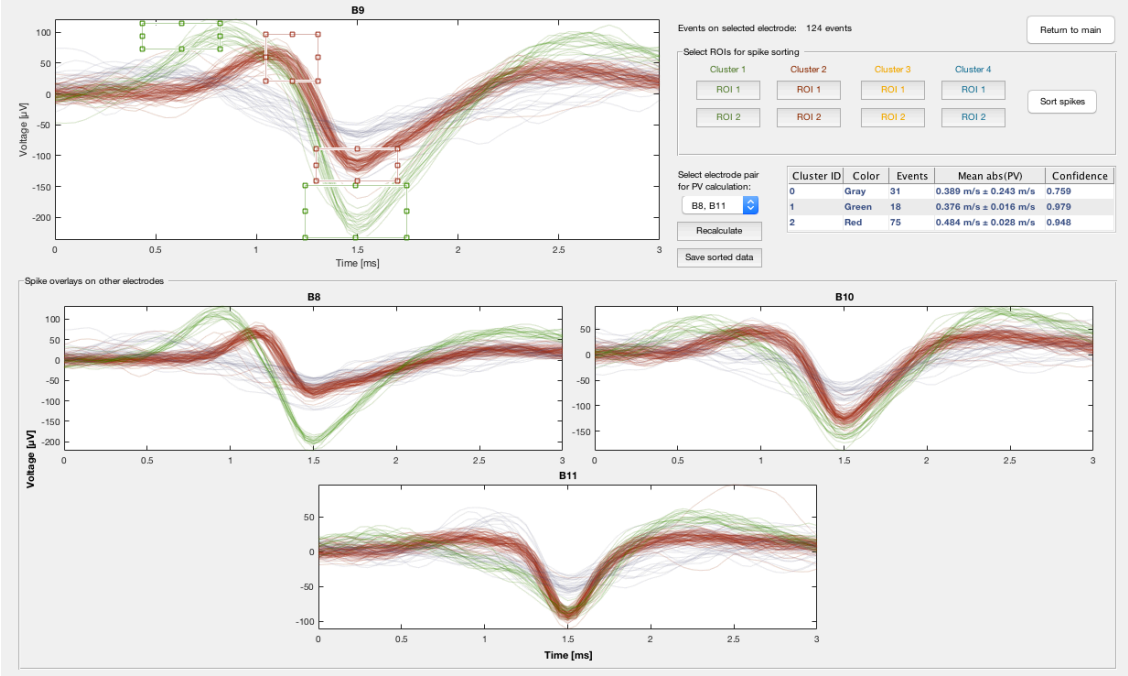

Fig. 5.2. Analysis panel of Main GUI. See the diagram on page 12 for names and labels of analysis objects.

Spikes are assigned to a cluster if the voltage trace passes through all of the ROIs drawn for that cluster and if they have not been sorted to a cluster with a lower cluster ID. The spike sorting algorithm progresses from Cluster 1 (green) to Cluster 4 (blue), and once a spike has been assigned to a cluster, it is removed from the sorting pool. The spikes in the Event Electrode Spike Overlay Plot (S1) and the Other Electrode Spike Overlay Plots (S2) are colored to correspond to the cluster to which they have been assigned.

Any spikes not assigned to Clusters 1–4 after the sorting process are assigned to Cluster 0 and remain the same color as in the original plot. Cluster 0 may be considered to correspond to a separate neurite or as a cluster of unsorted events. The ROIs remain on the event electrode plot after the spikes have been sorted, and the user may adjust or delete the ROIs and re-sort the spikes as desired.

In the example shown in Fig. 5.2, two source clusters, Clusters 1 (green) and 2 (red), have been defined using two ROIs each. Note that although a number of spikes in Cluster 1 pass through both ROIs for Cluster 2, these spikes are still assigned to Cluster 1. This is because of the sequential nature of the sorting process described

here and in Section 5.2: once the green spikes are assigned to Cluster 1, they are removed from the sorting pool and are no longer available to be assigned to Cluster 2.

The Sorting Results Table (S5) is then populated with the spike sorting results. The first two columns give the cluster ID and the corresponding color for that cluster. The third column gives the number of events in each cluster. The fourth and final columns give the average cluster propagation velocity (CPV) estimate for the cluster and the corresponding average confidence index. The CPV is calculated based on the cluster-based redefinitions of the event times, which are obtained using the procedure described in the next section, and the confidence index is an indication of the intra-cluster intra-electrode similarity of the spike shapes on the two electrodes selected for CPV estimation.

5.4 Cluster propagation velocity estimation

This section describes the method used to calculate the CPV estimate. First, each spike is realigned by maximizing the cross-correlation with every other event in the cluster. The new event time for each event in a cluster is then defined as the time at which the sum of all of the realigned traces is minimized or maximized (for negative or positive phase event detection, respectively). For a more detailed explanation of this process, the user is referred to the paper on this program []. Whereas using the timing of the peak voltage for each event would yield an unreliable approximation of the event time, minimizing or maximizing the sum of the aligned events yields a more accurate estimation.

This event time estimation procedure is performed for each electrode, and the propagation velocity of each propagation sequence is then defined based on the spike times on the two most distant electrodes. However, the user may choose to calculate the propagation velocity using any pair of electrodes by selecting the desired pair from the Cluster Propagation Velocity Electrode Selection (S6) and clicking the "Recalculate" button. The mean propagation speed for each cluster is then calculated and presented in the Sorting Results Table (S5) along with the standard deviation. If the standard deviation of the CPV is equal to or greater than the average CPV, the result is given as "Undefined" to indicate that the propagation sequences in the cluster likely do not correspond to a single neurite.

The Sorting Results Table (S5) also gives a confidence index for the CPV estimate. This confidence index is based on the spike realignment process. As stated above, the cross-correlation between each event and every other event on the same electrode sorted into the same cluster is calculated to perform the realignment. The maximum value of the autocorrelation-normalized cross-correlation is obtained for each of these cross-correlations and averaged for each event. Thus, each event on each electrode is assigned an event-based confidence index in the range [0, 1] that indicates the confidence of its realignment time based on the intra-electrode intra-cluster cross-correlations. When an electrode pair is selected for the CPV estimation, the CPV confidence index for each propagation sequence is obtained as the average of the two event-based indices for the events in the propagation sequence on the selected electrodes. This confidence index indicates the degree of similarity of the spike shapes on the two electrodes selected for CPV estimation for spikes within the same sorting cluster.

It should be noted that the CPV and the SPV are estimating different quantities: the CPV essentially estimates the delay between the peak voltages arriving on the two selected electrodes based on the timing of the peak voltage of a "master spike" for each cluster on each electrode, whereas the SPV estimates the lag for a single propagation sequence based on matching the waveforms recorded on the selected electrodes. Thus, if the waveforms on the two selected electrodes are different, the resulting propagation velocity estimates may also differ because the lag that yields the highest cross-correlation for the SPV may not correspond to the delay between the

peak voltages on the two electrodes. It should also be noted that the CPV is more robust against noise than the SPV.

5.5 Returning results to Main GUI

Clicking the Return to Main GUI Button (S7) or closing the Spike Sorting GUI after spike sorting has been conducted updates the Event List (A3) in the Main GUI with the cluster ID and the CPV estimate for each event. An example of the appearance of the analysis panel with this updated list is shown in Fig. 5.3.

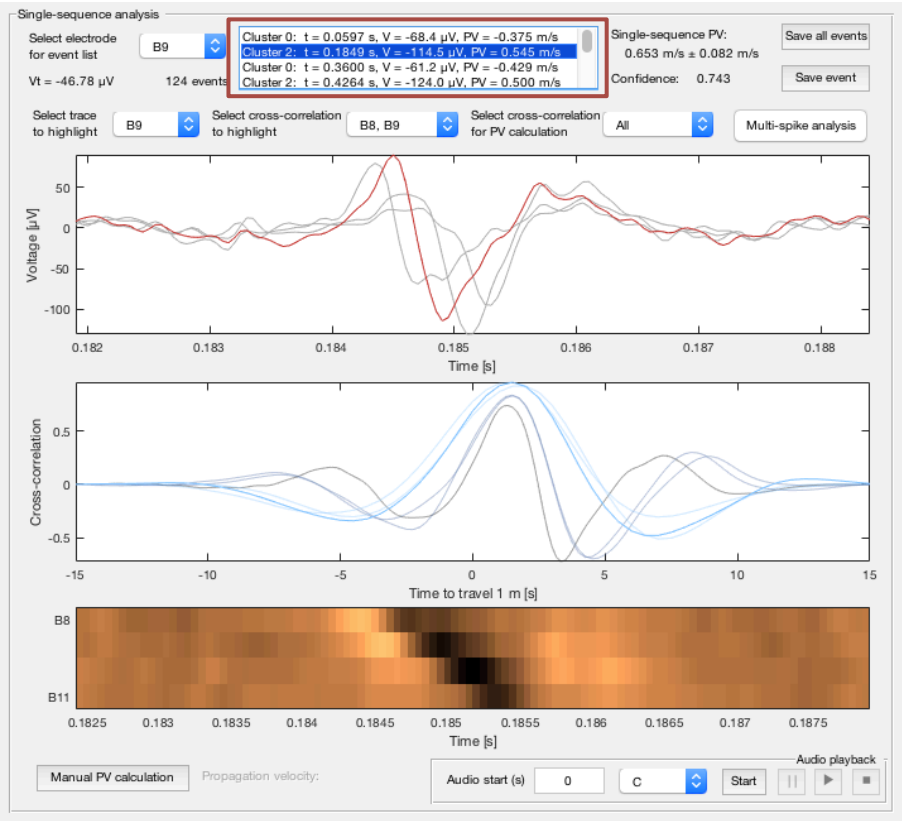

Fig. 5.3. Analysis panel of Main GUI with the Event List (A3) updated to include the cluster ID and CPV estimate for each event.

6 Saving files

The analysis results obtained using µSpikeHunter can be exported in different formats for further external analysis using a number of export buttons in the Main and Spike Sorting GUIs. This section presents descriptions of the four types of files that can be exported from µSpikeHunter.

6.1 Information contained in filenames and data file headers

All files are saved with filenames and headers containing information about the analysis so that the steps to analyze the data can be repeated to obtain the same results. The base filename and header for each type of saved file contains the following information: the filename of the recorded data file being analyzed, as given in the Filename Textbox (D2); the start and end electrodes selected for analysis, as defined in the Electrode Selection Menus (D7); the start time and duration selected for analysis, as defined in the Analysis Start Time and Duration Menus (D6); and the number of standard deviations selected for the event detection threshold, as defined in the Event Detector Parameters (D10).

Additional information is added for each specific type of saved file, as will be described in the corresponding sections here. An example of how the information is organized in the base filename is presented below. The same information is also included in the file header. In the case of a custom setup, the electrodes are simply assigned numbers for the second item in the list (e.g., "1-4" in the case of four electrodes), the start time and duration are not included in the filename, and the file header does not contain any information about the electrodes or analysis times.

Example: filename1_B1-B4_0s_60s_-5sig_[...].dat

- *Name of recording file*: filename1
- *Electrodes selected for analysis*: electrodes B1 to B4 (i.e., B1, B2, B3, B4)
- *Start time of analysis*: 0 s
- *Analysis duration*: 60 s
- *Event detection threshold*: 5 standard deviations, negative phase detection

6.2 All analyzed data

Clicking the Save Analysis Data Button (F1) in the Main GUI saves a CSV file with the time stamps in milliseconds and voltage data in microvolts for each selected electrode in the time range selected for analysis. This allows the user to analyze all the data selected for analysis using software other than µSpikeHunter or Multi Channel Analyzer. The organization of the data in the CSV file is the same as that required for custom setup recording files (see Fig. 3.1). The base filename described in Section 6.1 is appended with the word "data" for this type of file.

6.3 All detected propagation sequences

Clicking the Save All Events Button (F2) in the Main GUI saves a CSV file listing all detected propagation sequences in the analyzed data. Each pair of columns giving the time in milliseconds at which the peak voltage value occurred and the peak voltage value in microvolts for the set of events on each electrode in each propagation sequence. The data are organized in the CSV file as shown in Fig. 4.2. The base filename described in Section 6.1 is appended with the word “events” for this type of file.

	B1		B2		B3		B4	
	Time (ms)	Peak (µV)	Time (ms)	Peak (µV)	Time (ms)	Peak (µV)	Time (ms)	Peak (µV)
	1	2	3	4	5	6	7	8
1	184.7000	-69.1482	184.9000	-114.4701	185.1000	-130.9210	185.3000	-95.3324
2	426.1500	-74.9608	426.3500	-124.0116	426.6000	-120.3924	426.7500	-81.2121
3	547.4000	-59.0584	547.6000	-88.0666	547.8500	-104.7093	548	-83.1314
4	587.4000	-221.7842	587.6000	-226.4727	587.8500	-165.1386	588.1500	-92.6454
5	904.7500	-62.2663	905.0500	-109.7543	905.2000	-136.4320	905.4000	-103.1739
6	1.3728e+03	-84.6942	1.3730e+03	-123.0794	1.3733e+03	-143.2042	1.3734e+03	-94.8937
7	3.7134e+03	-83.6249	3.7136e+03	-118.5828	3.7139e+03	-130.7839	3714	-102.3788
8	4.4322e+03	-72.1916	4.4324e+03	-110.6316	4.4325e+03	-136.4868	4.4327e+03	-94.7840
9	6.0606e+03	-74.4673	6.0608e+03	-113.3734	6061	-106.8479	6.0612e+03	-92.7003
10	6.6605e+03	-94.2631	6.6607e+03	-129.0565	6.6609e+03	-143.8897	6.6611e+03	-95.4421
11	6.9086e+03	-78.4429	6.9088e+03	-122.3665	6909	-128.9743	6.9092e+03	-87.8473
12	7.6668e+03	-86.2570	7.6671e+03	-131.4693	7.6673e+03	-128.3985	7.6675e+03	-97.7452
13	7.9975e+03	-192.3921	7.9977e+03	-221.3455	7998	-145.5622	7.9983e+03	-88.2860
14	8.1491e+03	-93.3857	8.1493e+03	-108.3285	8.1496e+03	-116.0330	8.1497e+03	-97.4162
15	8.5761e+03	-70.6013	8.5763e+03	-116.2249	8.5766e+03	-124.6696	8.5767e+03	-85.3797

Fig. 6.1. Organization of file listing the times (ms) and amplitudes (µV) of the events in all propagation sequences. The columns are labeled to correspond to the electrodes in one of the microchannels in the example µEF configuration shown in Fig. 1.1.

6.4 Traces for a single propagation sequence

Voltage traces for a single propagation sequence can be exported by clicking the Save Event Button (F3) in the Main GUI. The created file contains the voltage trace data for the selected event in the Event List (A3) with the same time window as shown in the Voltage Trace Plot (A4). The file is a CSV file with the first column giving the time stamps and the second to last columns giving the recorded voltage at each sampling time on the selected electrode. This file can be used to make plots of propagation sequences with the desired format using external software. The data are organized in the CSV file as shown in Fig. 6.2.

	Time (ms)	B1 (µV)	B2 (µV)	B3 (µV)	B4 (µV)
	1	2	3	4	5
1	181.8500	-2.1660	3.5918	7.6770	11.7623
2	181.9000	4.2772	8.4173	9.1302	9.2399
3	181.9500	8.0609	11.4333	7.5674	4.4417
4	182	8.9657	13.4348	5.1820	2.8241
5	182.0500	9.2124	14.5590	5.7029	6.5529
6	182.1000	8.5818	13.1058	8.5544	12.0913
7	182.1500	6.0868	9.1576	10.2269	13.8187
8	182.2000	2.9337	4.8804	10.1447	11.5704
9	182.2500	1.9193	3.2902	10.9672	9.2124
10	182.3000	2.0289	3.7288	12.8316	8.6641

Fig. 6.2. First 10 samples of voltage traces for a single propagation sequence saved to a CSV file. The file lists the time stamps (ms) and the voltage (µV) recorded on each electrode at that time over the same window as shown in the Voltage Trace Plot (A4) for the selected event in the Event List (A3). The columns are labeled to correspond to the electrodes in one of the microchannels in the example µEF configuration shown in Fig. 1.1.

The additional information added to the filename and header for this type of file is the number of the saved event. For example, filename1_B1-B4_0s_60s_-5sig_**seq7**.dat corresponds to the single-sequence file for the seventh propagation sequence detected in the analyzed time range, and the event number is also given in the header. All other information included in the filename and header is as described in Section 6.1.

6.5 Spike sorting results

The spike sorting results can be saved to CSV files by clicking the Save Sorted Data Button (F4) in the Spike Sorting GUI. This button saves a CSV file for each source cluster, including Cluster 0. For example, for the spike sorting results shown in Fig. 5.2, clicking the Save Sorted Data Button (F4) would create three CSV files for Clusters 0, 1, and 2. The information included in each file is as follows for each propagation sequence in the cluster: the index of the propagation sequence, the time at which the spike arrives on the event electrode, the time at which the spike arrives on each of the electrodes, the CPV estimate and its confidence index, and the SPV and its confidence index. The CPV and SPV estimates are obtained using the electrode pairs selected in the Cluster Propagation Velocity Electrode Selection Menu (S6) and the Single-sequence Propagation Velocity Menu (A6), respectively. See Sections 5.4 and 4.3.3 for explanations of the CPV and SPV calculations. The data are organized in the CSV file as shown in Fig. 6.3.

	No.	B2 time (ms)	B1 time (ms)	B2 time (ms)	B3 time (ms)	B4 time (ms)	CPV	Conf.	SPV	Conf.
	1	2	3	4	5	6	7	8	9	10
1	8	587.6000	587.4000	587.6000	587.8500	588.1500	0.4000	0.9628	0.5000	0.7361
2	18	7.9977e+03	7.9975e+03	7.9977e+03	7.9979e+03	7.9982e+03	0.4286	0.9666	0.4615	0.7844
3	28	1.4090e+04	1.4090e+04	1.4090e+04	1.4090e+04	1.4090e+04	0.4000	0.9757	0.4615	0.8214
4	32	14601	1.4601e+04	14601	1.4601e+04	1.4602e+04	0.4000	0.9561	0.4615	0.6877
5	34	1.4639e+04	1.4639e+04	1.4639e+04	1.4640e+04	1.4640e+04	0.4286	0.9704	0.5455	0.7367
6	35	14812	1.4812e+04	14812	1.4812e+04	1.4813e+04	0.4000	0.9698	0.5000	0.8382
7	37	1.4929e+04	1.4928e+04	1.4929e+04	1.4929e+04	1.4929e+04	0.4000	0.9657	0.4286	0.8823
8	41	1.5270e+04	1.5269e+04	1.5270e+04	1.5270e+04	1.5270e+04	0.4286	0.9726	0.5455	0.7902
9	47	1.5621e+04	1.5621e+04	1.5621e+04	1.5622e+04	1.5622e+04	0.4000	0.9560	0.4286	0.8332
10	51	1.6038e+04	1.6038e+04	1.6038e+04	1.6038e+04	1.6039e+04	0.4000	0.9747	0.5000	0.7824

Fig. 6.3. Organization of the sorting results file. The first column gives the event number, the second gives the time of the peak voltage on the event electrode, the next columns give the times of the peak voltages on all electrodes, and the final four columns give the CPV and SPV estimates with their corresponding confidence indices. The columns are labeled to correspond to the electrodes in one of the microchannels in the example μEF configuration shown in Fig. 1.1 with B2 as the event electrode.

The additional information added to the filename and header for this type of file is the event electrode, the electrode pairs used for the CPV and SPV estimates, and the cluster ID. For example, filename1_B1-B4_0s_60s_-5sig_**selB2_CPVB1-B4_SPVall_clst1**.dat corresponds to the sorting results file for all propagation sequences assigned to Cluster 1 with sorting performed on electrode B2, and the CPV

and SPV estimates in the file were calculated using electrodes B1 and B4 and the average of all electrode pairs, respectively. The same information is included in the file header. All other information included in the filename and header is as described in Section 6.1.

7 Glossary of terms

A number of terms have been adopted for ease of explanation in this user manual. This section provides the definitions of these terms for reference by the user.

Cluster (or source cluster): When spike sorting is performed, the propagation sequences obtained based on event detection applied to a single electrode are sorted into source clusters. Clusters of propagation sequences are considered to arise from different APs propagating along the same axon.

Cluster identification (cluster ID): The cluster ID is a number ranging from 0 to 4 that corresponds to the cluster into which a given spike has been sorted.

Cluster propagation velocity (CPV): The CPV is an estimate of the propagation velocity obtained based on the alignment of all spikes sorted into a cluster, as described in Section 5.3.

Event: An event is any portion of a voltage trace recorded on an electrode in which the voltage signal surpasses the user-defined threshold for event detection. Events may be either electrode noise, instrument noise, or spikes.

Event electrode: The term “event electrode” is used to refer to the electrode selected to populate the list of events in the Main GUI. In the Spike Sorting GUI, the ROIs used for spike sorting are drawn on the spike overlay plot for the event electrode.

Graphical user interface (GUI): A GUI is a computer program that allows the user to interact with a computer through graphical elements, such as buttons, text boxes, and plots. µSpikeHunter consists of two GUIS: the Main GUI and the Spike Sorting GUI.

Instrument noise: The term “instrument noise” in this manual is used to refer to (usually large-amplitude) fluctuations in the voltage signal that are produced by disturbances in the environment of the recording system. These disturbances generally have approximately the same timing and shape across all recording electrodes.

Microelectrode array (MEA): An MEA consists of multiple microelectrodes embedded in a substrate. MEAs can be used to record spikes as well as evoke neuronal activity.

Microelectrode–microfluidic (µEF) device: A µEF device is a compartmentalized cell culture device that is composed of a microfluidic device with integrated microelectrodes for electrophysiology. In its simplest configuration, it is composed of a microfluidic device aligned with and mounted on a MEA. The dimensions of the microchannels in µEF devices are designed such that somata are excluded from the microchannels whereas axons are able to grow through the channels. See Fig. 1.1.

Propagation sequence (or sequence): A propagation sequence is defined as a collection of temporally linked events recorded on all electrodes selected for analysis. Sequences are considered to be representative of propagating APs.

Region of interest (ROI): An ROI is a rectangular region in event time–voltage space defined by the user in the Spike Sorting GUI. One or two ROIs can be defined for up to four clusters to perform spike sorting.

Signal noise: The term “signal noise” in this manual is used to refer to the combination of electrode noise and instrument noise that accompanies any electrical recording.

Single-sequence propagation velocity (SPV): The SPV is an estimate of the propagation velocity obtained based on the cross-correlation of the voltage traces in a single propagation sequence as described in Section 4.3.3.

References

[1] J. W. Park, B. Vahidi, A. M. Taylor, S. W. Rhee, and N. L. Jeon, “Microfluidic culture platform for neuroscience research,” *Nat. Protoc.*, vol. 1, no. 4, pp. 2128–2136, 2006.

[2] L. Pan *et al.*, “An in vitro method to manipulate the direction and functional strength between neural populations,” *Front. Neural Circuits*, vol. 9, no. July, pp. 1–14, 2015.

[3] T. T. Kanagasabapathi *et al.*, “Functional connectivity and dynamics of cortical-thalamic networks co-cultured in a dual compartment device,” *J. Neural Eng.*, vol. 9, no. 3, 2012.

[4] Y. Berdichevsky, K. J. Staley, and M. L. Yarmush, “Building and manipulating neural pathways with microfluidics,” *Lab Chip*, vol. 10, no. 8, pp. 999–1004, 2010.

[5] R. Habibey, S. Latifi, H. Mousavi, M. Pesce, E. Arab-Tehrany, and A. Blau, “A multielectrode array microchannel platform reveals both transient and slow changes in axonal conduction velocity,” *Sci. Rep.*, vol. 7, no. 1, pp. 1–14, 2017.

[6] B. J. Dworak and B. C. Wheeler, “Novel MEA platform with PDMS microtunnels enables the detection of action potential propagation from isolated axons in culture,” *Lab Chip*, vol. 9, no. 3, pp. 404–410, 2009.

[7] E. Biffi *et al.*, “A microfluidic platform for controlled biochemical stimulation of twin neuronal networks,” *Biomicrofluidics*, vol. 6, no. 2, pp. 1–10, 2012.

[8] E. Neto *et al.*, “Compartmentalized Microfluidic Platforms: The Unrivaled Breakthrough of In Vitro Tools for Neurobiological Research,” vol. 36, no. 46, pp. 11573–11584, 2016.